Strongly interacting matter:
Analysis of QCD phase diagram by Thermodynamic Geometry

Daniele Lanteri

UNIVERSITÀ degli
STUDI
di CATANIA

DIPARTIMENTO
di FISICA e
ASTRONOMIA

STRONGLY INTERACTING MATTER:
ANALYSIS OF QCD PHASE DIAGRAM BY THERMODYNAMIC GEOMETRY

by

DANIELE LANTERI

A Dissertation

Presented to the Department

of Physics and Astronomy

of Catania University

in Candidacy for the Degree
of Doctor of Philosophy

2020/2021

Author: *Daniele Lanteri*

Dipartimento di Fisica e Astronomia

Università di Catania

Italy

Supervisor: *Paolo Castorina*

Istituto Nazionale Fisica Nucleare

Sezione di Catania

Italy

Vincenzo Branchina

Dipartimento di Fisica e Astronomia

Università di Catania

Italy

Reviewers: *Marco Ruggieri*

School of Nuclear Science and Technology

Lanzhou University

China

Helmut Satz

Fakultät füur Physik

Universitäat Bielefeld

Germany

Contents

List of Figures

List of Tables

Chapter 1

Outline of the PhD research and publication list

My PhD research focused on the study of the Quantum Chromodynamics (QCD) phase transition, both from a phenomenological and a theoretical point of view.

Three main research lines have been considered (the number in parentheses refers to the list of publication 1.1):

- in papers [1], [2] and [3] the study of some phenomenological topics of the phase transition has been carried out. In particular, I studied universality in light and heavy particles collisions at high energy, by looking at some experimental observables: the strangeness suppression factor γ_s and the yields of multi-strange hadrons, the average transverse momentum, and the elliptic flow scaled by the participant eccentricity, in pp, pPb and AA collisions in Ref.s [1, 2], while in Ref. [3] the universality behaviour is analyzed in e^+e^- annihilation. These aspects are discussed in Sec. 2.6;

- in Ref. [4] I analyzed the effect of the crossover from quarks and gluons to hadrons in the early universe on the cosmological scalars and on the gravitational wave spectrum;

- the main line of my research regards the study of the phase transition in field theory, and in QCD in particular, in the framework of thermodynamic geometry: the thermodynamic theory of fluctuations allows

to define a manifold spanned by intensive thermodynamic variables, $\{\theta_k\}$ with $k = 1,\ 2,\ \ldots,\ N$, and to equip this with the notion of a distance, $d\ell^2 = g^{\mu\nu}(\theta_1, \theta_2, \cdots\ \theta_N)\ d\theta_\mu\ d\theta_\nu$, where $g^{\mu\nu}$ is the metric tensor. The metric tensor is defined as $g^{\mu\nu} = \partial^2 \log \mathcal{Z}/\partial\theta_\mu\, \partial\theta_\nu$, $\mathcal{Z}$ being the partition function, and measures the probability of fluctuation between two equilibrium states. I applied this method to LATTICE QCD and HRG models in Ref.s [5, 6], to Nambu-Jona Lasinio model in Ref. [7], and to study the effect of fluctuations in Quark-Meson model in Ref. [8]. Ref.s [5–8] are the first application of thermodynamic geometry to field theory at finite temperature and density.

The plan of the thesis is as follows: in Chapter 2 I introduce the theory of strongly interacting matter and the main topics regarding its phase diagram. In Chapter 3 I study same methods and models describing QCD at finite temperature and density. I study QCD phase transition in the early Universe in Chapter 4. In Chapter 5 I briefly review the theory of thermodynamic geometry, and apply it to the methods and models studied in Chap. 3. Finally, in Chapter 6, I draw some comments and conclusions.

1.1 List of publications regarding the Thesis

[1] Paolo Castorina, Alfredo Iorio, Daniele Lanteri, Martin Spousta, and Helmut Satz. Universality in Hadronic and Nuclear Collisions at High Energy. *Phys. Rev. C*, 101(5):054902, 2020, DOI: 10.1103/PhysRevC.101.054902.

[2] Paolo Castorina, Alfredo Iorio, Lanteri Daniele, Helmut Satz, and Martin Spousta. Universality in High Energy Collisions of small and large systems. Proceedings: 40th International Conference on High Energy Physics (ICHEP) 2020

[3] P. Castorina, D. Lanteri, and H. Satz. Strangeness enhancement and flow-like effects in e^+e^- annihilation at high parton density. *Under review*, arXiv:2011.06966.

[4] P. Castorina, D. Lanteri, and S. Mancani. Deconfinement transition effects on cosmological parameters and primordial gravitational waves

spectrum. *Phys. Rev. D*, 98(2):023007, 2018, DOI: 10.1103/PhysRevD.98.023007.

[5] Paolo Castorina, Mauro Imbrosciano, and Daniele Lanteri. Thermodynamic Geometry and Deconfinement Temperature. *Eur. Phys. J. Plus*, 134(4):164, 2019, DOI: 10.1140/epjp/i2019-12617-y.

[6] P. Castorina, M. Imbrosciano, and D. Lanteri. Thermodynamic Geometry of Strongly Interacting Matter. *Phys. Rev. D*, 98(9):096006, 2018, DOI: 10.1103/PhysRevD.98.096006.

[7] P. Castorina, D. Lanteri, and S. Mancani. Thermodynamic geometry of Nambu - Jona Lasinio model. *Eur. Phys. J. Plus*, 135(1):43, 2020, DOI: 10.1140/epjp/s13360-019-00004-3.

[8] Paolo Castorina, Daniele Lanteri, and Marco Ruggieri. Fluctuations and thermodynamic geometry of the chiral phase transitiont. *under review*, arXiv: 2010.03310 [hep-ph].

1.2 Publications in other research areas

[9] Daniele Lanteri, Shen-Song Wan, Alfredo Iorio, and Paolo Castorina. Stability of Schwarzschild (Anti)de Sitter black holes in Conformal Gravity. *Under review*, arXiv: 2009.14087 [hep-th].

[10] Paolo Castorina, Alfredo Iorio, Daniele Lanteri, and Petr Lukes. Gluon Shadowing and Nuclear Entanglement. *Under review*, arXiv: 2003.00112 [hep-ph].

[11] D. Lanteri, D. Carcò, P. Castorina, M. Ceccarelli, and B. Cacopardo. Containment effort reduction and regrowth patterns of the Covid-19 spreading. *Under review*, arXiv: 2004.14701 [q-bio.PE].

[12] D. Lanteri, D. Carco', and P. Castorina. How macroscopic laws describe complex dynamics: asymptomatic population and CoviD-19 spreading. *International Journal of Modern Physics C* 31(8):2050112, 2020, DOI: 10.1142/S0129183120501120.

[13] P. Castorina, A. Iorio, and D. Lanteri. Data analysis on Coronavirus spreading by macroscopic growth laws. *International Journal of Modern Physics C* 31(7):2050103, 2020,
DOI: 10.1142/S012918312050103X.

[14] Paolo Castorina, Silvia Castorina, and Daniele Lanteri. Unified description of thermal behaviors by macroscopic growth laws. *J. of Phys. Communications* 3:061001, 2019
DOI: 10.1088%2F2399-6528%2Fab227f.

[15] P. Castorina and D. Lanteri. Unruh thermalization, gluon condensation and freeze-out. *Phys. Rev. D* 94(7):074022, 2016, DOI: 10.1103/Phys- RevD.94.074022.

Chapter 2

QCD phase diagram

This chapter provides a short introduction to the theory of strongly interacting matter: starting from the theoretical point of view, and phenomenological topics of light and heavy particle collisions, I will go over the main topics of the phase diagram of QCD at finite temperature and baryon chemical potential, giving a schematic overview of the possible signature of the transition from the quark-gluon plasma (QGP) to the hadronic phase. In recent years a new form of matter, the quark-gluon plasma (QGP), was discovered at RHIC and LHC [1–4]. Consequently, the diagram of strongly interacting matter has become the focus of theoretical and experimental attention. Indeed, Quantum Chromodynamics (QCD), the theory of strong interaction, predicts two different phase transitions, which are associated with two opposite quark mass limits: a) for vanishing quark masses (the chiral limit) QCD has an exact global $U\left(N_f\right)_L \times U\left(N_f\right)_R$ symmetry (N_f being the number of quark flavours), to which the so-called chiral transition, responsible for the mass of bound quarks, is associated. b) In the "quenched" limit, i.e. for infinitely heavy quark masses, QCD reduces to a pure $SU(N_c)$ (N_c is the number of colours) gauge theory, which is invariant under a global $Z(N_c)$ center symmetry. The center symmetry is spontaneously broken at high temperatures and densities, i.e. in the QGP phase, and is associated with the confinement/deconfinement phase transition. Both phase transitions are broken explicitly when dynamical quarks are present and are conceptually distinct phenomena of QCD [5].

2.1 On QCD Lagrangian

Matter, in its most basic description, is essentially made of quarks, leptons, vector bosons and Higgs, which interact through four fundamental forces: strong, electromagnetic, weak and gravitation. The strong force is currently described by Quantum Chromodynamics (QCD). The seminal ideas of this theory date back to 1963/64, when the concept of quarks was introduced for the first time by Gell-Mann [6] and Zweig [7]. These new objects, allowed to understood mesons and baryons as bound states of quarks-antiquarks and three quarks, opened the way to define a more fundamental theory: matter is made of blocks of different species or "flavours" (u, d, s, ...), with different quantum numbers, but the same strong interaction. Quarks bring a new internal degree of freedom, named "colour" (the introduction of which is necessary to prevent violation of the Pauli principle), and must be spin-1/2 fermions with a fractional electric charge. Interactions between them are mediated by colourfull massless spin-1 bosons [8], named gluons. Thus, there is an $SU(3)$ symmetry in the interaction among the different colours of quarks. Moreover, this theory reproduces the non-interacting behaviour of quarks at short distances [9–12], i.e. the "asymptotic freedom", and it is a solid generalization of the "parton model", introduced by Feynman [13], i.e. the ideas that hadrons contain point-like constituents with simple properties, that interact each other. Although some of these constituents can be identified with quarks and the parton model has been strikingly successful in describing deep inelastic scattering initial data, it is only a phenomenological description, and the complete theory has been developed over the years starting from symmetries and group properties [11, 12, 14–21], e.g. the fact that only a non-abelian gauge theory has the property of asymptotic freedom. The theory that arises, called Quantum Chromodynamics (QCD), is a renormalized non-abelian gauge theory.

In particular, symmetries are connected with conservation law and are called gauge symmetry if associated with the conservation of a charge. Named N_c the number of colours, and $\psi(x)$ an N_c-component vector, the gauge symmetry acts as a phase when applied to the field ψ [22]:

$$\psi'(x) = \Omega\, \psi(x)\ , \tag{2.1}$$

where Ω is a unitary operator. For $N_c = 3$ colours, the space $SU(3)$ of unitary transformations in colour space is generated by eight infinitesimal transformations, λ_a, introduced by Gell-Mann:

$$\Omega = \exp\left\{ i\ g\ \frac{\lambda^a}{2}\ \theta_a \right\}\ . \tag{2.2}$$

Global symmetry is "promoted" to a local one by postulating that Ω depends on the space-time position, x. Is then added a connection to construct a coherent theory, since derivatives transform inhomogeneously,

$$\partial_\mu \psi'(x) = \Omega(x)\left[\partial_\mu \psi(x) + \Omega^{-1}(x)\partial_\mu \Omega(x)\ \psi(x)\right]\ , \tag{2.3}$$

and one has to include a correction term so that $D'\psi'$ and ψ' have the same homogeneous transformation law. This means that derivative is replaced by the covariant one, D, that transforms as

$$D'_\mu \psi'(x) = \Omega(x)\ D_\mu \psi(x)\ , \tag{2.4}$$

with

$$D_\mu = \partial_\mu + i\ g\ B_\mu(x) \tag{2.5}$$

and

$$B'_\mu(x) = \Omega(x)\ B_\mu(x)\ \Omega^{-1}(x) + \frac{1}{i\ g}\ \left[\partial_\mu \Omega(x)\right]\ \Omega^{-1}(x)\ . \tag{2.6}$$

$B_\mu(x)$ is a vector field of 3×3, traceless, Hermitian matrices, whose trace is an overall phase transformation of ψ. Thus, the invariant kinetic energy term for the matter field ψ is given by

$$\mathcal{L}_\psi = \overline{\psi}\ \overleftrightarrow{D}_\mu \gamma_\mu \psi\ , \tag{2.7}$$

where

$$\overleftrightarrow{D}_\mu = \frac{1}{2}\left(\overrightarrow{D}_\mu - \overleftarrow{D}_\mu\right)\ , \tag{2.8}$$

and γ_μ are the Dirac gamma matrices.

The kinetic energy term for B_μ,

$$\mathcal{L}_{B_\mu} = -\frac{1}{4}\ \mathrm{Tr} G_{\mu\nu} G^{\mu\nu}\ , \tag{2.9}$$

it is easily constructed similar to what is done in QED, by defining a tensor, $G_{\mu\nu}$, that transforms as

$$G'_{\mu\nu}(x) = \Omega(x)\, G_{\mu\nu}(x)\, \Omega^{-1}(x)\ . \tag{2.10}$$

Since

$$[D_\mu, D_\nu]\psi = i\, g[B_\mu, B_\nu]\ , \tag{2.11}$$

one finds

$$G_{\mu\nu} = \partial_\mu B_\nu - \partial_\nu B_\mu + i\, g\, [B_\mu, B_\nu]\ . \tag{2.12}$$

Finally, the Lagrangian assumes the canonical form

$$\mathcal{L}_{QCD} = -\frac{1}{4}\, \mathrm{Tr}\,(G_{\mu\nu}G^{\mu\nu}) + \sum_{f=1}^{N_f}\, \overline{\psi}_f\, \left(i\, \overleftrightarrow{D}_\mu\, \gamma_\mu - m_f\, \mathbb{1}_c\right)\, \psi_f\ , \tag{2.13}$$

where the sum run over the number of flavour, N_f, and $\mathbb{1}_c$ is the $N_c \times N_c$ matrix identity.

Because of the non-abelian character of the gauge group (see the commutator in EQ. (2.12)), QCD and abelian gauge theories, like QED, have several crucial differences [23]:

- there are vector bosons self-couplings (three-and four-gluon vertices), and thus gluons carry colour;

- the "asymptotic freedom": the coupling α_s becomes weak at short distances or large energy, since (at one-loop):

$$\alpha_s(Q^2) = \frac{4\pi}{\left(11 - \frac{2}{3}N_f\right) \ln \frac{Q^2}{\Lambda^2_{QCD}}}\ , \tag{2.14}$$

  where Λ_{QCD} is the QCD scale parameter ($\Lambda_{QCD} \simeq 200$ MeV for five flavours). Therefore, QCD is studied perturbatively in the high-momentum regime, where there is no Landau pole;

- conversely, at low momentum perturbative QCD is not applicable (the coupling becomes strong and perturbative QCD fails to describe

hadrons with masses below 2 GeV) and the so-called confinement occurs.

2.2 Symmetries of QCD

Critical behaviours are generally related to the spontaneous breaking of a global symmetry [24]. Indeed, according to the Noether theorem, each symmetry corresponds to a conservation law and a conserved charge. For example, energy and momentum conservation are due to Lorentz invariance. Not only symmetries, but their lack, or rather their breaking, are also of fundamental importance: e.g. masses in quantum theory (as well as many phase transitions - classical or not), are due to (spontaneous)-symmetry breaking. An "order parameter" describes each symmetry: it is a quantity that vanishes when the system shares the same symmetry of the Lagrangian, while it is different for zero when the symmetry is (spontaneously)-broken. It thus establishes the state of the system.

By construction, QCD is a gauge theory with gauge group $SU(3)_c$ and its main symmetries are:

2.2.1 Poincarè and CPT

The Poincarè group describes the full symmetry of special relativity, and all elementary particles fall in representations of this group. CPT (Charge conjugation, parity and time-reversal) is the only exacts discrete symmetry of a physical theory and is tightly connected to the Lorentz one. It also requires that the vacuum is Lorentz invariant and the energy bounded from below.

2.2.2 Flavour simmetry

Another important symmetry is the flavour one, that is broken due to the non zero value of the physical mass. Indeed, the kinetic term for the mass field can be written in terms of the chiral components,

$$q_{fL} = \frac{1-\gamma_5}{2}\, q_f \ , \qquad q_{fR} = \frac{1+\gamma_5}{2}\, q_f \ , \tag{2.15}$$

as

$$\mathcal{L}_{kin} = i \sum_{f=1}^{N_f} \left(\overline{q}_{fL} \not{D} \, q_{fL} + \overline{q}_{fR} \not{D} \, q_{fR} \right) \, . \tag{2.16}$$

Since left and right terms are additive, each of them can be rotated separately implying the maximal global flavour symmetry $U(N_f) \times U(N_f)$. Nevertheless, mass terms break this symmetry, because they couple the left and the right component of the quark field:

$$\mathcal{L}_m = i \sum_{f=1}^{N_f} m_f \left(\overline{q}_{fR} \, q_{fL} + \overline{q}_{fL} \, q_{fR} \right) \tag{2.17}$$

Generally, since the masses are non zero, the only flavour symmetry of $\mathcal{L}_{QCD}$ is obtained by rotating the left and the right component of the quark field by the same phase, θ_f, $q_{fL,R} \to e^{-i\,\theta_f} \, q_{fL,R}$, and the symmetry group reduce to $U(1) \times U(1) \times \cdots \times U(1) = U(1)^{N_f}$, with conserved charges given by the flavour quantum numbers, N_u, N_d, N_s, N_c, N_b and N_t. Besides, all these symmetries are broken by the weak interactions, and the only conserved charge is the sum (baryon number):

$$B = \left(N_u + N_d + N_s + N_c + N_b + N_t \right) / 3 \tag{2.18}$$

Other approximate symmetries can be recognized: since m_u, m_d, and m_s are smaller than the others, in some cases, one can approximate $m_u = m_d$ (Isospin symmetry - group $SU(2)_f$) or $m_u = m_d = m_s$ ($SU(3)_f$ symmetry).

2.2.3 Approximate chiral symmetry

Chiral symmetry is realized when $m_f = 0$. In some situations, like high-energy and high-momentum regimes, one can approximate $m_u = m_d = 0$ and also $m_s = 0$. This position makes $\mathcal{L}_{QCD}$ invariant under the transformation of the group $SU(n_F)_L \times SU(n_F)_R$, with $n_F = 2$ or 3, and q_{fL} and q_{fR} can again be rotated separately.

Chiral symmetry appears to be more hidden than, for example, the isospin one. While the second is responsible for the (almost) same mass of protons and neutrons, the first would result in hadrons with a partner

of opposite parity and approximately the same mass, that is obviously not the case. Thus, not only chiral symmetry is broken (also Isospin symmetry is broken due to the small difference between m_u and m_d, and hence the difference in the masses of the nucleons), but it is with more significant consequences than the Isospin symmetry breaking.

The spontaneous breaking is related to the dynamical generation of massive constituent quarks. Thus the chiral transition describes the transition from a state in which the effective quark masses are spontaneously generated to one with massless quarks. The order parameter is the chiral condensate, that is the trace of the quark propagator, S, or, equivalently, at finite temperature, the derivative of the thermodynamic potential, Ω, with respect to the bare quark masses, m:

$$< \bar{\psi}\psi >= -\frac{T}{V}\mathrm{Tr}S = \frac{\partial\Omega}{\partial m} \, . \tag{2.19}$$

For zero bare masses, i.e. when the chiral symmetry is exact, $< \bar{\psi}\psi >$ is zero in the symmetric phase (high energy), and it becomes finite at low energies when chiral symmetry is broken spontaneously. For finite masses, the $< \bar{\psi}\psi >$ is never zero, since the current quark masses break the symmetry explicitly. Nevertheless, it decreases suddenly at the (pseudo)-phase transition. Typical value in the vacuum for the lightest condensates are $< \bar{u}u > \simeq < \bar{d}d > \simeq (-230MeV)^3$.

2.2.4 Z_N symmetry

For pure Yang-Mills theory at finite temperature and densities, a new symmetry, called Z_N, is important to study deconfining, although it is not a symmetry of the full QCD Lagrangian. It is a topologically non-trivial gauge transformations [25, 26],

$$\begin{cases} \psi_f \mapsto U \; \psi_f \\ B_\mu \mapsto U \; B_\mu U^{-1} + \dfrac{1}{i \; g} \; (\partial_\mu U) \, U^{-1} \end{cases} \quad , \tag{2.20}$$

with periodic boundary conditions

$$\psi_f(x,\beta) = -z\ \psi_f(x,0)\ , \tag{2.21}$$

and with U an element of $SU(N)$, i.e.

$$U = \exp\left\{i\ \alpha_a\ t^a\right\}\ , \tag{2.22}$$

satisfying the boundary condition

$$U(x,\beta) = z\ U(x,0)\ . \tag{2.23}$$

Once the fermion fields are transformed as

$$\psi_f \mapsto \exp\left\{-i\ \theta_f\ T\ \tau\right\}\ \psi_f\ , \tag{2.24}$$

the resulting Lagrangian remains the same if one changes the covariant derivative, D, in eq, (2.5) with

$$D_\mu = \partial_\mu + i\ g\ \left(B_\mu + \widehat{\theta}\ \delta_{\nu,0}\ T\right)\ , \tag{2.25}$$

where T is the temperature and $\widehat{\theta}$ is a matrix in flavour space.

The order parameter to study the phase of the system with respect this symmetry is the Polyakov loop, which is the generalization at finite temperature of Wilson line. The Wilson line along some path in space-time describes a way to connect operators at different space-time points (from some initial, x_a, to some final, x_b, point) in a gauge-invariant way. It is defined as the path-ordering (P)

$$W_{a\,b} = P\ \exp\left\{i\ \int_{x_a,\,t_a}^{x_b,\,t_b} B_\mu\ dx_\mu\right\}\ . \tag{2.26}$$

The Polyakov loop is essentially the generalization at finite temperature of the trace of EQ. (2.26), when the initial and finial points differ only in the time component, i.e. the path is a straight line connecting t to $t+\beta$:

$$L = \frac{1}{N_c}\ Tr\left[T\ \exp\left\{i\ \int_0^\beta B_0\, dx_0\right\}\right]\ . \tag{2.27}$$

It is called a loop due to the periodicity. Moreover, it is gauge invariant, but it is not invariant under center transformations, i.e.

$$L \mapsto z\, L\ . \tag{2.28}$$

So center transformations have physical content since gauge-invariant objects change under it. Its physical meaning is related to the free energy of adding colour sources at infinite distance,

$$L(T) \sim \lim_{r\to\infty} \exp\left\{-\frac{V(r)}{T}\right\}\ , \tag{2.29}$$

where $V(r)$ is the potential between a static quark-antiquark pair separated by a distance r. For Yang-Mills theory without quarks, or for the quenched theory with quarks with infinite mass, QCD reduces to pure $SU(3)$ gauge theory, which is invariant under a global Z_3 symmetry, with a potential $V(r) \propto r$. Thus $L = 0$ at large distance, $r \to \infty$, while at finite r one has $L \neq 0$, and the Polyakov loop provides an order parameter of the state of the system under this symmetry: L vanishes for symmetric states, and becomes finite when the symmetry is spontaneously broken. This picture changes for a system with physical quarks since now, due to colour screening, $V(r)$ remains finite at large r: indeed, turning away two colour charges (quarks, antiquarks or gluons), when the energy equals the lowest hadron mass, it is more convenient produce a hadron and thus the "string" between these charges breaks. Consequently, L does not vanish in the confined phase, but its value is about

$$L(T) \sim \exp\left\{-\frac{M_h}{T}\right\} \sim 10^{-2}\ . \tag{2.30}$$

However, it continues to be significantly lower than in the deconfined phase, and it can be used to describe deconfinement: the Polyakov loop must (almost) vanish for unbroken center symmetry (when the action in pure Yang-Milles theory is invariant under center transformations and the Polyakov loop is not - unless it is $L = 0$), and it is finite in the broken phase.

2.3 QCD at finite temperature and density

In the real world, a physical system is made of many interacting bodies, and it is a typical example of Gran Canonical ensemble, where particles can be created and destroyed: in this sense, i.e. in a thermodynamically one, one introduces a temperature and a chemical potential to study strong interactions. It is a fundamental step to apply QCD to the study of collisions between light/heavy particles (which requires a theory at finite temperature, or finite density, or both), of neutron stars (where the density is much higher than the nuclear one) or at early eras of cosmological evolution (with temperature comparable to nucleon rest energies). For those systems, one has to know the phase of hadronic matter, since, as in many thermodynamic systems, phase transitions occur by varying temperature and/or density. In other terms, one has to know the properties of the entire phase diagram of the strongly interacting matter.

One of the first hints of a phase transition in QCD can be found in the works of Hagedorn [27, 28] on the statistical bootstrap model: since the density of hadronic states increases exponentially as a function of the resonance mass m, $\rho(m) \sim exp\{b\ m\}$, a limiting temperature, above which hadrons fade away, must exist. In 1975 was shown by Cabbibo and Parisi [29] that the limiting temperature of hadronic matter can be seen as a "transition" temperature to a phase of free quarks, named "quark-gluon plasma" (QGP). If indeed hadrons are bound states of more fundamental objects, then the exponential increase of the density might indicate a phase transition to a state composed of free constituents. In this phase, quarks can be considered as free due to the so-called "asymptotic freedom" of QCD: when the energy density of the system increases, and this happens for example at high temperature or density, strong interaction decreases. Therefore, at large density or temperature, where the equation of state (EoS) can be perturbatively calculated, one finds that the EoS approaches that of an ideal gas of free particles. As the temperature is lowered, unfortunately, perturbation theory can no longer be used. However, we know that, at some temperature and density (or baryon chemical potential), quarks condensate in confined objects named hadrons, although it is now clear that it is not a real phase transition, but rather a crossover at large temperature and small chemical potential.

At finite temperature and density, systems are described by the grand canonical Gibbs ensemble, by adding a "Lagrangian multiplier" term for each conserved number (notably nonzero net baryon number and zero net strangeness and charm). Thus, several additional terms, $\exp(-\mu_i/T)$, where μ_i are the chemical potentials associated with the conserved and mutually commuting number operators N_i, modifies the partition function. Let be H the Hamiltonian of the system. N_i must also commute with H and must be extensive. The equilibrium state of the system is described by the statistical density matrix [30–32]

$$\rho = \exp\left\{-\beta\,\left(H - \sum_i \mu_i\, N_i\right)\right\}\,, \tag{2.31}$$

that is the starting point to define the ensemble thermal average of any observable, A,

$$< A >_\beta = \frac{\mathrm{Tr}\, A\,\rho}{\mathrm{Tr}\rho}\,, \tag{2.32}$$

and to define all the thermodynamic potential of the systems, through the grand canonical partition function

$$\mathcal{Z} = \mathrm{Tr}\rho\,. \tag{2.33}$$

For example, the pressure, the particle number, the energy and the entropy densities, and the trace anomaly are given by

$$P = T\,\left(\frac{\partial \ln \mathcal{Z}}{\partial V}\right)_{T,\,\mu}\,, \tag{2.34}$$

$$n_i = \frac{T}{V}\left(\frac{\partial \ln \mathcal{Z}}{\partial \mu_i}\right)_{T,\,V}\,, \tag{2.35}$$

$$\varepsilon = \frac{T^2}{V}\,\left(\frac{\partial \ln \mathcal{Z}}{\partial T}\right)_{V,\,\mu}\,, \tag{2.36}$$

$$s\,T = P + \varepsilon - \sum_i\,\mu_i\,n_i\,, \tag{2.37}$$

and

$$\frac{\Theta^{\mu\mu}}{T^4} = \frac{\varepsilon - 3\ P}{T^4} = T\ \frac{\partial(P/T^4)}{\partial T}\ . \tag{2.38}$$

Equilibrium thermodynamic requires stationarity. Thus, one can introduce a temperature in the QCD Lagrangian through the imaginary time path-integral formulation. For example, the grand canonical partition function reads [8]

$$\mathcal{Z} = \int [dB]\ [d\psi]\ [d\bar{\psi}]\ \exp\left\{ - \int_V d^3x \int_0^\beta d\tau\ \mathcal{L}(B, \psi, \bar{\psi}) \right\}\ , \tag{2.39}$$

where the time component is rotated, and the integration over τ goes from 0 to the inverse temperature $\beta = 1/T$. Although the dynamic has been frozen, there is the advantage of simple prescriptions for the integration in $d\tau$. Indeed, all fields over which we integrate have to be periodic (boson) or antiperiodic (fermion) in the imaginary time direction, due to the trace operation. Consequently, fields can be expanded in eigenmodes in the time direction and the corresponding "Matsubara" frequencies are quantized. For boson fields one has

$$\phi(x,t) = \sum_{\omega_n = 2\ n\ \pi\ T} e^{i\ \omega_n\ t}\ \phi_n(t)\ , \tag{2.40}$$

while the fermions anti-periodic conditions lead to the expansion

$$\psi(x,t) = \sum_{\omega_n = (2\ n+1)\ \pi\ T} e^{i\ \omega_n\ t}\ \psi_n(t)\ , \tag{2.41}$$

where the sum runs over the Matsubara frequencies, with n even (odd) for bosons (fermions). This means that, in order to evaluate integrals, one expands fields in momentum space, and replace

$$\int \frac{d^4k}{(2\,\pi)^4} \quad \to \quad \frac{1}{\beta} \sum_n \int \frac{d^3k}{(2\,\pi)^3}\ . \tag{2.42}$$

Of course EQ. (2.39) is not solvable exactly in the strong coupling regime. However, in some simple cases like for systems of non-interacting fermions

or bosons at zero chemical potential, EQ. (2.39) can be solved analytically, and one finds

$$\ln \mathcal{Z}_B = -\frac{1}{2} \ln \det \frac{D_0^{-1}}{T^2} \ , \tag{2.43}$$

and

$$\ln \mathcal{Z}_F = \ln \det \frac{S_0^{-1}}{T} \ , \tag{2.44}$$

respectively. In eqs. (2.43) and (2.44) D_0 and S_0 are the free bosonic and the free fermionic propagators. By integration and for infinite volume, one finds that the pressure is

$$P_B = \frac{T}{V} \ln \mathcal{Z}_B = -\int \frac{d^3k}{(2\pi)^3} \left[\varepsilon_k + 2\, T \, \ln \left(1 - e^{-\varepsilon_k / T} \right) \right] \ , \tag{2.45}$$

for bosons, and

$$P_F = \frac{T}{V} \ln \mathcal{Z}_F = 2 \int \frac{d^3k}{(2\pi)^3} \left[\varepsilon_k + 2\, T \, \ln \left(1 + e^{-\epsilon_k / T} \right) \right] \ , \tag{2.46}$$

for fermions, with $\epsilon_k = \sqrt{k^2 + M^2}$, M being the mass.

For interacting systems, one needs models, as for example the Nambu-Jona Lasinio (see Sec. 3.3) and the Quark-Meson models (see Sec. 3.4), or computational methods, as Lattice QCD (see Sec. 3.1). Effective QCD models allow to study the whole phase diagram of QCD, whereas Lattice QCD cannot describe systems at finite density, because reliable first principle calculations are forbidden by the sign problem.

2.4 The phase diagram of QCD

In this section, the main topics of the phase of the strongly interacting matter are summarized. We have seen that there exist at least two phases of the strongly interacting matter. At low temperature and density the relevant d.o.f. are hadrons, the quark-gluon plasma (QGP) phase is at high temperature and/or densities. These two asymptotic regions are separated by some (pseudo) transition line, at which one can define a (pseudo) transition temperature, T_c, that depends, in principle, from the density, or the

chemical potential. Connecting these two phases is not a simple task, and the phase diagram which comes out is very rich, as schematically shown in Figure 2.1.

Although there are no exact solutions at finite temperature and baryon chemical potential, one can conceive the phase diagram structure starting from the two limiting cases recalled (free QGP and Hadron Gas) and by looking at existing properties or symmetries in different part of the diagram. For example, the transition line can be seen as a deconfinement one, since beyond T_c the hadrons are colourless bound states of quarks and gluons, while at high temperatures and/or densities hadronic matter turns into a QGP. Moreover, considering the symmetries of the QCD Lagrangian discussed in Sec. 2.2, if the masses disappear, the Lagrangian becomes chiral symmetric, and thus the deconfinement transition could be related to the restoration of this symmetry, whit order parameter given by the quark-antiquark condensate in EQ. (2.19). Indeed, in the vacuum and at zero temperature, quarks dress themselves with gluons to form the "constituent" quarks that makeup hadrons. As a result, the bare quark mass $m_q \sim 0$ is replaced by a constituent quark mass $M_q \sim 300$ MeV and the chiral symmetry is broken spontaneously. Another type of transition can be seen in the high density and low-temperature region: in the deconfined phase, the attractive interaction between quarks could lead to the formation of colored bosonic diquark pairs, like the Cooper's pair in superconductors, which could condense at low temperature to form different colour superconductor/superfluid phases [33, 34]. A review of our current understanding of the phase structure of QCD can be found in [35], and the phase diagram is depicted in Fig. 2.1.

The first part of the transition line, $T_c(\mu)$, i.e. the dashed one at low chemical potential in Fig. 2.1, does not describe a real phase transition, but instead a crossover: Lattice calculations show that there is no singularity in the thermodynamic potentials. Hence, in a strict sense, there is no phase transition between the two phases. At some chemical potential, $\mu^\star$, (the red "X" at the end of the crossover line) the transition changes becoming a II order one, and then, for $\mu > \mu^\star$, one finds a I order phase transition (black line). The colour superconductor phases are plotted in the bottom-right side of the figure. The regions probed by some relativistic heavy-ion collision experiments (LHC, RHIC, SPS, AGS, GSI) are also marked in the

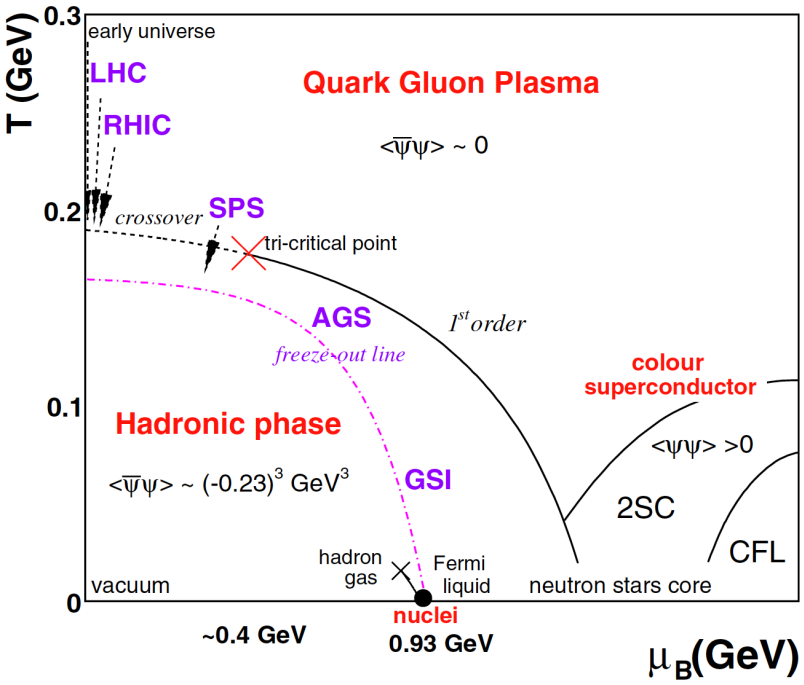

Figure 2.1: The phase diagram of Quantum Chromodynamics. Figure from [36]

figure, together with the two other possible "laboratories" to probing QGP like the early stage of the universe and the core of neutron stars.

It is still not clear if the change from QGP to hadronic matter coincides with the deconfinement or with the chiral phase transition. Indeed, the connection between these two different phases is theoretically not fully understood, and it is an open issue whether both, the chiral and deconfinement transition, take place at the same temperatures and densities. For example, McLerran and Pisarksi [37] suggested that, at large densities, at least in the large N_c limit, could exist a new confined and chiral symmetric phase of matter, named "quarkyonic", between these two lines.

2.5 Probing the Quark–Gluon Plasma

As discussed, the properties of QCD at finite temperature and density show that could exist a new form of matter named QGP. The question is, where and how one can find this new state of matter? There are at least three possible answers to the first question: the early universe, the core of neutron stars, and particles accelerators.

In fact, in the standard cosmological model, our universe has evolved through several eras, and its history can be described as a thermal one. From a thermodynamic point of view, in fact, one can introduce a temperature and describes the evolution of the universe as an adiabatic isentropic expansion with a temperature running from a very high value (at least of the order of 10^{15} GeV of the GUT era) to the current value of the Cosmic Microwave Background (CMB) radiation ($T \sim 2.73$ KeV). It is therefore natural to expect that, at some time, the temperature of the universe was that one of the QCD phase transition. According to the very small value of the photon to baryon density ratio [38], this transition happens for a zero value of the chemical potential.

The other "cosmological laboratory" to find QGP is the core of neutron star, where, although at small temperatures, the density is larger than those of ordinary nuclear matter. Thus nucleons can overlap and produce a gas of almost free quarks and gluons.

Finally, the most useful and straightforward way to probe QGP is through accelerator experiments (for some recent review see [39–44] and references

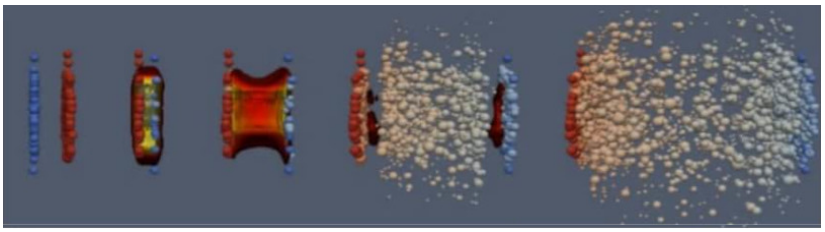

Figure 2.2: A schematic picture of particles collisions in the laboratory frame. Figure from [39]

therein). The study of ion collisions have been carried out since 1970 and since the international symposium "Statistical Mechanics of Quarks and Hadrons" [45], which, from the point of view of theory, was the starting point of the "Quark Matter" conferences, and the "Workshop on future relativistic heavy ion experiments" of 1980 [46] and "Quark Matter Formation and Heavy Ion Collisions" of 1982 [47], which started the series from the point of heavy ion experimentation [48].

Different experiments at various collision energies and nuclear targets allowed to cover a large part of the phase diagram in Fig. 2.1. More recent results have been obtained from experiments at the CERN Super-Proton-Synchrotron (SPS) accelerator [43, 49] at the Relativistic Heavy Ion Collider (RHIC) at Brookhaven National Laboratory (BNL) [3, 50], at the Alternating Gradient Synchrotron (AGS) [51], and subsequently at the CERN Large Hadron Collider (LHC) [41, 52, 53]. Regarding the colder and denser region of the QCD phase diagram, there are, among others, experiments at the GSI Helmholtz Center for Heavy Ion Research, e.g. the Facility for Anti-proton and Ion Research (FAIR), or at the Nuclotron-based Ion Collider Facility (NICA) at Joint Institute for Nuclear Research (JINR) [54, 55], and many others.

The second question concerns how can one say that the new kind of matter has been observed, especially if this new state appears without a phase transition, as happens at low chemical potential. In other words, what are the signatures of QGP formation? Before answering, I shall illustrate what happens in a nuclear collision, as schematically pictured in Figure 2.2 (see also ref. [56]).

Let consider two ultra-relativistic nuclei that collide. In the "laboratory

frame", each incident nucleus is a Lorentz contracted disc, with a diameter, d, of few fm (e.g. for large nuclei such Pb or Au d is about 14 fm), and low thickness (it is about d/γ), due to the considerable value of the relativistic Lorentz γ factor (γ is approximately 100 for RHIC and $\gamma \sim 2500$ for LHC energies). When the two disks overlap or collide, most of the incident partons (quarks, antiquarks and gluons) loss energy mainly due to "soft" interactions, i.e. those that involve small transverse momentum transfer. These interactions imply a colour exchange between the discs, so that new longitudinal colour fields fill the space between them, forming the so-called fireball (see Fig. 2.2). Then, these fields gradually decay into $\bar{q}q$ pairs and gluons and a droplet of quark-gluon plasma very far from equilibrium emerges. At this energy, the matter is better understood in terms of a soup of quarks and gluons, with almost no hadrons or other quasiparticles moving inside, and with a characteristic shear viscosity, η. Then gluons quickly thermalize (after a time of order 1 fm/c in its rest frame - τ_0 in Fig. 2.3), while the energetic partons traverse this plasma and end in a shower of particles. The fireball has an execs of energy density with respect that of a hadron gas (of about 500 MeV/fm^3) and also the entropy density is enormous (e.g. the final state after the collision can contain as many as 30,000 particles, while the initial one has an almost zero entropy density). In this medium, quarks and gluons are so close that they form a collective medium, that can be described as a relativistic hydrodynamic fluid with remarkably low viscosity to entropy density ratio, $\eta/s \sim 1/(4\pi)$ (it is precisely $1/4\pi$ in infinitely strongly coupled gauge theories). Curiously, although separately both η and s are enormously larger than those of any quotidian fluid, its specific viscosity η/s is smaller than that of any other known fluid. The QGP expands and cools as the disks cross each other, losing energy. Simplifying, when locally the energy density drops below that within an individual hadron, the fluid hadronizes (time τ_h in Fig. 2.3) and forms a fog of particles that, after a possible scattering period, then stream away freely (at the freeze-out time). Remnants of the original nuclei progress in the forward and backward directions. For non-central collisions, the final produced particles momentum distribution shows an azimuthal anisotropy since the droplet of QGP is formed with an initial approximately almond shape in the transverse plane. Occasionally, some high-energy partons are produced by large-angle scattering. They born at

very early times and appears in the final state as a "jet", i.e. a cone-shaped spray, of hadrons and/or high-energy photons, leptons or heavy $q\bar{q}$ pairs. Since they are produced early, they contain a wealth of information about the produced medium.

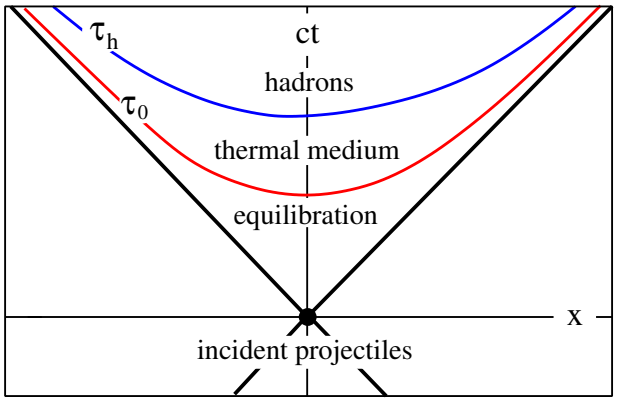

Figure 2.3: Different stages of the hadronization process. Figure from [57]

Summarizing (see Fig. 2.3):

- when two (highly Lorentz-contracted) nuclei collide, a bulk of QGP is formed in the very early stage, which is dominated by gluonic interactions. That is the "pre-equilibrium stage";
- this matter quickly thermalizes (after about $\tau_0 \simeq 1$ fm/c and with a temperature that, for example at top SPS and top RHIC energies, is about $200 - 300$ MeV [58], for the LHC at the energy of $\sqrt{s} \sim 5$ TeV T is about $400 - 600$ MeV) and expands hydrodynamically;
- at the time $\tau_h \sim 8 \div 10$ fm/c, the fireball hadronizes forming a fog of interacting particle. That is the hadronization time, and it happens at a temperature T_h that could be related to that of deconfinement and/or chiral phase transition;
- it is not known whether the hadrons are produced in chemical equilibrium or chemically equilibrate quickly, after the phase transition. All this is the so-called chemical freeze-out [56], that defines the freeze-out time, τ_f, and, consequently, a freeze-out temperature, T_f, of the

system. T_f can be studied, for example, statistically [27, 28, 59–64]. Chemical freeze-out fixes the abundance ratios of the hadronic species that, in nucleus-nucleus (AA) collisions, show a dramatic strangeness enhancement effect, characteristic of an extended QCD medium. After a period of possible subsequent scattering, the hadrons freeze-out kinetically and then, the non-interacting hadrons continue their path and are detected as final states. The freeze-out curves are less well-defined theoretically as well as experimentally [65]: at low chemical potential, since the hadrons interactions are dominated by resonance formation and decay, the system can be treated as an ideal gas of all possible resonances[27, 66] (e.g. through Hadron Resonance Gas (HRG) models), and this means that freeze-out effectively occurs at the point of confinement. Conversely, at large baryon density, the interaction (dominated by Fermi statistics and baryon repulsion) does not lead to resonance formation, and HRG models do not describe the system anymore.

Let us now discuss how we can probe the properties of this state.
There are different methods [58]:

1. **ELECTROWEAK RADIATION:** the medium emits photons and e^+e^- or $\mu^+\mu^-$ pairs [67, 68]. Since these particles do not interact strongly, they leave the medium without any modifications. Thus their spectra provide information about the place or the time they were formed, probing the entire volume of the plasma. The problem is that they can be formed anywhere and at any time, even at the hadronization surface or by the emitted hadrons until they freeze-out.

2. **SOFT PROBES: HADRON RADIATION.** Since the bulk temperature is higher than that of the environment, it radiates hadrons consisting of light (u, d, s) quarks. These hadrons are formed at the transition surface, like water drops that condensate on the glass of a container filled by a vapour in a cold outside environment [58]. As a result, soft hadrons provide information on the hadronization surface and almost nothing about the QGP interior. That also means the properties of soft hadrons, like their abundances, is the same in

all high energy collisions, from e^+e^- annihilation to heavy-ion interactions, and correspond to that of a HRG with a temperature of $T \simeq 150/160$ MeV (at zero chemical potential) [27, 28, 59–64, 69]. In a non-static more realistic picture, if the early medium has a very high energy density and expands freely, a "radial flow" depending on the initial energy density emerges (i.e. an additional overall boost in momentum to the produced hadrons). Moreover, for peripheral collisions, if the initial conditions were not spherically symmetric, this flow becomes "elliptic". Since both flows are created by partonic pressure gradients, that reflect the initial collisional impact geometry, they bring information about the earlier, pre-hadronic stages: indeed, for weakly interacting gas of particles, the initial spatial anisotropy is destroyed by random motion, and the azimuthal distribution of particles in the final state ends up isotropic. Conversely, in a strongly coupled QGP, the expansion proceeds faster in the direction of larger pressure gradients, and this results in momentum anisotropy. Indeed, the matter is subjected to enormous pressure driven by the density differential to the vacuum outside the medium [41, 70, 71]. The anisotropy are measured by performing a Fourier analysis of charged hadrons angular distribution in the final state:

$$\frac{d\bar{N}}{d\phi} = \frac{\bar{N}}{2\pi}\left(1 + 2\sum_{n=1}^{\infty}\bar{v}_n\,\cos\left(n\left(\phi - \bar{\Psi}_n\right)\right)\right), \tag{2.47}$$

where ϕ is the angle in the transverse plane, $\bar{\Psi}_n$ are the event plane angles, and $\bar{N}$ is the average number of particles of interest per event. The first order coefficient, v_1, is sensitive to details of the expansion in the early stages [72]. The second one, v_2, is usually said as "elliptic flow". It describes the helicity of the polar distribution $1 + v_2\,cos(2\phi)$, which major and minor axis are $1 + v_2$ and $1 - v_2$, respectively: $v_2 = 0$ is for an isotropic distribution (circle), $v2 \neq 0$ for an anisotropic one (ellipse). This elliptic flow is due to collective behaviour since it emerges as a consequence o subsequent re-scattering in the plasma phase, and, near midrapidity and for semi central collisions, is the dominant Fourier coefficient.

Particle correlations, $C(\Delta\eta, \Delta\phi)$, are proportional to $v_n^2\,\cos(n\Delta\phi)$ [73],

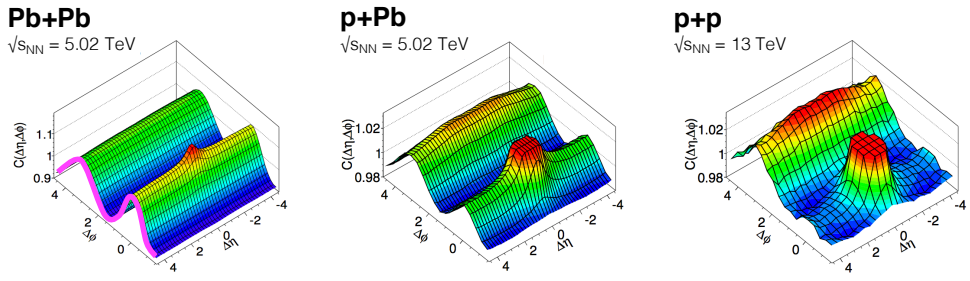

Figure 2.4: Two-particle correlations as a function of relative angles $\Delta\psi$ and $\Delta\eta$ as measured in (a) $PbPb$, (b) pPb, and (c) pp collisions at the LHC. In $PbPb$ collisions there is a large $\cos(2\Delta\phi)$ correlation with peaks at $\Delta\varphi = 0,\ \pi$ that extend long-range in pseudorapidity $\Delta\eta$. A similar feature is observed in pPb and pp collisions, thought it does not dominate the overall correlations to the same degree. Figure from [73].

$\Delta\phi$ and $\Delta\eta$ being the particles relative azimuthal angle in the transverse plane and the relative longitudinal pseudorapidity respectively. They contain crucial information regarding collectivity. For example, Figure 2.4 from [73] shows two-particle correlations as a function of relative angles $\Delta\phi$ and $\Delta\eta$ as measured in (a) lead-lead ($PbPb$), (b) proton-Lead (pPb), and (c) proton-proton (pp) collisions at the LHC: in $PbPb$ and pPb cases there is a $\cos(2\Delta\phi)$ correlation with peaks at $\Delta\phi = 0$ and π (magenta curve) that extend long-range in pseudorapidity $\Delta\eta$ (known as the ridge), and they mean that pairs of particles are preferentially emitted with small relative azimuthal angles ($\Delta\phi = 0$) or back to back ($\Delta\phi = \pi$) [36]. Surprisingly, this preference persists even when the particles are separated by large pseudorapidity. Moreover, there is a localized peak near $\Delta\phi \simeq \Delta\eta \simeq 0$ in all three cases [73]. For $PbPb$ the long-range correlations dominate. Significantly, high-multiplicity pp collisions at the LHC (Fig. 2.4.c) exhibit a long-range near-side ridge in azimuthal correlations, very similar to that observed in AA collisions. These features represent the first evidence of flow-like collective behaviour in a small system.

3. **HARD PROBES:**

- **QUARKONIUM SUPPRESSION:** bound state of heavy (c or b) quarks, which are stable with respect to strong decay, are known as "quarkonia". Examples are the J/ψ and Υ, the lightest quarkonium of quarks c and b, respectively. These particles are much smaller than the typical hadronic radius [74]. For example, the radius of the $J/\psi(1S)$ is about 0.2 fm, that of the $\chi_c(1P)$ is about 0.3 fm and that of the $\psi'(2S)$ is ~ 0.4 fm, while the typical hadron radius is about 1 fm. Different radius means different colour screening and thus different "melting temperatures" in a quark-gluon plasma, that permits these particles to survive in the QGP for temperatures above the hadronization one [74] as confirmed in lattice studies [75]. In fact, we know that colour charges are screened inside a (Debye)-radius r_D, as it happens in an electromagnetic plasma. We know also that r_D decreases with increasing temperature, as the medium increases in density, and deconfinement is expected when r_D is of the order of the average hadron size, i.e. of 1 fm. When it happens, a given quark can no longer see its former partner, but it sees many other particles and can move around freely, without encountering any confinement limit. Heavy quarks are produced through initial hard-scattering processes before the QGP formation (at time scales $\sim 1/(2\,m_{c,b}) \sim 0.07$ fm for charm and 0.02 fm for beauty) and they survive in the QGP medium since the annihilation rate of heavy quarks is small. At the transition temperature, T_h, quarkonium radius is less than the hadron size, and then of the r_D. This means that this structure survives beyond T_h and they disappear when the QGP temperature is such that $r_D(T)$ becomes of the order of their radius. Therefore, if one observes a suppression in the number of c/b-hadrons, this is due to the melting of quarkonium in the QGP and thus it is an unambiguous signature of quark-gluon plasma formation [74, 76]. In fact thermal hadrons are incapable of causing collisional dissociation of quarkonium [58]. Finally, at very high energies there is an enhancement of the number of charmonium

due to (re)combination of the charm quarks during the collision history [77] or at hadronization [78, 79]. Both dissociation and (re)combination implies the existence of a deconfined QGP state.

- **HIGH p_T HADRONS and HARD JETS:** particles with transverse momentum and/or mass larger than 2 GeV (so an order above the $\Lambda_{QCD} \sim 0.2$ GeV) originate from partonic scattering with large momentum transfer in the early collisions period (about ≤ 0.1 fm/c) and can be studied perturbatively. They emerge as the result of an elastic ($2 \to 2$) or inelastic ($2 \to 2+X$) scattering of two partons from each of the colliding hadrons. These partons thus fragment non-perturbatively into a jet o final hadrons. The features of this jet, like the collimation angle and the energy, depend on the plasma properties (temperature, particle–medium interaction coupling α, thickness, ...) and where the jets originate. Indeed, the "jet quenching", i.e. the attenuation or disappearance of the spray of hadrons resulting from the fragmentation of a parton due to energy loss in the dense plasma produced in the reaction (see Fig. 2.5), is a clear signal of the presence of strong interactions and thus of the formation of QGP [80] (e.g. a high energetic parton propagating inside the plasma losses up to tens of GeV of its initial transverse momentum while ploughing through the QGP). So, if one look at two jets that propagate in the opposite direction, i.e. originates due to the same scattering, if one of the jets is "quenched" it is a clear signature of QGP. Especially if one of the two jets is fully absorbed [80].

  Jet quenching can also be seen looking for a suppression (compared to *pp* collisions) of the spectrum (dN_{AA}/dp_T) of high-p_T hadrons [81, 82]. To do this, one defines the *nuclear modification factor*, which is the yield of a given observable (such as charged hadrons, identified particles and/or reconstructed jets) measured in nucleus-nucleus collisions, properly normalized to the *pp* mea-

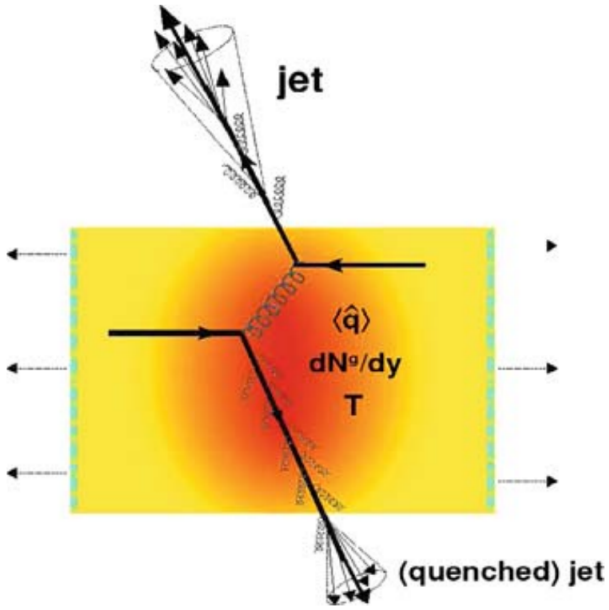

Figure 2.5: "Jet quenching" in a head-on nucleus–nucleus collision. Two quarks suffer a hard scattering: one goes out directly to the vacuum, radiates a few gluons, and hadronises; the other goes through the dense plasma formed in the collision, suffers energy loss due to medium-induced gluonstrahlung, and finally fragments outside into a (quenched) jet. Figure from [80]

surement at the same nucleon-nucleon energy [76]:

$$R_{AA} \equiv \frac{\frac{dN_{AA}}{dp_T}}{< N_{coll} >} \frac{1}{\frac{dN_{pp}}{dp_T}} = \frac{\frac{dN_{AA}}{dp_T}}{< T_{AA} >} \frac{}{\frac{d\sigma_{pp}}{dp_T}} , \tag{2.48}$$

where $< T_{AA} >$ is the nuclear overlap function, N_{AA} (N_{pp}) is the number of charged particles in AA (pp) collisions, N_{coll} is the number of the inelastic nucleon-nucleon collisions and σ_{pp} is the pp-cross section. Typically, N_{coll} (as well as the number of participants N_{part}) cannot be determined directly in AA collisions from measured cross-sections, but it can be evaluated through theoretical procedures, like the Glauber Model Calculation.
$R_{AA} = 1$ means that an AA collision behaves like $< N_{coll} >$ pp ones. Departure of R_{AA} from unity signals a change of physics in AA collisions. For example is found that $R_{AA} \sim 0.5$ in central $PbPb$ collisions at LHC up to $p_T \sim 400 GeV/c$ (ATLAS [83]), revealing that the medium created in $PbPb$ collisions is so opaque that it can quench even the most energetic jets.

4. **Strangeness enhancement:** The number of hadrons with strange quarks increases in the plasma phase [84, 85] and it is a clear indication of QGP formation since there is no known explanation of these results other than QGP [86] (abundant strangeness production is due to gluon excitation, a characteristic feature of deconfined phase [84]). Indeed, the hadronic channels, e.g. $N+N \to N+\Lambda+K$ and $\pi+\pi \to K+K^-$, are less efficient than the $s\bar{s}$ production in the QGP (especially with respect the gluon fusion channel $gg \to s\bar{s}$). In fact, in AA collisions the strangeness equilibration time in the confined matter is about 10 times longer than the lifetime of the hadronic phase since the mass of all strange hadrons is much larger than the hadron resonance gas maximum temperature [39]. This results in an enhancement in the number of hadrons made entirely from newly created strange quarks in AA collisions of about 20 times (or more) compared to proton-nucleus (pA) reference measurement [84, 86–89].

   To study enhancement one typically defines a double ratio to compare

the same yields in AA and pp collisions: e.g. [39]

$$\frac{< K^+ >_{AA} / < \pi^+ >_{AA}}{< K^+ >_{pp} / < \pi^+ >_{pp}} , \tag{2.49}$$

where $< \cdots >_{AA}$ and $< \cdots >_{pp}$ denote the event averages of K^+ and π^+ yields. It's found that this ratio in SS collisions at $200A$ GeV (NA35 [90]) is about two times higher than in nucleon-nucleon interactions at the same energy per nucleon and that enhancement increases with decreasing collision energy (e.g. at the AGS at $2A-10A$ GeV [91, 92]), and for multi-strange hyperons (WA97 [93], NA57 [94], ALICE [95]).

Besides, one of the most striking observations in high energy multi-hadron production is that both species abundances and transverse momentum spectra (provided effects of collective flow and gluon radiation are removed) follow the thermal pattern of an ideal hadron-resonance gas, with a universal temperature $T \simeq 150 \pm 10$ MeV [69, 96](see Fig. 2.6). More precisely, the relative yields of the different hadron species are well accounted for by an ideal gas of all hadrons and hadronic resonances with one well-known caveat: strangeness production is reduced with respect to the predicted Grand Canonical values. This suppression can, however, be taken into account by one further parameter, $0 < \gamma_s \leq 1$. If the predicted rate for a hadron species containing $\nu = 1, 2, 3$ strange quarks is suppressed by the factor γ_s^ν [97]. The basic quantity for the resonance gas description is the grand-canonical partition function for an ideal gas at temperature T in a spatial volume V

$$\ln Z(T) = V \sum_i \frac{d_i \gamma_s^{\nu_i}}{(2\pi)^3} \phi(m_i, T), \tag{2.50}$$

with d_i specifying the degeneracy (spin, isospin) of species i, and m_i its mass; the sum runs over all species. Here

$$\phi(m_i, T) = \int d^3p \ \exp\left\{\frac{\sqrt{p^2 + m_i^2}}{T}\right\} \simeq \exp\left\{-\frac{m_i}{T}\right\} \tag{2.51}$$

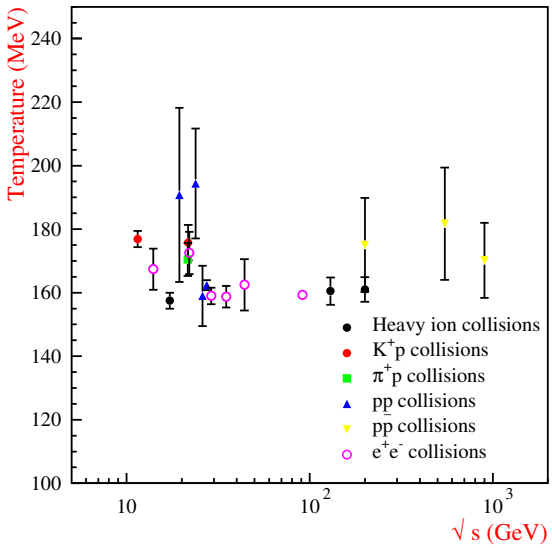

Figure 2.6: Hadronization temperature in the Statistical Hadronization model. Figure from REf. [96]

is the Boltzmann factor for species i, so that the ratio of the production rates N_i and N_j for hadrons of species i and j is given by

$$\frac{N_i}{N_j} = \frac{d_i \gamma_s^{\nu_i} \phi(m_i, T)}{d_j \gamma_s^{\nu_j} \phi(m_j, T)}, \tag{2.52}$$

where $\nu_i = 0, 1, 2, 3$ specifies the number of strange quarks in species i. We note that in the grand-canonical formulation the volume cancels out in the form for the relative abundances. The Statistical Hadronization model (SHM) is in agreement with the high energy data for large (nucleus-nucleus) and small (proton-proton and e^+e^-) initial settings with the same hadronization temperature as shown in Fig. 2.6 [96].

As mentioned earlier, the QGP formation would enhance strange particle production in nucleus-nucleus collisions and, indeed, $\gamma_s \simeq 1$ well describe the high energy AA data, but $\gamma_s < 1$ for proton-proton scattering at energies less than the Large Hadron Collider (LHC) ones.

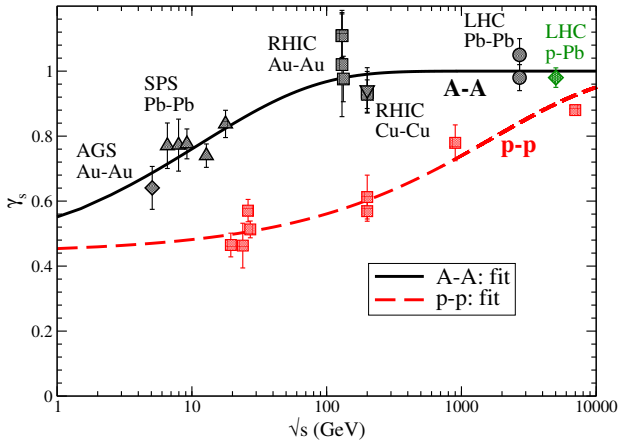

Figure 2.7: γ_s: energy dependence for pp, pA, AA

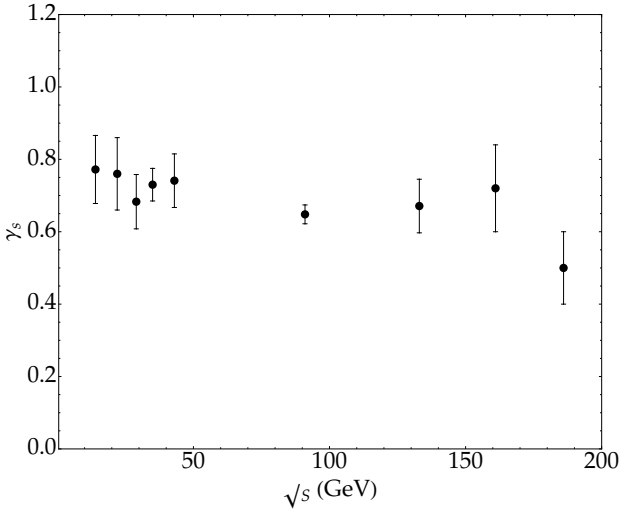

Figure 2.8: γ_s: energy dependence for e^+e^-

Figs. 2.7 and 2.8 show γ_s as a function of the collision energy in pp, pA and AA collisions, and in e^+e^- annihilation [98], respectively.

More recently, ALICE collaboration reported for pp collisions [95] the enhanced production of multi-strange hadrons, previously observed in $PbPb$ collisions, in high energy, high multiplicity, proton-proton pp events.

2.6 Universality in particles collisions

As seen in sec. 2.5, collective effects are signatures for the QGP formation in nucleus-nucleus collisions. These effects were not expected in pp and pA collisions. Surprisingly, recently, experimental results in proton-proton and proton-nucleus collisions at the Large Hadron Collider (LHC) and Relativistic Heavy Ion Collider (RHIC) showed substantial similarity to those observed in the nucleus-nucleus ones [99]. E.g. correlations that are long-range in rapidity have been observed at the LHC (in high-multiplicity pp collisions [100], and in high multiplicity pPb [101–103] collisions) and at the RHIC (dAu collisions [104]). This new interesting aspect started in 2010 with the observation of ridge-like structures in pp collisions by the CMS experiment at the LHC [100] (like that observed in $PbPb$ at $\Delta\phi \sim 0$ that extend to $|\Delta\eta|$ of at least four units - see Fig. 2.4), by using the particle cut $1 < p_T < 3$ GeV/c in conjunction with a high multiplicity cut. Subsequent experiments [105–112], and especially multi-particle measurements in high multiplicity pA [101, 103, 113–120] and high multiplicity pp [100, 121–123] collisions show unambiguously that the observed correlations are collective [124]. More recently, the e^+e^- annihilation LEP data have been reconsidered [125] to verify if a flow-like behaviour is generated with this initial, small, non-hadronic, setting. The answer is negative and confirmed at lower energy by BELLE collaboration [126]. Unlike elliptic flow, the jet quenching phenomenon is typical of AA collisions, and in pA it was found that the number of jets seen is the same expected from N_{coll} pp collisions [127]. Other measurements confirming this "Universality" are instead the rapidity distribution [128], particle ratios [95, 129], or the relationship between the total number of charged particles produced and the number of participants, that was found from the lowest energies measured [130], through RHIC [131]

to LHC [132] energies, for all AA, pA, πA and KA collisions. Even more surprisingly, if one takes into account the leading particle effect, i.e. the energy removed from the genuine hadronization cascade due to the leading particles, the total number of produced charged particles per participant in AA collisions is the same as that in pp and e^+e^- annihilation [133–135].

Although pp collisions are much simpler than pA and AA (that have hundreds of participants), all of these have similar behaviour [95, 108, 123, 136–141], which suggest the presence of a common origin in the hadronization process: the formation of a quark gluon plasma in the early stage. On the other hand, e^+e^- annihilation data at LEP and lower energies indicate that there is no strangeness enhancement and no flow-like effect. In Ref. [142], we show that the parton density in the transverse plane generated in e^+e^- annihilation at the available energy is too low and therefore there is no way to detect the previous signatures. The event-by-event multiplicity and the corresponding energy where strangeness suppression and the flow-like phenomenon could show up in e^+e^- turns out to be quite large.

In Refs. [142–144], we discuss the comparison between small colliding systems and nucleus-nucleus collisions, for:

- the strangeness suppression factor γ_s and yields of multi-strange hadrons (see sec. 2.6.1 of this thesis);
- the average transverse momentum, p_t, with particular attention to the low p_t region where soft, non-perturbative effects are essential (sec. 2.6.2);
- the elliptic flow scaled by the participant eccentricity, ϵ_{part}, defined for example in [145–148] (sec. 2.6.3).

The universal behaviour in small and nuclear high energy collisions emerges for all these observables in terms of a specific dynamical variable which corresponds to the entropy density of the initial system in the collision, s_0. It takes into account the transverse size of the initial configuration and its fluctuations and indicates that a few dynamical ingredients, common to the different initial settings, drive the particle production, independently of the complexity of the non-equilibrium dynamics with annihilation/creation of many interacting quarks and gluons and hadronization of final partons.

Let us recall that the initial entropy density s_0 is given in the one-dimensional hydrodynamic formulation [149] by the form

$$s_0\,\tau_0 \simeq \frac{1.5}{A_T}\,\frac{dN^x_{ch}}{dy} = \frac{1.5}{A_T}\,\frac{N^x_{part}}{2}\,\frac{dN^x_{ch}}{dy}\bigg|_{y=0}\,, \tag{2.53}$$

with $x \simeq pp$, pA, AA, e^+e^-. Here A_T is the transverse area, $(dN^x_{ch}/dy)_{y=0}$ denotes the number of produced charged secondaries, normalized to half the number of participants N^x_{part}, in reaction x, and τ_0 is the formation time. The initial entropy density is directly related to the number of partons per unit of transverse area and, due to the large fluctuations in high multiplicity events, one needs a reliable evaluation of the transverse area for different collisions.

In studying the strangeness enhancement and the average p_t, we use results from Glauber Monte Carlo (MC) [150] to obtain A_T as a function of multiplicity for AA and pPb collisions. For pp collisions, the effective transverse area is sensitive to the fluctuations of the gluon field configurations. Therefore, we apply the CGC parameterization of the transverse size as a function of multiplicity [151–153]. In e^+e^- annihilation, the transverse size can be evaluated by looking at the transverse size of a quark-antiquark string in the hadronization cascade [154, 155] (see app. A.1).

On the other hand, for the scaling behaviour of the elliptic flow, namely of the ratio v_2/ϵ_{part}, the effective transverse area, S, of the initial setting is the one related to ϵ_{part}. The S is evaluated by Monte Carlo simulations in Refs. [148, 156] for AA and in Ref. [157] for pp collisions. The definition of S in e^+e^- is meaningless since it is related to the event by event fluctuations of the projectile/target constituents.

2.6.1 Enhanced production of multi-strange hadrons

The ALICE collaboration reported [95] the enhanced production of multi-strange hadrons, previously observed in $PbPb$ collisions [158], in high energy, high multiplicity, pp events. The strangeness enhancement was suggested to be present in high-multiplicity pp collisions on theoretical grounds in Refs. [159, 160] by considering a specific dynamical variable corresponding to the initial entropy density of the collisions, which takes into account

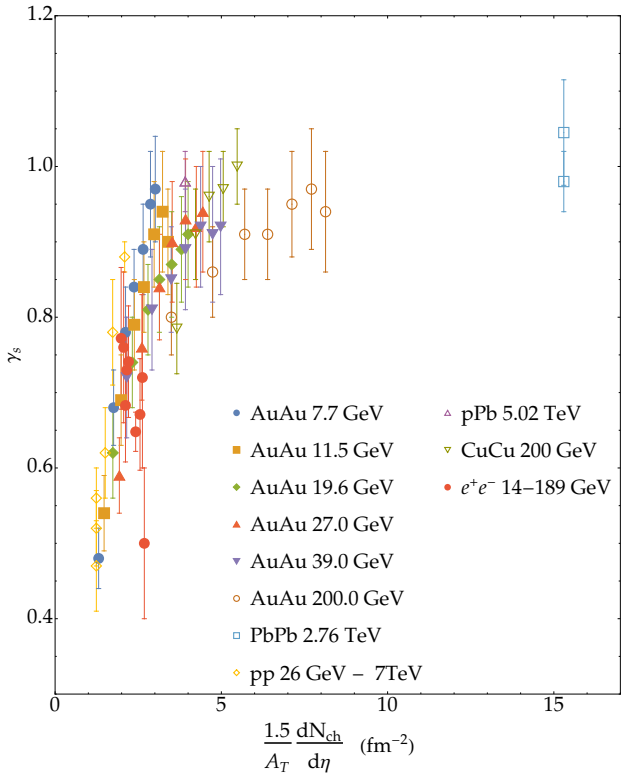

Figure 2.9: The strangeness suppression factor γ_s as a function of initial entropy density evaluated for data from Refs. [63, 166–168]. The Phobos parameterization [131] for the relation between charge multiplicity, energy and the number of participants is applied for RHIC data.

the transverse size (and its fluctuations) of the initial configuration in high multiplicity events [57, 161]. Noticeably, the energy loss in AA collisions was also shown to scale in the same dynamical variable [162].

In Refs. [163, 164] the parameter $\gamma_s \leq 1$, which describes the strangeness suppression in the statistical hadronization model (SHM) [69, 98, 165], was studied as a function of the variable from EQ. (2.53), by using an approximate evaluation of the transverse area for pp, pPb, and AA collisions. On the other hand, there is no strangeness enhancement in e^+e^- annihilation and Figs. 2.7 and 2.8 show the strangeness suppression factor, γ_s, in the statistical hadronization model (SHM) as a function of the available energy

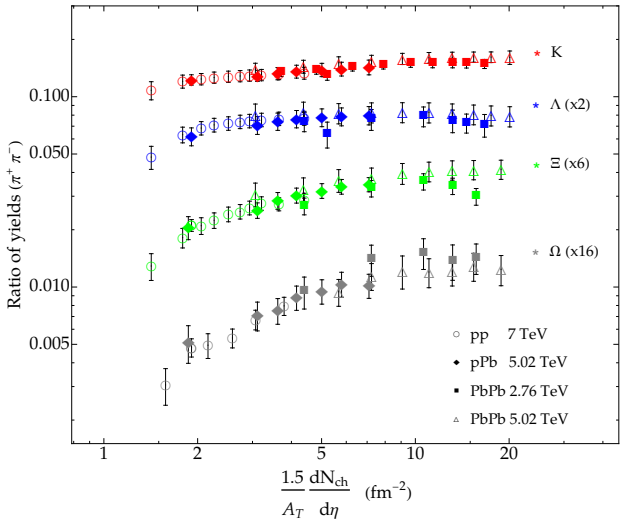

Figure 2.10: The strangeness production quantified in terms of the ratio of yields of K, Λ, Ξ, and Ω hadrons to pions evaluated as a function of initial entropy density for data from Refs. [95, 108, 158, 172–176].

($\gamma_s \simeq 1$ means no suppression, i.e. enhancement). Within the error bars, there is no sign of an enhancement of the strangeness production in the energy range $14-186$ GeV for e^+e^-: a clear difference concerning pp and AA collisions. Therefore the question of the universality in e^+e^- annihilation and the saturation (if any) to $\gamma_s \to 1$ arises. The energy range $14-186$ GeV corresponds to rather a narrow interval of s_0, 2 fm$^{-2} \lesssim s_0 \lesssim 3$ fm^{-2} and the γ_s data in Fig. 2.8 can be plotted on the universal curve as a function of s_0 for comparison with pp and AA.

The resulting scaling behaviour for the strangeness production is reported in Fig. 2.9, where γ_s for AA at different energies and centralities are shown along with those for pPb, pp collisions and e^+e^- annihilation. The data refers to pp at energy $\sqrt{s} = 26$ GeV-7 TeV [63, 166], to pPb at $\sqrt{s} =$ 2.76 TeV [163, 164, 169–171], to $PbPb$ at $\sqrt{s} = 2.76$ TeV [167], to $AuAu$ at $\sqrt{s} = 19.6$, 27, 39 and 200 GeV [168], to $CuCu$ at $\sqrt{s} = 200$ GeV [166], and to e^+e^- at $\sqrt{s} = 14 - 189$ GeV [96]. In proton-proton, proton-nucleus and heavy-ion collisions at high energies, high multiplicities, the universal trend shows that γ_s increases with the parton density in the transverse plane, up to the fixed point $\gamma_s = 1$, where any suppression disappears. It becomes

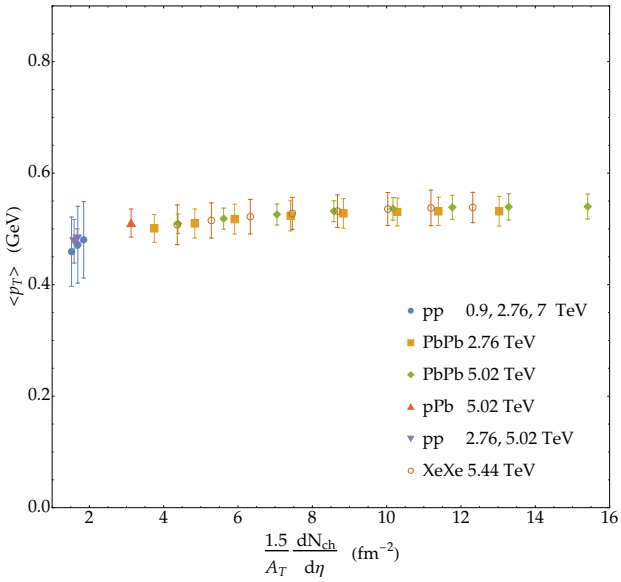

Figure 2.11: Average p_t as a function of initial entropy density evaluated in the interval of $0.15 < p_t < 1.15$ GeV for the data from Refs. [181–184].

a universal function of $s_0\,\tau_0$ as shown in Fig. 2.9 [142–144]. Notice that the strangeness saturation, say $\gamma_s \gtrsim 0.95$, requires $s_0 \geq 6$. For e^+e^- annihilation, γ_s follow the same curve, but the corresponding s_0 is too low to observe an enhancement of strange hadrons.

The universal trend of strangeness production versus entropy density in *PbPb* [158, 172–174], *pPb* [108, 175], *pp* [95, 176] is shown in Fig. 2.10 for different particle species.

2.6.2 The average transverse momentum

The similarity of the average transverse momentum (p_t) between *pp*, *pA*, and *AA* collisions was discussed in Refs. [177–179] where the scaling of p_t as a function of the variable N_{track}/A_T (N_{track} being the multiplicity and A_T the transverse area of the initial system) was explored in the framework of Color Glass Condensate (CGC), where also the geometrical scaling of direct-photon production in hadron collisions at RHIC and LHC energies has been obtained in terms of the saturation scale, proportional to the

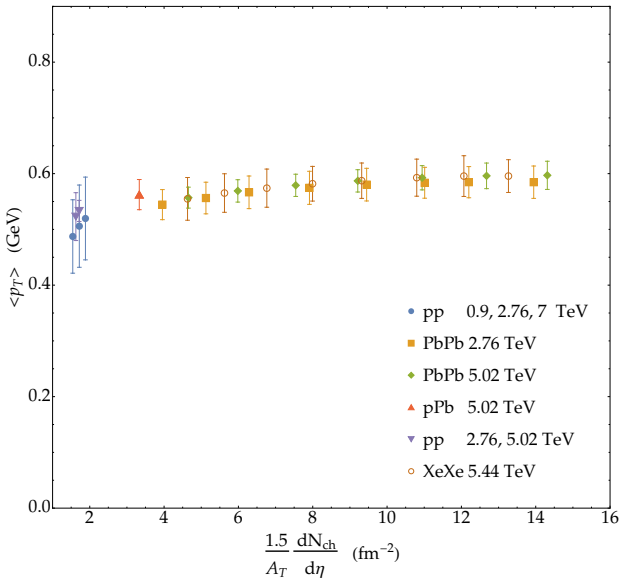

Figure 2.12: Average p_t as a function of initial entropy density evaluated in the interval of $0.15 < p_t < 1.5$ GeV for the data from Refs. [181–184].

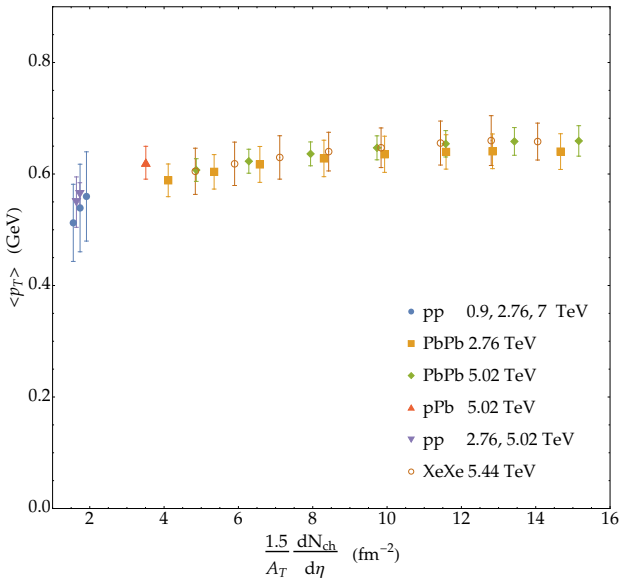

Figure 2.13: Average p_t as a function of initial entropy density evaluated in the interval of $0.15 < p_t < 2$ GeV for the data from Refs. [181–184].

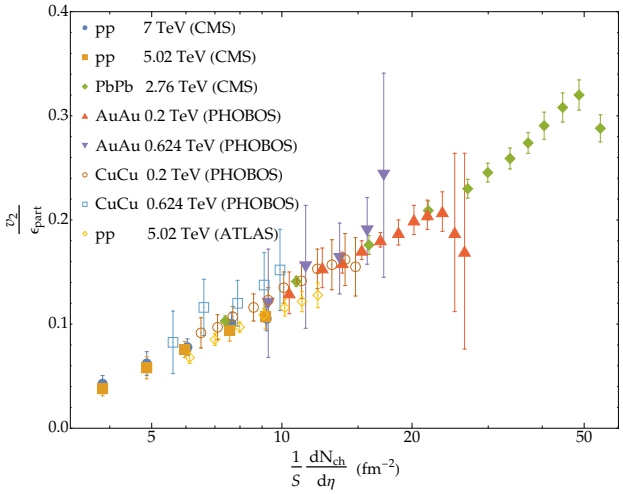

Figure 2.14: The v_2/ϵ_{part} values for pp, $PbPb$, $AuAu$, and $CuCu$ evaluated as a function of entropy density for data from Refs. [120, 123, 156, 186].

transverse entropy density [180]. As recalled, the scaling of the average p_t as a function of the variable N_{track}/A_T has been discussed in [151–153].

In Refs. [143, 144] we analyze the average p_t in the low transverse momentum region where the soft, non-perturbative effects in the particle production are more important due to running of the strong coupling constant than in the higher p_t range. The behaviour of the average p_t is evaluated in the region $0.15 < p_t < 1.15$ GeV for different colliding systems as a function of the dynamical variable from EQ. (2.53).

The results are shown in Fig. 2.11 for the data from Refs. [181–184]. One can see that the average p_t for soft particle production follows the same slowly increasing trend for all the collisional systems. Equally, good scaling was also obtained for the region $0.15 < p_t < 1.5$ GeV (Fig. 2.12) and $0.15 < p_t < 2$ GeV (Fig. 2.13).

2.6.3 Universality in the elliptic flow

In non-central collisions, the beam direction and the impact parameter vector define a reaction plane for each event. If the nucleon density within the nuclei is continuous, the initial nuclear overlap region has an “almond-like”

shape, and the impact parameter determines uniquely the initial geometry of the collision. In a more realistic description, where the position of the individual nucleons that participate in inelastic interactions is considered, the overlap region has a more irregular shape, and the event-by-event orientation of the almond fluctuates around the reaction plane [147, 185]. Therefore, in the analysis of the elliptic flow where the fluctuations are important, the geometrical eccentricity is replaced by the participant eccentricity, ϵ_{part}, defined using the actual distribution of participants. The size of the fluctuation in ϵ_{part} and its correlated transverse area S (different from the geometrical one) are evaluated by Glauber MC as previously described.

We show the scaling behaviour in pp and AA of the ratio between the elliptic flow, v_2, and the participant eccentricity, ϵ_{part} in Ref. [144], extending the results obtained in Refs. [145, 156, 186]. The plot of v_2/ϵ_{part} versus $x = dN_{ch}/S$, where S is the transverse area associated with ϵ_{part}, is depicted in Fig. 2.14 for AA [156, 186] and pp [120, 123] and shows a universal trend starting from $x \geq 2.5$, i.e. $s_0 \geq 3.8$. One can see that the pp trend, at lower values, is smoothly followed by the data-points from AA collisions. Moreover, the difference between the geometrical transverse area A_T (i.e. the overlapping almond shape in AA collisions) and S is crucial to obtain the smooth interpolation among pp and AA data. where

2.6.4 How to check the universal trend

The analyses of γ_s, average p_T, and v_2/ϵ_{part} presented above support the conclusion that at fixed entropy density the "coarse-grain" features of the quark-gluon system formed in high energy collisions are independent of the initial configuration. The scaling variable (EQ. (2.53)) is a function of multiplicity and the transverse area, and one can evaluate at which multiplicity one can expect the same behaviour in high-multiplicity pp, $PbPb$ collisions, and e^+e^- annihilation, by solving the equation $(dN/d\eta)_{AA}/A_T^{AA} = x/A_T^{pp}(x)$ for x being the multiplicity in pp. The result is shown in TAB. 2.1 for $PbPb$ collisions at 5.02 TeV which represent the largest available heavy-ion dataset at the LHC. The values from TAB. 2.1 can be used in subsequent experimental or phenomenological studies aiming to further check the universal trends in hadronic and nuclear collisions using high-multiplicity pp collisions

$\frac{1.5}{A_T}\frac{dN_{ch}}{d\eta}$	$\left(\frac{dN_{ch}}{d\eta}\right)_{e^+e^-}$	$\left(\frac{dN_{ch}}{d\eta}\right)_{pp}$	$\left(\frac{dN_{ch}}{d\eta}\right)_{PbPb}$	$PbPb$ Cent.
20.1 ± 0.8	58 ± 3	$100. \pm 4.$	$1943. \pm 56.$	0-5%
17.5 ± 1.1	49 ± 4	$87. \pm 5.$	$1587. \pm 47.$	5-10%
15.4 ± 0.9	42 ± 3	$76. \pm 4.$	$1180. \pm 31.$	10-20%
12.2 ± 0.6	31 ± 2	60.6 ± 3.1	$649. \pm 13.$	20-40%
8.3 ± 0.7	19 ± 2	41.2 ± 3.4	$251. \pm 7.$	40-60%
5.2 ± 0.8	10 ± 2	$26. \pm 4.$	70.6 ± 3.4	60-80%
3.1 ± 1.1	5 ± 3	12.4 ± 3.0	17.5 ± 1.8	80-90%

Table 2.1: $dN_{ch}/d\eta$ in $PbPb$ at 5.02 TeV, pp and e^+e^- for different values of the variable in EQ. (2.53).

at the largest available LHC energies.

2.6.5 Comments and Conclusions

High energy, high multiplicity events produced in small colliding systems show dynamical behaviour very similar to that present in AA collisions [144], and it was assumed that the dynamical behaviour is driven mainly by the initial entropy, a density that is by the parton density in the transverse plane. A clear quantification of limits on the presence of jet quenching in small colliding systems (see, e.g. discussions and new measurements in Refs. [187–189]) or more detailed correlation measurements (see, e.g. recent work in Refs. [190–192]) may help to improve understanding of this similarity. This kind of measurements can be done in details at the LHC or RHIC or at a 100 TeV pp collider which is considered for the future [193] and which would significantly enhance the reach of pp collisions in multiplicities.

Moreover, the previous analysis [142] clarifies that in e^+e^- annihilation at the LEP or lower energies there is no chance of observing the enhancement of the strangeness production, that is $\gamma_s \gtrsim 0.95$, because the parton density in the transverse plane is too small: s_0 turns out to be ≤ 3, but a value larger than 6 is required. The multiplicity one needs in e^+e^- annihilation to obtain the same value of s_0 determined for pp and $PbPb$ collisions are reported in Table 2.1, by extrapolating to very high energy the fit of the

multiplicity in Fig. A.1, i.e. at LEP and lower energies. Analogously, the value $s_0|_{e^+e^-}$ is too small for observing the flow-like effect, although in this case, a precise value is difficult to determine, due to the uncertainty in the estimate of the transverse area associated with the eccentricity. In conclusions, one can expect in e^+e^- annihilation some similarity with pp and AA collisions only at very high energy. There is a hierarchy in energy and multiplicity to see the "collective" effects starting from low energy in AA to larger energy and multiplicity in pp collisions and much more large energies in e^+e^- annihilation.

Chapter 3

Quantum Chromodynamics and effective models

The QCD coupling constant grows as the energy decreases. Therefore, at the transition temperature, non-perturbative methods are needed to determine the low energy properties of QCD. In this chapter, I treat some of the main methods and models to study QCD around the phase transition, where one can not evaluate the observables of the system perturbatively.

3.1 Lattice QCD

LATTICE QCD (LQCD) is a theoretical framework to evaluate the observables of QCD at zero chemical potential. The idea is to do the calculations in a discrete space-time and then, after all, to evaluate the continuum limit. The method, proposed by K. Wilson in 1974 [194] (for recent reviews see for example [195–197]), consists of discretizing the partition function, $\mathcal{Z}$, usually on a hypercubic lattice with lattice spacing a. The $\mathcal{Z}$ is written as the path integral

$$\mathcal{Z} = \int [dU]\, e^{-S_g[U]} \prod_f \det\left(D[U] + m_f\right) \ , \tag{3.1}$$

where S_g is the gauge action, U is the gluon field, $D[U]$ is the covariant derivative and m_f is the fermionic mass. Such partition function depends

on the inverse temperature $\beta = 1/T$ (since the time component is rotated). Thus, the temperature T and the three-volume V are discretized on a hypercubic lattice with spacing N_t and N_s such that

$$T = \frac{1}{N_t\, a}\,, \qquad\qquad V = (N_s\, a)^3\ . \tag{3.2}$$

The quark fields are placed on sites, while the gauge fields are associated with the links among them. These links, in the continuum, are Wilson lines connecting different points. The simplest gauge action (the Wilson's one) is

$$\begin{aligned} S_g =& \frac{6}{g^2} \sum_{x,\mu,\nu} \left[1 - \frac{1}{3} \Re\mathrm{Tr} \left[U_\mu(x) U_\nu(x + a\,\widehat{\mu}) U_\mu^\dagger(x + a\,\widehat{\nu}) U_\nu^\dagger(x) \right] \right] \\ & \xrightarrow{a\to 0} \frac{1}{4\,g^2} \int d^4x\ \mathrm{Tr}\left[F_{\mu\nu}^2(x) \right]\ . \end{aligned} \tag{3.3}$$

It corresponds to the product of gauge links around an elementary lattice cell, and, in the continuum limit, produces the kinetic gluonic term. The derivative in EQ. (3.1) can be discretized in several ways, and the simplest one is with a symmetric difference. The naive fermion action that arises suffers from the fermion doubling problem: it describes 2^d equivalent fermion fields for each physical quark flavor (d is the space-time dimension), and these spurious d.o.f.s survive in the continuum limit. That happens because chiral theory can not be formulated on a lattice in even dimensions and with periodic boundary conditions (because the Nielsen–Ninomiya theorem [198]).

The lattice spacing plays the role of an ultraviolet regulator, rendering the quantum field theory finite, and the continuum theory is recovered by taking the limit of vanishing a. However, it leads to discretization errors, as for example the breaking of the Euclidean rotational invariance (the Euclidean version of the Lorentz invariance). Statistical errors come up, e.g., from the use of Monte-Carlo integration methods. Some of these discretization errors are proportional to powers of $a\, m_q$ (m_q is the mass of the quark). Consequently, one can study only theories with quarks whose masses are smaller then the lattice cutoff (typically $1/a = 2 - 4$ GeV).

Several ways in which the QCD action can be discretized were built:

Symanzik effective action [1], staggered [2] quarks, by considering only 2 or $2+1$ flavours, etc..

3.1.1 Equation of state at $\mu = 0$

One method to evaluate the equation of state (EoS) at $\mu = 0$ consists in defining the trace anomaly on the lattice as

$$\Theta^{\mu\mu} = -\frac{T}{V}\,\frac{d\ln\mathcal{Z}}{d\ln a}\,. \tag{3.4}$$

This method is used, for example, by the HotQCD collaboration [201–203], and their results concerns simulations of $2+1$ flavours QCD in the temperature range $130-400$ MeV, using the highly improved staggered quark (HISQ) action and the tree-level improved gauge action, with the Goldstone pion mass tuned to about 160 MeV in the continuum limit and temporal extent $N_t = 6$, 8, 10 and 12.

Once the trace anomaly $\Theta_{\mu\mu}$ is given, one evaluates all other thermodynamical quantities, i.e. the pressure

$$\frac{p(t)}{T^4} = \frac{p_0}{T_0^4} + \int_{T_0}^{T} dT'\,\frac{\Theta^{\mu\nu}(T')}{T'^5}\,, \tag{3.5}$$

where p_0 is the pressure at a fixed temperature T_0, the energy density

$$\varepsilon = 3\,p + \Theta^{\mu\nu}\,, \tag{3.6}$$

[1] The discretization errors are reduced by adding higher-dimensional operators (connected to the interactions between quarks and gluons with momenta lower of the lattice cutoff, $1/a$) suppressed by powers of a. E.g. for the gauge action, one adds Wilson loops involving six gauge links (instead of the four links in EQ. (3.3) [199].

[2] Staggered fermions are fermions with only a single fermion Dirac component on each lattice site, with the full Dirac structure built up from neighbouring sites [200]. They allow to have faster simulations, preserve some chiral symmetry, have discretization errors of $O(a^2)$, and are constructed in order to partially reduce the number of doublers (in dimension four, the action describes four degenerate fermions in the continuum limit for each physical quark flavor).

c_t	a_n	b_n	c_n	d_n
3.8706	-8.7704	3.9200	0	0.3419
t_0	a_d	b_d	c_d	d_d
0.9761	-1.2600	0.8425	0	-0.0475

Table 3.1: Parameters used in Eqs. (3.9) and (3.10) for the pressure of (2+1)-flavours QCD in the temperature interval $T \in [130, 400]$ MeV [202, 203].

the entropy density s

$$s = \frac{\varepsilon + p}{T} \,, \tag{3.7}$$

and the speed of sound

$$c_s^2 = \frac{\partial p}{\partial \varepsilon} = \frac{s}{C_V} = \frac{\partial p / \partial T}{\partial \varepsilon / \partial T} \,, \tag{3.8}$$

where C_V is the specific heat.

The pressure obtained by lattice simulations, $p_{lattice}$, by the HotQCD collaboration can be parametrized as follows [202, 203]:

$$p_{lattice}(T) = \frac{T^4}{2} \left[1 + \tanh\left[c_t \left(t - t_0\right)\right]\right] f(T), \tag{3.9}$$

where

$$f(T) = \frac{p_{id} + \frac{a_n}{t} + \frac{b_n}{t^2} + \frac{c_n}{t^3} + \frac{b_n}{t^4}}{1 + \frac{a_d}{t} + \frac{b_d}{t^2} + \frac{c_d}{t^3} + \frac{b_d}{t^4}} \tag{3.10}$$

and $t = T/T_c$, $T_c = 154\, MeV$, $p_{id} = 95/180\pi^2$ is the ideal gas value of p/T^4 for massless 3-flavours QCD and the value of the other parameters are summarized in Table 3.1.

3.1.2 Equation of state at $\mu \neq 0$

LQCD fails at $\mu \neq 0$ because of the so-called "sign problem": the determinant in EQ. (3.1) becomes complex, since non zero value for the chemical potential breaks charge-conjugation symmetry. For small values of the chemical potential, one way to proceed is to consider Taylor series expansion

that includes contributions from higher order in the baryon, strangeness and electric charge chemical potentials.

In Ref. [204], the QCD equation of state in the temperature range $T \in [135, 330]$ MeV and for chemical potential up to $\mu \sim 2\ T_c \sim 300$ MeV has been studied by the HotQCD collaboration, by Taylor expansion up to sixth order. Calculations have been performed with the HISQ action, with lattice space corresponding to $N_s/N_t = 4$, with $N_t = 6 - 16$, with a strange quark mass tuned to its physical value and two choices for the strange to light quark mass ratios, $m_s/m_l = 20$ and 27 (which correspond to a pion mass of about 160 MeV and 140 MeV respectively).

The expansion series for the pressure is

$$P(\beta, \gamma) \simeq P_0 + \sum_{n=1}^{\infty} \frac{P_{2n}}{\beta^4}\, \gamma^{2n}\ , \tag{3.11}$$

where $\beta = 1/T$ is the inverse temperature, $\gamma = -\mu/T$ is the parameter of development, P_0 is the pressure at zero chemical potential, and

$$P_{2n}(\beta) \equiv \frac{\chi_{2n}(\beta)}{(2\,n)!}\ , \tag{3.12}$$

with

$$\chi_{2n}(\beta) = \left.\frac{\partial^{2n} P(\beta, \gamma)\, \beta^4}{\partial \gamma^{2n}}\right|_{\gamma=0} \tag{3.13}$$

the cumulants. For strangeness neutral systems with a fixed ratio of electric charge to baryon density (see [204] for details), one has

$$P_2(\beta) = \frac{1}{2}\left[N_1^B(\beta) + r\ q_1(\beta)\, N_1^B(\beta)\right] \tag{3.14}$$

$$P_4(\beta) = \frac{1}{4}\Big[N_3^B(\beta) + r\ \Big(q_1(\beta)\, N_3^B(\beta) + 3\, q_3(\beta) N_1^B(\beta)\Big)\Big] \tag{3.15}$$

$$P_6(\beta) = \frac{1}{6}\Big[N_5^B(\beta) + r\ \Big(q_1(\beta)\, N_5^B(\beta) + 3\, q_3(\beta) N_3^B(\beta + 5\ q_5(\beta)\, N_1^B(\beta))\Big)\Big]\ , \tag{3.16}$$

being N_{2n-1}^B the $(2n-1)$-th coefficient for the power expansion of the baryon

number density divided by T^3,

$$\frac{n_B}{T^3} = \sum_{n=1}^{\infty} N^B_{2n-1}\, \gamma^{2n-1} \,, \tag{3.17}$$

q_{2n-1} are the expansion coefficients for the electric charge chemical potential, and

$$r \equiv \frac{n_Q}{n_B} \,, \tag{3.18}$$

with n_Q and n_B the charge and baryon number densities respectively.

3.2 Hadron Resonance Gas models

The confined phase can be described by a statistical approach in terms of a gas of hadrons and resonances: the hadron resonance gas (HRG) model. There are several versions of the HRG model which give different results [205] with some ambiguity and dependence on the specific model. Some of them are build by using as Hamiltonian the sum of kinetic energies of relativistic Fermi and Bose particles of mass m_i (eventually adding some terms to reproduce repulsive or attractive interaction). Indeed, this Hamiltonian contains all relevant degrees of freedom of the confined, strongly interacting matter, including (implicitly) the interactions that result in resonances formation [206].

The "Ideal" Hadron Resonance Gas (iHRG) model is the minimal version to study a system of hadrons statistically. It consists of non-interacting particles, and its partition function is simply the sum over all particles one include of the single-particle partition function. Although mathematically it is made as a gas of non-interacting particles (with mass less than some threshold value, m_{max}), it includes the interactions that are implicit, i.e. it includes only that resulting in resonance formation. This minimal version is surprisingly in good agreement with the experimental data concerning particle multiplicity (see, e.g., Refs. [60, 207–211]), that are only weakly affected by the repulsive corrections [212]. However, extensions of the iHRG are build to include repulsive or attractive interactions and to improve the match with other observables (especially observables of density type, and not ratio) or LATTICE predictions on cumulants.

3.2.1 Basic model: the ideal HRG

In the HRG model with point-like constituents, the partition function is simply expressed as

$$\mathcal{Z} = \prod_i \mathcal{Z}_i^1 \ , \tag{3.19}$$

where the sum is over all hadrons and resonances. The one-particle partition functions, $\mathcal{Z}_i^1$, for particle "i" with mass m_i, baryon number B_i, strangeness S_i, electric charge Q_i and isospin degeneracy factor g_i, is

$$\ln \mathcal{Z}_i^1 = \eta_i \, \frac{V \, d_i}{2\pi^2} \int_0^\infty dk \; k^2 \ln \left[1 + \eta_i \; \lambda_i \; e^{-\beta \sqrt{k^2 + m_i^2}} \right] \ , \tag{3.20}$$

with $\eta_i = -1(+1)$ for bosons (fermions), and

$$\lambda_i = e^{\beta \left(B_i \, \mu_B + S_i \, \mu_S + Q_i \, \mu_Q \right)} \ , \tag{3.21}$$

where μ_B, μ_S and μ_Q are the chemical potential related to baryon number, strangeness and electric charge, respectively. Due to the factorization of the partition function in EQ. (3.19), the number density, the energy density, and the pressure are also expressed as sums over single-particle contributions, and, expanding the logarithm and performing the momentum integration, they can be written as [206, 213]

$$\frac{n}{T} = \sum_{m_i \leq m_{max}} \frac{d_i}{2\,\pi^2} \sum_{k=1}^{\infty} \frac{(-\eta_i)^{k+1}}{k} \; m_i^2 \; \lambda_i^k \; K_2 \left(\frac{k \, m_i}{T} \right) \ , \tag{3.22}$$

$$\frac{\varepsilon}{T^4} = \sum_{m_i \leq m_{max}} \frac{d_i}{2\,\pi^2} \sum_{k=1}^{\infty} \frac{(-\eta_i)^{k+1}}{k} \; \lambda_i^k \left(\frac{m_i}{T} \right)^3 \left[\frac{3\,T}{k \, m_i} \; K_2 \left(\frac{k \, m_i}{T} \right) + K_1 \left(\frac{k \, m_i}{T} \right) \right] \ , \tag{3.23}$$

and

$$\frac{P}{T^4} = \sum_{m_i \leq m_{max}} \frac{d_i}{2\,\pi^2} \sum_{k=1}^{\infty} \frac{(-\eta_i)^{k+1}}{k} \; \lambda_i^k \left(\frac{m_i}{T} \right)^3 \frac{T}{k \, m_i} \; K_2 \left(\frac{k \, m_i}{T} \right) \ , \tag{3.24}$$

where K_1 and K_2 are the modified Bessel function.

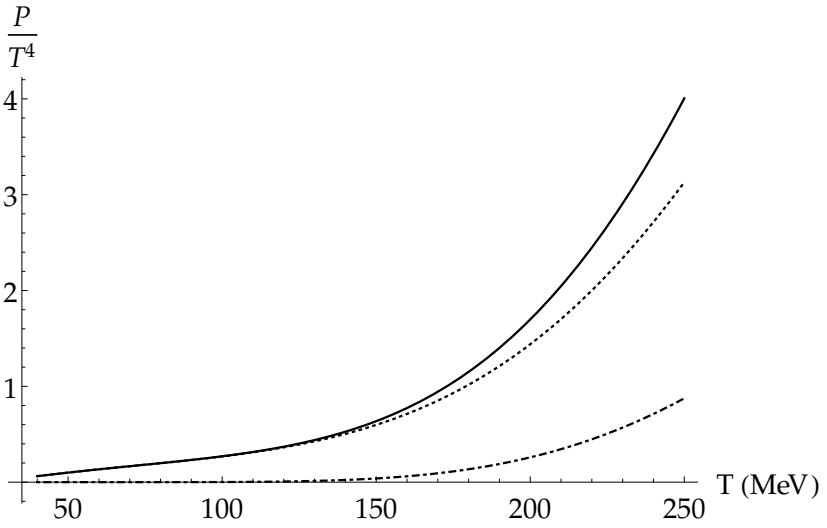

Figure 3.1: The total pressure of a HRG gas $P_0^H(\beta)$ (black line), the meson contribution $P_M^H(\beta)$ (dotted line) and the $P_B^H(\beta)$ (dot-dashed line) at $\mu_B = 0$.

For small μ_B, and $\mu_S = \mu_Q = 0$, the baryon sector of an HRG can be described by the Boltzmann approximation. The pressure thus becomes [204]

$$P(\beta, \gamma) = P_0(\beta) + P_B(\beta)\,(\cosh\gamma - 1)\ , \tag{3.25}$$

where $P_0(\beta) = P_M(\beta) + P_B(\beta)$ is the total pressure at $\mu_B = 0$ (EQ. (3.24)). Here $P_M(\beta)$ and $P_B(\beta)$ are the mesonic and the baryonic contributions to EQ. (3.24), respectively, and $\gamma = -\mu_B/T$. In Figure 3.1 are plotted the total pressure $P_0(\beta)$ at $\mu_B = 0$ (black line), the mesonic part (dotted line), $P_M(\beta)$, and the baryonic part (dot-dashed line), $P_B(\beta)$.

3.2.2 HRG with repulsive and attractive interactions

The ideal HRG includes interaction only implicitly. Recently, however, extensions including repulsive and attractive interactions are considered in order to consider quantum statistical effects and to apply the EoS to hadronic and nuclear systems. The repulsive one at short distances are usually described as a hard-core description, treated as an excluded volume correction

(à la Van-der-Waals) [60]. In a thermodynamically consistent way [214, 215], these corrections can be seen as a shift in the baryon–chemical potential. Indeed, for particles with hard volume V_0, the number density can be written as [214]

$$n = \frac{n^{id}}{1 + n^{id}\, V_0} \,, \tag{3.26}$$

where n^{id} is the number density of point-like particles. Similarly, the energy and entropy densities are

$$\varepsilon = \frac{\varepsilon^{id}}{1 + n^{id}\, V_0} \,, \tag{3.27}$$

and

$$s = \frac{s^{id}}{1 + n^{id}\, V_0} \,, \tag{3.28}$$

being ε^{id} and s^{id} the point-like values. Since the pressure is

$$P = -\left(\frac{\partial(E/N)}{\partial(V/N)}\right)_{S/N} = n^2 \, \left(\frac{\partial(\varepsilon/n)}{\partial n}\right)_{s/n} \,, \tag{3.29}$$

one find that

$$P = P^{id} \,, \tag{3.30}$$

i.e. the pressure of an interacting gas, when interaction is taken into account by hard-core repulsive only, is the same as that of an ideal gas [214].

However, the change of the system configuration from point-like to extended nucleons also affects the phase structure through the Gibbs free energy: the Gibbs free energy ϕ per extended particle in our formalism is not equal to the chemical potential, μ, but [215]

$$\phi = 2\mu^\star = \mu - V_0 \; P \,, \tag{3.31}$$

and

$$P(T, \mu) = P^{id}(T, \mu^\star) \,. \tag{3.32}$$

Other kinds of repulsive interactions can be included similarly: one starts by writing the pressure as [216]

$$P_{ev} = T \, Z(\eta) \, n \,, \tag{3.33}$$

where $\eta = b\,n/4 = 4\,\pi\,n\,r^3/3$ is the packing fraction, n is the number density, and $Z(\eta)$ is a dimensionless "compressibility" factor. Specific models can be then obtained by defining, for example, an excluded volume repulsion term by the van der Waals (VdW) equation as

$$Z_{VdW}(\eta) = \frac{1}{1-4\,\eta} \tag{3.34}$$

or by the Carnahan-Starling (CS) term [217]

$$Z_{CS}(\eta) = \frac{1+\eta+\eta^2-\eta^3}{(1-\eta)^3}\ . \tag{3.35}$$

The CS compressibility factor (3.35), introduced to describe a gas of rigid spheres and to improve the approximation of the virial expansion [217], indeed reproduces rather accurately the virial expansion terms up to the eighth order, where the VdW approach fails (recall that higher-order terms describe the contribution of non-binary interactions).

The previous expression (3.33) can be extended to the Grand Canonical ensemble and generalized to include an attractive interaction. The "shift" in the chemical potential in EQ. (3.31) now becomes [216, 218, 219]

$$\mu = \mu^\star - \frac{b}{4}\,f'(\eta)\,P^{id}(T,\mu^\star) + u(n) + n\,u'(n) \tag{3.36}$$

where $f(\eta)$ gives the permitted volume region, $u(n)$ is the mean total energy per particle of the attractive interaction and $n = n(T,\mu)$ is the particle number density.

The pressure turns out to be [218, 219]

$$P(T,\mu) = [f(\eta) - \eta\,f'(\eta)]\ P^{id}(T,\mu^\star) + n^2\,u'(n)\ , \tag{3.37}$$

and entropy, energy density and number density are related to the corresponding quantities of the ideal HRG by the equations:

$$s(T,\mu) = f(\eta)\,s^{id}(T\,\mu^\star)\ , \tag{3.38}$$

$$\varepsilon(T,\mu) = f(\eta)\,\varepsilon^{id}(T,\mu^\star) + n\ u(n), \tag{3.39}$$

and

$$n(T,\mu) = f(\eta)\; n^{id}(T,\mu^\star)\;. \tag{3.40}$$

The quantities (3.34) and (3.35) are now replaced by [216, 218, 219]

$$f_{VdW}(\eta) = 1 - 4\;\eta \tag{3.41}$$

and

$$f_{CS}(\eta) = \exp\left\{-\frac{(4-3\;\eta)\;\;\eta}{(1-\eta)^2}\right\}\;. \tag{3.42}$$

The attractive term can have different expressions also: for example, a VdW approach leads to

$$u_{VdW}(n) = -a\;n \tag{3.43}$$

and the Clausius form is

$$u_{Cl}(n) = -\frac{a\;n}{1+b\;n}\;. \tag{3.44}$$

Finally, the previous models can be easily generalized to a multi-component gas by defining the ideal pressure as a sum over meson, M, baryon, B and anti-baryon $\overline{B}$ contributions [218, 219],

$$p^{id}(T,\mu^\star) = \sum_{j\in M} p_j^{id}(T,\mu_j^\star) + \sum_{j\in B} p_j^{id}(T,\mu_j^\star) + \sum_{j\in \overline{B}} p_j^{id}(T,\mu_j^\star)\;, \tag{3.45}$$

with different packing fraction for each species.

3.3 Nambu - Jona Lasinio model

The Nambu - Jona Lasinio (NJL) model was first introduced in 1961 [220, 221] (even before the introduction of the quarks and the QCD) to describe interacting nucleons. It answers the request to find a method to explain the large nucleon mass, despite the existence of a (partially) conserved axial vector current, i.e., in the QCD language, the chiral symmetry. Indeed, chiral symmetry requires massless fermions (whether they are nucleons or quarks). To overcome this problem, the idea is that mass can be generated

dynamically, analogously to the energy gap of a superconductor in the BCS theory developed a few years earlier [222]. In the mid 80's it was reinterpreted as a quarks model [223, 224], by replacing the nucleon field with a quark one with at least two flavours and three colour degrees of freedom. However, this choice is not unique, but one can add many other chirally symmetric interaction terms. It was used, among other things, to study the symmetric and the asymmetric matter, phase transition at finite temperature and chemical potential, colour superconductivity and the structure of some Astro-objects [212, 225–238].

The main characteristics of the NJL model are the chiral symmetry and its spontaneous breakdown in the vacuum. On the other hand, the NJL model does not confine. It is an effective approach that, for fermions with equal masses, is described by a Lagrangian for a fermion field ψ with a point-like, chirally symmetric four-fermion interaction [23, 221, 239–242]:

$$\mathcal{L}_{SU(2)} = \overline{\psi}_f \left(i \not{\partial} - m\right) \psi_f + G \left[\left(\overline{\psi}_f \psi_f\right)^2 + \left(\overline{\psi}_f i\gamma_5 \overrightarrow{\tau} \psi_f\right)^2 \right] . \tag{3.46}$$

Here G is a dimensionful coupling, m is the current fermion mass ($m = 0$ is the chiral limit) and $\overrightarrow{\tau}$ are the Pauli matrices. The Hartree approximation can be obtained via the substitution [242]

$$(\bar{\psi}_f O \psi_f)^2 \longmapsto 2 \left\langle \bar{\psi}_f \, O \, \psi_f \right\rangle \bar{\psi}_f \, O \, \psi_f - \left\langle \bar{\psi}_f \, O \, \psi_f \right\rangle^2 , \tag{3.47}$$

in which O is an operator. Thus, in the Nambu–Jona Lasinio (NJL) model with two flavours ($f = u,\ d$), the $SU(2)$ Lagrangian in EQ. (3.46) becomes

$$\mathcal{L}_{SU(2)} = \overline{\psi}_f \left(i \not{\partial} - M\right) \psi_f - \frac{(M-m)^2}{4\,G} , . \tag{3.48}$$

where $M = m - 2\,G \left\langle \bar{\psi}_f \, \psi_f \right\rangle$ is the constituent quark mass.

The self-energy is then generated by the local four-fermion interaction, and it generates dynamically an effective mass M considerably larger than m, even in the chiral limit. Moreover, the pion emerges as the Goldstone boson of the spontaneously broken chiral symmetry, with zero mass in the

chiral limit. Indeed,

$$M = m + 2\, i\, G \int \frac{d^4p}{(2\pi)^4}\, \mathrm{Tr} S(p)\,, \tag{3.49}$$

where $S(p) = (\not{p} - M + i\,\varepsilon)^{-1}$ is the dressed quark propagator. The trace is to be taken in colour, flavour, and Dirac space. For a sufficiently strong coupling G, this allows for a non-trivial solution $M \neq m$, even in the chiral limit m = 0, producing a gap of $\Delta E = 2M$ in the quark spectrum.

The thermodynamic potential, Ω, at finite temperature and chemical potential turns out to be the same of a system of non-interacting particles with mass M [23] (apart for a constant):

$$\Omega(M_f) = \frac{(M_f - m)^2}{4\,G} + N_f\, \Omega_f\ . \tag{3.50}$$

Here M_f is the dynamically generated mass, and the free Fermi-gas contribution is

$$\Omega_f = -T \sum_n \int \frac{d^3p}{(2\pi)^3}\, \mathrm{Tr} \ln \left(\frac{1}{T}\, S_f^{-1}(i\,\omega_m; \overrightarrow{p}) \right)\ , \tag{3.51}$$

with the inverse fermion propagator given by $S_f^{-1}(p) = \not{p} - \mu\gamma^0 - M_f$. $p^0 = i\ \omega_n = (2n+1)\,\pi\ T$ are fermionic Matsubara frequencies, and the trace is to be taken in colour, flavour, and Dirac space. Using the relations

$$\mathrm{Tr} \ln(\not{Q} - M_f) = \ln \det(\not{Q} - M_f) = 2\ N_f\ N_c\ \ln(Q^2 - M_f^2)\ , \tag{3.52}$$

and

$$T\ \sum_n \ln \left(\frac{\omega_n^2 + \lambda_k^2}{T^2} \right) = \lambda_k + 2\ T\ \ln\left(1 + e^{-\lambda_k/T}\right)\ , \tag{3.53}$$

one finally gets

$$\Omega_f = -2N_c \int \frac{d^3p}{(2\pi)^3} E_f - 2N_c T \int \frac{d^3p}{(2\pi)^3} \ln \left[\left(1 + e^{-\frac{E_f + \mu_f}{T}} \right) \left(1 + e^{-\frac{E_f - \mu_f}{T}} \right) \right]\ , \tag{3.54}$$

where $E_f = \sqrt{p^2 + M_f^2}$, and N_c and N_f are the numbers of colours and

flavours respectively, μ_f is the quark f chemical potential, and a cutoff Λ regulates the integrals. For $m_u = m_d$, $\mu = \mu_u = \mu_d$, the generated quark mass is $M = M_u = M_d$.

To evaluate the minimum of Ω by EQ. (4.59), one has to solve the self-consistent gap equation

$$\frac{\partial \Omega}{\partial M} = 0 \; , \tag{3.55}$$

i.e.

$$M = m - 2\,G\,\left\langle \overline{\psi}\psi \right\rangle \; , \tag{3.56}$$

where $\left\langle \overline{\psi}\psi \right\rangle$ is the quark-antiquark condensate:

$$\left\langle \overline{\psi}\psi \right\rangle = -2\,N_c\,N_f \int \frac{d^3p}{(2\,\pi)^3}\,\frac{M}{E}\;\Psi(T,\mu) \; , \tag{3.57}$$

with

$$\Psi(T,\mu) = 1 - n_+(\mu) - n_-(\mu) \tag{3.58}$$

and

$$n_\pm(\mu) = \frac{1}{1 + \exp\left\{\frac{E \pm \mu}{T}\right\}} \; . \tag{3.59}$$

For three flavours, the NJL version has been developed in the mid-80s [243, 244], and there are many terms which are consistent with the symmetries and which could be added to the Lagrangian.

The isospin symmetric ($m_u = m_d = m$), with explicitly breaking of the $SU(3)$-flavour symmetry ($m_s \neq m$, and thus $M_u = M_d \neq M_s$), most commonly used Lagrangian is [23, 245, 246]

$$\mathcal{L}_{SU(3)} = \overline{\psi}\,(i\,\partial\!\!\!/ - \widehat{m})\,\psi + \mathcal{L}_4 + \mathcal{L}_6 \; , \tag{3.60}$$

with

$$\mathcal{L}_4 = G\,\sum_a \left[\left(\overline{\psi}\lambda_a\,\psi\right)^2 + \left(\overline{\psi} i\gamma_5 \lambda_a \psi\right)^2 \right] \tag{3.61}$$

and

$$\mathcal{L}_6 = -K \left[\det \overline{\psi}\,(1+\gamma_5)\,\psi + \det \overline{\psi}\,(1-\gamma_5)\,\psi \right] \; , \tag{3.62}$$

where $\psi = (u, d, s)^T$, $\widehat{m} = \mathrm{diag}\,(m, m, m_s)$, $\lambda_0 = \sqrt{2/3}\,\mathbb{1}_{3\times3}$, and $\mathbb{1}_{3\times3}$ is the 3×3 identity matrix. The λ_as ($a = 1, \ldots, 8$) are the Gell-Mann matrices and K and G are dimensionful coupling constants. $\mathcal{L}_4$ is a $U(N_f)_L \times U(N_f)_R$ symmetric 4-point interaction. The 't Hooft interaction term, $\mathcal{L}_6$, which represents a maximally flavour-mixing $2\,N_f$-points interaction involving an incoming and an outgoing quark of each flavour, is phenomenologically essential to get the correct mass splitting of the η and η' mesons (because it is $SU(N_f)_L \times SU(N_f)_R$ symmetric, but breaks the $U_A(1)$ symmetry). It is also responsible for the additional two quark loops term in the GAP equations,

$$M_i = m_i - 4\,G\,\left\langle\overline{\psi}_i\psi_i\right\rangle + 2\,K\,\left\langle\overline{\psi}_j\psi_j\right\rangle\left\langle\overline{\psi}_k\psi_k\right\rangle \qquad (j,\ k \neq i)\ , \tag{3.63}$$

that contains, in addition to the usual term $4\,G\,\left\langle\bar{\psi}_i\psi\right\rangle$, a new flavour mixing term proportional to the coupling constant K. Moreover, Eqs. (3.63) are coupled with the quark condensates

$$\left\langle\overline{\psi}_i\psi_i\right\rangle = -2\,N_c\int\frac{d^3p}{(2\,\pi)^3}\,\frac{M_i}{E_i}\,\Psi_i\ , \tag{3.64}$$

where

$$\Psi_i = 1 - \frac{1}{1+e^{\frac{E_i+\mu_i}{T}}} - \frac{1}{1+e^{\frac{E_i-\mu_i}{T}}}\ . \tag{3.65}$$

Finally, the thermodynamic potential Ω turns out to be [23]

$$\Omega = \sum_{f=u,d,s}\Omega_f + 2\,G\sum_{f=u,d,s}\left\langle\overline{\psi}_f\psi_f\right\rangle^2 - 4\,K\,\left\langle\overline{u}u\right\rangle\left\langle\overline{d}d\right\rangle\left\langle\overline{s}s\right\rangle\ , \tag{3.66}$$

with Ω_f in EQ. (3.54).

Main problems of the model:

- The NJL model is not renormalizable, and typically one uses a 3-momentum cut-off to regularize integrals, since this method preserves the analytical structure of the equations of the theory, although it violates the Lorentz covariance of the model. A 3-momentum cut-off regularization leaves the two flavours NJL model with three parameters: the bare quark mass m, the coupling constant G, and the cut-off Λ. The three flavours NJL model contains two other parameters: the

coupling constants K, and the bare mass m_s.

These parameters are usually fixed by fitting some observables: the pion mass, m_π, the pion decay constant, f_π, and the quark condensate for the two flavours NJL model; f_π, m_π, and the masses of the mesons K, η and η' for the three flavours one.

- NJL model does not confine, and it lacks the corrects degrees of freedom. Indeed it is a model with point-like quarks, ma no gluons. Surprisingly, at temperatures above the transition one, it reproduces the results obtained with BAG model or LQCD quite well (since at high temperatures confinement becomes less relevant). These issues (confinement and gluon degrees of freedom) are also irrelevant for cold deconfined quark matter, as for superconductivity. Moreover, there are other situations where chiral symmetry, and not confinement, is the relevant feature of QCD: for example, to understand the Goldstone nature of the pion.

Results

Let us first discuss the chiral limit ($m = 0$) for two flavours, starting from the breaking of chiral symmetry at $T = \mu = 0$, with the value of the dynamical mass $M_0(0,0) = 300\,MeV$, corresponding to $\Lambda = 650$ MeV and $G = 5.01 \times 10^{-6}\ MeV^{-2}$ [239, 240]. The well-known solution $M(T,\mu)$ of the gap equation (3.56), for different values of the temperature and of the quark chemical potential, is plotted in Figs. 3.2.a and 3.2.b. The restoration of the chiral symmetry is a first-order phase transition at large chemical potential and a second-order one at low μ.

With finite chiral quark masses, at high temperature and low chemical potential, there is a smooth crossover rather than a second-order phase transition. Moreover, the first-order phase boundary ends in a second-order endpoint [23]. The solution of the gap equation (3.56) (with $\Lambda = 650$ MeV and $G = 5.01 \times 10^{-6}$ MeV^{-2} and $m_0 = 5.5$ MeV) as a function of T and μ is shown in Figs. 3.3.a and 3.3.b.

Finally, three flavours NJL model is studied with the parameter val-

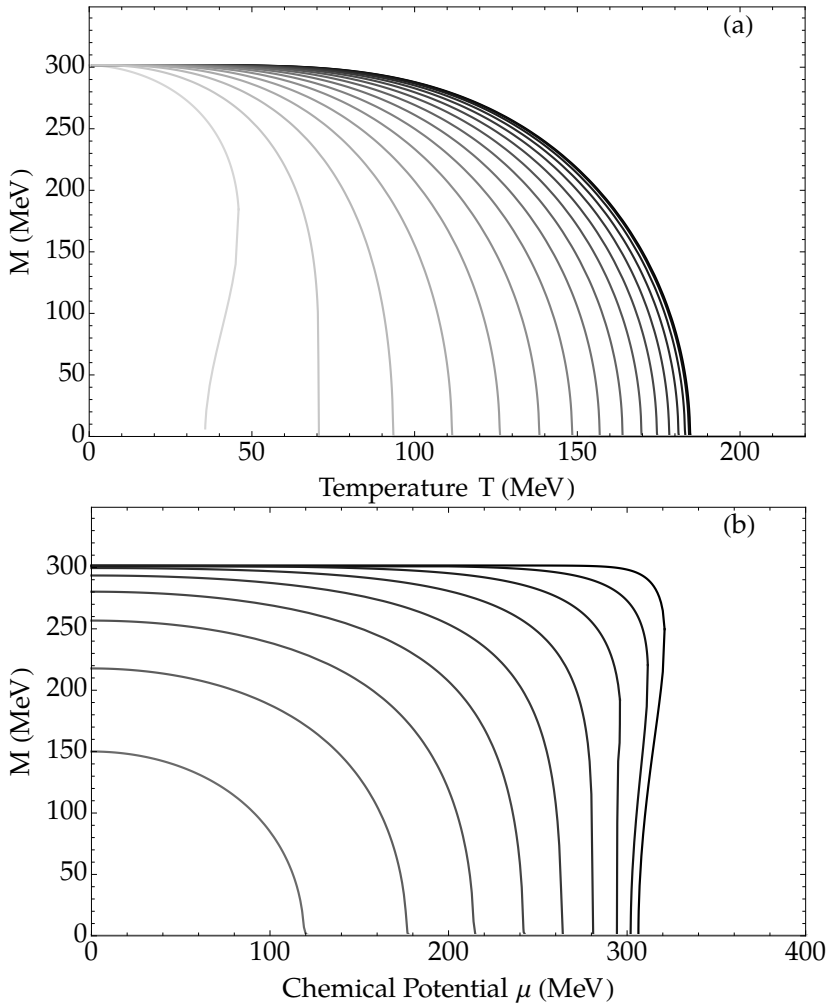

Figure 3.2: a) The dynamically generated mass, M, in the NJL model with two favors in the chiral limit ($m_u = m_d = 0$ MeV) and again the temperature. Black line is for $\mu = 0$ MeV; the others are for growing μ, up to $\mu = 300$ MeV and with step of $\Delta\mu = 20$ MeV. b) M as a function of the chemical potential μ. Black line is for $T = 10$ MeV; the others are for growing T, up to $T = 170$ MeV and with step of $\Delta T = 20$ MeV.

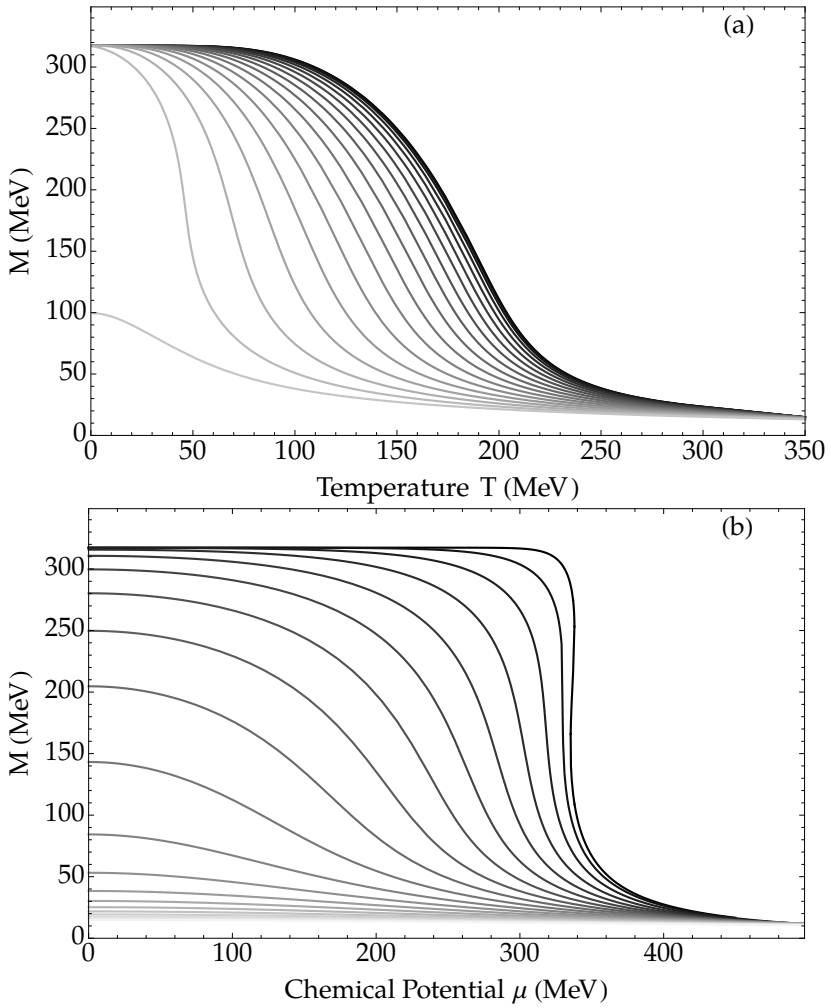

Figure 3.3: a) The dynamical generated mass, M, in the NJL model with two favors of identical mass ($m_u = m_d = 5.5$ MeV) and again the temperature. Black line is for $\mu = 0$ MeV; the others are for growing μ, up to $\mu = 340$ MeV and with step of $\Delta\mu = 20$ MeV. b) M as a function of the chemical potential μ. Black line is for $T = 10$ MeV; the others are for growing T, up to $T = 400$ MeV and with step of $\Delta T = 20$ MeV.

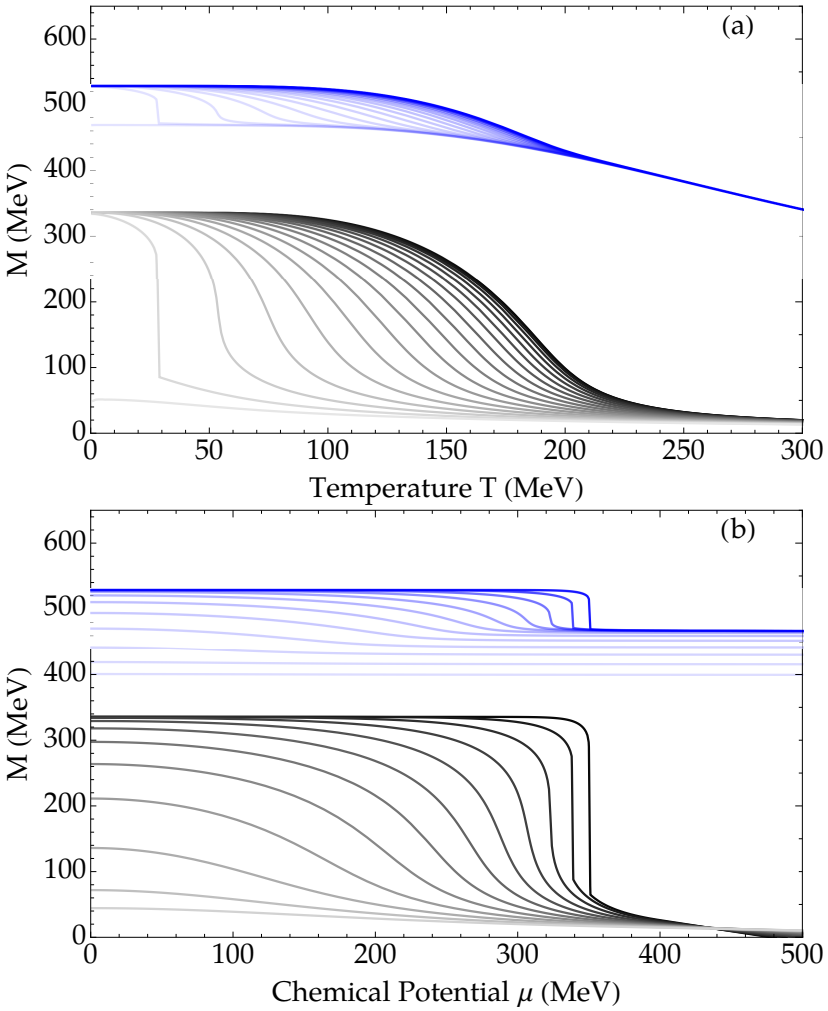

Figure 3.4: a) The dynamical generated mass, $M_u = M_d$ (black) and M_s (blue), in the NJL model with three favors and again the temperature. Black and blue lines are for $\mu = 0$ MeV; the others are for growing μ, up to $\mu = 360$ MeV and with step of $\Delta\mu = 20$ MeV. b) $M_u = M_d$ and M_s as a function of the chemical potential μ. Black and blue lines are for $T = 10$ MeV; the others are for growing T, up to $T = 230$ MeV and with step of $\Delta T = 20$ MeV.

ues [247]

$$\begin{gathered}\Lambda = 631.4 \text{ MeV} , \qquad G\,\Lambda^2 = 1.835 , \qquad K\,\Lambda^5 = 9.29 , \\ m = 5.5 \text{ MeV} , \qquad m_s = 135.7 \text{ MeV}\end{gathered} \tag{3.67}$$

and only one chemical potential ($\mu = \mu_d = \mu_u$, $\mu_s = 0$). The dynamically generated masses $M_u = M_d$ and M_s are now solutions of the system of EQs. (3.63) and (3.64). Their behaviour is similar to those ones depicted in Fig. 3.3, but with different values for light and strange quarks, as in Figs. 3.4.a and 3.4.b. Also, in this case, there is a crossover at low chemical potential and large T and a first-order phase transition at low temperature and large μ.

3.4 Quark-Meson model

Another effective theory to study low energy regime of QCD is the Quark-Meson (QM) model (see [248–259] and references therein), in which we introduce the fluctuations in the simplest way possible, namely using the Cornwall-Jackiw-Toumbulis (CJT) effective action formalism for composite operators [260] and limiting ourselves to the largely used Hartree approximation [258, 259] in which momentum dependent self-energy diagrams are neglected. Within these approximations, the effect of the interaction of the fluctuations with the medium is a shift in their mass that can be computed solving self-consistently the Schwinger-Dyson equations for the propagators and the mean-field condensate.

In this section, we review the QM model in which fermions (in our context, quarks) interact with mesons (that are the σ-meson and the pions in our work). It is based on the Lagrangian density

$$\mathcal{L} = \mathcal{L}_m + \mathcal{L}_f , \tag{3.68}$$

with the mesonic and fermionic parts respectively given by

$$\mathcal{L}_m = \text{Tr}\left[(\partial_\nu \Phi)^\dagger (\partial^\nu \Phi)\right] - m^2 \text{ Tr}\left(\Phi^\dagger \Phi\right) - \lambda \left[\text{Tr}\left(\Phi^\dagger \Phi\right)\right]^2 + h\,\sigma \tag{3.69}$$

and

$$\mathcal{L}_f = \overline{\Psi} i \, \gamma^\mu \partial_\mu \Psi - 2 \, g \, \overline{\Psi} \Phi \Psi \ . \tag{3.70}$$

Here Φ is the matrix field

$$\Phi \equiv \frac{1}{2} \, \sigma \, \tau^0 + \frac{i}{2} \, \overrightarrow{\pi} \cdot \overrightarrow{\tau} \ , \tag{3.71}$$

with τ^0 the unity matrix and $\overrightarrow{\tau} = (\tau_1, \tau_2, \tau_3)$ the Pauli matrix, $\overrightarrow{\pi} = (\pi_1, \pi_2, \pi_3)$ is an isotriplet of pion fields, σ is the isosinglet field and Ψ is a massless isodoublet quark field. m^2 is the bare mass, λ and g are coupling constants, and the term $h \, \sigma$, that breaks explicitly the chiral symmetry, is included in order to give the correct low temperature mass to the pion.

The partition function at finite temperature ($\beta = 1/T$) and chemical potential μ is

$$\begin{aligned} \mathcal{Z} &= \int [d\Phi] \left[d\overline{\Psi} \right] [d\Psi] \ \exp \left\{ - \int_0^\beta d\tau \int_V d^3x \left(\mathcal{L}_m + \mathcal{L}_f - \mu \, \Psi^\dagger \Psi \right) \right\} = \\ &= \int [d\sigma] \, [d\pi_i] \ \mathcal{Z}_f \ \exp \left\{ - \int_0^\beta d\tau \int_V d^3x \ \mathcal{L}_m \right\} \ , \end{aligned} \tag{3.72}$$

where, in the last step, an integration over the fermionic degree of freedom has been done, in order to integrate the fermionic part $\mathcal{Z}_f$.

A standard approximation, done in particular in the context of effective field theories for the quark chiral condensate of QCD, is that of mean-field in which the meson fields are replaced by their uniform, time-independent saddle point values, $\sigma = f_\pi$ and $\overrightarrow{\pi} = 0$. We want to go beyond the mean-field approximation, including the quantum fluctuations of the meson fields (the functional integral over the fermion fields can be done exactly on top of the mean-field solution). Within a Gaussian approximation, the partition function in EQ. (3.72) is given by

$$\mathcal{Z} = \mathcal{Z}_f \ \mathcal{Z}_m \ , \tag{3.73}$$

where the subscripts f and m stand for fermions and mesons respectively,

and

$$\mathcal{Z}_f = \int \left[d\overline{\Psi}\right] [d\Psi] \, \exp\left\{ - \int_0^\beta d\tau \int_V d^3x \left(\mathcal{L}_f - \mu \, \Psi^\dagger \Psi \right) \right\} \tag{3.74}$$

and

$$\mathcal{Z}_m = \int [d\sigma] \, [d\pi_i] \, \exp\left\{ - \int_0^\beta d\tau \int_V d^3x \, \mathcal{L}_m \right\} \, . \tag{3.75}$$

In this model, both quarks and meson fluctuations propagate on the background of the condensate of the σ field, the value of which is determined consistently by solving the gap equations (see Eqs. (3.109-3.111 below)). The thermodynamic Grand potential is

$$\Omega = \Omega_f + \Omega_m \, . \tag{3.76}$$

3.4.1 Fermionic term

The fermionic partition function (EQ. (3.74)) is usually approximated trough the so-called "bosonization" method: let's start by defining the covariant derivatives

$$D_\nu = \partial_\nu - i \, \mu \, \delta_{\nu 0} \tag{3.77}$$

and the operator

$$\widehat{D} = i \, \gamma^\mu D_\mu - 2 \, g \, \Phi \, . \tag{3.78}$$

Defining $M_f = 2 \, g \, \Phi$, and

$$\widehat{D} = i \, \gamma^\mu \, \partial_\mu + \gamma^0 \, \mu - M_f = G_f^{-1} \, , \tag{3.79}$$

that is the free inverse fermion propagator, the fermionic partition function becomes

$$\mathcal{Z}_f = \int \left[d\overline{\Psi}\right] [d\Psi] \, \exp\left\{ - \int_0^\beta d\tau \int_V d^3x \, \Psi^\dagger \widehat{D} \Psi \right\} \, . \tag{3.80}$$

By standard methods, one has

$$\begin{aligned}\ln \mathcal{Z}_f =& \mathrm{Tr} \ln \widehat{D} = \\ =& \frac{N_f\, N_c}{2\,\pi^2} \int_0^\infty k^2\, dk \left[\beta\, \omega_{\mathbf{k}} + \ln\left(1 + e^{-\beta\, \omega_{\mathbf{k}} - \gamma}\right) + \ln\left(1 + e^{-\beta\, \omega_{\mathbf{k}} + \gamma}\right)\right] \,,\end{aligned} \tag{3.81}$$

with $\omega_{\mathbf{k}}^2 = k^2 + M_f^2$.

M_f is the effective fermion mass that can be taken as

$$M_f^2 = 4\, g^2\, \mathrm{Tr}\left(\Phi \Phi^\dagger\right) = g^2 \left(\sigma^2 + \overrightarrow{\pi} \cdot \overrightarrow{\pi}\right) = g^2 \sigma^2 \,. \tag{3.82}$$

Finally, standard renormalization procedure (see for example [261]) gives

$$\begin{aligned}\Omega_f = \frac{g^4 N_c N_f}{8\,\pi^2} \sigma^4 \ln \frac{Q_f}{g\sigma} &- 2 N_c N_f T \int \frac{d^3k}{(2\pi)^3} \ln\left(1 + e^{-\beta(\sqrt{k^2 + g^2\,\sigma^2} - \mu)}\right) - \\ &- 2 N_c N_f T \int \frac{d^3k}{(2\pi)^3} \ln\left(1 + e^{-\beta(\sqrt{k^2 + g^2\,\sigma^2} + \mu)}\right) \,.\end{aligned} \tag{3.83}$$

In EQ. (3.83) we recognize the standard relativistic free gas thermodynamic potential at finite temperature and chemical potential (the last two terms), and the zero temperature, zero chemical potential contribution, that is potentially divergent and has been renormalized at the scale Q_f.

3.4.2 Mesonic term

The mesonic contribution, Ω_m, can be obtained via the Cornwall-Jackiw-Toumbulis (CJT) effective action formalism for composite operators [260], in the Hartree approximation [258, 259].

Cornwall-Jackiw-Toumbulis effective action theory

Systems at finite temperature and chemical potential can be studied by defining a partition function

$$\mathcal{Z} = \mathrm{Tr} e^{-\beta(H - \mu\, N)} \,. \tag{3.84}$$

That is equivalent to define a new Lagrangian explicitly depending to the chemical potential, with the requirement to replace

$$\int \frac{d^4k}{(2\,\pi)^4} \quad \rightarrow \quad \frac{1}{\beta}\sum_n \int \frac{d^3k}{(2\,\pi)^3}\;, \tag{3.85}$$

where the sum is over the Matsubara frequencies and with n even (odd) for bosons (fermions).

In the CJT formalism [260], this partition function is designed as the $J,\ K \rightarrow 0$ limit of a two sources (J and K) action

$$\mathcal{Z} = \int d\Psi \exp\left\{ i\,I + i\int d^4x\,\Psi(x)\,J(x) + \frac{i}{2}\int d^4x\,d^4y\,\Psi(x)\;K(x,y)\;\Psi(y)\right\}\;. \tag{3.86}$$

Here the field Ψ may have components, $d\Psi$ is functional integration, I is the classical effective action,

$$I = \int d^4x\,\mathcal{L}(x)\;, \tag{3.87}$$

and $\mathcal{L}$ is the effective Lagrangian, containing gauge and ghost terms. Then, the thermal effective action, Γ, is a double Legendre transformation of $W \equiv \ln \mathcal{Z}$. By defining

$$\frac{\partial W(J,K)}{\partial J(x)} = \phi(x) \tag{3.88}$$

and

$$\frac{\partial W(J,K)}{\partial K(x,y)} = \frac{1}{2}\left[G + \phi(x)\,\phi(y)\right]\;, \tag{3.89}$$

it is shown that the physical solution requires $J = K = 0$ or

$$\frac{\delta\Gamma(\phi,G)}{\delta\phi} = \frac{\delta\Gamma(\phi,G)}{\delta G} = 0\;. \tag{3.90}$$

Now ϕ takes the meaning of the expected value of the quantum field Ψ and $G(x,y)$ that of $T\Psi(x)\Psi(y)$. If the system is also translational invariant, one

defines an effective potential V_{eff} such that [262]

$$\Gamma = -V_{eff} \int d^4x \; . \tag{3.91}$$

By defining the auxiliary operator

$$i \; \mathcal{D}^{-1}_{ab} = \frac{\delta^2 I}{\delta\psi_a \, \delta\psi^*_b} = i \; D^{-1}_{ab} + \frac{\delta^2 I_{int}}{\delta\psi_a \, \delta\psi^*_b} \; , \tag{3.92}$$

where $I(x)$ is the classical effective lagrangian (EQ. (3.87)),

$$I_{int}(\phi) = \int d^4x \, \mathcal{L}_{int}(x) \tag{3.93}$$

that for the interaction term, $\mathcal{L}_{int}(x)$, $D_{ab}(x-y)$ is the free propagator and a and b are indices over the Ψ's components, the effective action is given by

$$\Gamma(\phi, G) = I_{cl}(\phi) + \frac{i}{2} \; \mathrm{Tr} \ln G^{-1} + \frac{i}{2} \; \mathrm{Tr} \, \mathcal{D}^{-1} \; G + \Gamma^{(2)}(\phi, G) + const. \; , \tag{3.94}$$

with $\Gamma^{(2)}(\phi, G)$ given by all the two-particle irreducible vacuum graphs in a theory with propagator equal to $G(x, y)$ and vertices of a theory obtained by shifting the field ϕ and defining the interaction term, I^{shift}_{int}, by all the terms cubic and higher in ϕ one obtains.

Moreover, the physical condition $\delta\Gamma/\delta G = 0$ gives the GAP equations

$$G^{-1}_{ab}(x, y) = \mathcal{D}^{-1}_{ab}(x, y) - 2 \; i \; \frac{\delta\Gamma^{(2)}}{\delta G_{ab}} \; , \tag{3.95}$$

that must be solved together with that obtained from $\delta\Gamma/\delta\phi = 0$.

The mesonic thermodynamic grand potential, Ω_m

We start by writing the mesonic lagrangian as

$$\mathcal{L}_m = \frac{1}{2} \; \sum_{\ell=1}^{4} \left(\partial_\nu \phi_\ell\right) \left(\partial^\nu \phi_\ell\right) - \frac{m^2}{2} \; \sum_{\ell=1}^{4} \; \phi^2_\ell - \frac{\lambda}{4} \left(\sum_{\ell=1}^{4} \; \phi^2_\ell \right)^2 + h \; \phi_1 \; , \tag{3.96}$$

where $\phi_\ell = \{\sigma, \pi_0\, \pi_1, \pi_2\}$.

The operators in EQ. (3.92) become

$$\mathcal{D}^{-1}_{ab}(k) = \left[k^2 + m^2 + \lambda \left(\sum_{\ell=1}^{4} \phi_\ell^2\right)\right] \delta_{ab} + 2\, \lambda\, \phi_a\, \phi_b\ . \tag{3.97}$$

If one expresses the spontaneous symmetry breaking as

$$\langle \phi_1 \rangle = \sigma \neq 0 \quad \text{and} \quad \langle \phi_\ell \rangle = 0 \quad \forall \ell \in \{2,\ 3,\ 4\}\ , \tag{3.98}$$

and performs the shift

$$\phi_\ell \longmapsto \phi_\ell + \sigma\ \delta_{\ell 1}\ , \tag{3.99}$$

the propagators $\mathcal{D}^{-1}_{ab}(k)$, evaluated at $< \phi_\ell >$, become

$$\begin{cases} \mathcal{D}^{-1}_{\sigma}(k) = k^2 + m^2 + 3\ \lambda\, \sigma^2 \\ \\ \mathcal{D}^{-1}_{\pi}(k) = k^2 + m^2 + \lambda\, \sigma^2 \end{cases} . \tag{3.100}$$

The interaction term of the shifted theory is given by

$$I^{shift}_{int} = -\frac{\lambda}{4} \left(\sum_{\ell=1}^{4} \phi_\ell^2\right)^2 - \lambda\ \sigma\ \phi_1 \left(\sum_{\ell=1}^{4} \phi_\ell^2\right)\ , \tag{3.101}$$

and contains a four-point vertex proportional to λ and a three-point vertex proportional to $\sigma\ \lambda$:

The 2-loop term, $\Gamma^{(2)}$, in Hartree-Fock approximation, i.e. with only the lowest contribution in λ, is (by means $G_\ell := \int_k\ G_\ell$, etc..):

$\Gamma^{(2)}_{HF} =$ 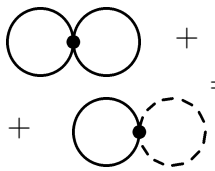 $= -\frac{\lambda}{4}\Big(3\,G_\sigma\,G_\sigma + 6\,G_\sigma\,G_\pi + 15\,G_\pi\,G_\pi\Big)\,,$ (3.102)

and the effective potential is given by

$$\begin{aligned}\Omega^{eff}_m = \Omega^{cl}_m + \frac{1}{2}\,\ln G^{-1}_\sigma + \frac{3}{2}\,\ln G^{-1}_\pi + \frac{1}{2}\,\mathcal{D}^{-1}_\sigma\,G_\sigma + \frac{3}{2}\,\mathcal{D}^{-1}_\pi\,G_\pi + \\ + \frac{\lambda}{4}\Big(3\,G^2_\sigma + 6\,G_\sigma\,G_\pi + 15\,G^2_\pi\Big) + const.\,.\end{aligned} \tag{3.103}$$

By deriving the effective potential of EQ. (3.103) with respect its variables G_σ and G_π, one finds

$$\begin{cases} G^{-1}_\sigma = \mathcal{D}^{-1}_\sigma + 3\,\lambda\,\,(G_\sigma + G_\pi) \\ \\ G^{-1}_\pi = \mathcal{D}^{-1}_\pi + \lambda\,\,(G_\sigma + 5\,G_\pi) \end{cases}, \tag{3.104}$$

and the effective potential becomes

$$\Omega^{eff}_m = \Omega^{cl}_m + \frac{1}{2}\,\ln G^{-1}_\sigma + \frac{3}{2}\,\ln G^{-1}_\pi - 3\,\frac{\lambda}{4}\Big(G^2_\sigma + 2\,G_\sigma\,G_\pi + 5\,G^2_\pi\Big)\,. \tag{3.105}$$

Differently from [258, 259], we do not include the vacuum term of the meson potential, so the pressure of the pions and $\sigma-$meson is zero at $T = \mu = 0$: the condensation energy takes contributions only from the classical potential plus the fermion loop, while the mesons appear as the excitation of the ground state at finite temperature. This choice is also made for the sake of simplicity because including a further zero temperature, and zero chemical potential renormalized term of the mesons would introduce an additional renormalization scale that would lead to unexpected behaviours of the thermodynamic quantities [259]. Within these approximations we have

[258, 259]

$$\Omega_m = \frac{m^2}{2}\,\sigma^2 + \frac{\lambda\,\sigma^4}{4} - h\,\sigma + 3\,B_\pi^F + B_\sigma^F - \frac{3\,\lambda}{4}\,\left(2\,A_\pi^F\,A_\sigma^F + 5\,A_\pi^{F\,2} + A_\sigma^{F\,2}\right)\,. \tag{3.106}$$

where for $\ell = \sigma, \pi$ we have put

$$A_\ell = -\int \frac{d^3k}{(2\pi)^3}\frac{1}{E_\ell}\,\frac{1}{1 - e^{\beta\,E_\ell}}\,, \tag{3.107}$$

with $E_\ell = \sqrt{k^2 + M_\ell^2}$, and

$$B_\ell = 2\,T\,\int \frac{d^3k}{(2\pi)^3}\,\ln\left(1 - e^{-\beta\,E_\ell}\right)\,. \tag{3.108}$$

3.4.3 GAP equations

Within this model, for a given temperature and chemical potential, the unknowns are the value of the condensate, namely the expectation value of σ, as well as the in-medium meson masses M_σ and M_π: these are obtained by solving the gap equations, that are

$$h = \left[m^2 + \lambda\,\sigma^2 + 3\,\lambda\,\left(A_\sigma + A_\pi\right)\right]\,\sigma - \frac{g^4\,N_c\,N_f\,\sigma^3}{8\,\pi^2}\,\left(1 + 4\,\ln\frac{g\,\sigma}{Q_f}\right) - \\ - \frac{2\,N_c\,N_f}{\beta}\,\frac{\partial\Omega_{fT}}{\partial\Sigma}\bigg|_{\substack{\Sigma=\sigma\\ \Pi=0}}\,, \tag{3.109}$$

$$M_\sigma^2 = m^2 + 3\,\lambda\,\left(A_\pi + A_\sigma + \sigma^2\right) - \frac{g^4\,N_c\,N_f\,\sigma^2}{8\,\pi^2}\,\left(7 + 12\,\ln\frac{g\,\sigma}{Q_f}\right) - \\ - \frac{2\,N_c\,N_f}{\beta}\,\frac{\partial^2\Omega_{fT}}{\partial\Sigma^2}\bigg|_{\substack{\Sigma=\sigma\\ \Pi=0}}\,, \tag{3.110}$$

$$M_\pi^2 = m^2 + \lambda\ \left(5\ A_\pi + A_\sigma + \sigma^2\right) - \frac{g^4\ N_c\ N_f\ \sigma^2}{8\ \pi^2}\ \left(1 + 4\ \ln\frac{g\ \sigma}{Q_f}\right) - \\ - \frac{2\ N_c\ N_f}{\beta}\ \frac{\partial^2\Omega_{fT}}{\partial\Pi^2}\bigg|_{\substack{\Sigma=\sigma\\ \Pi=0}}\ , \tag{3.111}$$

with

$$\Omega_{fT} = \int \frac{d^3k}{(2\ \pi)^3}\ln\left(1 + e^{-\beta(\sqrt{k^2+g^2(\Sigma^2+\Pi^2)}-\mu)}\right)\left(1 + e^{-\beta(\sqrt{k^2+g^2(\Sigma^2+\Pi^2)}+\mu)}\right)\ . \tag{3.112}$$

The gap equations depend on the renormalization scale, Q_f, as well as of three parameters, m, λ and h. At the tree-level, namely, when no meson and quark loops are considered, the parameters m, λ and h are fixed to reproduce the physical values m_σ, m_π as well as $\sigma = f_\pi$ at $T = 0$ and $\mu = 0$, where we use small letters to denote physical masses at $T = \mu = 0$; without the fermion and meson loops, these give

$$h \equiv h_{\rm tree} = m_\pi^2\ f_\pi\ , \tag{3.113}$$

$$m^2 \equiv m^2_{\rm tree} = -\frac{m_\sigma^2 - 3\,m_\pi^2}{2} - \frac{f_\pi^2\ g^4\ N_c\ N_f}{4\ \pi^2}\ , \tag{3.114}$$

$$\lambda \equiv \lambda_{\rm tree} = \frac{m_\sigma^2 - m_\pi^2}{2\ f_\pi^2}\ , \tag{3.115}$$

where the subscript tree reminds that these are quantities computed using the tree-level potential. In order to fix the renormalization scale, we have to adopt one renormalization condition, that is

$$\lambda = \lambda_{\rm tree}, \tag{3.116}$$

where λ results from the gap equations at $T = \mu = 0$, namely

$$\lambda = \frac{m_\sigma^2 - m_\pi^2}{2\ f_\pi^2} + \frac{g^4\ N_c\, N_f}{8\,\pi^2}\ \left(3 + 4\ \ln\frac{g\ f_\pi}{Q_f}\right)\ . \tag{3.117}$$

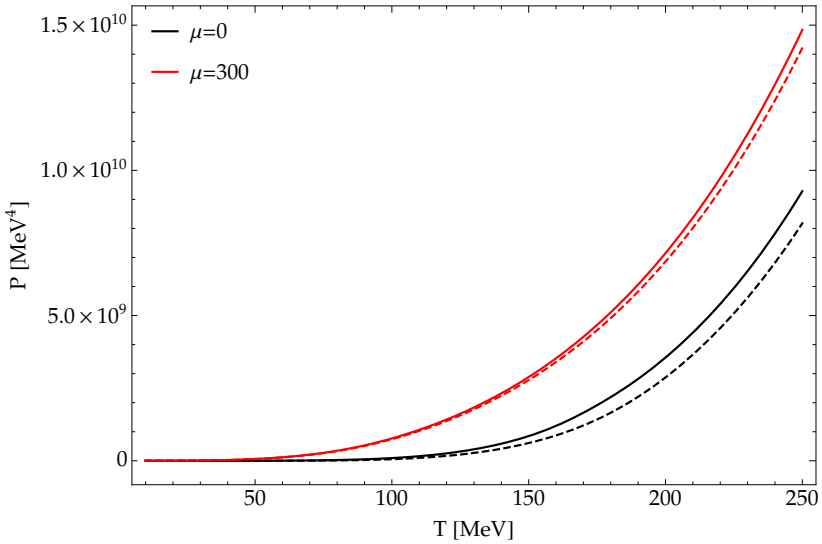

Figure 3.5: Pressure versus temperature for the models with (solid lines) and without (dashed lines) meson fluctuations, for $\mu = 0$ (black lines) and $\mu = 300$ MeV (red lines).

m^2 and h from the gap equations at $T = \mu = 0$ are always equal to the tree value:

$$m^2 = m^2_{tree} \ , \qquad h = h_{tree} \ . \tag{3.118}$$

Finally, from EQ.s (3.116) and (3.117) we have

$$Q_f = e^{3/4} \ f_\pi \ g \ . \tag{3.119}$$

3.4.4 Results

For the parameters we take $f_\pi = 93$ MeV, $m_\sigma = 700$ MeV, $m_\pi = 138$ MeV and finally $g = 3.6$: the latter is chosen so that the constituent quark mass at $T = \mu = 0$ is $M = 335$ MeV. The resulting value of the renormalization scale is $Q_f = 709$ MeV.

Figure 3.5 shows the pressure versus the temperature for the models with and without fluctuations, for $\mu = 0$ (black lines) and $\mu = 300$ MeV (red lines). At fixed μ and T, the fluctuations increase the pressure as

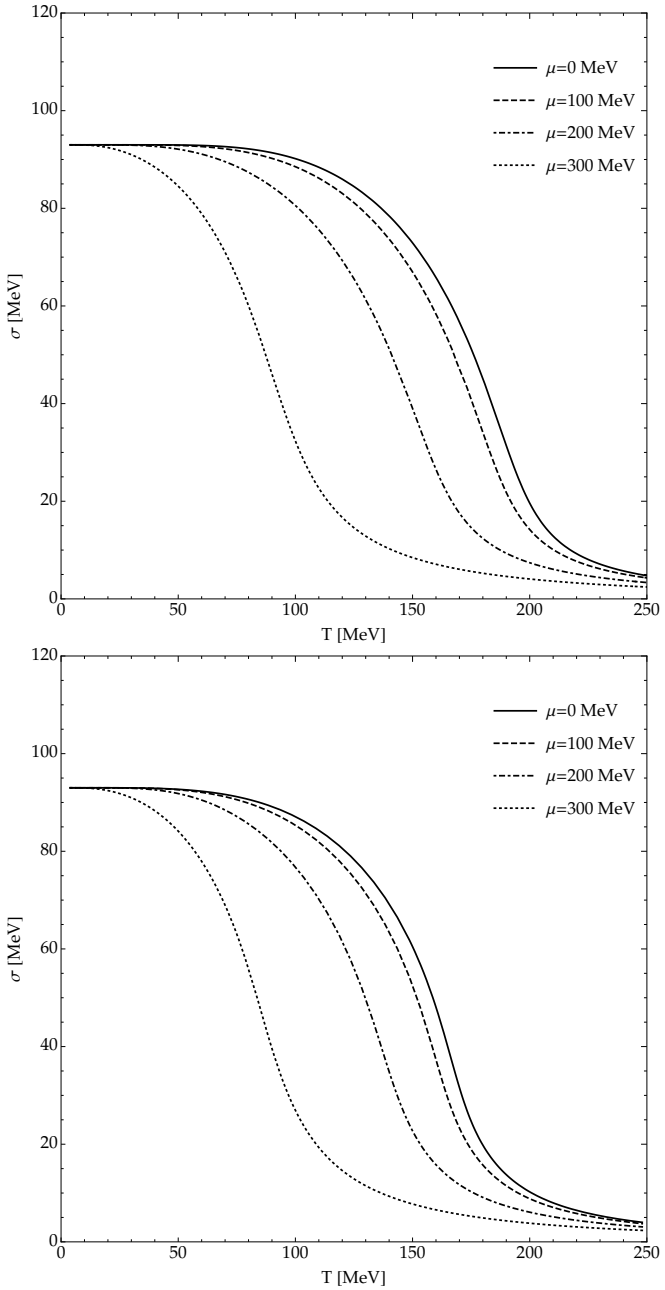

Figure 3.6: Condensate, σ, as a function of T and for different values of the chemical potential. Upper panel corresponds to the case in which meson fluctuations are neglected, lower panel to the case in which meson fluctuations are included.

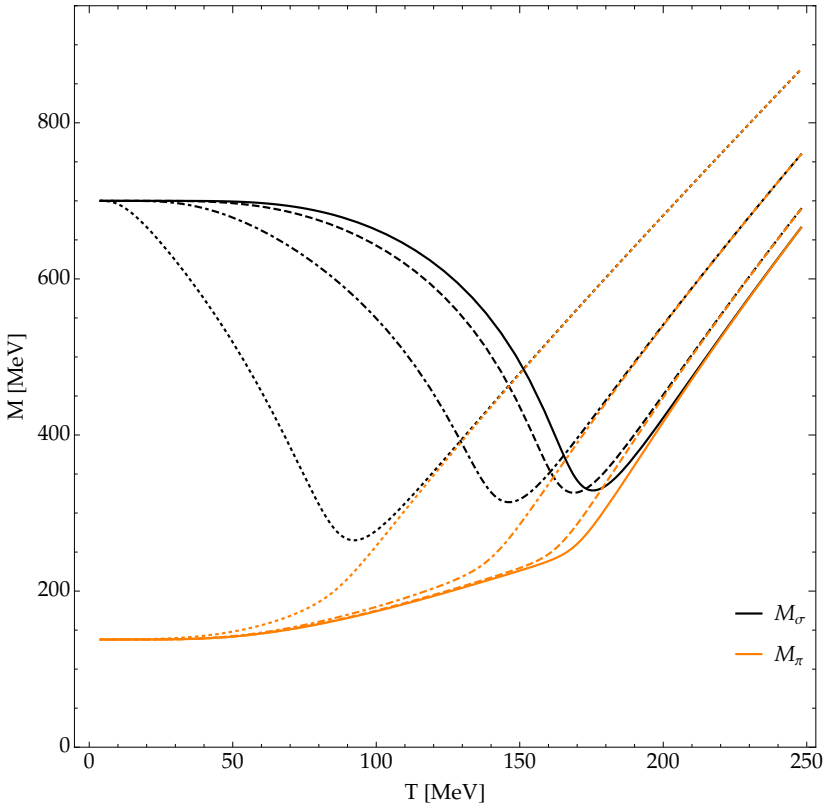

Figure 3.7: In-medium masses M_σ (black) and M_π (orange) as a function of T, for several values of the chemical potential: $\mu = 0$ MeV (continuous line), $\mu = 100$ MeV (dashed), $\mu = 200$ MeV (dot-dashed) and $\mu = 300$ MeV (dotted). Case with mesonic fluctuations.

expected; however, we notice that at large values of μ, the contribution of the fluctuations becomes less important in comparison with the mean-field pressure.

In Fig. 3.6, we plot the condensate, σ, as a function of T for several values of the chemical potential: $\mu = 0$ MeV (continuous line), $\mu = 100$ MeV (dashed), $\mu = 200$ MeV (dot-dashed) and 300 MeV (dotted). The upper panel corresponds to the case in which meson fluctuations are neglected, lower panel to the case in which the fluctuations are included. In both cases, a range of temperature where σ decreases exist, that signals the partial restoration of chiral symmetry (chiral symmetry cannot be restored exactly due to the explicit soft breaking in the action). Figure 3.7 shows the in-medium masses of the σ-meson and pions as a function of temperature, for several values of the quark chemical potential. These have been computed for the model with fluctuations included. We notice that, for each of the values of μ considered, a range of temperature exists in which the σ-meson mass decreases. Conversely, the pions mass increases, and the two-match at high temperature signalling the approximate restoration of the $O(4)$ symmetry, as well as the decoupling of these particles from the low energy spectrum of the model. Moreover, the lowering of M_σ to a minimum is a sign that the fluctuations of the scalar field are enhanced near the chiral crossover.

Finally, Figures 3.8 and 3.9 show the derivative of σ, M_σ and M_π, with respect to β and γ at $\mu = 100$ MeV (black) and $\mu = 300$ MeV (orange).

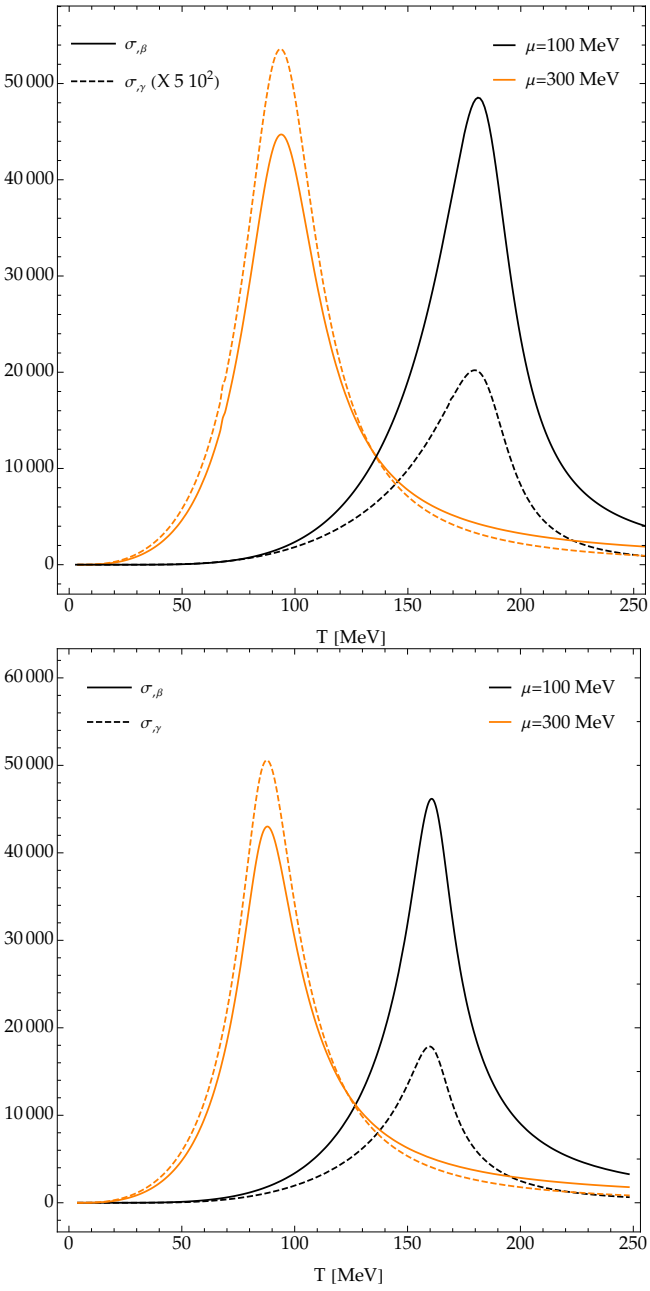

Figure 3.8: Derivative of σ with respect to β (continuous line) and γ (dashed line) at $\mu = 100$ MeV (black) and $\mu = 300$ MeV (orange), as a function of T. Upper panel corresponds to the case in which meson fluctuations are neglected, lower panel to the case in which meson fluctuations are included.

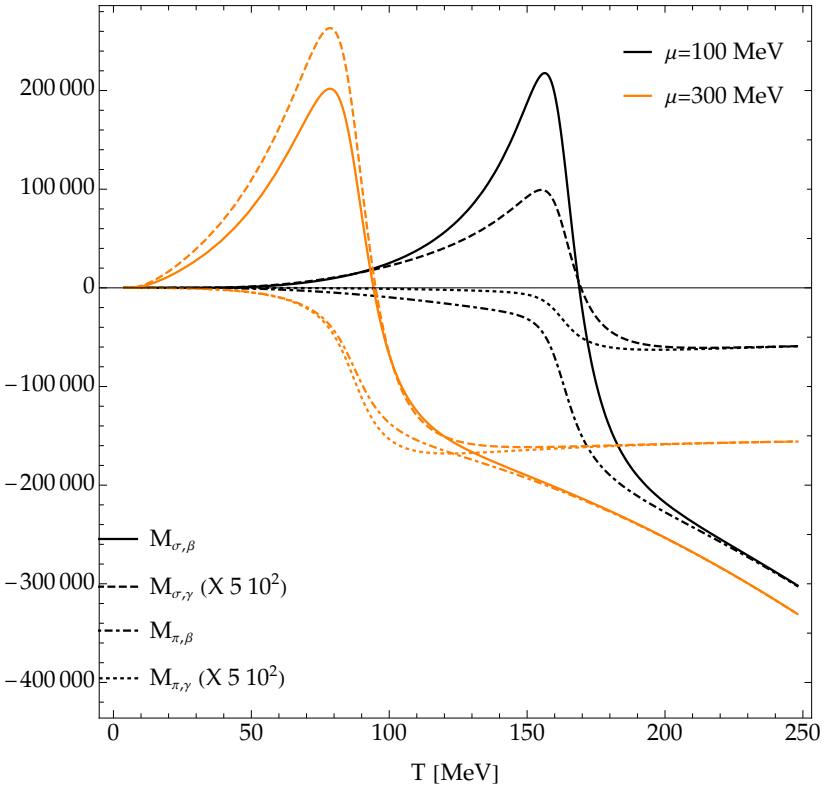

Figure 3.9: Derivative of M_σ with respect to β (continuous line) and γ (dashed), and derivative of M_π with respect to β (dot-dashed) and γ (dotted), at $\mu = 100$ MeV (black) and $\mu = 300$ MeV (orange). Case with mesonic fluctuations.

Chapter 4

Cosmological consequence of the QCD phase transition

Quantum Chromodynamics deconfinement phase transition has an interesting role at the cosmological level. [263–267]. Indeed, in the modern understanding, i.e. the Standard Cosmological model (ΛCDM) with cold dark matter and a cosmological constant, Universe evolution is a thermal history: the Universe evolves from a very hot period (with a temperature of the order of 10^{19} GeV of the total unification, or 10^{16} GeV of the grand one [268]) to the current Cosmic Microwave Background Radiation temperature (about $T \sim 2.725$ MeV). As a consequence, the evolution of the Universe can be seen as a useful laboratory to study fundamental physics across energy scales that span about 25 orders of magnitude [268]: starting from the very high temperature said, the Universe has expanded and cooled adiabatically and isentropically, and different phases transitions occurred. Figure 4.1 shows the thermal history of the Universe, and in Fig. 4.2 is plotted the effective number of degree of freedom predicted by the standard model (SM) of particles physics. The first conjectured period was that of the total unification (all the four interactions are unified at the Planck scale) or that of the grand unification (strong and electroweak interactions are described as a gauge theory based on a single larger gauge group: e.g. $SU(5)$, $SO(10)$, E_8, etc.). When the temperature was about $T_{ew} \sim 100$ GeV, the earliest phase transition that is predicted by the SM occurred: at a temperature higher than T_{ew}, in the SM, weak and electromagnetic interactions are unified in the electroweak

theory based on the gauge group $SU(2) \otimes U(1)_Y$, that breaks spontaneously into the $U(1)_{em}$ abelian symmetry group of the electromagnetic interactions. The breaking happened at a temperature of the order of the vector bosons (Z^0, $W^{\pm}$) masses. These bosons are massless in the symmetric phase ($T > T_{ew}$) and acquire masses through the Higgs mechanism at $T < T_{ew}$, while the photon remains massless. The Universe was then in a state of plasma of quarks, leptons and bosons, and additional cooling, reached the temperature of about 150 MeV, led to a new phase transition, with the appearance of the first hadrons. This phase transition was the same that occurs in particle collisions experiments, with the formation of a quark-gluon plasma, that subsequently hadronizes. The QCD deconfinement transition rapidly reduced the number of the strongly interacting d.o.f., g_s. However, lattice QCD simulations indicate that the transition is not so sharp, and it is indeed a crossover between a system of quarks and gluons and a hadron gas [202, 269, 270]. It was the last predicted phase transition by the SM. After that, other non-SM transitions occurred, like those shown in Fig. 4.1, that led to the current structure of the Universe.

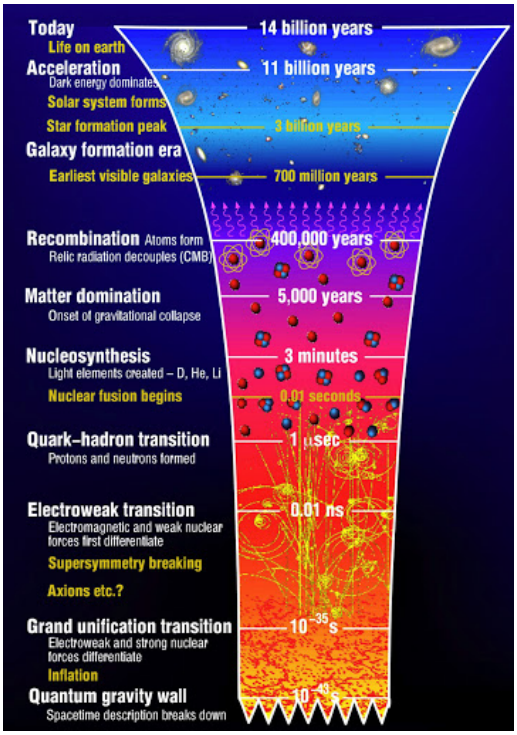

Figure 4.1: Universe thermal history.

Therefore, Universe history is a thermal one. To describe it, one needs several theories:

- the gravitational interaction is described geometrically by the Einstein theory of General Relativity: the Universe is modeled as a homogeneous and isotropic expanding manifold, whose metric is given by the

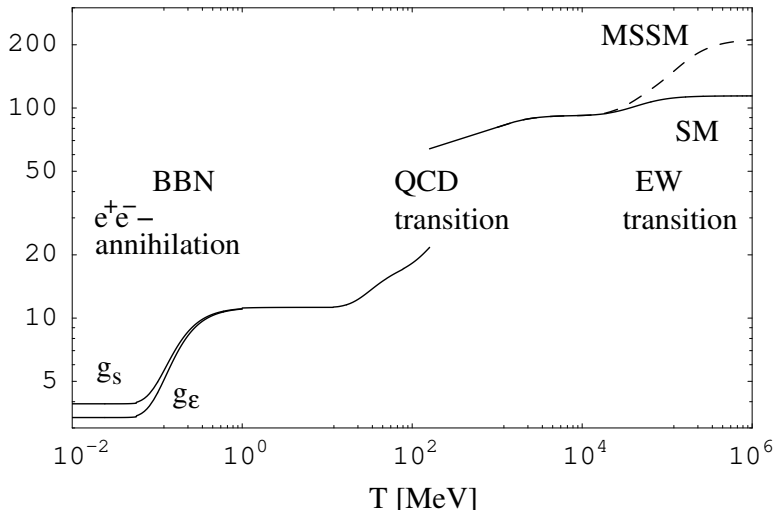

Figure 4.2: The effective number of degree of freedom predicted by the standard model of particles physics. Figure from [264]

Friedmann - Lemaître - Robertson - Walker (FLRW) one,

$$ds^2 = dt^2 - a^2(t)\left(dr^2 + r^2\, d\Omega^2\right) \ . \tag{4.1}$$

Here t is the comoving time, i.e. the proper time of a comoving observer, and the scale factor,

$$a(t) = \frac{\ell_{phys}}{\ell_{com}} \ , \tag{4.2}$$

describes the stretched of the physical lengths, ℓ_{phys}, with respect the comoving ones, ℓ_{com}.

In the FLRW universe, also matter distribution is homogeneous and isotropic, i.e. it is described via an energy-momentum tensor with the fluid form:

$$T^{\mu}_{\nu} = \mathrm{diag}\left(\varepsilon, -p, -p, -p\right) \ , \tag{4.3}$$

where ε is the energy density and p the pressure of the matter fluid.

The connection between the space-time geometry and the matter-

energy content is given by Einstein's equations that, for a flat universe described by the FLRW metric, are given by

$$\left(\frac{1}{a(t)}\,\frac{da(t)}{dt}\right)^2 = \frac{8\,\pi\,G}{3}\,\varepsilon_T(t)\ , \tag{4.4}$$

and

$$\frac{1}{a(t)}\,\frac{d^2a(t)}{dt^2} = -\frac{4\,\pi\,G}{3}\,\left(\varepsilon_T(t) + 3\,p_T(t)\right)\ . \tag{4.5}$$

Here $\varepsilon_T(t)$ and $p_T(t)$ are the total energy density and the pressure, respectively.

- According to ΛCDM model, the total energy density of the Universe has as main ingredients: 5% of baryonic matter, 25% of dark matter and 70% of dark energy (described by a cosmological constant) [195]. The next point is thus to give the matter and energy content of the Universe:

$$\varepsilon_T = \varepsilon_s + \varepsilon_{ew} + \varepsilon_{dm} + \varepsilon_\Lambda\ , \tag{4.6}$$

$$p_T = p_s + p_{ew} + p_{dm} + p_\Lambda\ , \tag{4.7}$$

where

$$\varepsilon_\Lambda = \frac{\Lambda}{8\,\pi\,G}\ , \tag{4.8}$$

and

$$p_\Lambda = -\varepsilon_\Lambda\ , \tag{4.9}$$

are the dark energy contributions, and the other terms correspond to strong (s), electroweak (ew) and dark matter (dm) sectors.

- Finally, one uses the ordinary thermodynamic relationship between energy density, pressure and entropy density, s, in Eqs. (2.34-2.37), and supposes that Universe expands isentropically, i.e. the total entropy is constant and thus since the volume of the Universe is proportional to $a(t)^3$, one has

$$dS \propto d(a^3\,s) = 0\ . \tag{4.10}$$

EQs. (2.34-2.37) and EQ. (4.10) provide the link between temporal

and thermal evolution. Moreover, the Universe evolves at $\mu \sim 0$ [38], since

$$\eta \equiv \frac{n_B}{n_\gamma} = 6\ 10^{-10}\ . \tag{4.11}$$

Indeed, η allows determining the value of entropy per baryon ratio, S/B, in the Universe, which is conserved in adiabatic evolution. Thus

$$\frac{\mu}{T} \sim \frac{n_B}{s} \sim \frac{\eta}{10} \sim 0\ . \tag{4.12}$$

If the temperature is a function of time only, $T = T(t)$, by defining the function

$$h(T) = \frac{1}{a(T)}\frac{da}{dT}\ , \tag{4.13}$$

it is easy to show that

$$\frac{dT}{dt} = \frac{H}{h}\ , \tag{4.14}$$

where $H \equiv (da/dt)/a$ is the Hubble parameter. By the FLRW equations and by the isentropic expansion condition, one obtains

$$h = -\frac{1}{3\,c_s^2\,T} = -\frac{C_V}{3\ (\varepsilon + p)}\ , \tag{4.15}$$

where C_V is the specific heat and $c_s^2 = \partial p_T/\partial \varepsilon_T$ is the speed of sound.

4.1 Cosmological parameter

The cosmological evolution can be described by the cosmological parameters, defined as [271, 272]

$$H \equiv \quad \frac{1}{a}\frac{da}{dt} \quad , \tag{4.16}$$

$$q \equiv \ -\frac{1}{a\ H^2}\frac{d^2a}{dt^2} \quad , \tag{4.17}$$

$$A_n \equiv \quad \frac{1}{a\ H^n}\frac{d^na}{dt^n} \qquad (n > 2)\ . \tag{4.18}$$

The first is the Hubble parameter, H, the second is the deceleration, q, then the jerk j, the snap ($s = A_4$), etc.. They specify the various terms of the Taylor expansion of the scale factor:

$$\frac{a(t)}{a(t^\star)} = 1 + H(t^\star)\,(t - t^\star) - \frac{(qH^2)\,(t^\star)}{2}\,(t - t^\star)^2 + \frac{(jH^3)\,(t^\star)}{2}\,(t - t^\star)^2 + \cdots \,. \tag{4.19}$$

The evolution of the cosmological parameter is directly related to the EoS. Indeed, A_n can be written as the sum of terms containing the first $n-1$ derivatives of the Hubble parameter H, which can be expressed in terms of the $w \equiv p_T/\varepsilon_T$, of the speed of sound, $c_s^2 = \partial p_T/\partial \varepsilon_T$, and its derivatives [267]. Indeed, since

$$\frac{d^n a}{dt^n} = \frac{d^{n-1}\,(a\,H)}{dt^{n-1}}\,, \tag{4.20}$$

it is easy to show that [267]

$$q = -1 - \frac{\dot{H}}{H^2}\,, \tag{4.21}$$

$$j = A_3 = 1 + 3\,\frac{\dot{H}}{H^2} + \frac{\ddot{H}}{H^3}\,, \tag{4.22}$$

$$s = A_4 = 1 + 6\,\frac{\dot{H}}{H^2} + 3\left(\frac{\dot{H}}{H^2}\right)^2 + 4\,\frac{\ddot{H}}{H^3} + \frac{\dddot{H}}{H^4}\,, \tag{4.23}$$

$$A_5 = 1 + 10\,\frac{\dot{H}}{H^2} + 15\left(\frac{\dot{H}}{H^2}\right)^2 + 10\,\frac{\ddot{H}}{H^3} + 5\,\frac{\dddot{H}}{H^4} + 10\,\frac{\dot{H}}{H^2}\,\frac{\ddot{H}}{H^3} + \frac{H^{(4)}}{H^5}\,, \tag{4.24}$$

$$A_6 = 1 + 15\,\frac{\dot{H}}{H^2} + 45\,\left(\frac{\dot{H}}{H^2}\right)^2 + 20\,\frac{\ddot{H}}{H^3} + +15\,\frac{\dddot{H}}{H^4} + 60\,\frac{\dot{H}}{H^2}\,\frac{\ddot{H}}{H^3} + 6\,\frac{H^{(4)}}{H^5} + \\ + 15\,\left(\frac{\dot{H}}{H^2}\right)^3 + 15\,\frac{\dot{H}}{H^2}\,\frac{\dddot{H}}{H^4} + 10\,\left(\frac{\ddot{H}}{H^3}\right)^2 + \frac{H^{(5)}}{H^6}\ , \tag{4.25}$$

where the "dot" means derivative with respect t. Recalling that

$$\frac{1}{H^{n+1}}\frac{d^n H}{dt^n} = -\frac{4\,\pi\,G}{H^{n+1}}\,\frac{d^{n-1}\,(\varepsilon + p)}{dt^{n-1}}\ , \tag{4.26}$$

each of the previous derivatives can be express as

$$\frac{\dot{H}}{H^2} = -\frac{3}{2}\left(1 + \frac{p}{\varepsilon}\right)\ , \tag{4.27}$$

$$\frac{\ddot{H}}{H^3} = \frac{9}{2}\,\left(1 + c_s^2\right)\,\left(1 + \frac{p}{\varepsilon}\right)\ , \tag{4.28}$$

$$\frac{\dddot{H}}{H^4} = \frac{9}{2}\,\left(1 + \frac{p}{\varepsilon}\right)\left[\frac{dc_s^2/dt}{H} - 3\,\left(1 + c_s^2\right)^2 - \frac{3}{2}\,\left(1 + c_s^2\right)\left(1 + \frac{p}{\varepsilon}\right)\right]\ , \tag{4.29}$$

$$\frac{H^{(4)}}{H^5} = \frac{9}{2}\left(1 + \frac{p}{\varepsilon}\right)\Big[9\left(1 + c_s^2\right)^3 + 18\,\left(1 + c_s^2\right)^2\,\left(1 + \frac{p}{\varepsilon}\right) - \\ - 3\,\left(4 + \frac{p}{\varepsilon} + 3\,c_s^2\right)\,\frac{dc_s^2/dt}{H} + \frac{d^2c_s^2/dt^2}{H^2}\Big]\ , \tag{4.30}$$

$$\frac{H^{(5)}}{H^6} = \frac{9}{2}\left(1 + \frac{p}{\varepsilon}\right)\left[\frac{d^3c_s^2/dt^3}{H^3} - 9\left(\frac{dc_s^2/dt}{H}\right)^2 - 27\left(1 + c_s^2\right)^2\left(1 + \frac{p}{\varepsilon}\right)^2 - \right. \\ - \frac{3}{H^2}\left(\frac{11}{2} + \frac{3\,p}{2\,\varepsilon} + 4\,c_s^2\right)\frac{d^2c_s^2}{dt^2} + \frac{9\,(1 + c_s^2)}{H}\left(15 + 9\,\frac{p}{\varepsilon} + 6\,c_s^2\right)\frac{dc_s^2}{dt} - \\ \left. - 27\left(1 + c_s^2\right)^4 - \frac{297}{2}\left(1 + c_s^2\right)^3\left(1 + \frac{p}{\varepsilon}\right)\right]\ . \tag{4.31}$$

Finally, since $w(\varepsilon) \equiv p/\varepsilon$, one can show that

$$c_s^2 = w + \varepsilon\,\frac{dw}{d\varepsilon} \tag{4.32}$$

and thus all the cosmological parameters can be express in terms of w, c_s^2 and its derivatives. For the first three parameters one gets

$$q = \frac{1}{2}\left(1 + 3\, w\left(\varepsilon\right)\right) \ , \tag{4.33}$$

$$j = 1 + 3\, c_s^2\ (1+q) = q\ (1 + 2\, q) + 3\,(1+q)\,\varepsilon\,\frac{dw}{d\varepsilon} \ , \tag{4.34}$$

$$\begin{aligned} s =& 1 - 3\,(1+q) - 9\, c_s^4\,(1+q) - 3\, c_s^2 (1+q)(3+q) + 3(1+q)\frac{dc_s^2/dt}{H} = \\ =& -\,q\,(1+2\,q)\,(2+3\,q) - 3(1+q)(1+5\,q)\varepsilon\,\frac{dw}{d\varepsilon} - \\ & - 9\,(1+q)\left(\varepsilon\,\frac{dw}{d\varepsilon}\right)^2 + 3\,(1+q)\,\frac{dc_s^2/dt}{H} \ , \end{aligned} \tag{4.35}$$

Eqs. (4.21-4.35), together with eqs. (4.14,4.15), permit to write the cosmological parameters in terms of the temperature of the universe if one specifies which fluids fill the universe and assigns an equation of state (EoS) for each of them:

$$\varepsilon_T = \varepsilon_s + \varepsilon_{ew} + \varepsilon_{dm} + \varepsilon_\Lambda \ , \tag{4.36}$$

s: The strong sector is build interpolating the high temperature regime obtained via Lattice QCD, with the low temperature one obtained in the HRG model. The first is discussed in sec. 3.1, the last in sec. 3.2.

ew: The electroweak sector is included as a relativistic gas of massless particles, i.e.,

$$\varepsilon_{ew} = 3\, p_{ew} = \frac{\pi^2}{30}\, g_{ew}\, T^4 \ , \tag{4.37}$$

where $g_{ew} = 14.45$ is the effective number of electroweak d.o.f. [266].

dark: the dark sectors are omitted due to their low contributions in the early stage.

4.2 Gravitational waves

In the inflation era, the wavelengths of the quantum fluctuations are stretched to scales greater than the casually connected region, and fluctuations of the metric tensor result in a background of stochastic gravitational waves [273]. In the transverse traceless (TT) gauge, tensor perturbations h_{ij} of the FLRW metric satisfy the linearized equation of motion

$$h_{ij;\mu}{}^{;\mu} = 0 \ , \tag{4.38}$$

where ";" indicates the covariant derivative, and the corresponding Fourier modes take the form

$$h_{ij} = \int \frac{d^3k}{(2\pi)^{3/2}} \sum_{\lambda} e_{ij}^{\lambda} \ h_{\boldsymbol{k},\lambda} \ e^{i\boldsymbol{k}\cdot\boldsymbol{x}} \ . \tag{4.39}$$

Here $\lambda = (+, \times)$ are the two polarization states and e_{ij}^{λ} is the symmetric polarization tensor ($e_{ii} = 0$, $k^i e_{ij} = 0$). In conformal time, η, the equation of motion for the perturbations reads [265]

$$h''_{\boldsymbol{k},\lambda}(\eta) + 2\frac{a'}{a} h'_{\boldsymbol{k},\lambda}(\eta) + k^2 h_{\boldsymbol{k},\lambda}(\eta) = 0 \ , \tag{4.40}$$

where $d/d\eta$ is denoted by prime "′". By defining $\mu_{\boldsymbol{k}\lambda} = a \ h_{\boldsymbol{k}\lambda}$, EQ. (4.40) can be written as

$$\mu''_{\boldsymbol{k},\lambda}(\eta) + \left(k^2 - \frac{a''}{a}\right) \mu_{\boldsymbol{k},\lambda}(\eta) = 0 \ . \tag{4.41}$$

Two different regimes are physically relevant and correspond to fluctuations well inside the Hubble horizon or well outside the horizon. Since $a''/a \sim (a \ H)^2$, when $k \gg a \ H$ the wavelength is smaller than the horizon: this is the *subhorizon* regime. In this case EQ. (4.41) is that of a harmonic oscillator, hence, $\mu_{\boldsymbol{k}}(\eta) \sim e^{ik\eta}$ and for the perturbation one obtains

$$h_{\boldsymbol{k}} \sim a^{-1} \ , \tag{4.42}$$

which implies that the amplitude decreases in time. In the *superhorizon* regime, i.e. for $k \ll a\ H$, EQ. (4.41) has two independent solutions: a decaying mode $\mu_{\boldsymbol{k}} \sim a^{-2}$, which we neglect, and $\mu_{\boldsymbol{k}} \sim a$ that leads to

$$h_{\boldsymbol{k}} \sim const.\ . \tag{4.43}$$

The amplitudes are almost frozen, being outside the casually connected region, and, in the inflation era, are stretched to size larger than the horizon, where they remain constant.

When inflation ends the comoving Hubble horizon $(a\ H)^{-1}$ grows in time and each mode crosses the horizon and reenters inside the casually connected region when $k = a\ H$ (i.e. when the wavelength is comparable to the horizon size). In this case, a general solution of EQ. (4.41) can be written introducing a factor depending on mode's amplitude in superhorizon regime and a transfer function, $\mathcal{T}_k(\eta)$, as

$$h_{\boldsymbol{k},\lambda}(\eta) = h^{prim}_{\boldsymbol{k},\lambda}\mathcal{T}_k(\eta)\ , \tag{4.44}$$

where $h^{prim}_{\boldsymbol{k},\lambda}$ is the amplitude when the mode left the horizon in the inflationary period and $\mathcal{T}_k(\eta)$ describes the evolution of the gravitational wave after it crosses the horizon. For radiation dominated universe, the solution reads

$$h_{\boldsymbol{k},\lambda}(\eta) = h^{prim}_{\boldsymbol{k},\lambda} j_0(k\eta)\ , \tag{4.45}$$

where $j_0(x)$ is the spherical Bessel function [273].

Let us define the power spectrum of gravitational waves. The energy density is given by

$$\varepsilon_h(\eta) = \frac{1}{32\pi G a^2} < h'_{ij} h'^{ij} >\ , \tag{4.46}$$

and in k space the spatial average reads

$$< h'_{\boldsymbol{k},\lambda} h'_{\boldsymbol{k}',\lambda'} >= (2\pi)^3 \delta_{\lambda\lambda'} \delta^3(\boldsymbol{k} + \boldsymbol{k}') |h'_{\boldsymbol{k},\lambda}|^2\ . \tag{4.47}$$

Moreover, one assumes that the primordial gravitational waves are unpolarized, that is $|h'_{\boldsymbol{k},+}(\eta)|^2 = |h'_{\boldsymbol{k},\times}(\eta)|^2$.

Using EQ. (4.44), we can write the energy density as

$$\varepsilon_h(\eta) = \frac{1}{32\pi G a^2} \int \frac{dk}{k} \Delta^2_{h,prim} \left[\mathcal{T}'_k(\eta)\right]^2 \ , \tag{4.48}$$

where $\Delta^2_{k,prim}$ is the primordial amplitude which in de Sitter inflation turns out to be

$$\Delta^2_{h,prim} = \frac{2}{\pi^2} k^3 |h^{prim}_{\boldsymbol{k}}|^2 = \frac{16}{\pi} \left(\frac{H_{dS}}{M_{Pl}}\right)^2 \ , \tag{4.49}$$

H_{dS} and M_{Pl} being the Hubble constant in de Sitter inflation and the Planck mass, respectively.

The logarithmic energy density is defined as $d\varepsilon_h/d\ln k$ and the fractional energy density is given by

$$\Omega(\eta, k) = \frac{d\varepsilon_h(\eta, k)}{d\ln k} \frac{1}{\varepsilon_c(\eta)} = \frac{\Delta^2_{h,prim} \ \left[\mathcal{T}'_k(\eta)\right]^2}{32\pi \, G \, a^2 \, \varepsilon_c(\eta)} \ , \tag{4.50}$$

where ε_c is the critical energy density.

From the Friedman equations we finally get

$$\Omega(\eta, k) = \frac{\Delta^2_{h,prim}}{12 \, H^2(\eta) \, a^2} \left[\mathcal{T}'_k(\eta)\right]^2 \ . \tag{4.51}$$

A gravitational wave of mode k has frequency $f = 2\pi k/a$. Because of redshift, once a wave crosses the horizon its frequency decreases. From the definition of fractional energy density follows that Ω decreases as $a^{-4}H^{-2}$, since gravitational waves are decoupled from the rest of the Universe and $\varepsilon_c \sim H^2$ from Friedman equation. For waves that reentered at a certain time η, the fractional energy density today is

$$\Omega_0 = \Omega(\eta, f) \frac{a^4(\eta) H^2(\eta)}{a_0^4 H_0^2} \ , \tag{4.52}$$

and the frequency today is $f_0 = 2\pi k/a_0$, where a_0 and H_0 are the scale factor and the Hubble parameter today.

The evolution of the $h_{\boldsymbol{k}}$ modes and of the crossing condition, $k = a \, H$, are controlled by the scale factor a and the modification of the spectrum

of gravitational waves from the primordial one depends on the content of matter in the epoch they reenter the horizon. We will show that the QCD transition modifies the speed of sound c_s^2, since the Universe stands no longer in a pure radiation era and, correspondingly, the primordial gravitational waves cross the horizon near that transition time at different rates.

It is more useful to write EQ. (4.40) for the transfer function as a function of the temperature. Let us consider the equation of motion for the transfer function, $\mathcal{T}_k$, with respect to cosmic time, t,

$$\frac{d^2\mathcal{T}_k}{dt^2} + 3\frac{1}{a}\frac{da}{dt}\frac{\mathcal{T}_k}{dt} + \frac{k^2}{a^2}\mathcal{T}_k = 0 \ . \tag{4.53}$$

By eqs.(4.14) and (4.15) one has

$$\frac{d^2\mathcal{T}_k}{dT^2} + f(T)\frac{d\mathcal{T}_k}{dT} + \kappa^2(T,k)\mathcal{T}_k = 0 \ , \tag{4.54}$$

where

$$f(T) = \frac{1}{T}\frac{w-1+2c_s^2}{2c_s^2} + \frac{1}{c_s^2}\frac{dc_s^2}{dT} \ , \tag{4.55}$$

and

$$\kappa(T,k) = -\frac{k}{a}\frac{1}{3c_s^2 TH} \ . \tag{4.56}$$

In radiation era, the solution of EQ. (4.53) reads

$$\mathcal{T}_k = A\, j_0\left(\alpha\,\frac{k}{T}\right) \ , \tag{4.57}$$

where j_0 is a spherical Bessel function of the first kind and A and α are appropriate constants. In order to integrate numerically EQ. (4.54), we set boundary conditions at high temperature, such as 10^4 MeV, where the modes $h_{\boldsymbol{k}}$ are given by the radiation era solutions (EQ. (4.57)).

4.3 Results

We analyze the EoS of the entire system in the temperature range 70 MeV $\leq T \leq$ 400 MeV, by interpolating the lattice data and the HRG results at

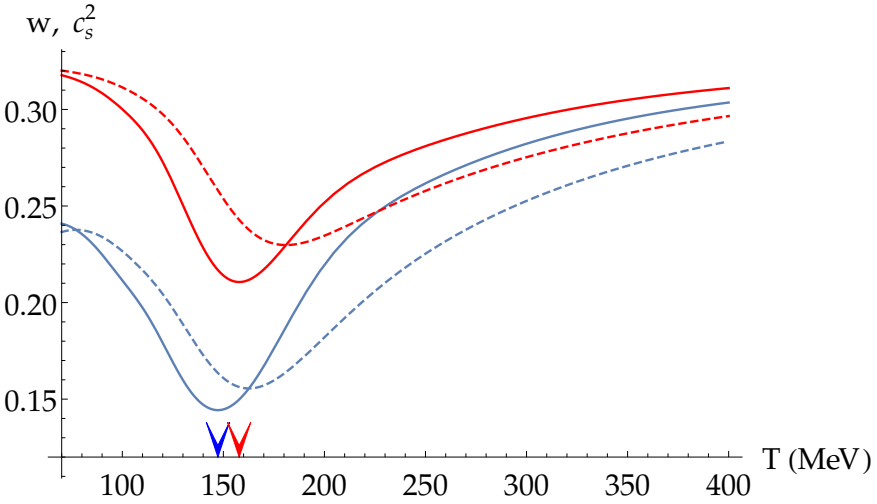

(a) As a function of temperature.

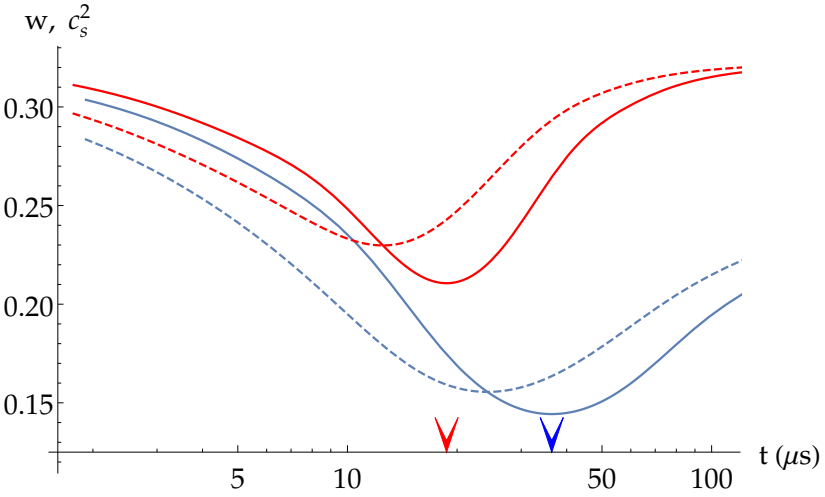

(b) As a function of time.

Figure 4.3: The speed of sound c_s^2 (continuous curves) and w (dashed lines) for the different sectors: QCD (blue) and QCD plus electroweak sector (red).

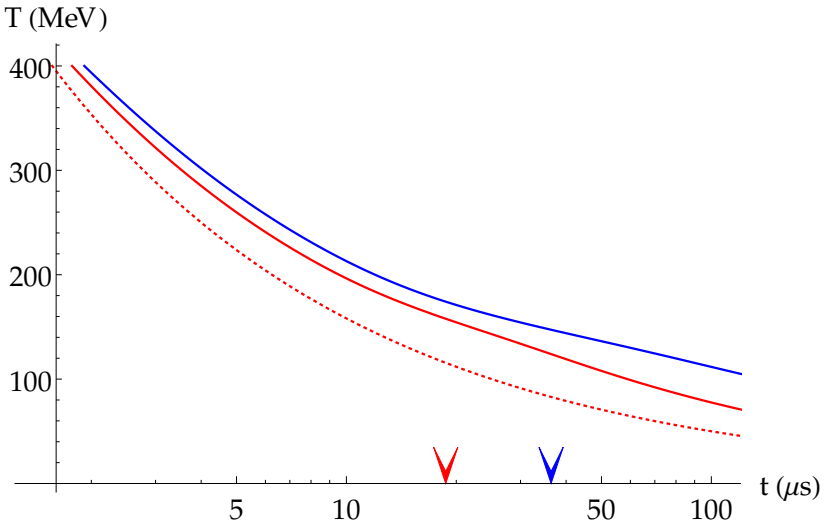

Figure 4.4: Temperature as a function of the cosmological time in the different sectors (blue for QCD and red for QCD plus EW), compared with the behavior of the pure radiation era (red dotted line).

$T_l = 130$ MeV. The lattice pressure is parameterized by the HotQCD [202, 203] collaboration functions of Eqs. (3.9) and (3.10). The HRG one by EQ. (3.24).

The results for the $w = p_T/\varepsilon_T$ and for the speed of sound c_s^2 are summarized in Fig. 4.3a, where the continuous curves indicate the speed of sound and the dashed lines the value of w. The blue lines give the results for the strong sector, and the red ones contain the electroweak sector. The arrows indicate the temperature of the transition, defined as the temperature at the minimum of the speed of sound, which goes from the $T_s = 147$ MeV including the strong interaction only to $T_{ew} = 158$ MeV adding the electroweak sector.

Figure 4.3b shows the behaviour of the speed of sound as a function of the cosmological time. For the whole system, after about $100\mu s$ the values of w and c_s^2 come back to be those of a radiation dominated era.

The relation between the temperature and the cosmological time is

$$t = t_0 + \frac{1}{\sqrt{24\,\pi\,G}} \int_T^{T_0} \frac{d\overline{T}}{\overline{T} c_s^2\,\sqrt{\varepsilon}}\,, \tag{4.58}$$

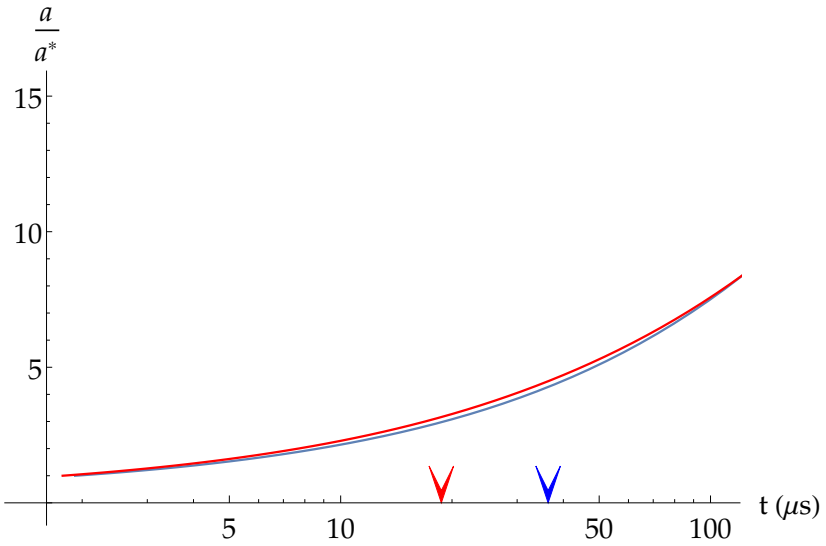

Figure 4.5: The scale factor a/a^* as a function of cosmological time: QCD only (blue) and QCD plus electroweak sector (red).

which is numerically solved (with $T_0 = 500$ MeV and $t_0 = 1\ \mu s$ [266]). In Figure 4.4, we have shown how the temperature decrease in the different cases previously discussed and in the pure radiation era (red dotted line). The transition time is reduced by adding the electroweak sector: $t_t^s = 36.39\ \mu s$, $t_t^{ew} = 18.71\ \mu s$.

4.3.1 Evolution of the cosmological parameters

The results in the previous sections are the starting point to study the behaviour of the cosmological parameters during the deconfinement transition. Since the cosmological parameters can depend on the higher-order derivatives of the Hubble parameter, i.e. on the higher-order derivative of the thermodynamical quantities, it could be possible that some effects show up near the critical temperature [266]. We have analyzed two different cases: the strong sector only (blue curves in the Figures) and the strong plus the electroweak sector (red curves). In all Figures, the arrows indicate the transition time.

In Figure 4.5 and Figure 4.6a are respectively depicted the time behaviour of the scale factor $a(t)$ (normalized to the value at 400 MeV, a^*) and of $H(t)$. The final result is essentially independent of the specific set-

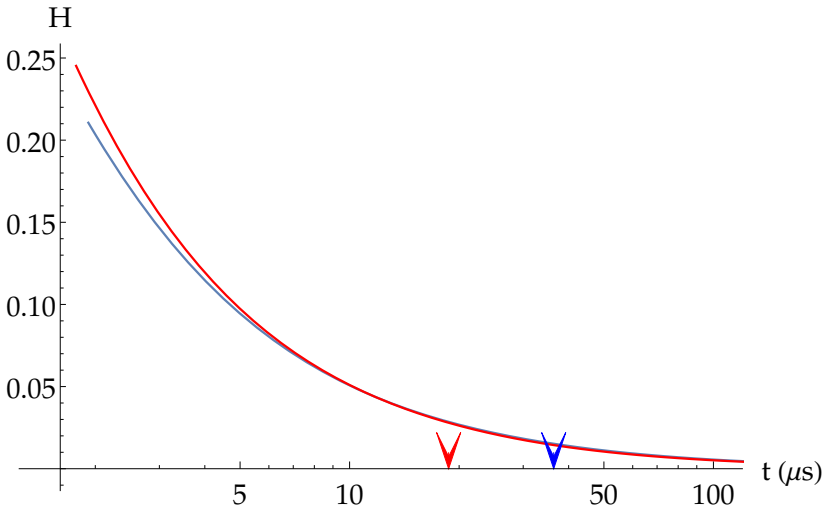

(a) The Hubble parameter H.

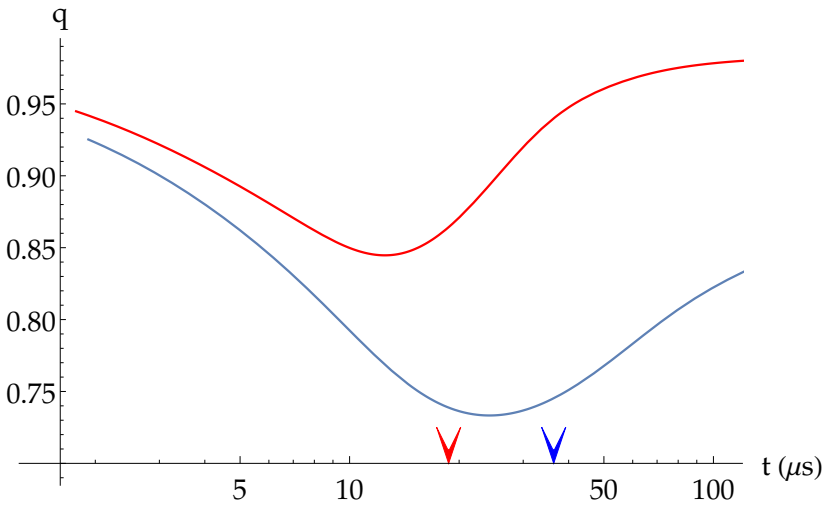

(b) Cosmological deceleration q.

Figure 4.6: Evolution of the cosmological parameters as a function of cosmological time: QCD only (blue) and QCD plus electroweak sector (red):

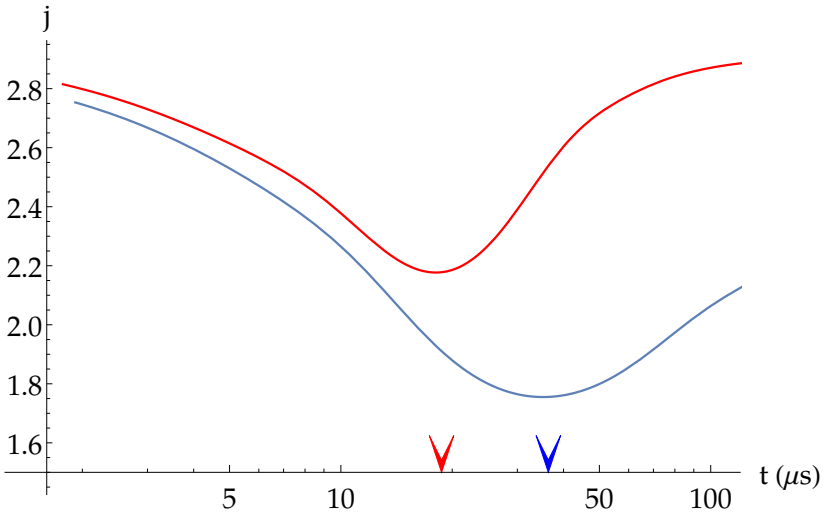

(a) The jerk, j.

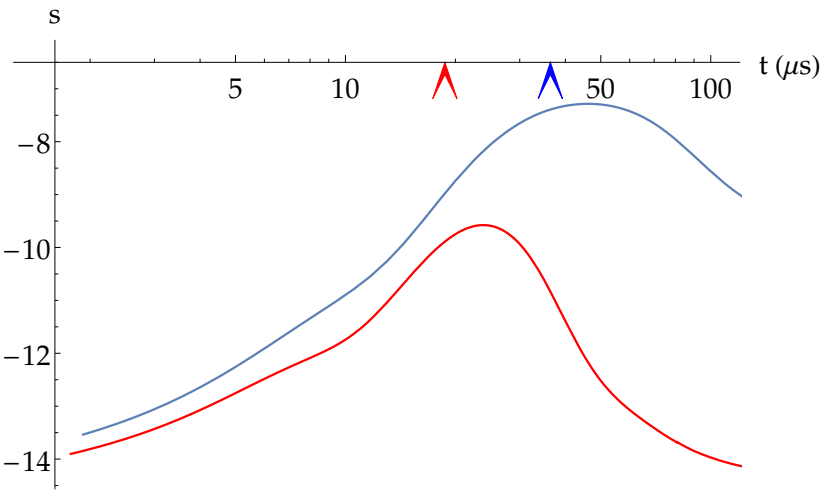

(b) The snap, s.

Figure 4.7: Evolution of the cosmological parameters as a function of cosmological time: QCD only (blue) and QCD plus electroweak sector (red):

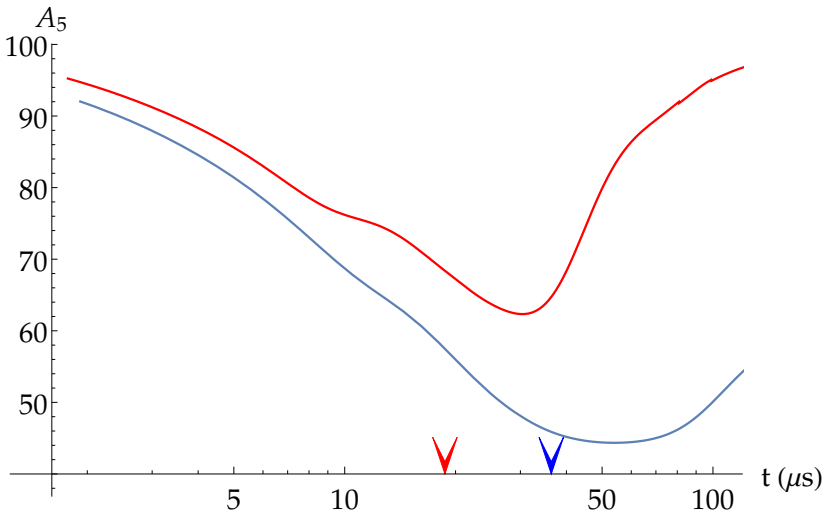

(a) A_5.

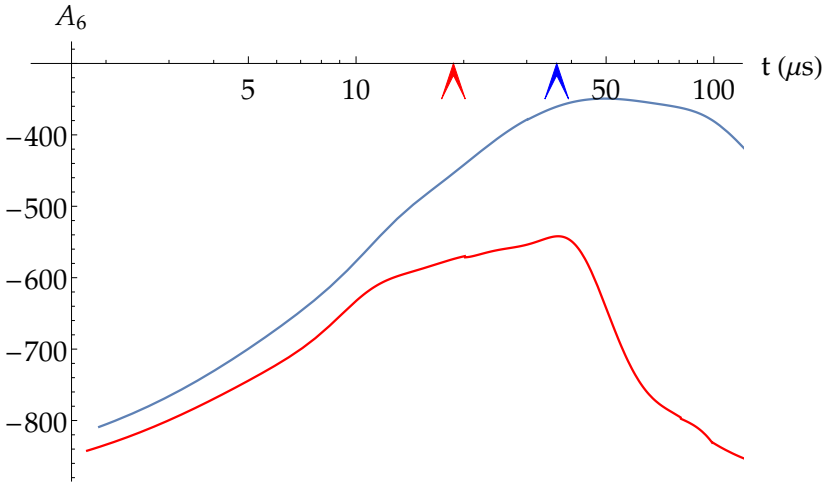

(b) A_6.

Figure 4.8: Evolution of the cosmological parameters as a function of cosmological time: QCD only (blue) and QCD plus electroweak sector (red):

ting.

In Figures 4.6b, 4.7a, 4.7b, 4.8a and 4.8b the time evolution of q, j, s, A_5 and A_6 is plotted, respectively. As expected, the parameters with high order derivative show larger deviations from the typical values of the radiation dominated era. However, once the transition is over, the Universe is again dominated by radiation. The fluctuations of the cosmological parameters in the whole system are limited to a short time interval of about 100 μs.

4.3.2 Modification of the primordial spectrum of the gravitational waves

According to previous results, the fluctuations of the cosmological parameters in the whole system are limited to a short time interval of about 100 μs. From this point of view, the deconfinement transition turns out to be more effective in modifying the primordial spectrum of the gravitational waves, as proposed in [263]. By lattice QCD simulations, by the HRG model and including the electroweak sector, we now discuss a detailed analysis of this effect by numerical integration of Eqs. (4.40)-(4.41), improving previous analysis [263, 265].

In Figure 4.9 the numerical results for different values of k are reported: waves with higher frequencies cross the horizon earlier and waves that reentered at $T \sim 150$ MeV have frequencies of about 10^{-7} Hz, the typical frequency f_* of waves from the QCD transition. The effects of the transition are expected to be impressed in the fractional energy density Ω and, in particular, one computes [263] the quantity $\Omega(f)/\Omega(\bar{f} \ll f_*)$, that is the fractional energy density of the gravitational waves with respect to the same quantity evaluated for waves that do not encounter the transition ($\bar{f}$ being a fixed frequency much lower than f_*).

From EQ. (4.52), this quantity evaluated today is

$$\frac{\Omega_0(f)}{\Omega_0(\bar{f} \ll f_*)} = \frac{\Omega(f)}{\Omega(\bar{f} \ll f_*)} \frac{a^4(f)H^2(f)}{a^4(\bar{f})H^2(\bar{f})} \,. \tag{4.59}$$

The redshift factor gives the shape of the step, and the final result is showed in Fig. 4.10. The size of the step is about 38%, larger than previous results [263, 265]. In particular, in [263] the step size was $\simeq 30\%$, obtained by

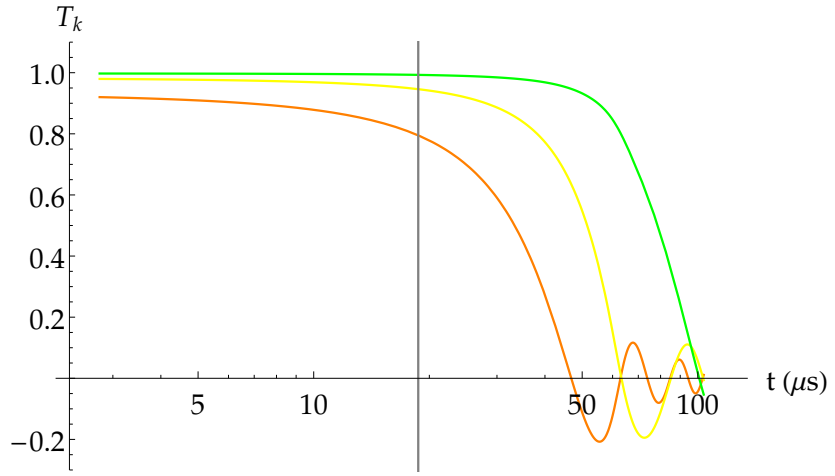

Figure 4.9: Transfer function $\mathcal{T}_k$ against cosmic time at different values of the wave number k. It describes the evolution of a gravitational wave. Green is for $k = 2.17 \times 10^{-14}\ \mu s^{-1}$, yellow $k = 6.02 \times 10^{-14}\ \mu s^{-1}$, orange $k = 1.20 \times 10^{-13}\ \mu s^{-1}$. Vertical line indicates the QCD transition.

a numerical computation of a first-order transition between the quark-gluon plasma phase and the hadronic phase. Figure 4.11 shows a direct comparison between the latter result and our evaluation (see also ref. [274]).

In order to verify these results, we need to detect primordial gravitational waves with frequencies around 10^{-7} Hz. They could be detected indirectly by seeking effects on physical observables, such as the Cosmic Microwave Background (CMB) polarization, or by direct detection with interferometers [273]. However, we can only put upper limits on the energy density of gravitational waves from current data. In the future, other detectors as the Kamioka Gravitational Wave Detector (KAGRA) [275], the Einstein Telescope [276] and LIGO-India [277] will improve our knowledge on the gravitational waves.

4.4 Comments and conclusions

The fluctuations of conserved charges at the deconfinement transition are a clear sign of the different behaviour between the quark-gluon plasma and

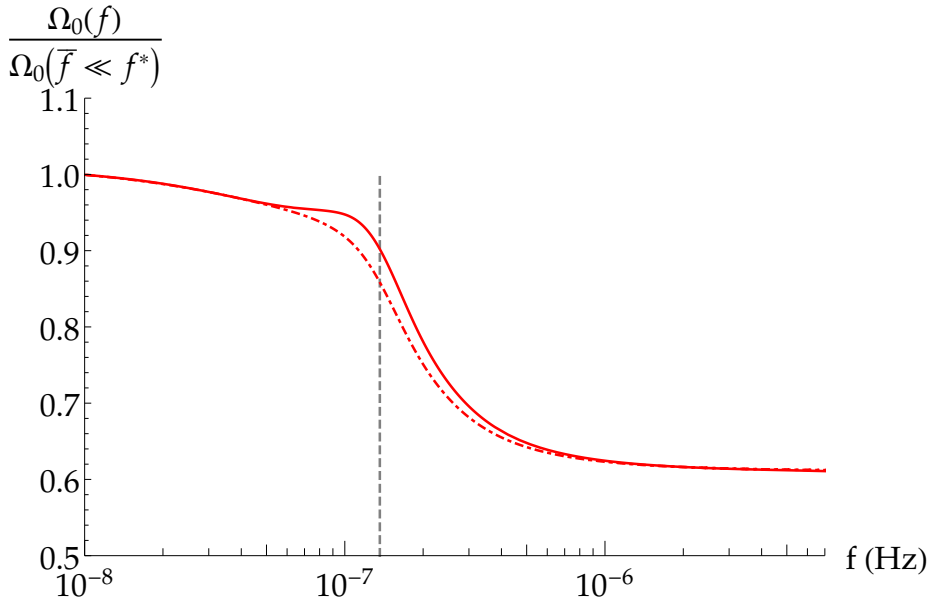

Figure 4.10: Fraction of energy density of gravitational waves with respect to waves that do not encounter the QCD transition in continuous lines, only the redshift factor to today values in dashed lines. Both against frequency f. Vertical line represents the transition. The size of the step is about 38%.

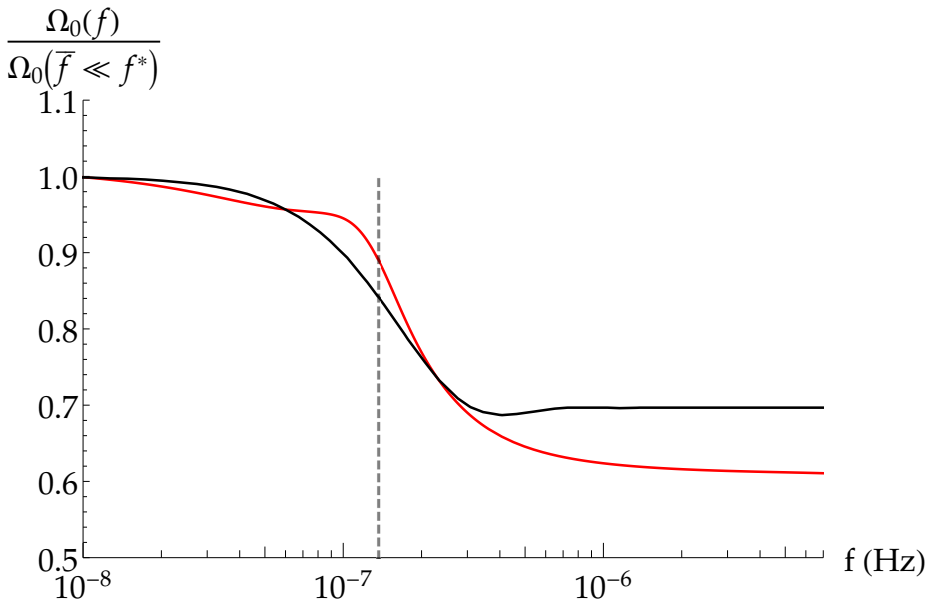

Figure 4.11: Comparison of the fraction of energy density of gravitational waves with respect to waves that do not encounter the QCD transition between the evaluation made in [263], in black, and our evaluation, in red. Vertical line represents the transition.

the hadron resonance gas model. However, their detection in relativistic heavy-ion collisions is difficult.

The fluctuations of the cosmological parameters at the QCD transition have, in principle, the same physical basis, i.e. they originate from the combined effect of the equation of state and of the calculation of higher-order derivatives of the relevant physical parameters, that is, in early Universe, the scale factor. We have shown, by a complete treatment of the thermodynamics of the whole system (strong and electroweak contributions), that after about $100\mu s$ the cosmological parameters return to the typical values of a radiation dominated era, i.e. to their values before the transition. This result remains valid also for cosmological scalars involving higher-order derivatives of the scale factor (see Figs. (4.5-4.8b)). We have preliminary verified by different dark matter models that the dark matter contribution to the EoS of the whole system, in the temperature range relevant for the deconfinement transition, turns out to be negligible and, as shown in ref. [278], the effects of the QCD transition on the density fluctuations are small. Therefore the possible signature of the deconfinement transition in early Universe is restricted to the modification of the primordial gravitational wave spectrum.

By using the recent lattice QCD simulation data and the HRG below T_c to describe the transition, one evaluates the fraction of energy density of gravitational waves with respect to waves that do not encounter the QCD transition. A difference of about 10% is observed concerning previous analyses [263]. However, direct and indirect detection of gravitational waves from inflation is required to verify these results. While it seems unlikely in the present, promising experiments are planned for the future.

Chapter 5

Geometrical description of the QCD phase transition

The introduction of Riemannian geometry to the analysis of the phase diagram of thermal systems is not intuitive, and the concept of distance between equilibrium configurations requires an in-depth study. Nevertheless, it turns out to be a useful and predictive tool for analyzing phase transitions.

The first application of differential geometry to statistical systems dates back to 1945 with a seminal paper by the Indian mathematician C. Rao [279] who started the entire branch of information theory called "information geometry" [280], while the first metric structure for thermodynamic systems is due to F. Weinhold [281, 282]. Weinhold's main idea has been to represent differentials of thermodynamic functions as elements of a vector space and then to define an inner product: the matrix elements of the metric, g_{ij}, were introduced as the second derivatives of the internal energy with respect to extensive parameters. In this formulation, the minimum energy principle for an isolated system is the basis of the geometry, implying the tensor character of g_{ij} and its euclidean character. Despite the interesting aspects of this approach, which permits to derive the fundamental laws of equilibrium thermodynamics from geometric postulates, it did not produce any significant result. Some years later, shifting from the energy to the entropy representation, G. Ruppeiner [283] was able to create a thermodynamic geometry with a clear physical meaning. He defined the metric tensor as the Hessian of the entropy density, and he noticed that the resulting line

element, i.e. the infinitesimal distance between neighbouring equilibrium states, is in inverse relation with the fluctuation probability defined by the classical theory: a spontaneous fluctuation between points of the manifold is less likely when they are far apart.

The previous concept of thermodynamic metric gave rise to some interesting developments in finite-time thermodynamics, where the increase in entropy due to non-equilibrium aspects can be related with the geodetic distance between the initial and final states of a real process [284]. Moreover, it has been shown that Weinhold's and Ruppeiner's metrics are conformal [285], and both are limiting cases of Rao's metric [286].

The main result of thermodynamic geometry within Ruppeiner's formulation is the "interaction hypothesis" which states that the absolute value of the scalar curvature R, calculated by the metric, is proportional to the cube of the correlation length, ξ^3, of the underlying thermodynamic system. This liaison has been initially suggested by the observation that the Riemannian manifold of a classic ideal gas is flat, and $|R|$ calculated for a Van der Waals gas diverges at the liquid-vapour critical point precisely with the same exponent of ξ^3, predicted by scaling laws.

Finally, another significant property concerns the sign of the curvature scalar, which seems to carry information on the dominant interaction in the system, even when its microscopic properties are not known.

5.1 Thermodynamic Geometry

5.1.1 The thermo-metric

Let us consider a system which entropy, S, is a function of some thermodynamic variables, X^μ, that specify the Hamiltonian of the system (for instance, $X^\mu = \{E,\ N,\ V\ , \ldots\}$, where E is the energy, N the particle number, V the volume, etc.), and consider the quantity [283, 287–290]

$$g_{\mu\nu} \equiv -\frac{\partial^2 S}{\partial X^\mu \partial X^\nu}\ . \tag{5.1}$$

Under a change of coordinates, $g_{\mu\nu}$ transforms as a second-rank tensor: indeed, if one considers the coordinate transformation $X^\mu \mapsto X'^\mu$, the second

derivative in EQ. (5.1) changes according to [283, 287–290]

$$\frac{\partial^2 S}{\partial X'^{\mu'} \partial X'^{\nu'}} = \frac{\partial X^\mu}{\partial X'^{\mu'}} \frac{\partial X^\nu}{\partial X'^{\nu'}} \frac{\partial^2 S}{\partial X^\mu \partial X^\nu} + \frac{\partial S}{\partial X^\mu} \frac{\partial^2 X^\mu}{\partial X'^{\mu'} \partial X'^{\nu'}} = \frac{\partial^2 S}{\partial X^{\mu'} \partial X^{\nu'}} \, . \tag{5.2}$$

Moreover, if one defines the free entropy or Massieu function as [291, 292]

$$\phi = \ln \mathcal{Z} = S - \theta_\mu X^\mu \, , \tag{5.3}$$

where θ_μ are intensive conjugated variables,

$$\theta_\mu \equiv \frac{\partial S}{\partial X^\mu} \, , \tag{5.4}$$

it easy to show that the quantity [284, 291–294]

$$g^{\mu\nu} = \frac{\partial^2 \phi}{\partial \theta^\mu \partial \theta^\nu} \tag{5.5}$$

is the inverse of $g_{\mu\nu}$ in EQ. (5.1), i.e. [291]

$$g^{\mu\nu} g_{\mu\nu} = \frac{\partial X^\mu}{\partial \theta_\nu} \frac{\partial \theta_\nu}{\partial X^\mu} = \delta^\mu_\nu \, . \tag{5.6}$$

The variables X^μ can be obtained from the intensive ones and the Massieu function as

$$X^\mu = -\frac{\partial \phi}{\partial \theta_\mu} \, . \tag{5.7}$$

For example, the variable conjugated to the energy E is the inverse temperature $\theta_1 = \beta = 1/T = \partial S/\partial E$, or that conjugated to the particle number is related to the chemical potential, μ_N: $\theta_2 = \gamma = -\mu_N/T = \partial S/\partial N$.

The metric, $g_{\mu\nu}$, is symmetric with respect to the exchange $\mu \leftrightarrow \nu$ (because the symmetry of second derivatives - Schwarz's theorem), and it is non-degenerate (indeed one defines the inverse metric $g^{\mu\nu}$ by EQ. (5.5)). Thus, $g_{\mu\nu}$ is a metric tensor, which line element is

$$d\ell^2 = g_{\mu\nu} \, dX^\mu \, dX^\nu = g^{\mu\nu} \, d\theta_\mu \, d\theta_\nu = -d\theta_\mu \, dX^\mu = -dS^2 = d^2\phi \, . \tag{5.8}$$

Geometrically, the first law of thermodynamics can be equivalently ex-

pressed as:

$$dS = \theta_\mu \, dX^\mu \ , \text{ or} \qquad\qquad d\phi = -X^\mu \, d\theta_\mu \ . \tag{5.9}$$

The metric and its inverse have a clear meaning in terms of the second moment of thermodynamic fluctuations:

$$g^{\mu\nu} = \langle \Delta X^\mu \, \Delta X^\nu \rangle \ , \qquad \text{and} \qquad g_{\mu\nu} = \langle \Delta\theta_\mu \, \Delta\theta_\nu \rangle \ . \tag{5.10}$$

Once a metric is given, one defines some scalars related to the geometry, and the most famous is the scalar curvature, R. It is a well-known quantity defined as the trace of the *Ricci* tensor and in two dimensions contains all the information about the geometry. For example, for the two-sphere of radius r, its value is $R = -2/r^2$ (in the Weinberg sign convention). In our evaluation of R, we will use the definition of the metric $g^{\mu\nu}$ in EQ. (5.5). In this "frame", the metric depends on the derivatives of the thermodynamic potential $\phi = P/T$, where P is the total pressure of the system [288].

In two dimensions the expression for R is considerably simplified:

$$R = \frac{k_B}{2} \begin{vmatrix} \phi_{,11} & \phi_{,12} & \phi_{,22} \\ \phi_{,111} & \phi_{,112} & \phi_{,122} \\ \phi_{,112} & \phi_{,122} & \phi_{,222} \end{vmatrix} / \begin{vmatrix} \phi_{,11} & \phi_{,12} \\ \phi_{,21} & \phi_{,22} \end{vmatrix}^2 \ , \tag{5.11}$$

where k_B is the Boltzmann's constant,

$$g = \begin{vmatrix} \phi_{,11} & \phi_{,12} \\ \phi_{,21} & \phi_{,22} \end{vmatrix} \tag{5.12}$$

is the determinant of the metric and the usual comma notation for derivatives has been used (for example $\phi_{,12}$ indicates the derivative of ϕ with respect to θ_1 and θ_2).

In the following, we'll study systems depending on the temperature, T, and on the baryon chemical potential, μ. In this case, the thermodynamic manifold are described in terms of the two intensive variables $\theta_1 = \beta = 1/T$

and $\theta_2 = \gamma = -\mu/T$. Moreover, for constant volume,

$$\phi_{,\beta\beta} = \frac{1}{V}\,\langle (U - \langle U\rangle)^2\rangle, \tag{5.13}$$

$$\phi_{,\beta\gamma} = \frac{1}{V}\,\langle (U - \langle U\rangle)(N - \langle N\rangle)\rangle, \tag{5.14}$$

$$\phi_{,\gamma\gamma} = \frac{1}{V}\,\langle (N - \langle N\rangle)^2\rangle, \tag{5.15}$$

where U, N denote the internal energy and the particle number respectively.

Note also that $-\theta_\mu$ is not the covariant component of the vector X^μ (i.e. in general $-\theta_\mu \neq g_{\mu\nu}\,X^\nu$), but, only for infinitesimal variations, it holds [288]

$$-\,d\theta_\mu = g_{\mu\nu}\,dX^\nu\ . \tag{5.16}$$

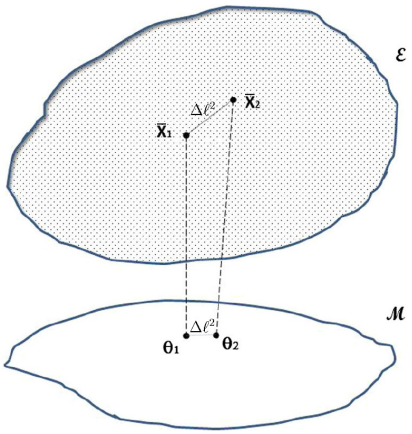

Figure 5.1: The state space manifold ($\mathcal{E}$) along with the parameter manifold ($\mathcal{M}$). Each point on the parameter manifold M fixes an equilibrium point on E about which there is a distribution of state space fluctuations. Figure and caption from ref. [291].

According to EQ. (5.8), if one indicates the equilibrium state space as $\mathcal{E}$ (see Fig. 5.1), i.e. the manifold whose points are the coordinates X^μ, and the parameter space, i.e. that of the conjugate variables θ_μ, as $\mathcal{M}$, the line element between two nearby equilibrium points in $\mathcal{E}$, $\Delta\ell^2$, is equivalently interpreted as the distance measure between two nearby probability distributions in the parameter manifold [291]. For each equilibrium point, $\bar{X}^\mu$, in $\mathcal{E}$, the tangent space $T_{\bar{X}}$ is spanned by the spontaneous fluctuation vectors $\Delta X^\mu = \bar{X}^\mu - X^\mu$ around the equilibrium state. The directions of statistically independent fluctuations around an equilibrium state are fixed by the eigenvectors of the metric $g^{\mu\nu}$. These eigenvalues, or more precisely the square root, also fix the variance along

their respective independent direction and could provide a measure of the statistical distinguishability of two nearby distributions. Furthermore, if one considers two points in the space $\mathcal{M}$, θ_1 and θ_2, and defines the geodetic from θ_1 to θ_2 as $\theta = \theta(t)$ (parametrized in terms of the affine parameter t, with $0 \leq t \leq \tau$), the length of θ is [284]

$$L_{th} \stackrel{\text{def}}{=} \int_0^\tau \sqrt{g^{\mu\nu}(\theta)\, \frac{d\theta_\mu}{dt}\, \frac{d\theta_\nu}{dt}}\; dt \; . \tag{5.17}$$

L_{th} is called "*Thermodynamic Length*", and it provides a measure of the number of natural fluctuations along the path: the larger the fluctuations, the closer points are together [286]. Another related quantity is the "*Thermodynamics Divergence*" of the path defined as [284, 286, 292, 295]

$$\mathcal{J} = \tau\, \Lambda_{dissipated} \; , \tag{5.18}$$

where

$$\Lambda_{dissipated} \stackrel{\text{def}}{=} \int_0^\tau g^{\mu\nu}(\theta)\, \frac{d\theta_\mu}{dt}\, \frac{d\theta_\nu}{dt}\; dt \; , \tag{5.19}$$

is the availability loss (or, dissipated availability) in a thermodynamic process. In Riemannian geometry $\mathcal{J}/2\,\tau$ is called the energy, or action, of the curve, due to similarity with the kinetic energy integral in classical mechanics. The length and divergence are related by the inequality,

$$\mathcal{J} \geq L_{th}^2 \; . \tag{5.20}$$

Both L_{th} and $\mathcal{J}$ are useful quantities to study thermodynamics at finite-time or non non-equilibrium thermodynamics.

The covariance metric, $g^{\mu\nu}$, relates directly to the information geometry of equilibrium thermodynamics and is the Fisher-Rao metric on the statistical manifold parameterized by the variables θ. Indeed, recalling that the configurational probability distribution in the Gibbs ensemble is given by

$$p(x|\theta) \stackrel{\text{def}}{=} \frac{1}{\mathcal{Z}}\, e^{-\beta\mathcal{H}(x,\theta)} = \frac{1}{\mathcal{Z}}\, e^{-\theta_\mu(t) X^\mu(x)} \; , \tag{5.21}$$

where x is the configuration, t is time, $\mathcal{Z}$ is the partition function, and $\mathcal{H}$ is the Hamiltonian of the system, which is expressed in terms of the

collective variables X^μ and of the conjugate generalized forces θ_μ (the sub-Hamiltonians X^μ are time-independent functions of the configurations. The conjugate variables θ_μ are time-dependent, configuration independent, and are the experimentally controllable parameters), the thermodynamic metric tensor can be shown to be equal to the Fisher-Rao information metric tensor [279, 286, 292, 296],

$$g^{\mu\nu}(\theta) = \int p(x|\theta)\, \frac{\partial \ln p(x|\theta)}{\partial \theta_\mu}\, \frac{\partial \ln p(x|\theta)}{\partial \theta_\nu}\, dx\ , \tag{5.22}$$

which is a more general and fundamental definition, that can be easily extended to non-equilibrium systems or for Hamiltonians that are not a linear function of the control parameters [286].

5.1.2 Differential Geometry and Fluctuation Theory

Unlike the Rao's or the Weinold's definition of $g^{\mu\nu}$, the Ruppeiner metric provides a clear interpretation in terms of the fluctuations theory. The Classical Fluctuation Theory (ClFT) defines a probability distribution for the equilibrium thermodynamic states, and it is based on the same principle of statistical mechanics but from a different perspective. Indeed, let us consider a system and a reservoir (r) in a mutual equilibrium, with additive total entropy $S_{tot} = S + S_r$ and conserved and additive charges $X_{tot} = X + X_r$. The thermodynamic state is defined by the intensive variables, θ_r, that fix the equilibrium point $\bar{X}$ of the state space $\mathcal{E}$. As long as the system is at the point $\bar{X}$, it is in equilibrium with the reservoir. At any other point X in its state space (hence points of *internal equilibrium*) it is not in mutual equilibrium with the reservoir. Thus its intensive variables θ are different from θ_r. In the framework of Classical Fluctuation Theory (ClFT), the probability distribution of a spontaneous fluctuation of the system from the equilibrium point $\bar{X}$ to a different point X in its state space is determined by the entropy of the overall microcanonical system [283, 287–291],

$$p(x|\theta) d^n X = C\ \exp\left\{S_{tot}(X;\theta)\right\} d^n X\ , \tag{5.23}$$

where

$$S_{tot}(X;\theta) = S(X) + S_{r,\theta}(X_r) \leq S_{tot}(\bar{X};\theta) \tag{5.24}$$

is the total entropy evaluated at the point $X \neq \bar{X}$. By Taylor expanding the total entropy around its maximum value ($dS = 0$) at equilibrium, one gets

$$S_{tot}(X;\theta) = S_{tot}(\bar{X};\theta) + \frac{1}{2}\, dS^2 + \cdots \,, \tag{5.25}$$

where

$$d^2S = \frac{\partial^2 S}{\partial X^\mu \partial X^\nu} \left(\bar{X}^\mu - X^\mu\right) \left(\bar{X}^\nu - X^\nu\right) = -g_{\mu\nu} \Delta X^\mu \, \Delta X^\nu \,, \tag{5.26}$$

and the probability of EQ. (5.23) can be approximated as

$$p(\bar{X} + \Delta X)\, d^n X = \frac{\sqrt{g(\bar{X})}}{(2\,\pi)^{n/2}} \, \exp\left\{-\frac{1}{2}\, g_{\mu\nu} \, \Delta X^\mu \Delta X^\nu\right\} \, d^n X \,. \tag{5.27}$$

Here $g(\bar{X})$ is the determinant of the metric $g_{\mu\nu}$ at $\bar{X}$. EQ. (5.27) is the classical gaussian normalized fluctuation probability density where the quadratic form

$$(\Delta\ell)^2 = g_{\mu\nu} \, \Delta x^\mu \, \Delta x^\nu \tag{5.28}$$

defines a metric on the space of thermodynamic states, that quantifies the probability of a spontaneous deviation from the state of equilibrium. For a stable equilibrium $g_{\mu\nu}$, is positive definite. Thus the expression inside the exponential becomes invariant under coordinate changes and supplies a natural definition of an invariant distance between equilibrium points.

Greene and Callen [297] showed that the ClFT is entirely equivalent to statistical mechanics in its full form. At the same time, in gaussian approximation, the equivalence holds up to second fluctuation moments, but not at higher orders.

Unlike the full probability distribution in EQ. (5.23), the Gaussian approximation above becomes covariant since, besides the line element, the expression outside the exponential is invariant, too. The central role of the distribution $P(x, x_0)$ for the meaning of thermodynamic distance suggested to revising the fluctuation theory [288] due to the several shortcomings (first of all the lack of covariance) of the classical theory, which inhibited a coherent geometric method. To address this problem, one assumes Markovicity: at some instant in time, the properties of a subsystem are determined solely

by the thermodynamic state of this subsystem at that instant of time. Indeed, if one defines two subsystems A and A_2 of A_U, with $A \subseteq A_2$, and defines the densities ρ_U and ρ_2 of A_U and A_2, the probability that A has a density between ρ and $\rho + \delta\rho$ depends on ρ_2 and not on ρ_U. By including another subsystem A_1 such that $A \subseteq A_1 \subseteq A_2$, this probability depends on ρ_1 and not on ρ_2 and so on. Thus, by considering a hierarchy of open concentric subsystems $A_U \supseteq \cdots A_n \supseteq \cdots \supseteq A_1 \supseteq A$ of decreasing size and assuming Markovicity at all steps, the conditional probability density for finding the density of A between ρ and $\rho+\delta\rho$ at some instant of time, given the density ρ_U of A_U at that instant of time,

$$P\left(\begin{array}{c|c} \rho & \rho_U \\ t & t_U \end{array} \right) , \tag{5.29}$$

with $t = 1/V$, is given by a Chapman-Kolmogorov (CK) equation

$$P\left(\begin{array}{c|c} \rho & \rho_U \\ t & t_U \end{array}\right) = \int P\left(\begin{array}{c|c} \rho & \rho_n \\ t & t_n \end{array}\right) P\left(\begin{array}{c|c} \rho_n & \rho_{n-1} \\ t_n & t_{n-1} \end{array}\right) \cdots P\left(\begin{array}{c|c} \rho_1 & \rho_U \\ t_1 & t_U \end{array}\right) d\rho_n \cdots d\rho_1 \ . \tag{5.30}$$

This principle may be invoked not just when the largest of the systems is the infinite closed A_U, but also when it is another open finite subsystem whose state is sampled at some instant in time. CK equation (5.30) is satisfied if one defines the probability P as the solution of a Fokker-Planck like equation

$$\frac{\partial P}{\partial t} = -\frac{\partial}{\partial x^\mu}\left[K^\mu(x)P\right] + \frac{1}{2}\frac{\partial^2}{\partial x^\mu \partial x^\nu}\left[g^{\mu\nu}(x)P\right] \ , \tag{5.31}$$

where $t \equiv 1/V$, K^μ are coefficients (for a complete explanation see [288]) and $g_{\mu\nu}$ is the inverse of the metric $g_{\mu\nu}$ in order that the new theory reduces to the classical one in the thermodynamic limit. Notice that the tensor character of $g^{\mu\nu}$ emerges as a direct consequence of the covariance of the fluctuation equation.

In the new approach, called the Covariant and Consistent Fluctuation Theory, the absolute value of the scalar curvature of the metric, R, is a threshold point for the scale length of the system: if $V >> |R|$, the complete solutions of the fluctuation equation are well approximated by the classical

gaussian. On the other hand, one knows that the classical theory is right in the thermodynamic limit only, i.e. when the typical correlation length in the system is much smaller than V. This property of R supports the interaction hypothesis.

5.1.3 Sign of R

Another interesting aspect of the geometrical approach to phase transitions is that the sign of the scalar curvature brings information on the microscopic interactions. Calculations show that R is positive for classical systems whose interactions are repulsive, and it is negative for attractive interactions [299–303]. The thermodynamic curvature is known to be identically zero only for the ideal classical gas.

A similar behavior has been found for quantum gases, but with a different meaning: R is positive for fermi statistical interactions and it is negative in the bosonic case [298, 304–308].

Analogous results apply for ideal quantum gases obeying Gentile's statistics [305] and for quantum group invariant systems (see [306] and references therein).

A interesting analysis concerns an anyon gas [298] with a parametric statistical distribution given by

$$n_i = \frac{1}{e^{(e_i-\mu)/T} + 2\,\alpha - 1}\ , \tag{5.32}$$

where α is the parameter that specifies the statistical behavior ($\alpha = 0$ corresponds to bosons, $\alpha = 1$ to fermions, and $0 < \alpha < 1$ to intermediate statistics). The sign of R changes

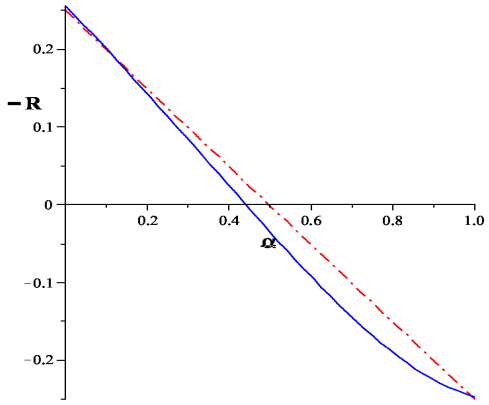

Figure 5.2: $-R$ for an ideal anyon gas of particles obeying fractional statistics as a function of the parameter α that specifies the particle content: $\alpha = 0$ (bosons), $\alpha = 1$ (fermions). The dot-dashed line is for the classical limit and the continuous one shows the change in R due to non-classical behavior. Figure from [298], where their scalar curvature corresponds to $-R$ with our definition.

at $\alpha = 1/2$ in the classical limit (dot-dashed line in Fig. 5.2) and the $R = 0$ condition is satisfied by slightly lower values of α (continuous line) when deviations from the classical behavior are included (see ref. [298] for details).

5.1.4 Phase transition in thermodynamic geometry

The main results of the thermodynamic geometry within Ruppeiner's formulation are the (inverse) relation between the line element and the fluctuation probability between equilibrium states and the, so called, *Interaction hypothesis*: the absolute value of the scalar curvature R is proportional to a power of the correlation length, i.e. $R \sim \xi^d$, where d is the effective spatial dimension of the underling thermodynamic system (because both R and ξ^d are proportional to the specific heat. See, e.g., Ref. [283]). The meaning of the correlation length and of the scalar curvature can be represented as in Fig.5.3 (a schematic picture due to Widom [309]): the intricate line represents what the surface of density $\rho(r) = \rho_0$ might look at any instant. This surface separates two sides with local mean densities $\rho > \rho_0$ and $\rho < \rho_0$. By tracing any straight line, the intersection points with the surface ρ_0 are separated by an average distance equal to ξ: thus, the correlation length is the mean distance between two points at the same density. Because such points are separated by the same mean distance ξ, whatever the direction of the line, it is convenient to think that regions

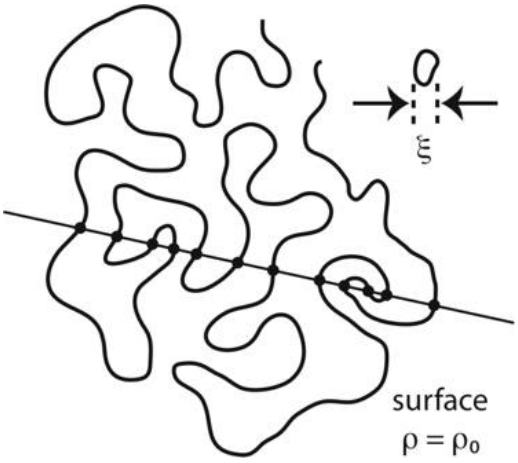

Figure 5.3: A schematic picture of the meaning of ξ: the intricate line represents the surface of $\rho(r) = \rho_0$, i.e. that separating two sides with local mean densities $\rho > \rho_0$ and $\rho < \rho_0$. By tracing any straight line, the intersection points are separated by an average distance equal to ξ. Figure from [300].

as volume elements ("droplets") of dimension $R \sim \xi^d$. Figure 5.4 shows a schematic summary of different possible configurations.

First confirmations of the interaction hypothesis come from the study of the classical ideal gas, represented by a flat space ($R = 0$ [283]), and of the van der Waals gas [288], for which, near the liquid-vapor critical point, T_c, the curvature is $R \sim |(T - T_c)/T_c|^{-2}$. Other confirmations come from the study of the Takahashi Gas [288], the Curie-Weiss model [310], the ferromagnetic monodimensional Ising model [311], mean field theory [287], real fluids [299, 312, 313], and others (see for example Tab. I in Ref. [314]).

The possibility to estimate the correlation length with no, a priori, knowledge of the microscopic structure of the system is very appealing. Indeed, as a consequence of the relationship $|R| \propto \xi^d$, R diverges at a second order phase transition, and by means of R it is possible to estimate ξ by virtue of pure thermodynamic functions. In general, the divergence of R at a second order phase transition occurs in correspondence of the condition $g = 0$, therefore looking for phase transitions in the $\{\theta_\mu\}$ space it is equivalent to look for the zeros of g or for the divergences of R; there are however other possibilities, like the divergence of one of the metric elements or of their derivatives (see EQ. (5.11)).

The relation between $|R|$ and ξ^d is easy to verify for second-order phase transitions, since R diverges, but the criterion to define a new phase in term of the curvature R for a first order phase transition or a crossover is less clear.

The approach called *R-Crossing Method* (RCM) [299] is often applied to define first order phase transitions. It is based on the continuity of the scalar curvature: knowing the thermodynamic quantities in the two phases, i.e. R, one can build up the transition curve by imposing the continuity of R. The RCM, coherent with Widom's microscopic description of the liquid-gas coexistence region (i.e. with the idea that the correlation lengths of the two phases must be the same at the transition) has been tested in systems with different features: vapor-liquid coexistence line for the Lennard-Jones fluids [301, 302], first order phase transition of mean-field Curie-Weiss model (ferromagnetic systems), liquid-liquid phase transitions [315], phase transitions of cosmological interest as the liquid-gas-like first order phase

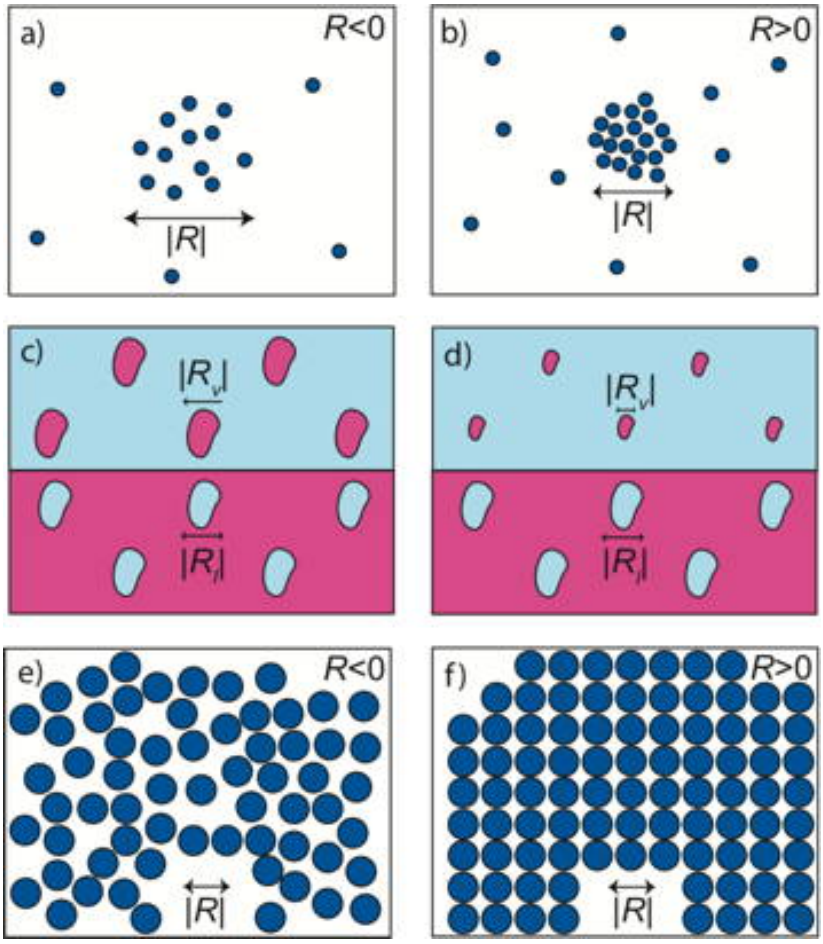

Figure 5.4: Schematic pictures of different possible particle arrangements: (a) cluster of particles with volume $|R|$ pulled together by the attractive part of the interparticle interaction ($R < 0$); (b) a repulsive solid-like cluster held up by hard-core particle repulsion ($R > 0$); (c-d) a fluid in two phases near the critical point: the bottom half is a liquid phase containing vapor droplets with volume $|R_l|$. The top half is a coexisting vapor phase containing liquid droplets with volume $|R_v|$. In (c) $|R_v| = |R_l|$ and the droplets are commensurate, in (d) liquid and vapor phases have incommensurate droplets; (e) liquid phase; (f) solid phase with $R > 0$. Figure from [300].

transition in dyonic charged AdS black hole [316]. Another criterion, applied to the study of first order phase transitions in real fluids [300] and Lennard-Jones systems [302] is a first kind discontinuity in R.

Finally, two different phases can be linked by a crossover. Also in this case there is no definitive conclusion on the behavior of R, and the main results in the following sections regard the study of the crossover in the QCD deconfinement transition within the thermodynamic geometry.

We have investigated two different criteria:

- the first is the so-called $R = 0$ criterion. We know that, the sign of the scalar curvature brings information on the underlying microscopic interactions in the systems, since R turns out to be positive for fermi statistical interactions and negative in the bosonic case. Therefore a change in sign of R is an indication of the balance between effective interactions, even when no transition occurs. For example, theoretical curves with $R = 0$ in pure fluids identify some anomalous behaviors observed in the experimental data of several substances (in particular, water) [300, 312]. A transition from $R > 0$ to $R < 0$ has been also shown for the Lennard-Jones system [301, 302] and Anyon gas [298, 307]. For black holes [317], the change in sign of the curvature occurs at the Hawking-Page transition temperature, therefore associated with the condition $R = 0$.

  In this picture the transition associated with $R = 0$ correspond with a change of the dominant interactions: the transition is from attractive to repulsive interactions, or vice versa.

- local maximum of $|R|$. This criterion is constructed by applying the interaction hypothesis also to a crossover: if $R \sim \xi^d$, and ξ diverge at a II order phase transition, it is natural to expect that a crossover will occur at a maximum value of the correlation length, as the Widom line is characterized as the locus of points with maximum ξ [299, 318]

5.2 Stability

5.2.1 Extensive thermodynamic

In extensive thermodynamic, stability is defined through the Hessian of the entropy. Indeed, by considering for simplicity two systems in thermal contact with entropy $S(M, J)$ (where M is the mass and J is some other extensive parameter), a transfer of some mass dM from the first to the second subsystem, would produce a new configuration with total entropy given by [319, 320]:

$$S(M + dM, J) + S(M - dM, J) \leq 2\ S(M, J)\ . \tag{5.33}$$

The differential form of EQ. (5.33) is

$$H_{,MM} = \frac{\partial^2 S}{\partial M^2} \leq 0\ . \tag{5.34}$$

Similarly, if one transfers dJ, at fixed mass, from one subsystem to the other, one gets

$$H_{,JJ} = \frac{\partial^2 S}{\partial J^2} \leq 0\ , \tag{5.35}$$

and in the case of transfer of dM and dJ

$$\det H = \frac{\partial^2 S}{\partial J^2}\ \frac{\partial^2 S}{\partial M^2} - \left(\frac{\partial^2 S}{\partial M\ \partial J}\right)^2 \geq 0\ . \tag{5.36}$$

Only two of eqs. (5.34-5.36) are independent and the entropy extensivity is a crucial hypothesis to obtain EQ. (5.33). Thus, in ordinary thermodynamic the stability can be achieved by requiring two of eqs. (5.34-5.36). This is not the case for non-extensive systems, such as BHs.

Ruppeiner metric is essentially the opposite of the Hessian of the entropy and a generalization of the condition (5.34-5.36) for systems with more extensive variables can be easily done. Let us consider a system with entropy S, in thermal contact and in equilibrium with an environment, of entropy S_e. The total entropy is $S_{tot} = S + S_e$ and recall the relationship between

Ruppeiner metric and the Gaussian fluctuation theory [321]:

$$dP \propto \exp\left\{-\frac{\Delta\ell^2}{2}\right\} \; dX^1 \cdots dX^\mu \; , \tag{5.37}$$

where

$$\Delta\ell^2 = g_{\mu\nu} \, \Delta X^\mu \, \Delta X^\nu \simeq -2 \, \Delta S_{tot} \; , \tag{5.38}$$

is the distance between X^μ and $X^\mu + \Delta X^\mu$ in the thermodynamic manifold. EQ. (5.38) allows to easily generalize the conditions of eqs. (5.33-5.35) to systems with more variables: after the fluctuations ΔX^μ have taken place, the new state is less stable of the previous one, if and only if its entropy is smaller than or equal to the entropy of the initial one, so that $\Delta S_{tot} \leq 0$. This implies that $g_{\mu\nu}$ must be a positive definite matrix, that can be studied, e.g., through the Sylvester criteria.

5.2.2 Stability in non extensive thermodynamics

Without requiring extensiveness of the potentials, the system stability can be studied by the Poincaré method [320, 322] which is constructed in analogy with ordinary thermodynamics.

Let us consider a system out of equilibrium with entropy $\widehat{S}(Y^\mu, X^\mu)$, being $X^\mu = \{E, \; N \; , \cdots\}$ the usual equilibrium variables (with conjugate variables, θ_μ, as discussed in the previous section) and Y^μ other variables characterizing the non equilibrium condition. Clearly, equilibrium takes place when the system depends only on X^μ, i.e., when [320, 323, 324]

$$Y^\mu = Y^\mu(X^\nu) \; . \tag{5.39}$$

These can be regarded as solution of the equilibrium equations

$$\left.\frac{\partial \widehat{S}}{\partial Y^\mu}\right|_{eq} = 0 \; . \tag{5.40}$$

Let us define now some non-equilibrium functions (in the same way as in

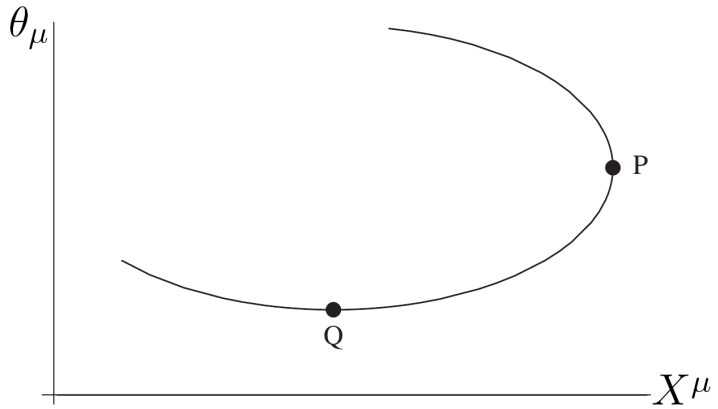

Figure 5.5: Generic plot of a conjugate variable θ_μ against X^μ along an equilibrium sequence. The point P is a turning point. The upper branch is unstable, while the lower branch can be stable or more stable. The sign of the slope also changes at the horizontal tangent at Q', but this has no relation with a change of stability, even if the slope changes sign there. Figure from. [320].

EQ. (5.4))

$$\widehat{\theta}_\mu(Y^\nu, X^\nu) \equiv \frac{\partial \widehat{S}}{\partial X^\mu} \,, \tag{5.41}$$

and such that at the equilibrium

$$\widehat{\theta}_\mu(Y^\nu, X^\nu)\Big|_{eq} = \theta_\mu(X^\nu) \,. \tag{5.42}$$

If one assumes that Y^μ can be chosen in such a way the Hessian of $\widehat{S}$ is diagonal, the "Poincarè coefficients of stability" are defined through the equations

$$\lambda_\rho(X^\mu) \equiv \partial^2_\rho \widehat{S}(Y^\nu(X^\mu), X^\mu)\Big|_{eq} \,. \tag{5.43}$$

where $\lambda_\rho(X^\mu)$ are the Hessian eigenvalues and an instability appears if some $\lambda_\rho > 0$.

Without any knowledge about the out of equilibrium function, $\widehat{S}$, due to eqs. (5.40,5.41), one can link the equilibrium variables θ_μ and X^μ, with the non equilibrium ones by [320]

$$\frac{\partial \theta_\mu}{\partial X^\mu} = \left(\frac{\partial^2 \widehat{S}}{\partial Y^{\mu 2}} \right)_{eq} - \sum_\rho \frac{1}{\lambda_\rho} \left(\frac{\partial \widehat{\theta}_\mu}{\partial Y^\rho} \right)^2_{eq} . \tag{5.44}$$

The left-hand side involves only equilibrium variables, while the right-and side contains only the non equilibrium ones.

Therefore, by previous equation, one obtains information on the non equilibrium states if the properties of the system at equilibrium are known. For example, if the function $\theta_\mu = \theta_\mu(X^\mu)$ has an inflection point (point P in Fig. 5.5) and $\partial\theta_\mu/\partial X^\mu$ changes sign, also the right-hand side of EQ. (5.44) changes its sign. This could be due to an eigenvalue turning from negative to positive value (or vice versa), describing a new phase in the stability of the system. In fact, when at least one of the eigenvalues λ_ρ changes sign, the Hessian has a zero, and $\partial\theta_\mu/\partial X^\mu$ diverges. This implies that the plot of $\theta^\mu(X^\nu)$ along the equilibrium points has a vertical tangent and one can study a change in stability by inspection of the plot of the equilibrium functions $\theta^\mu(X^\nu)$. Moreover, one has to verify which branch is stable and in ref. [320, 325, 326] the following criteria have been suggested:

1. if one can prove the stability of even a single point, then all the other ones in the same stability sequence are stable, until the first turning point is reached. After the turning point the system is unstable;

2. if a stable point is unknown, one can never say anything about the branch with positive slope. Instead, the branch with negative slope, near the turning point, is always unstable;

3. changes of stability can only occur at turning points or bifurcations. Indeed, according to EQ. (5.44), there are other stability points besides the turning points, since it is possible that $(\partial_\rho \widehat{\theta}_\nu)_{eq} = 0$ when the sign of λ_ρ changes, but $\partial_\mu \theta_\nu$ does not diverge. It can be shown that this can only happen at a bifurcation point [320, 325, 326];

4. a vertical asymptote signals the endpoints (boundary) of the (non) equilibrium sequence and it is not related to stability. Finally, there

are points where the slope of θ_μ changes, but $\partial\theta_\mu/\partial X^\mu = 0$ (see points Q in Figure 5.5), but they do not correspond to system instability. These points could indicate a sign variation in the specific heat, as in the case of the four dimensional Kerr BH in the microcanonical ensemble [320]. Therefore, they are stable according to the Poincaré method, but unstable if one considers the sign of the specific heat only.

5.3 Results at low chemical potential

5.3.1 LATTICE QCD: Thermodynamic Geometry of QCD

We start the results section with the application of the thermodynamic geometry to the simulations of LATTICE QCD made by the HotQCD collaboration and recalled in Sec. 3.1.2 of this thesis. These results are available as a series expansion up to the 6th order on the thermodynamic variables $\gamma^2 = (-\mu/T)^2$. Thus, we investigate the thermodynamic geometry of the deconfinement transition by considering two thermodynamic variables, $\beta = 1/T$ and $\gamma = -\mu/T$, i.e. a 2-dimensional thermodynamic metric, which scalar curvature is Taylor expanded up to the 4th order in γ (see App. A.3), and it is simple given by EQ. (A.81-A.84), with

$$\begin{aligned} A^L =& P_0^L\ \beta\ , \\ B^L =& \frac{P_2^L}{\beta^3}\ , \\ C^L =& \frac{P_4^L}{\beta^3}\ , \\ D^L =& \frac{P_6^L}{\beta^3}\ , \end{aligned} \tag{5.45}$$

where, for strangeness neutral systems with a fixed ratio of electric charge to baryon density (see [204] for details), P_i^L are in eqs. (3.14-3.16). Three special cases are considered: the electric neutral systems, $r = 0$, the isospin symmetric limit $r = 1/2$, i.e. $q_k = 0\ \forall k$, which gives the same result

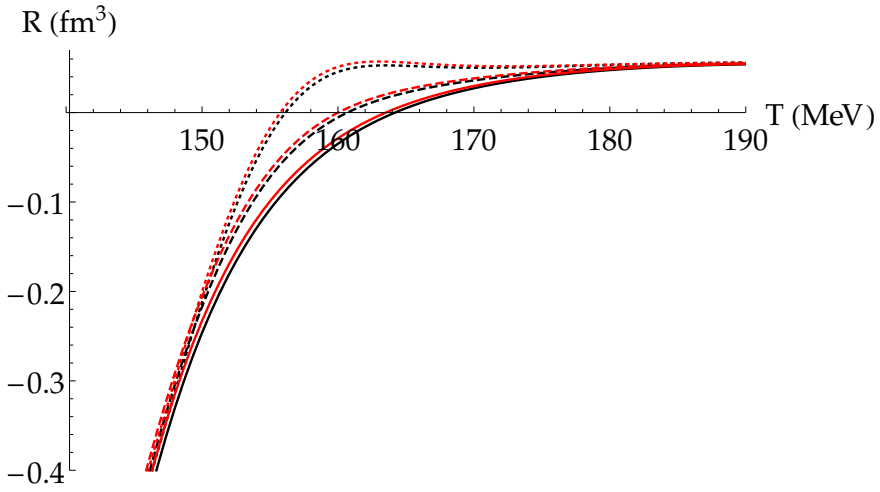

Figure 5.6: The scalar curvature R from EQ. (A.81): the black curves are for lattice data obtained for the condition $n_S = n_Q = 0$ (or equivalent for the isospin symmetric limit), while the reds are for $n_S = 0$ and $n_Q/n_B = 0.4$ [204, 328]. The continuous lines are for $\mu_B = 0$ MeV, the dashed ones for $\mu_B = 80$ MeV and the dotted lines for $\mu_B = 135$ MeV.

of $r = 0$, and $r = 0.4$, usually considered for applications to heavy ion collisions [204, 327].

Figure 5.6 shows the scalar curvature R evaluated by EQ. (A.81). The black curves are based on lattice data with the condition $n_S = n_Q = 0$ (or equivalent for the isospin symmetric limit), whereas the red ones are for $n_S = 0$ and $n_Q/n_B = 0.4$. The continuous lines are for $\mu_B = 0$ MeV, the dashed ones for $\mu_B = 80$ MeV and the dotted lines for $\mu_B = 135$ MeV.

As one can see in Figure 5.6, R is positive (like for repulsive systems) for temperature well above the transition one, and becomes negative around the transition. In the language of thermodynamic geometry this means that at high temperature the system is dominated by fermionic degree of freedom, like happen in the quark gluon plasma, which effective d.o.f. are [329]

$$g_{eff} = g_g + g_f \ , \tag{5.46}$$

with

$$g_g = 8 \times 2 = 16 \tag{5.47}$$

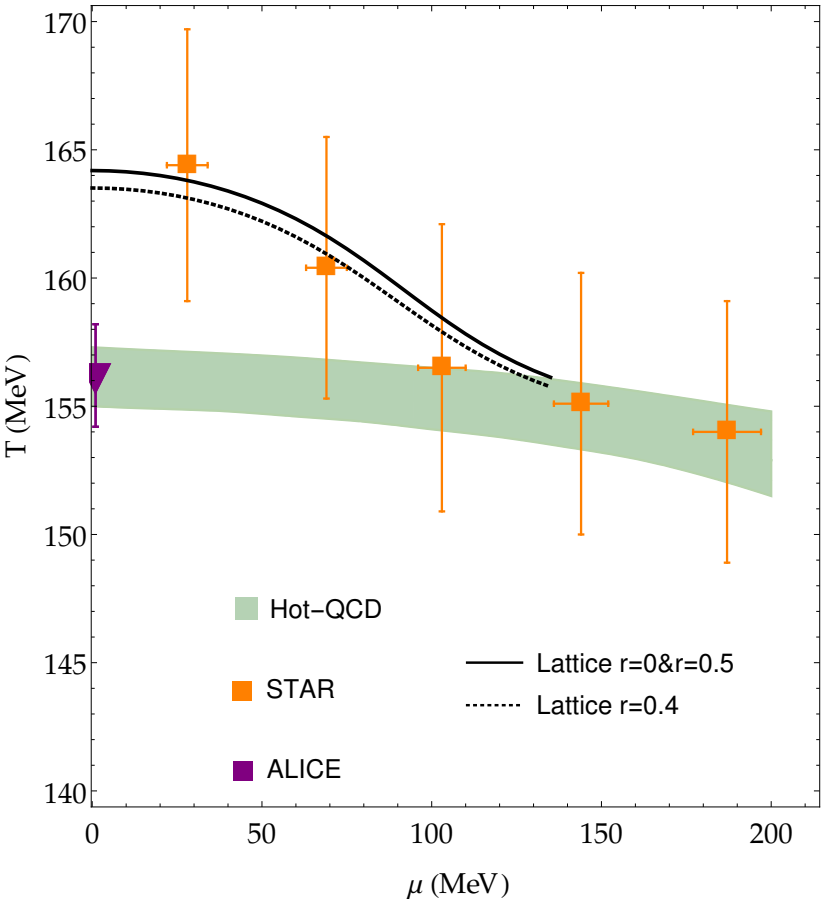

Figure 5.7: The crossing temperature evaluated by $R = 0$, both for $n_Q = n_S = 0$ (continuous black line) and for $n_S = 0$ and $n_Q/n_B = 0.4$ (black dotted line), compared with lattice data (light-blu-gray band) and the results of the freeze out temperature from ALICE (purple point [330]) and STAR (orange points [168, 331]) collaborations.

for gluons (8 colors and 2 spin states) and at least

$$g_f = \frac{7}{8} \times 2 \times 2 \times 2 \times 3 = 21 \tag{5.48}$$

(3 colors, 2 spins, 2 flavors, q and $\bar{q}$) for fermions.

A reduction in temperature leads to a change in the sign of R, and this can happen for two reasons:

1. on the one hand, R is negative for attractive interaction between the system components, and it is true at phase transitions, since to form quark condensates one needs an attractive interaction;

2. on the other hand, R is negative for an ideal gas of bosons, and also this condition can describe the hadronization process at zero chemical potential, in which a transition from a fermionic dominated system (QGP) to one dominated by mesons, and therefore by bosonic d.o.f., occurs.

The criterion $R = 0$ has been applied and the resulting line is reported in Fig. 5.7 and compared with lattice results on the critical temperature deduced by chiral susceptibility [204, 328] (green band) and the freeze-out temperature obtained by ALICE [330] (purple point) and STAR [168, 331] collaborations (orange points). The continuous black curve is from lattice data obtained by the condition $n_S = n_Q = 0$, while the dotted black one is for $n_S = 0$ and $n_Q/n_B = 0.4$ (n_S, n_Q, n_B being the strangeness, charge and baryon number densities respectively), following the procedure of Ref. [204, 328] where n_Q is considered as a function of μ_B. The calculation based on the $R = 0$ criterion agrees with lattice QCD results within 10%.

5.3.2 Hadron Resonance Gas models

Although HRG models do not foresee phase transitions, a study of the scalar curvature is still useful to see how R changes by adding interactions of different nature. In Section 3.2 generalizations of the ideal HRG model have been dealt, and for comparison with the QCD calculations in Sec. 5.3.1, one evaluates the series expansion in γ^2 of the pressure in the different HRG models, and the temperature obtained by applying the criterion $R = 0$ turns out to be in agreement with the QCD deconfinement temperature.

We have considered three different HRG models:

- the ideal HRG model of point-like constituents is studied by EQ. (3.25) in the Boltzmann approximation (i.e. all baryon number susceptibili-

	a $\left(\text{MeV fm}^3\right)$	b $\left(\text{fm}^3\right)$
VdW	329	3.42
Clausius-CS	423	2.80

Table 5.1: The values of the parameter used in Eqs. (3.43) and (3.44) [218, 219].

ties are identical, $\chi^H_{2k} = \chi^H_2 = 2\ P^H_B\ \beta^4$) to obtain

$$P^H(\beta,\gamma) \simeq P^H_0(\beta) + \frac{\chi^H_2(\beta)}{\beta^4} \sum_{n=1}^{\infty} \frac{\gamma^{2n}}{(2n)!} \tag{5.49}$$

and the coefficients of the thermodynamical potential for the hadronic (H) sector are given by

$$\begin{aligned} A^H =& P^H_0\ \beta\ , \\ B^H =& \frac{\chi^H_2}{\beta^3}\ , \\ C^H =& \frac{2\ B^H}{4!}\ , \\ D^H =& \frac{2\ B^H}{6!}\ . \end{aligned} \tag{5.50}$$

- attractive and repulsive interactions are included by Eqs. (3.45), (3.36) and (3.37) and different compressibility factor.
  - the Clausius-CS-HRG model, where the repulsive excluded volume interaction is give by the Carnahan-Starling term (see EQ. (3.42)) and the attractive one by the Clausius form (See EQ. (3.44));
  - the VdW-HRG model which describes a gas of hadrons and resonances where, repulsive and attractive, interactions follow the standard VdW equation (Eqs. (3.41) and (3.43)).

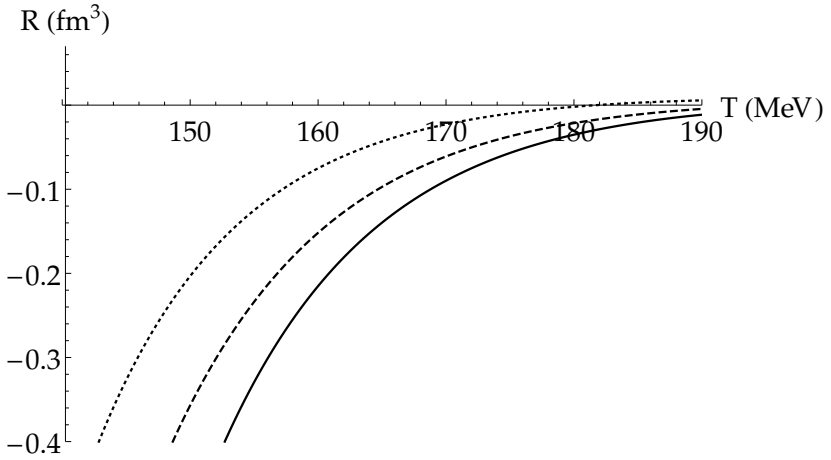

Figure 5.8: The scalar curvature R for the ideal HRG model (Eqs. (5.49, 5.50) and different values of the baryonchemical potential, $\mu = 0$ MeV (continuous lines), $\mu_B = 80$ MeV (dotted lines) and $\mu_B = 135$ MeV (dashed lines), obtained by the expansion of EQ. (A.81) at the 4-th order.

In all previous models: a) only baryon-baryon (anti-baryon - anti-baryon) interactions have been included, neglecting the other ones; b) mesons are considered point-like; c) the parameters a and b to describe all (anti)baryons are assumed to be equal to those of nucleons and are fixed by the nuclear matter properties [218, 219] (see Tab. 5.1); d) all strange and non-strange hadrons in the Particle Data Table have been included with the exception of σ and κ mesons (see [216, 332] for details).

In Fig. 5.8 is plotted the scalar curvature R for the ideal HRG model (Eqs. (5.49, 5.50 and (A.81-A.84)) and different values of the baryonchemical potential: $\mu_B = 0$ MeV (continuous lines), $\mu_B = 80$ MeV (dotted lines) and $\mu_B = 135$ MeV (dashed lines), obtained by the expansion of EQ. (A.81) at order γ^4. Around the pseudo-transition temperature of the QCD crossover, R si negative as expected for a bosonic gas.

Figure 5.9 shows the scalar curvature R for different HRG models at $\mu = 0$, ideal HRG (black continuous curve), Clausius-CS-HRG model (dashed curve) and the VdW-HRG model (dotted curve), compared with the LQCD one (continuous gray curve). The presence of repulsive/attractive interac-

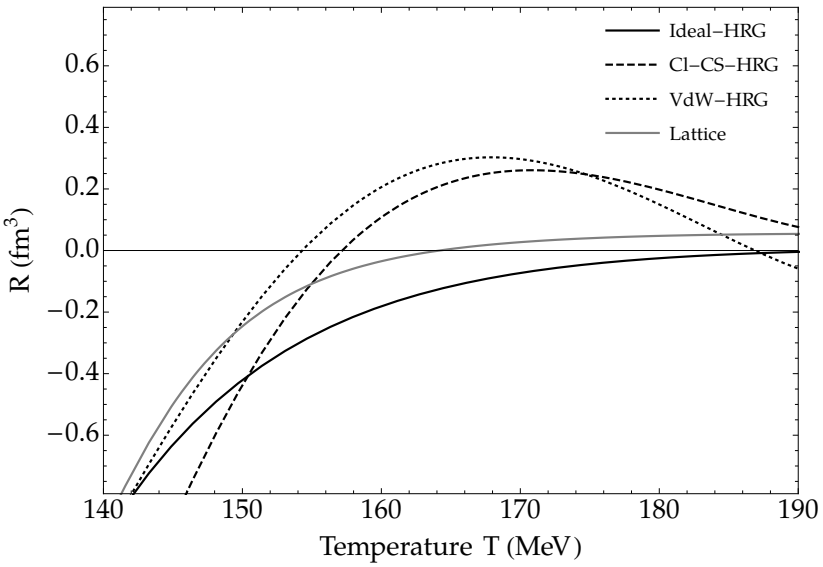

Figure 5.9: The scalar curvature R for different HRG models at $\mu = 0$, ideal HRG (black continuous curve), Clausius-CS-HRG model (dashed curve) and the VdW-HRG model (dotted curve), compared with the LQCD one (continuous gray curve).

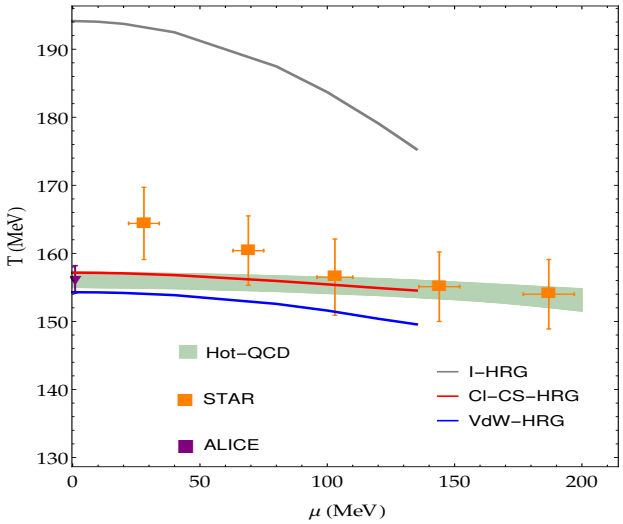

Figure 5.10: The temperature from the $R = 0$-criterion obtained from the ideal-HRG model (gray curve), the Clausius-CS-HRG model (red curve) and the VdW-HRG model (blue curve). The band is for lattice results [204, 328], orange points are for the freeze-out temperature [168, 330, 331].

tions modify the shape of the scalar, particularly changing the temperature at which $R = 0$.

In Figure 5.10 are plotted the temperature from the $R = 0$-criterion for the three considered HRG-like models.

5.3.3 Comments and Conclusions

The introduction of a thermodynamic metric and the calculation of the corresponding scalar curvature, R, is a useful tool to estimate the deconfinement temperature. Figure 5.11 shows the temperature obtained via the criterion $R = 0$ in the CS-Clausius-HRG model (red curve) and in the VdW-HRG (blue curve), compared with that from lattice QCD (black curves). The results, obtained by the criterion $R = 0$ on the quark-gluon plasma phase, are in good agreement with lattice data and freeze-out calculations in the low density region. The same criterion applied in the confined phase, described by different HRG models, give a "critical" line and the result is completely consistent with Lattice QCD data if the hadron excluded volume

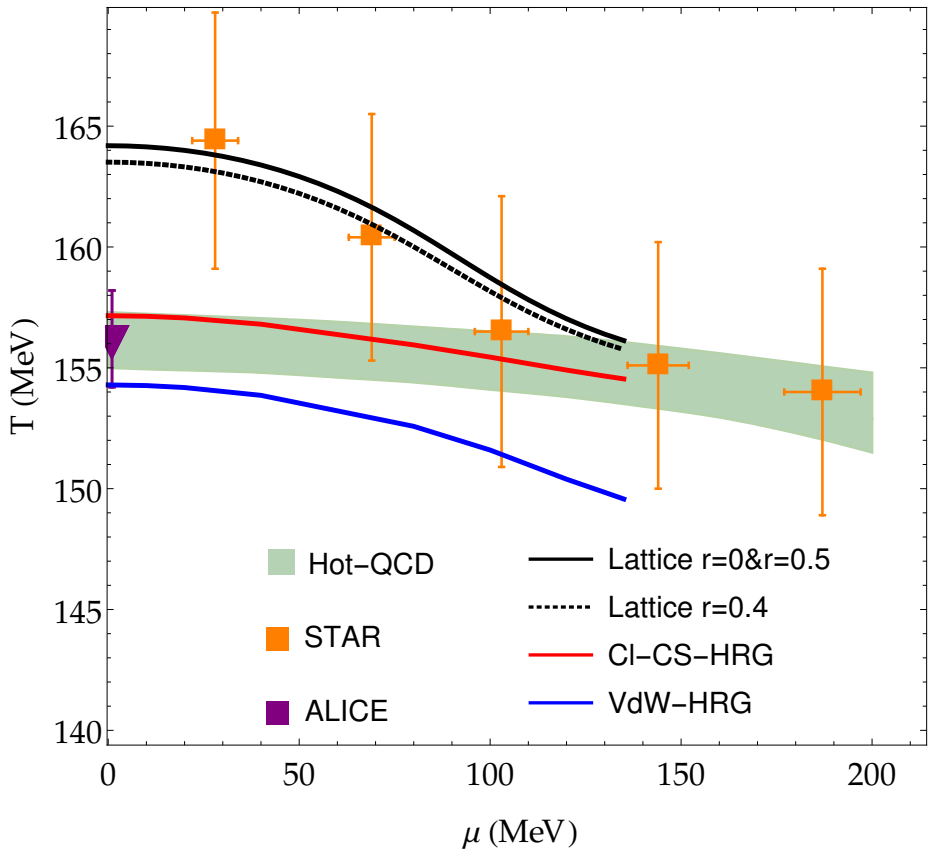

Figure 5.11: The temperature in the CS-Clausius-HRG model (red curve), in the VdW-HRG model (blue curve) and from lattice data (black curves), compared with lattice results on the critical temperature deduced by chiral susceptibility [204, 328] (light-blu-gray band) and the freeze-out temperature obtained by ALICE [330] (purple point) and STAR [168, 331] collaborations (orange points).

and the interaction effects are taken into account. The approch has been applied for small baryon density since it requires a reliable evaluation of the thermodynamic potential ϕ. However the geometrical approach is quite general and the calculations at large baryon density can be analytically done once ϕ is known.

However, the $R = 0$ line identifies a transition between a fermionic system to one dominated by bosonic d.o.f., and it is not clear if it identify the deconfining. Different in the two temperatures have a possible interpretation if one recalls that, since the deconfinement transition is a cross-over, one can expect remnants of confinement slightly above T_c. Indeed the persistence of string-like objects above T_c has been obtained by many different methods: lattice simulations [333, 334], quasiparticle approach [335, 336], NJL correlator [337, 338], Mott transitions [339] and confinement mechanisms [340]. Following this interpretation, while T_c is the deconfinement temperature, that obtained via $R = 0$ is the one of the complete melting of a light meson. However this is model dependent, because we used specific models of the HRG. The introduction of other dynamical details, like the excluded volume, changes the HRG evaluation of R, by including some effective repulsive interaction similar to Fermi statistic effects and then closing, in part, the gap with the value of R for a fermionic system.

Finally an important aspect of thermodynamic geometry has to be clarified: the evaluation of the scalar curvature R involves derivatives up to third order with respect to the thermodynamic variables, T and μ, of the potential ϕ and, therefore, the criterion $R = 0$ is a constraint on high order derivatives of the thermodynamic quantity P/T. From this point of view, if the dynamical system has a phase transition or a strong crossover, one can expect that the results obtained by the thermodynamic geometry approach merely reproduce the standard statistical thermodynamics ones, because some derivative diverges or some specific quantity (as the chiral susceptibility) has a strong peak at the critical temperature, then "driving" the condition $R = 0$. However the previous results in the HRG approach show that this is not the case. Indeed in the HRG models there is no phase transition and the constraint $R = 0$ gives clear information on the dynamical balance between the effective interactions. In fact, the curve $T(\mu)$ which turns out by the criterion $R = 0$ depends on the specific model and lattice data on T_c are reproduced when the various interactions have a spe-

cific relative weights. In this respect, thermodynamic geometry is a useful complementary method to the standard thermodynamical approach since it takes into account the effective dynamics, independently on the presence of a phase transition.

5.4 Results from models

5.4.1 Nambu - Jona Lasinio model

In this section we apply the thermodynamic geometry to the study of chiral restoration in Nambu - Jona Lasinio (NJL) model, that was recalled in Sec. 3.3, where we have described the two and three flavor version of the model.

The study of the critical line of the symmetry restoration, $T(\mu)$, by thermodynamic geometry requires the, straightforward but laborious, calculation of the scalar curvature R, reported in appendix A.2.1.

Two flavor in the chiral limit

Let us start to discuss the chiral limit (i.e. $m = 0$) for two flavors: it turns out that $|R|$ diverges at the critical temperature, i.e. there is a second order phase transition, for $\mu < \mu^\star \simeq 290$ MeV, as shown in Fig. 5.12 for $\mu = 0$. For $\mu > \mu^\star$ there is, instead, a first order phase transition. The dynamically generated mass, M, now takes the characteristic behavior plotted in Figure 5.13, where the black curves (both the continuous and the dotted) are for $T = 30$ MeV and the two light-gray lines define the spinodal points. Between the two spinodal (light-gray) lines one can evaluate three different scalar curvatures: the first one for the higher-mass branch (black curve in Figure 5.13); the second one for $M = 0$ MeV and the last one is related to the M-branch that interpolates between $M = 0$ and the upper M-curve (dotted curve in Figure 5.13). At fixed temperature and between the spinodal lines (see Fig. 5.13), there is a discontinuity in $|R|$ which identifies the two dashed curves in Fig. 5.14. The crossing temperature from the I order phase transition to the II order turns out to be about 58 MeV.

For small μ and near the transition the curvature is negative, i.e. the

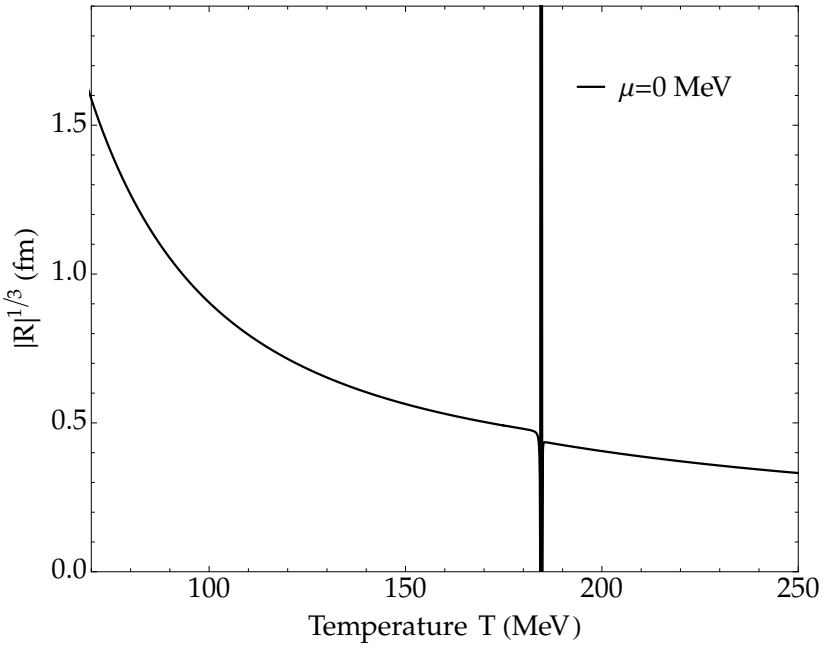

Figure 5.12: R from $\mu = 0$ MeV: second order phase transition.

interaction is mostly attractive, suggesting that the chiral symmetry restoration is due to thermal fluctuations. On the other hand, at large chemical potential R turns out to be positive, indicating a screening of the potential. The complete critical line obtained by thermodynamic geometry is depicted in Figure 5.14 where the continuous line shows the II order phase transition and the dashed lines the spinodal curves of the first order one. The green band is the region of negative R.

Two flavors with chiral masses

With finite chiral quark masses, at high temperature and low chemical potential, there is a smooth crossover rather than a second-order phase transition. Moreover, the first-order phase boundary ends in a second-order endpoint [23]. The solution of the gap equation (3.56) (with $\Lambda = 650$ MeV and $G = 5.01 \times 10^{-6}$ MeV^{-2} and $m_0 = 5.5$ MeV) as a function of T and μ is shown in Figs. 3.3.a and 3.3.b.

To clarify the effect of the chiral mass in the calculation of the scalar

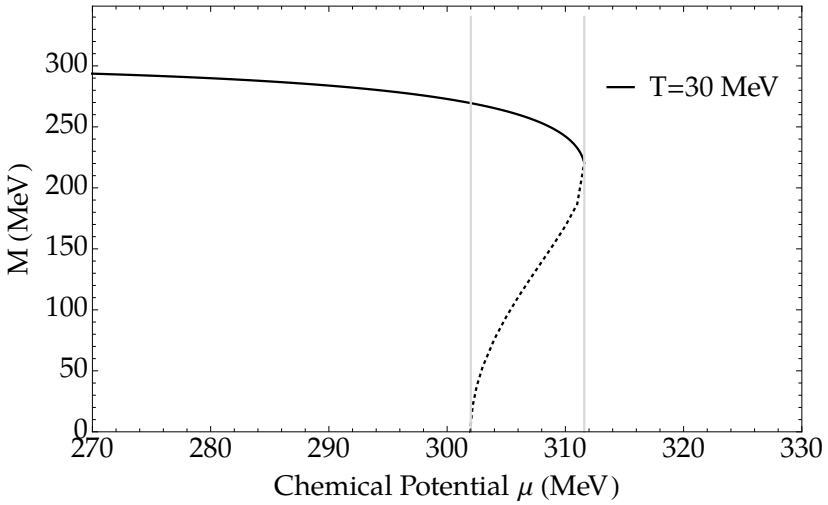

Figure 5.13: The dynamically generated mass M in the 2 flavors NJL chiral model and temperature $T = 30$ MeV.

curvature, Fig. 5.15 shows that R diverges in the chiral limit but for $m_0 \neq 0$, near the transition temperature, it has a minimum, corresponding to a maximum of $|R|$, i.e. to a finite correlation length. Therefore, $m_0 \neq 0$ changes the behavior of R near the critical temperature: the divergence of the II order phase transition turns into a minimum in the negative R region and the transition temperature evaluated by the maximum of $|R|$ is completely in agreement with that one obtained by chiral susceptibility (see EQ. (A.29) in appendix A.2.1).

For low temperature and large chemical potential, the scalar curvature R has the same behavior previously discussed in the chiral limit, i.e. a first order phase transition. The critical point, $(T^\star, \mu^\star)$ between the crossover and the first order phase transition depends on m_0 and for (the generally accepted value) $m_0 = 5.5$ MeV one has $\mu^\star \simeq 329$ MeV and $T^\star \sim 32$ MeV.

Figure 5.16 shows the critical line for $m_0 = 5.5$ MeV: the continuous line is obtained by the maximum of $|R|$ and the dashed ones are the spinodal curves. The black circle is at $\mu^\star = 329$ MeV and $T^\star = 32$ MeV. The green band is the region of $R < 0$.

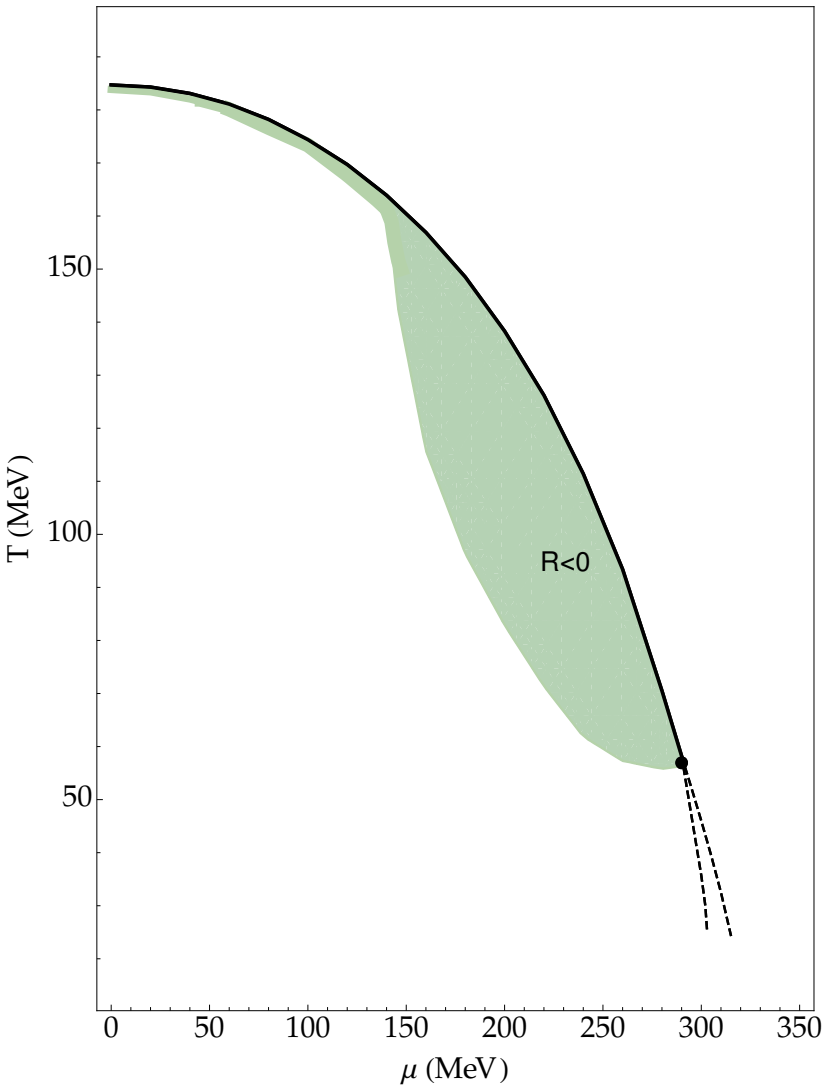

Figure 5.14: The transition temperature: continuous line is for II order phase transition and the dashed ones for the first order one. The transition point is at $\mu_\chi^\star = 290$ MeV and $T_\chi^\star = 58$ MeV. The green band is the region of $R < 0$

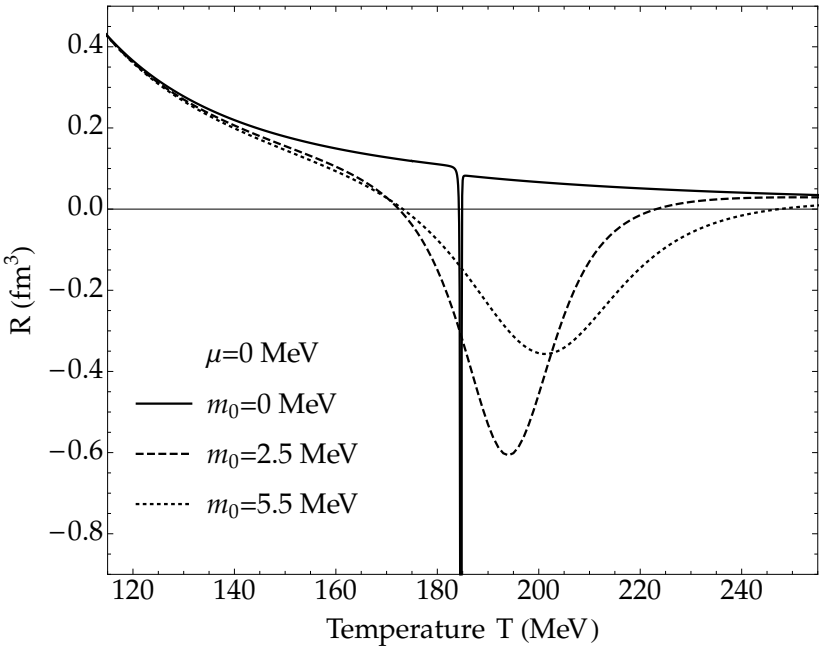

Figure 5.15: R from $\mu = 0$ MeV and different values of the bare mass m_0: continuous line is from $m_0 = 0$ MeV (the chiral limit) and R shows a negative divergence. Dashed line is from $m_0 = 2.5$ MeV and the dotted from $m_0 = 5.5$ MeV; both show a finite region with negative R around the transition temperature, which corresponds to the local maximum of $|R|$.

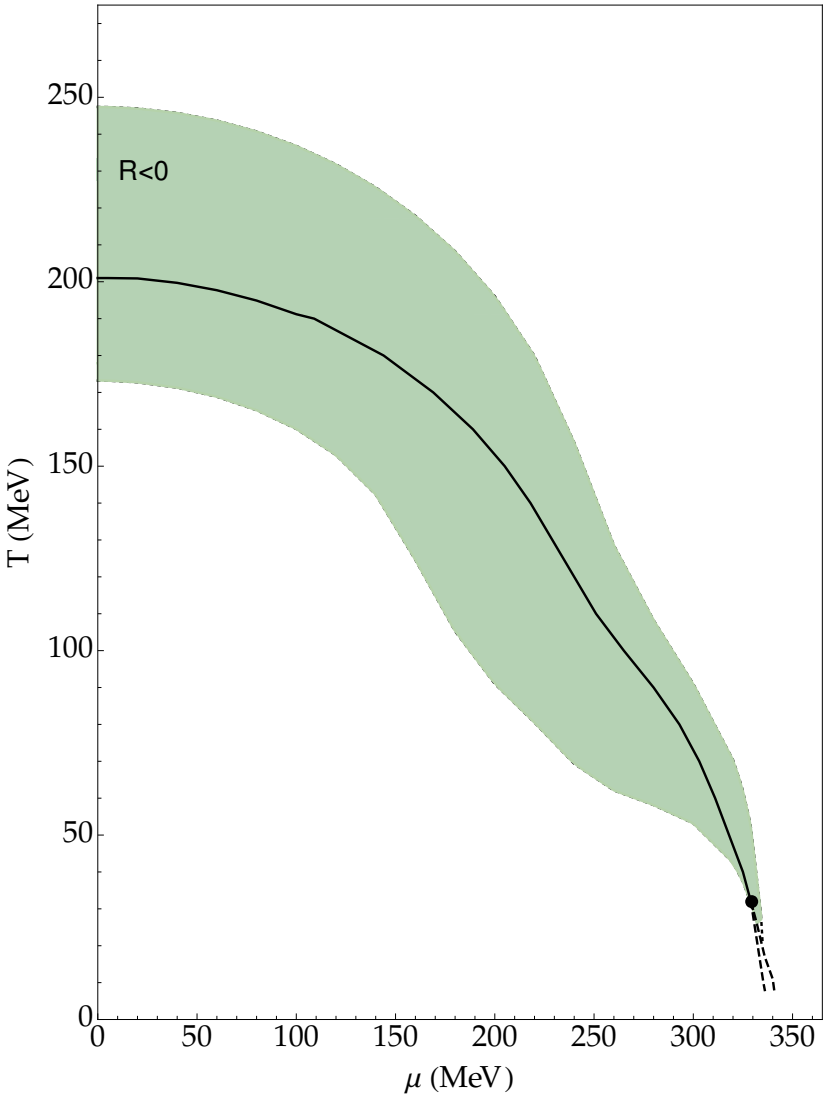

Figure 5.16: The transition temperature by the R conditions and from $m_0 = 5.5$ MeV: continuous line is obtained by the local maximum of $|R|$, the dashed ones indicate the spinodal lines. The circle is at $\mu^\star = 329$ MeV and $T^\star = 32$ MeV. The green band is the region of $R < 0$.

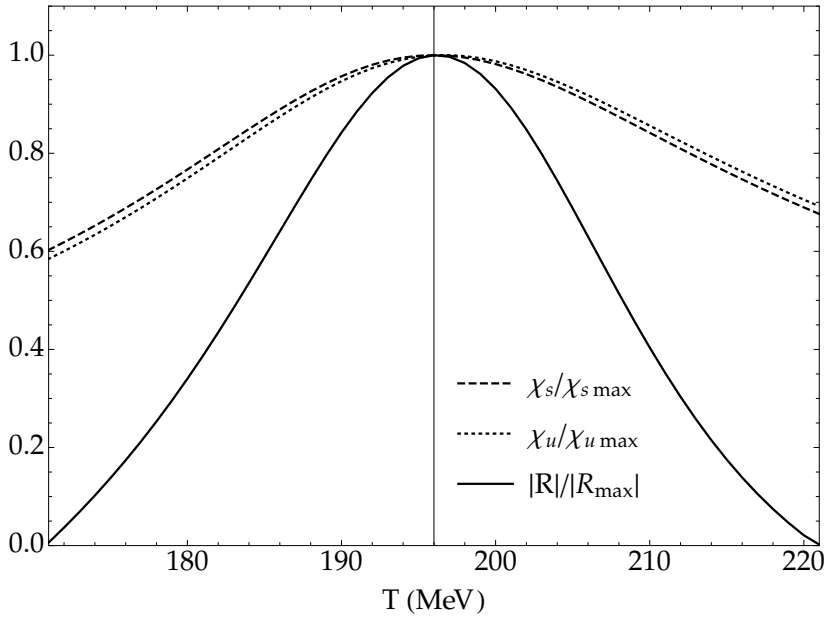

Figure 5.17: The ratio χ_s/χ_{smax} (dashed line), χ_u/χ_{umax} (dotted line) and $|R|/|R|_{max}$ (continuous line) at $\mu = 0$ MeV.

Three flavors

Three flavor NJL model is studied with only one chemical potential ($\mu = \mu_d = \mu_u$, $\mu_s = 0$). Also in this case there is a crossover at low chemical potential and large T and a first order phase transition at low temperature and large μ. The behavior of the scalar curvature is essentially the same of the previous case with two flavors and physical masses.

In Figure 5.17 the ratios χ_s/χ_{smax} (dashed line), χ_u/χ_{umax} (dotted line) and $|R|/|R|_{max}$ (continuous line) are depicted to visualize that the maximum in $|R|$ corresponds to the peak of chiral susceptibilities.

Figure 5.18 shows the transition temperature by the evaluation of R: the continuous line is again obtained by the maximum of $|R|$ and the dashed ones are the spinodal curves. The black circle is at $\mu^\star \sim 335$ MeV and $T^\star \sim 35$ MeV. The green band is the region of negative R.

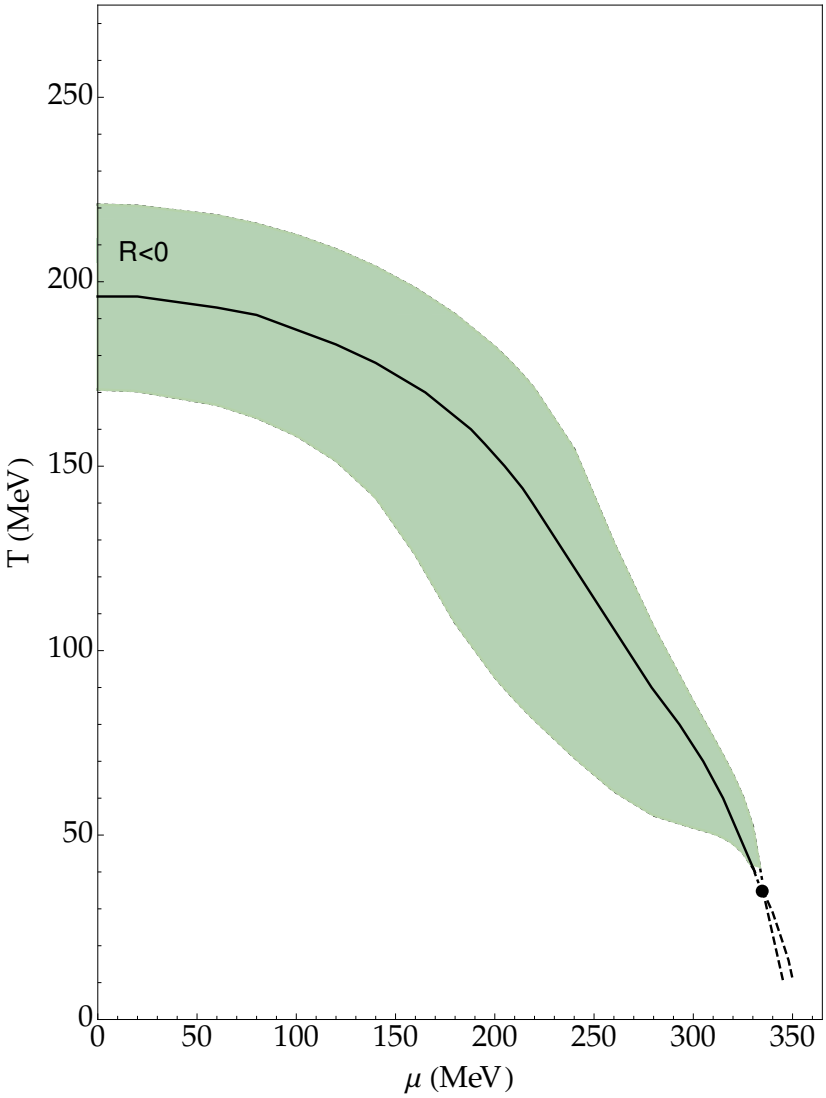

Figure 5.18: The transition temperature by the R conditions: continuous line is obtained by the local maximum of $|R|$, the dashed ones indicate the spinodal lines. The circle is at $\mu^\star \sim 335$ MeV and $T^\star \sim 35$ MeV.The green band is the region of $R < 0$

Thermal geometric definition of the phase transitions in NJL model: summary

It is useful to conclude this section by summarizing the geometrical definition of the phase transitions:

- a II order phase transition occurs for two flavors in the chiral limit ($m = 0$) at low chemical potential. This transition is characterized by a divergent scalar curvature;
- for chiral masses, there is a crossover, both for two and three flavors, at low chemical potential and large T. The transition temperature is defined as the maximum of $|R|$ in the negative-R region and it is in agreement with the chiral susceptibility analysis χ [261] (eqs. (A.29), (A.70) and (A.71) in appendix);
- there exists a I order phase transition at low temperature and large μ, both with two and three flavors and both in the chiral limit or with chiral masses. This transition is related with a discontinuity in R.

Finally, a comment on the sign of the scalar curvature is in order.

The scalar curvature brings information on the statistical natural of the particles and on the dynamical interactions. The region with $R < 0$ in Figs. 5.14, 5.15, 5.16 and 5.18 indicates that the balance between NJL attractive interactions and statistical effects is dominated by the former. On the other hand, Fermi statistics is always part of the dynamics and, at large μ, the statistical effects turn out to be more and more relevant, suggesting $R > 0$ as in a Fermi gas in thermodynamic geometry.

Comments and Conclusions

Thermodynamic geometry has been applied to a (although not renormalizable) field theory, with ab-initio calculations. The phase diagram in NJL model has been evaluated on the basis of the thermodynamic metric and of the corresponding scalar curvature, R, which contains not only the second derivatives but also higher order and mixed derivatives (up to third order). The "sensitivity" to the phase transition, naturally contained in the cumulants, does not automatically imply that the quantitative results are

reliable: only after carrying out our specific calculations one can state if the method of thermodynamic geometry could be a useful tool for future analyses in field theory at finite temperature and density.

Our results show that thermodynamic geometry reliably describes the phase diagram of NJL model, both in the chiral limit and for finite mass, and indicates a geometrical interplay between chiral symmetry restoration/breaking and deconfinement/confinement regimes.

5.4.2 Quark-Meson model

Finally, in this section we study the thermodynamic scalar curvature around the chiral phase transition at finite temperature and chemical potential, within the quark-meson model augmented with meson fluctuations (see Sec. 3.4).

The thermodynamic curvature

In Fig. 5.19 we plot the scalar curvature, R, versus temperature for three values of the quark chemical potential: the upper panel corresponds to the case without fluctuations, the lower panel to that with fluctuations. We notice that in both cases, R develops a peak structure around the chiral crossover, in agreement with the results from NJL model [341] (see Sec. 5.4.1) and from QM model without meson fluctuations [342]. This is expected thanks to the relation between R and the correlation volume around a phase transition: as a matter of fact, at a second order phase transition R diverges due to the divergence of the correlation volume, while at a crossover the correlation length increases but remains finite and susceptibilities are enhanced so R is expected to grow up in the pseudocritical region. Therefore, the thermodynamic curvature can bring information about the correlation volume also near a crossover.

In addition to this, we find that at small μ the peaks of R are more pronounced when the fluctuations are included. This is an interesting, new observation about the thermodynamic geometry and is related to the fact that fluctuations make the chiral broken phase more unstable. This can be seen from the determinant of the thermodynamic metric, g, see Fig. 5.20: at small μ in the critical region the determinant with fluctuations is smaller

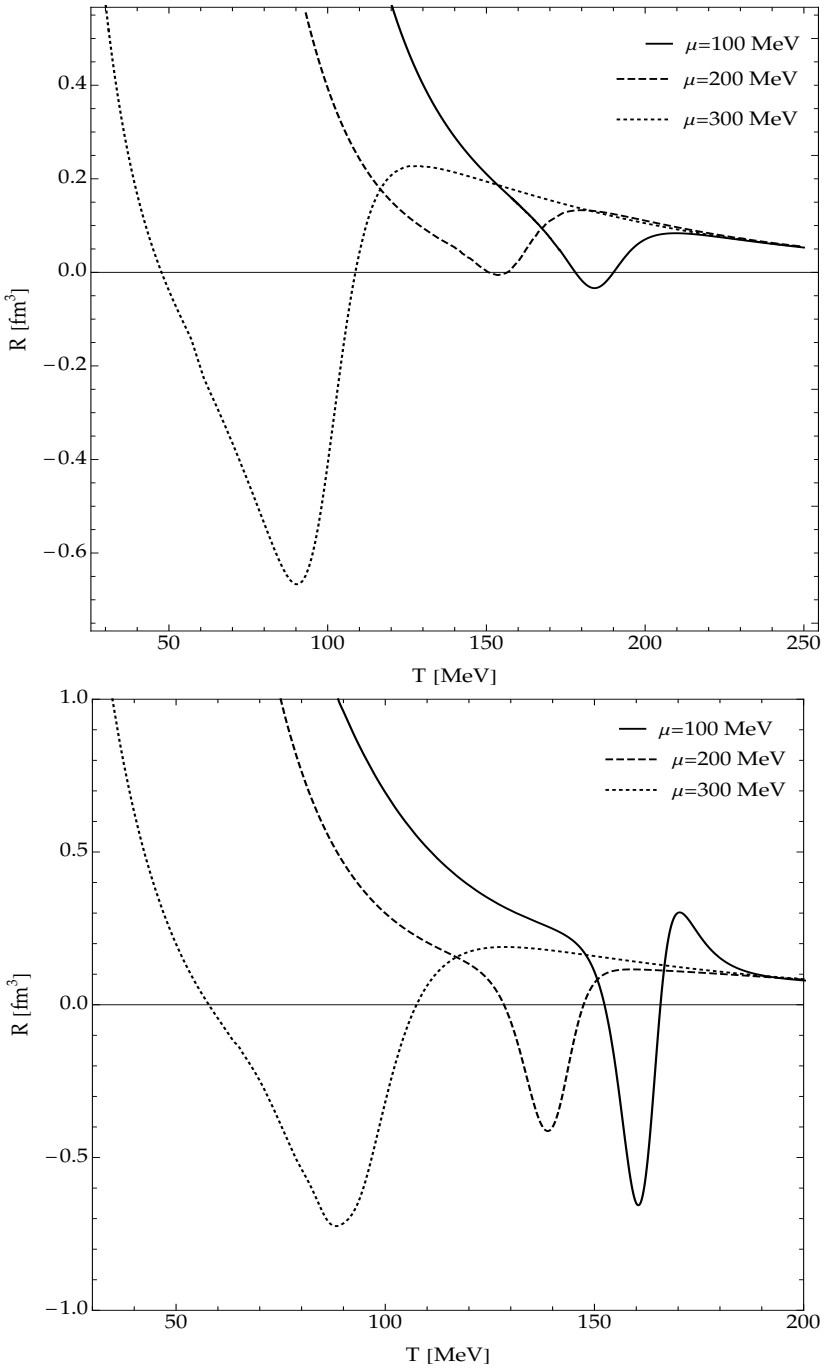

Figure 5.19: Scalar curvature, R, as a function of T for $\mu = 100$ MeV (continuous), $\mu = 200$ MeV (dashed) and $\mu = 300$ MeV (dotted). Upper and lower panels correspond to the cases without and with mesonic fluctuations.

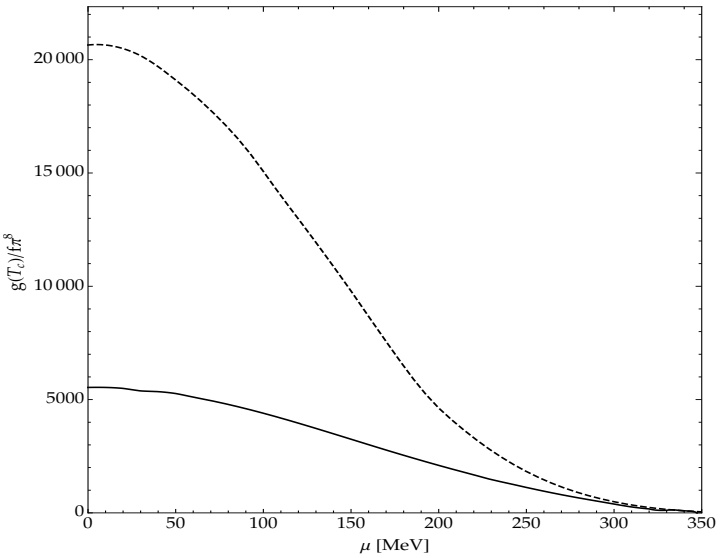

Figure 5.20: Determinant of the thermodynamic metric versus μ computed at the chiral crossover temperature: solid line corresponds to the case with fluctuations while dashed line to the mean field thermodynamics.

than the one without fluctuations ($g = 0$ corresponds to thermodynamic instability and infinite curvature), while increasing μ the determinant in the critical region is not very affected by the presence of the fluctuations. This is in line with the results of the pressure in Fig. 3.5 in which we show that fluctuations do not give a substantial contribution in the critical region at large μ. When μ is increased, R is enhanced in the critical region both with and without fluctuations. This is most likely related to the fact that the critical endpoint with the second order phase transition and the divergent correlation length already appears within the mean field approximation, so the main role of the fluctuations is that to change the critical exponents but not to change the phase structure.

The scalar curvature changes sign around the crossover, both with and without fluctuations: this is in agreement with the results from NJL model (Sec. 5.4.1), but also from LATTICE and HRG models (Sec. 5.3), and can be interpreted as a rearrangement of the collective interactions in the hot medium around the chiral crossover, from statistically repulsive (due to the fermionic nature of the bulk) to attractive. This piece of information was

not accessible to previous model calculations on the QCD phase diagram and represents a merit of the thermodynamic geometry.

The critical temperature and the endpoint

The crossover nature of the transition to the chiral symmetric phase at high temperature leaves an ambiguity on the definition of a critical temperature: in fact, it is possible to adopt several definitions to identify the critical region, in which the order parameter decreases substantially. We compare the predictions of the model using four different definitions. Firstly, we define the pseudocritical temperature, $T_c(\mu)$, as the temperature corresponding to the maximum of $\partial\sigma/\partial\beta$ (which coincides with the maximum of $\partial\sigma/\partial\gamma$). A second definition is the temperature at which $\partial M_\sigma/\partial\beta$ is maximum (the same of $\partial M_\sigma/\partial\gamma$). Thirdly, we can define T_c as the one at which M_σ is minimum (since at this temperature the correlation length of the fluctuations of the order parameter is the largest). Finally, the peculiar structure of $R = R(T)$ at a given μ allows for the fourth definition, namely the temperature at which R presents its local minimum.

In Fig. 5.21 we show T_c versus μ obtained with the four definitions. We notice that the different definitions give consistent results with each other. This supports the idea that we can use the peaks of R to identify the chiral crossover, which in turn suggests that R is sensitive to the crossover from the broken to the unbroken phase even though this is not a real second order phase transition.

In the phase diagram shown in Fig. 5.21 the crossover line terminates at a critical endpoint, CEP, located at $(\mu_{\rm CEP}, T_{\rm CEP}) = (350\ {\rm MeV}, 30\ {\rm MeV})$. Approaching this point along the critical line, the crossover turns into a second order phase transition with divergent susceptibilities, then the transition becomes first order with jumps of the condensate across the transition line.

In Fig. 5.22 we plot R versus temperature for values of μ close to the critical endpoint: upper and lower panels correspond to the results without and with fluctuations respectively. As expected, approaching the critical endpoint the magnitude of the peak value of R becomes larger, as it should be since the crossover becomes a second order phase transition there and R should diverge at the CEP.

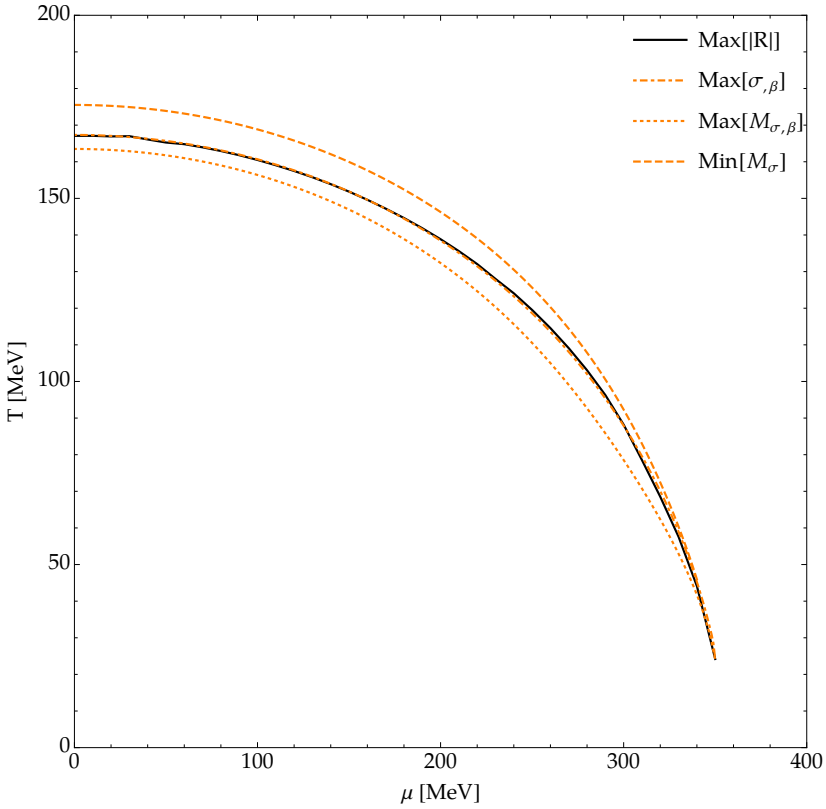

Figure 5.21: Crossover temperature versus μ obtained with four definitions: from the maximum of $M_{\sigma,\beta}$ (orange dotted line), from the maximum of $\sigma_{,\beta}$ (orange dot-dashed line), from the minimum of M_σ (orange dashed line) and from the peak of R (black line). Case with mesonic fluctuations.

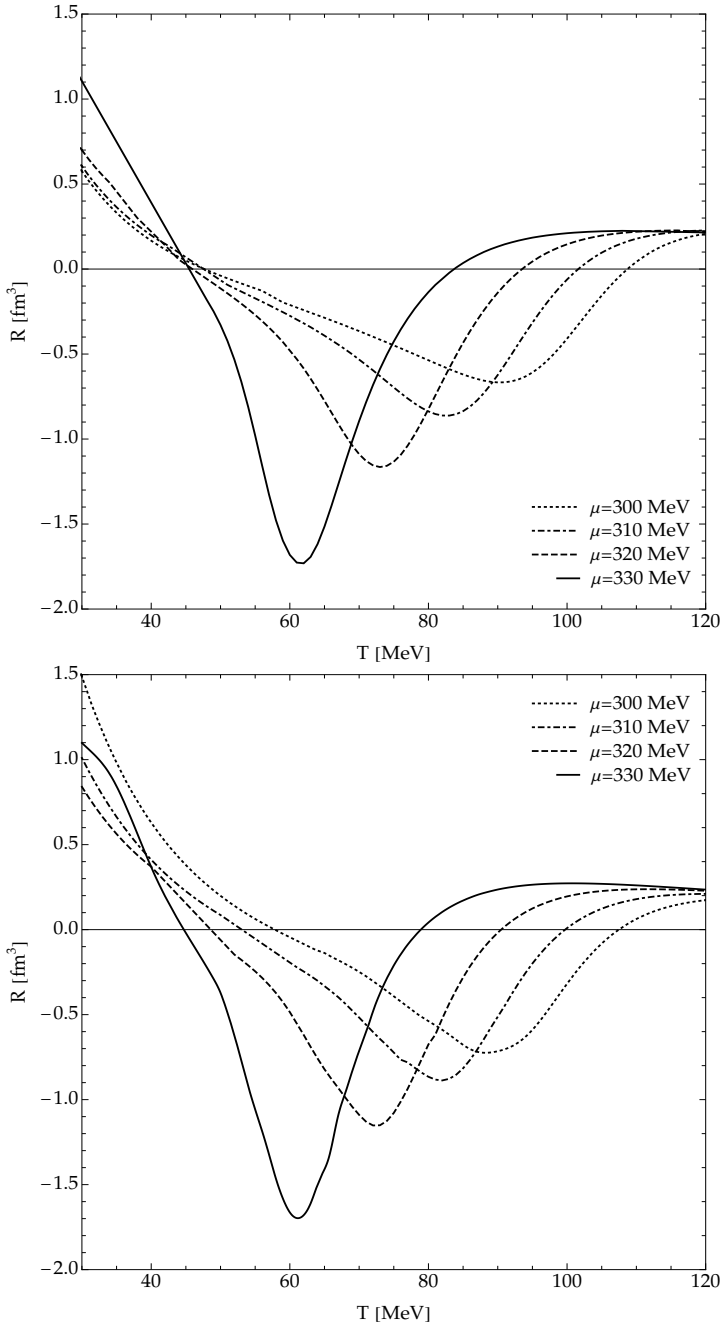

Figure 5.22: Thermodynamic curvature versus temperature for several values of μ close to the critical endpoint. Upper and lower panels correspond to the cases without and with mesonic fluctuations.

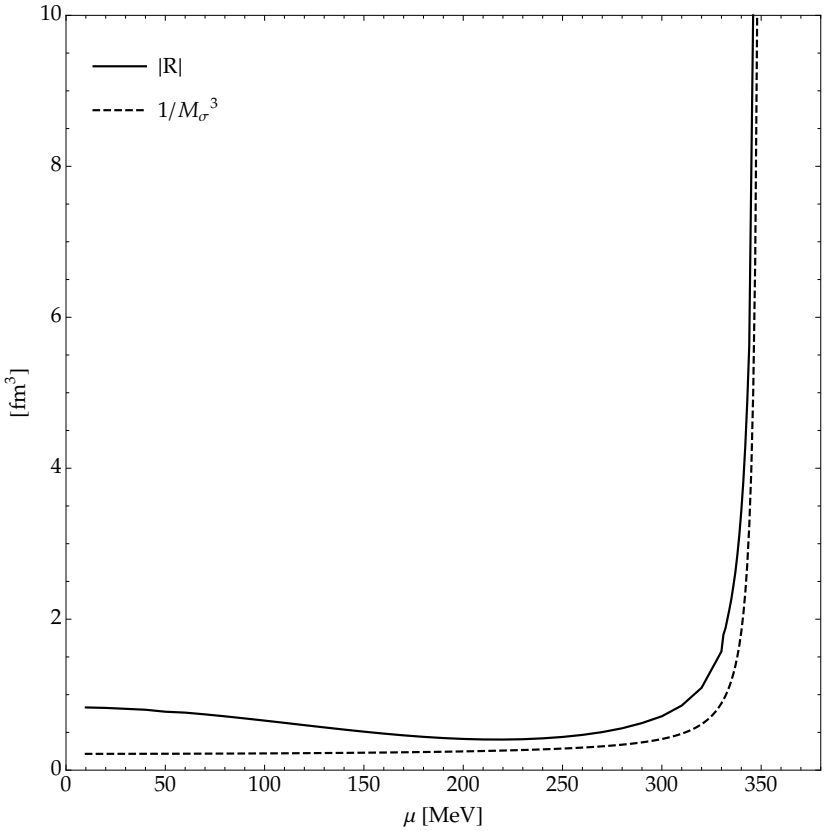

Figure 5.23: Thermodynamic curvature versus μ at the critical line, compared with the inverse of the correlation volume $1/M_\sigma^3$. Case with mesonic fluctuations.

Thermodynamic curvature and correlation volume

It is interesting to compare the thermodynamic curvature around the critical line, with the correlation volume ξ^3, where ξ is the correlation length. This comparison is interesting since according to hyperscaling arguments, around a second order phase transition $|R| = K\xi^3$ with K of the order of unity; restoration of chiral symmetry is a crossover rather than a real phase transition, at least far from the critical endpoint, therefore we can check how the hyperscaling relation works around such a smooth crossover and how it changes approaching the CEP.

In Fig. 5.23 we compare the thermodynamic curvature, computed along the critical line, with the correlation volume, the latter being estimated by taking $\xi = 1/M_\sigma$ as a measure of the correlation length of the fluctuations of the order parameter. We find that both the correlation volume and the thermodynamic curvature behave qualitatively in the same way near the CEP; moreover, the numerical values of the two quantities is comparable in the critical region. We conclude that our study supports the idea that $|R| = K\xi^3$ in proximity of the second order phase transition.

In the small μ regime the relation between the curvature and the correlation volume does not need to be satisfied since in this regime the critical line is a smooth crossover. In fact, we find that for small values of μ the agreement between $|R|$ and ξ^3 is not as striking as the one in proximity of the CEP; nevertheless, we still find that the two quantities behave qualitatively in the same way, namely they stay approximately constant for a broad range of μ then grow up as the CEP is reached.

Comments and Conclusions

In this section we have studied the effect of the fluctuations, pions and $\sigma-$meson, on the top of the mean field thermodynamics and how these affect the thermodynamic curvature around the crossover. Fluctuations have been introduced within the Cornwall-Jackiw-Toumbulis effective potential formalism [260] in the Hartree approximation; we have neglected the zero point energy contributions of the meson fields, both for the sake of simplicity and to avoid the unexpected behavior of thermodynamic quantities when these are included and two renormalization scales are needed [259].

We have found that in the region of small values of μ, the fluctuations enhance the magnitude of the curvature. We understand this in terms of the stability of the phase with broken chiral symmetry, that can be analyzed by the determinant of the metric, g: in fact, the condition of stability reads $g > 0$ while $g = 0$ corresponds to a phase boundary where a phase transition happens and R diverges, so the smaller the g the closer the system is at a phase transition and the larger is R. We have found that the determinant with fluctuations and around the crossover is smaller than g without fluctuations in the same range of T and μ, meaning that fluctuations make the chiral broken phase less stable. This result is expected, since fluctuations

of the order parameter represented by the $\sigma-$meson tend to wash out the $\sigma-$condensate.

On the other hand, at larger values of μ and in proximity of the critical endpoint, the fluctuations do not bring significant changes to the mean field solution around the critical line and R is less sensitive to the fluctuations. This is also easy to understand, because the mean field thermodynamics already predicts the existence of the critical endpoint with a divergent curvature [341, 342], so the role of the fluctuations is just that to change the mean field critical exponents.

We have verified that in the critical region around the critical endpoint $|R|$ scales with the correlation volume, $|R| = K\xi^3$ with $K = O(1)$, in agreement with hyperscaling arguments: thus $|R|$ brings information on the correlation volume. In proximity of the crossover at small μ the correspondence between $|R|$ and the correlation volume is not as good as the one we have found at large μ, which is not surprising because at small μ the chiral crossover is quite smooth; nevertheless, we have found that R develops a characteristic peak structure, suggesting that it is still capable to capture the pseudocritical behavior of the condensate.

Chapter 6

Comments and Conclusions

This thesis is the cumulative effort of the three years of my PhD. It concerns three different topics about QCD deconfinement phase transition.

The first (see Sec. 2.6) regards the universality in light and heavy ion collisions: in fact, it is increasingly noticeable that, high energy, high multiplicity events produced in small colliding systems show dynamical behaviour very similar to that one observed in AA collisions. These experimental results can be understood by drawing different observables, like the strangeness suppression factor γ_s and the yields of multi-strange hadrons, the average transverse momentum, and the elliptic flow scaled by the participant eccentricity, in terms of the the initial entropy density, that is the parton density in the transverse plane. Moreover, the previous analysis clarifies that in e^+e^- annihilation at the LEP or lower energies there is no chance of observing the enhancement of the strangeness production, that is $\gamma_s \gtrsim 0.95$, because the parton density in the transverse plane is too small.

The second aspect we studied (see Chapter 4) is the role of the QCD transition during the evolution of the Universe. Indeed, the fluctuations of the cosmological parameters at the QCD transition originate from the combined effect of the equation of state and of the calculation of higher-order derivatives of the relevant physical parameters, that is, in early Universe, of the scale factor. We have shown, by a complete treatment of the thermodynamics of the whole system (strong and electroweak contributions), that after about 100 μs the cosmological parameters return to the typical val-

ues of a radiation dominated era, i.e. to their values before the transition. Therefore the possible signature of the deconfinement transition in early Universe is restricted to the modification of the primordial gravitational wave spectrum.

Finally, the main goal is the study of the phase transition from the quark-gluon plasma to the hadronic matter within the framework of thermodynamic geometry: the thermodynamic theory of fluctuations allows to define a manifold spanned by intensive thermodynamic variables, $\{\theta_k\}$ with $k = 1,\ 2,\ \ldots,\ N$, and to equip this with the notion of a distance, $d\ell^2 = g^{\mu\nu}(\theta_1, \theta_2, \cdots\ \theta_N)\ d\theta_\mu\ d\theta_\nu$, where $g^{\mu\nu}$ is the metric tensor. The metric tensor is defined as $g^{\mu\nu} = \partial^2 \log \mathcal{Z}/\partial\theta_\mu\,\partial\theta_\nu$, $\mathcal{Z}$ being the partition function, and measures the probability of fluctuation between two equilibrium states.

The phase transition has been studied evaluating the scalar curvature, R, of the thermo-metric, $g^{\mu\nu}$, obtained from different techniques and models: LATTICE QCD (Sec. 5.3.1), Nambu-Jona Lasinio model (Sec. 5.4.1), and quark-meson model augmented with meson fluctuations (Sec. 5.4.2). Within this models the phase transition at large temperature and small chemical potential is actually a smooth crossover, which turns to a second order phase transition at the critical endpoint and then becomes a first order phase transition at large values of the chemical potential. The scalar curvature has been studied also for Hadron-Resonance gas models (Sec. 5.3.2).

In all the studied models, R is positive (like for statistical repulsive) for temperature well above the transition one, and becomes negative around the transition. The two possible meanings suggest by the previous behavior are:

- R is negative because an attractive interaction is needed to form quark condensates;

- R is negative because the system is now dominated by bosonic d.o.f.s, like for a hadron gas at zero chemical potential.

This suggests that around the chiral crossover, the interaction changes at mesoscopic level and there is a rearrangement of the collective interactions in the hot medium, from statistically repulsive (due to the fermionic nature

of the bulk [1]) to attractive. This piece of information was not accessible to previous model calculations on the QCD phase diagram and represents a merit of the thermodynamic geometry.

Moreover, we have investigated two different criteria to study the phase transition:

- the first is the so-called $R = 0$ criterion, that describe a "transition" from a system dominated by attractive interactions to one dominated by the repulsive, or vice versa.
- local maximum of $|R|$, i.e. as a local maximum of the correlation length ξ.

The results, obtained by the criterion $R = 0$ on the quark-gluon plasma phase diagram, are in good agreement with lattice data and freeze-out calculations in the low density region. Moreover, as shown in Fig. 6.1, $R = 0$ exactly corresponds to the maximum of chiral susceptibility from LATTICE QCD. The same criterion applied in the confined phase, described by different HRG models, gives a "critical" line which within 10% is consistent with the critical temperature evaluated in lattice QCD, if the hadron excluded volume and the interaction effects are taken into account. Let us recall that for QCD the thermodynamic approach has been applied for small baryon density since it requires a reliable evaluation of the thermodynamic potential ϕ, but has no problem to be used for systems with large barion-chemical potential.

The previous difference between QCD and HRG temperatures obtained by the $R = 0$ line can be understood by recalling that this criterion identifies a transition between systems dominated by fermionic and bosonic d.o.f.s and a possible difference in the transition temperature with respect to the deconfinement one has a possible interpretation if one recalls that, since the deconfinement transition is a crossover, one can expect remnants of confinement slightly above T_c. Indeed the persistence of string-like objects above T_c has been obtained by many different methods: lattice simulations [333, 334], quasiparticle approach [335, 336], NJL correlator [337, 338], Mott

[1] The number of quark and antiquark d.o.f.s is larger than the gluon ones. For two flavours, the effective fermionic d.o.f.s are $g_f = 21$, while the bosonic ones are $g_g = 16$.

transitions [339] and confinement mechanisms [340]. Following this interpretation, while T_c is the deconfinement temperature, that one obtained via $R = 0$ is the temperature of the complete melting of a light meson.

As discussed in Sec. 5.1.4, another way to identify the crossover temperature is by the local maximum of $|R|$. Indeed, in NJL model the maximum of chiral susceptibility is obtained for a non zero scalar curvature and this different behavior confirms, in the thermodynamic geometrical description, the interplay between confinement and chiral symmetry breaking in QCD [343–346]. To clarify this point, one has to recall that NJL model misses color confinement and therefore there is no a priori reason to apply the criterion $R = 0$. In a recent paper [347], the chiral phase transition temperature T_c^0, corresponding to a "true" chiral transition in the limit $m_s/m_l \gg 1$, turns out to be about 25 MeV less than the pseudo-critical temperature, and Fig. 6.1 suggests that a small variation from $m_s/m_l = 20$ to $m_s/m_l = 27$ changes the maximum of chiral susceptibility from $R = 0$ to a finite value of $|R|$, as in NJL model. It could be possible that considering the effective chiral limit, i.e. $m_s/m_l >> 1$ one recovers by thermodynamic geometry a "true" chiral phase transition at lower temperature, with typical scaling laws.

Our results concerning the NJL model and QM model show that thermodynamic geometry reliably describes the phase diagram. We notice that in both cases, R develops a peak structure around the chiral crossover. This is expected due to the relation between R and the correlation volume around a phase transition: as a matter of fact, at a second order phase transition R diverges due to the divergence of the correlation volume, while at a crossover the correlation length increases but remains finite. In this case susceptibilities are enhanced so R is expected to grow up in the pseudocritical region. Therefore, the thermodynamic curvature can bring information about the correlation volume also near a crossover.

We have found that in the region of small values of μ, the mesonic fluctuations enhance the magnitude of the curvature, and we understand this in terms of the stability of the phase with broken chiral symmetry. Indeed, fluctuations reduce the value of the determinant of the metric, g, meaning that fluctuations make the chiral broken phase less stable. This result is expected, since fluctuations of the order parameter represented by the σ-meson tend to wash out the σ-condensate. On the other hand, at

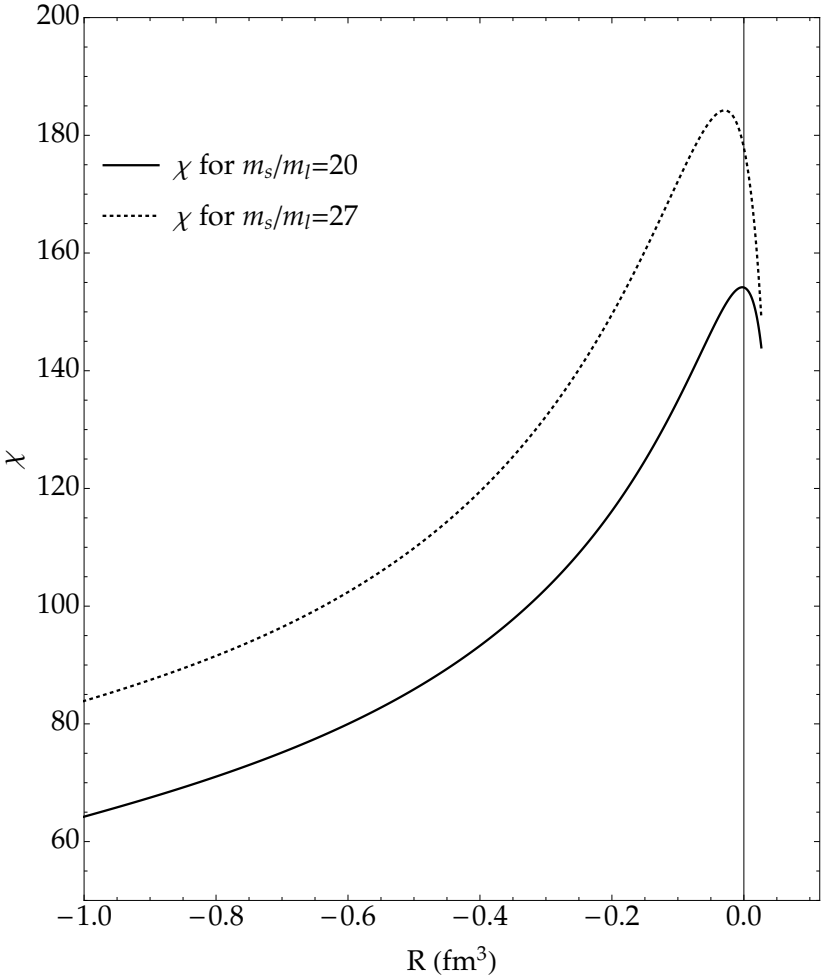

Figure 6.1: The chiral susceptibility χ from LATTICE QCD at $\mu = 0$ MeV and as a function of the scalar curvature R for physical value of the strange quark mass, m_s, and $m_s/m_\ell = 20$ (dotted line) or $m_s/m_\ell = 27$ (continuous line).

larger values of μ and in proximity of the critical endpoint, the fluctuations do not bring significant changes to the mean field solution, since it already predicts the existence of the critical endpoint with a divergent curvature.

In conclusion, thermodynamic geometry is a useful complementary method to the standard thermodynamical approach since it takes into account the effective dynamics, independently on the presence of a phase transition.

Appendix A

Appendices

A.1 Transverse parton density in e^+e^- annihilation

According to the previous discussion, a universal behaviour emerges if the parton density in the transverse plane is used as the relevant dynamical variable to define the initial setting of the collisions and if it is large enough.

Let us now study this quantity in e^+e^- annihilation at different energies and multiplicities, starting from some phenomenological indications. To evaluate the effective parton density in the transverse plane for this particular, not hadronic, setting one has to know the multiplicity and the transverse area (which are not independent quantities). Indeed, the problem is a reliable evaluation of the effective transverse size for e^+e^-, since, in the energy range up to $\simeq$ 200 GeV, the multiplicity is similar to the nucleus-nucleus one (normalized to half the number of participants N_{part}) and dN/dy at $y = 0$, with respect to thrust axis, is plotted in Fig. A.1 versus the cms energy. Let us recall, in a simplified way, the steps of the hadronization cascade of a primary quark or antiquark produced in e^+e^- annihilation. The colour field flux tube (string), initially created along the direction of the separating q and $\bar{q}$, produces a further pair q_1, $\bar{q}_1$ and then provides an increase of their longitudinal momentum. When q_1, $\bar{q}_1$ reaches the critical distances for the string breaking still another pair q_2, $\bar{q}_2$ is created and the state q_2, $\bar{q}_1$ is emitted as a hadron. The string multifragmentation produces

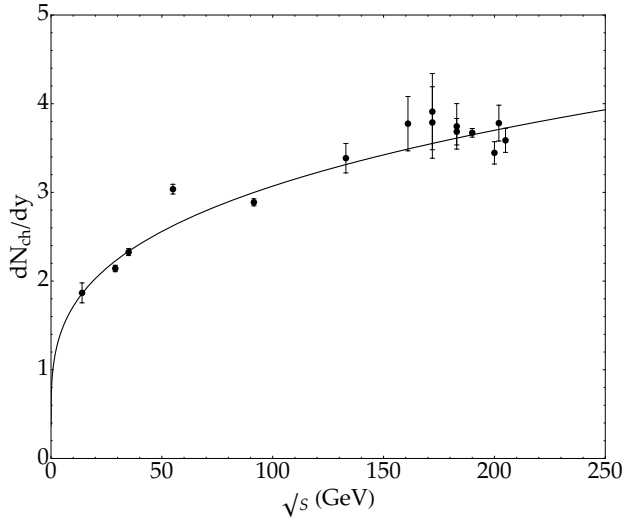

Figure A.1: dN_{ch}/dy in e^+e^-. Black line is the fit $(dN_{ch}/dy)^{e^+e^-} = 0.3493 + 0.6837\ (\sqrt{s})^{0.3}$.

the final multiplicity in Fig. A.1. Lattice evaluation [154] of the transverse size, R_T, of a quark-antiquark string at centre mass-energy $\sqrt{s}$ turns out to be [154, 155]

$$R_T^2 = \frac{2}{\pi\sigma}\sum_{k=0}^{N}\frac{1}{2k+1} \tag{A.1}$$

where σ is the string tension and $N = \sqrt{\pi s/2\sigma}$. Moreover

$$\sum_{k=0}^{N}\frac{1}{2k+1} = \frac{\gamma}{2} + ln(2) + \frac{1}{2}\left[\Psi(N+3/2)\right] \tag{A.2}$$

where γ is the Eulero-Mascheroni constant and Ψ is the di-gamma function which, for large values of the argument, can be approximated as

$$\Psi(x) \simeq ln(x)\ . \tag{A.3}$$

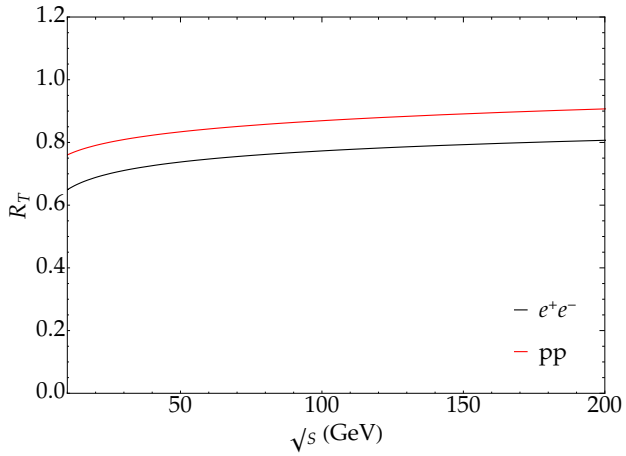

Figure A.2: Transverse radius, R_T, in e^+e^- (black) and pp (red).

Finally the transverse size can evaluated by

$$R_T^2 = \frac{2}{\pi\sigma}\left[\frac{\gamma}{2} + ln[2\left(N + \frac{3}{2}\right)^{1/2}\right] \tag{A.4}$$

The result is plotted in Fig. A.2 and compared with the transverse size of a pp collision, evaluated by the Color Glass parameterization, which takes into account the event-by-event fluctuations of the initial gluon configuration [151–153], and by the phenomenological fit of the multiplicity

$$\left.\frac{dN}{dy}\right|_{pp} = a_p + b_p\sqrt{s}^{0.22} \tag{A.5}$$

with $a_p = 0.04123$ and $b_p = 0.797$ [348]. The similarity between the transverse size in e^+e^- and pp should not be surprising; in fact, it is well known that the multiplicity in pp collisions is related with the multiplicity in e^+e^- annihilation if one takes into account the leading particle effect, i.e. the energy removed from the genuine hadronization cascade due to the leading particles [134, 135]. The initial entropy density s_0 in e^+e^- annihilation can now be estimated by data in Fig. A.1, fitted by $(dN_{ch}/dy)^{e^+e^-} = 0.3493 + 0.6837\ (\sqrt{s})^{0.3}$, and by R_T in Fig. A.2.

A.2 NJL model

This appendix contains some functions necessary to calculate the curvature scalar R (see cap. 5) and the susceptibility in the NJL model. To evaluate R one needs the derivatives of the potential

$$\phi(\beta,\gamma) = \frac{P}{T} = -\Omega(\beta,\gamma)\ \beta\ , \tag{A.6}$$

up to third order ($P = -\Omega$ being the pressure). These derivatives can be written in terms of the dynamical generated mass M. Therefore, the solution of the GAP equation uniquely determines all those functions.

A.2.1 NJL model with two flavours

After a straightforward calculation, one gets (a comma indicates partial derivative)

$$M_{,\beta} = \frac{b_1\ M}{1 - f_1 - f_2\ M^2}\ , \tag{A.7}$$

$$M_{,\gamma} = \frac{g_1\ M}{1 - f_1 - f_2\ M^2}\ , \tag{A.8}$$

$$M_{,\beta\beta} = d\ \left[b_3\ M + (b_2 + f_{1,\beta})\ M_{,\beta} + (b_4 + 2\,T\,f_2)\ M^2\ M_{,\beta} + f_3\ M\ M_{,\beta}^2 \right]\ , \tag{A.9}$$

$$M_{,\gamma\gamma} = d\ \left[g_3\ M + (g_2 + f_{1,\gamma})\ M_{,\gamma} + g_4\ M^2\ M_{,\gamma} + f_3\ M\ M_{,\gamma}^2 \right]\ , \tag{A.10}$$

$$M_{,\beta\gamma} = d\ \left[g_5\ M + b_2\ M_{,\gamma} + f_{1,\gamma} M_{,\beta} + g_4\ M^2\ M_{,\beta} + f_2\ T\ M^2\ M_{,\gamma} + f_3\ M\ M_{,\beta} M_{,\gamma} \right]\ , \tag{A.11}$$

with

$$d = \left(1 - f_1 - f_2\ M^2\right)^{-1}\ , \tag{A.12}$$

$$f_1 = \kappa_M\ \int_0^\Lambda dp\ \frac{p^4\ \Psi}{E^3}\ , \tag{A.13}$$

$$f_2 = \kappa_M \int_0^\Lambda dp\, p^2\, \frac{n_-\,(1-n_-) + n_+\,(1-n_+)}{T\; E^2}\;, \tag{A.14}$$

$$f_3 = \kappa_M \int_0^\Lambda dp\, p^4\, \frac{n_-\,(1-n_-) + n_+\,(1-n_+)}{T\; E^4}\;, \tag{A.15}$$

$$b_1 = \kappa_M \int_0^\Lambda dp\, p^2\; \left[n_-\,(1-n_-) + n_+\,(1-n_+)\right]\;, \tag{A.16}$$

$$b_2 = \kappa_M \int_0^\Lambda dp\, p^4\, \frac{\Psi_\beta}{E^3}\;, \tag{A.17}$$

$$b_3 = \kappa_M \int_0^\Lambda dp p^2\; \left[n_{-,\beta}\,(1-2n_-) + n_{+,\beta}\,(1-2n_+)\right]\;, \tag{A.18}$$

$$b_4 = \kappa_M \int_0^\Lambda dp p^2\; \frac{n_{-,\beta}\,(1-2n_-) + n_{+,\beta}\,(1-2n_+)}{T\; E^2}\;, \tag{A.19}$$

$$g_1 = \kappa_M \int_0^\Lambda dp\, p^2\, \frac{n_-\,(1-n_-) - n_+\,(1-n_+)}{E}\;, \tag{A.20}$$

$$g_2 = \kappa_M \int_0^\Lambda dp\, p^4\, \frac{\Psi_\gamma}{E^3}\;, \tag{A.21}$$

$$g_3 = \kappa_M \int_0^\Lambda dp p^2\; \frac{n_{-,\gamma}\,(1-2n_-) - n_{+,\gamma}\,(1-2n_+)}{E}\;, \tag{A.22}$$

$$g_4 = \kappa_M \int_0^\Lambda dp p^2\; \frac{n_{-,\gamma}\,(1-2n_-) + n_{+,\gamma}\,(1-2n_+)}{T\; E^2}\;, \tag{A.23}$$

$$g_5 = \kappa_M \int_0^\Lambda dp p^2\; \left[n_{-,\gamma}\,(1-2n_-) + n_{+,\gamma}\,(1-2n_+)\right]\;, \tag{A.24}$$

$$\kappa_M = 2\; G\; \frac{N_c\, N_f}{\pi^2} \tag{A.25}$$

and $n\pm$ in EQ. (3.59).
By deriving EQ. (A.6) and EQ. (4.59) and defining

$$\kappa_\Omega = \frac{\kappa_M}{2\, G}\;, \tag{A.26}$$

one gets

$$\phi_{,\beta} = \kappa_\Omega \int_0^\Lambda dp\, p^2\, E\, \Psi - \frac{(M-m)^2}{4\,G}\ , \tag{A.27}$$

$$\phi_{,\gamma} = \kappa_\Omega \int_0^\Lambda dp\, p^2\ (n_+ - n_-)\ . \tag{A.28}$$

The calculation of second and third order derivatives is straightforward. Finally, the two flavours chiral susceptibility, χ, is defined as [261]

$$\chi^{2f} = \frac{\partial M}{\partial m} = \frac{1}{1 - f_1 - f_2\, M^2} = \frac{M_{,\beta}}{b_1\, M} = \frac{M_{,\gamma}}{g_1\, M}\ . \tag{A.29}$$

A.2.2 NJL model with three flavours

In a three flavours system, the derivatives of the dynamically generated mass $M_u = M_d$ and M_s are

$$M_{u,\beta}\,(\delta - b_u\, M_u\, \epsilon) = a_u\, \epsilon - M_{s,\beta}\, \zeta\ , \tag{A.30}$$

$$M_{s,\beta} = \frac{(a_s\, \theta - a_u\, \lambda)\,(\delta - b_u\, M_u\, \epsilon) - a_u\, \epsilon\, b_u\, \lambda\, M_u}{(\ \eta - b_s\, M_s\, \theta)\,(\delta - b_u\, M_u\, \epsilon) - b_u\, \lambda\, M_u\, \zeta}\ , \tag{A.31}$$

$$M_{u,\gamma}\,(\delta - b_u\, M_u\, \epsilon) = c_u\, \epsilon - M_{s,\gamma}\, \zeta\ , \tag{A.32}$$

$$M_{s,\gamma} = \frac{(c_s\, \theta - c_u\, \lambda)\,(\delta - b_u\, M_u\, \epsilon) - c_u\, \epsilon\, b_u\, \lambda\, M_u}{(\ \eta - b_s\, M_s\, \theta)\,(\delta - b_u\, M_u\, \epsilon) - b_u\, \lambda\, M_u\, \zeta}\ , \tag{A.33}$$

$$\begin{aligned} M_{u,\beta\beta}\,(\delta - b_u\, M_u\, \epsilon) &= d_u\, \epsilon + A_{u,\beta}\, \epsilon_{,\beta} - \\ &- (M_{u,\beta}\delta_{,\beta} + M_{s,\beta}\zeta_{,\beta} + \epsilon\, D_{u,\beta}\, M_u\, M_{u,\beta}) - M_{s,\beta\beta}\, \zeta\ , \end{aligned} \tag{A.34}$$

$$
\begin{aligned}
M_{s,\beta\beta} =& \frac{(\delta - b_u\, M_u\, \epsilon)}{(\eta - b_s\, M_s\, \theta)\,(\delta - b_u\, M_u\, \epsilon) - \zeta\, \lambda\, b_u\, M_u} \times \\
& \times \Bigg(d_s\, \theta - d_u\, \lambda + A_{s,\beta}\, \theta_{,\beta} - A_{u,\beta}\, \lambda_{,\beta} + \\
& \qquad + \lambda\, D_{u,\beta}\, M_u\, M_{u,\beta} - \theta\, D_{s,\beta}\, M_s\, M_{s,\beta} \Bigg) - \\
& - \frac{\lambda\, b_u\, M_u}{(\eta - b_s\, M_s\, \theta)\,(\delta - b_u\, M_u\, \epsilon) - \zeta\, \lambda\, b_u\, M_u} \Big[d_u\, \epsilon + A_{u,\beta}\, \epsilon_{,\beta} - \\
& - (M_{u,\beta}\delta_{,\beta} + M_{s,\beta}\zeta_{,\beta} + \epsilon\, D_{u,\beta}\, M_u\, M_{u,\beta}) \Big]
\end{aligned}
\tag{A.35}
$$

$$
\begin{aligned}
M_{u,\gamma\gamma}\,(\delta - b_u\, M_u\, \epsilon) =& e_u\, \epsilon + A_{u,\gamma}\, \epsilon_{,\gamma} - M_{s,\gamma\gamma}\, \zeta - \\
& - (M_{u,\gamma}\delta_{,\gamma} + M_{s,\gamma}\zeta_{,\gamma} + \epsilon\, D_{u,\gamma}\, M_u\, M_{u,\gamma}) \,,
\end{aligned}
\tag{A.36}
$$

$$
\begin{aligned}
M_{s,\gamma\gamma} =& \frac{(\delta - b_u\, M_u\, \epsilon)}{(\eta - b_s\, M_s\, \theta)\,(\delta - b_u\, M_u\, \epsilon) - \zeta\, \lambda\, b_u\, M_u} \times \\
& \times (e_s\, \theta - e_u\, \lambda + A_{s,\gamma}\, \theta_{,\gamma} - A_{u,\gamma}\, \lambda_{,\gamma} + \lambda\, D_{u,\gamma}\, M_u\, M_{u,\gamma} - \theta\, D_{s,\gamma}\, M_s\, M_{s,\gamma}) - \\
& - \lambda\, b_u\, M_u\, \frac{[e_u\, \epsilon + A_{u,\gamma}\, \epsilon_{,\gamma} - (M_{u,\gamma}\delta_{,\gamma} + M_{s,\gamma}\zeta_{,\gamma} + \epsilon\, D_{u,\gamma}\, M_u\, M_{u,\gamma})]}{(\eta - b_s\, M_s\, \theta)\,(\delta - b_u\, M_u\, \epsilon) - \zeta\, \lambda\, b_u\, M_u} \,,
\end{aligned}
\tag{A.37}
$$

$$
\begin{aligned}
M_{u,\beta\gamma}\,(\delta - b_u\, M_u\, \epsilon) =& f_u\, \epsilon + A_{u,\beta}\, \epsilon_{,\gamma} - M_{s,\beta\gamma}\, \zeta - \\
& - (M_{u,\beta}\delta_{,\gamma} + M_{s,\beta}\zeta_{,\gamma} + \epsilon\, D_{u,\beta}\, M_u\, M_{u,\gamma}) \,,
\end{aligned}
\tag{A.38}
$$

and

$$M_{s,\beta\gamma} = \frac{(\delta - b_u\, M_u\, \epsilon)}{(\eta - b_s\, M_s\, \theta)\,(\delta - b_u\, M_u\, \epsilon) - \zeta\, \lambda\, b_u\, M_u} \times$$
$$\times \left(f_s\, \theta - f_u\, \lambda + A_{s,\beta}\, \theta_{,\gamma} - A_{u,\beta}\, \lambda_{,\gamma} + \right.$$
$$\left. + \lambda\, D_{u,\beta}\, M_u\, M_{u,\gamma} - \theta\, D_{s,\beta}\, M_s\, M_{s,\gamma} \right) -$$
$$- \lambda\, b_u\, M_u\, \frac{[f_u\, \epsilon + A_{u,\beta}\, \epsilon_{,\gamma} - (M_{u,\beta}\delta_{,\gamma} + M_{s,\beta}\zeta_{,\gamma} + \epsilon\, D_{u,\beta}\, M_u\, M_{u,\gamma})]}{(\eta - b_s\, M_s\, \theta)\,(\delta - b_u\, M_u\, \epsilon) - \zeta\, \lambda\, b_u\, M_u} \tag{A.39}$$

where

$$a_f = \frac{N_c}{\pi^2} \int_0^\Lambda dp\, p^2\, [n_{-f}\,(1 - n_{-f}) + n_{+f}\,(1 - n_{+f})]\ , \tag{A.40}$$

$$b_f = \frac{N_c}{\pi^2} \int_0^\Lambda dp\, p^2 \frac{n_{-f}\,(1 - n_{-f}) + n_{+f}\,(1 - n_{+f})}{T\ E_f^2}\ , \tag{A.41}$$

$$c_f = \frac{N_c}{\pi^2} \int_0^\Lambda dp\, p^2 \frac{n_{-f}\,(1 - n_{-f}) - n_{+f}\,(1 - n_{+f})}{E_f}\ , \tag{A.42}$$

$$d_f = \frac{N_c}{\pi^2} \int_0^\Lambda dp\ p^2 \left\{ \left(\frac{2\, M\, M_{,\beta}}{E^2} + p^2\ \frac{M_{,\beta}^2}{T\, E^4} \right) [n_{-f}\,(1 - n_{-f}) + n_{+f}\,(1 - n_{+f})] + \right.$$
$$\left. + \left(1 + \frac{M\, M_{,\beta}}{T\, E^2} \right) [(1 - 2\, n_{-f})\, n_{-f,\beta} + (1 - 2\, n_{+f})\, n_{+f,\beta}] \right\}\ , \tag{A.43}$$

$$e_f = \frac{N_c}{\pi^2}\int_0^\Lambda dp\, p^2 \Bigg\{ p^2\, \frac{M_{,\gamma}^2}{T\,E^4}\left[n_{-f}\,(1-n_{-f}) + n_{+f}\,(1-n_{+f})\right] + \\ + \frac{M\,M_{,\gamma}}{T\,E^2}\left[(1-2\,n_{-f})\,n_{-f,\gamma} + (1-2\,n_{+f})\,n_{+f,\gamma}\right] + \\ + \frac{(1-2\,n_{-f})\,n_{-f,\gamma} - (1-2\,n_{+f})\,n_{+f,\gamma}}{E} \Bigg\}\,, \tag{A.44}$$

$$f_f = \frac{N_c}{\pi^2}\int_0^\Lambda dp\, p^2 \Bigg\{ \left(\frac{M\,M_{,\gamma}}{E^2} + p^2\,\frac{M_{,\beta}M_{,\gamma}}{T\,E^4}\right)\left[n_{-f}\,(1-n_{-f}) + n_{+f}\,(1-n_{+f})\right] + \\ + \left(1 + \frac{M\,M_{,\beta}}{T\,E^2}\right)\left[(1-2\,n_{-f})\,n_{-f,\gamma} + (1-2\,n_{+f})\,n_{+f,\gamma}\right] \Bigg\}\,, \tag{A.45}$$

$$A_{f,\beta} = a_f + b_f\; M_f\, M_{f,\beta}\;, \tag{A.46}$$

$$A_{f,\gamma} = c_f + b_f\; M_f\, M_{f,\gamma}\;, \tag{A.47}$$

$$C_{f,\beta\beta} = d_f + b_f\; M_f\, M_{f,\beta\beta}\;, \tag{A.48}$$

$$C_{f,\gamma\gamma} = e_f + b_f\; M_f\, M_{f,\gamma\gamma}\;, \tag{A.49}$$

$$C_{f,\beta\gamma} = f_f + b_f\; M_f\, M_{f,\beta\gamma}\;, \tag{A.50}$$

$$B(M_u, M_s) = 4\,G - 2\,\frac{K^2}{G}\;u^2 - 2\,K\,s\;, \tag{A.51}$$

$$\delta(M_u, M_s) = (1 - F_{1u}\,B)\;, \tag{A.52}$$

$$\zeta(M_u, M_s) = 2\,K\,u\;, \tag{A.53}$$

$$\epsilon(M_u, M_s) = B\,M_u\;, \tag{A.54}$$

$$\eta(M_u, M_s) = (1 - 4GF_{1s})\,(1 - F_{1u}B) - \\ - 8K^2u^2F_{1u}\;, \tag{A.55}$$

$$\theta(M_u, M_s) = 4\,G\;(1 - F_{1u}B)\,M_s\,, \tag{A.56}$$

$$\lambda(M_u, M_s) = 4\,K\,u\,M_u\;, \tag{A.57}$$

$$F_{1f} = \frac{N_c}{\pi^2}\int_0^\Lambda dp\, p^4\, \frac{\Psi_f}{E_f^3}\ , \tag{A.58}$$

$$n_{f\pm} = \frac{1}{1+\exp\left\{\frac{\sqrt{p^2+M_f^2}\pm\mu_f}{T}\right\}} \tag{A.59}$$

and $u \equiv \langle \overline{u}u\rangle$, $s \equiv \langle \overline{s}s\rangle$.

About the thermodynamic potential $\phi = -\Omega\,\beta$, one has

$$\phi_{,\beta} = \sum_{f=u,d,s}\frac{N_c}{\pi^2}\int_0^\Lambda dp\, p^2\, E_f\Psi_f + 2Gs^2 + u\,(M_u - m_u) + s\,(M_s - m_s) = \sum_{f=u,d,s}\frac{N_c}{\pi^2}\int_0^\Lambda dp\, p^2\, E_f\Psi_f + Ku^2 s + u\,(M_u - m_u) + \frac{s\,(M_s - m_s)}{2}\ , \tag{A.60}$$

$$\phi_{,\gamma} = \sum_{f=u,d,s}\frac{N_c}{\pi^2}\int_0^\Lambda dp\, p^2\ (n_{+f} - n_{-f}) \tag{A.61}$$

$$\phi_{,\beta\beta} = -\sum_{f=u,d,s}\frac{N_c}{\pi^2}\int_0^\Lambda dp\, p^2 E_f\,(n_{+f,\beta} + n_{-f,\beta}) \tag{A.62}$$

$$\phi_{,\beta\gamma} = \sum_{f=u,d,s}\frac{N_c}{\pi^2}\int_0^\Lambda dp\, p^2\ (n_{+f,\beta} - n_{-f,\beta}) \tag{A.63}$$

$$\phi_{,\gamma\gamma} = \sum_{f=u,d,s}\frac{N_c}{\pi^2}\int_0^\Lambda dp\, p^2\ (n_{+f,\gamma} - n_{-f,\gamma}) \tag{A.64}$$

$$\phi_{,\beta\beta\gamma} = \sum_{f=u,d,s}\frac{N_c}{\pi^2}\int_0^\Lambda dp\, p^2\ (n_{+f,\beta\beta} - n_{-f,\beta\beta}) \tag{A.65}$$

$$\phi_{,\beta\gamma\gamma} = \sum_{f=u,d,s}\frac{N_c}{\pi^2}\int_0^\Lambda dp\, p^2\ (n_{+f,\beta\gamma} - n_{-f,\beta\gamma}) \tag{A.66}$$

$$\phi_{,\gamma\gamma\gamma} = \sum_{f=u,d,s}\frac{N_c}{\pi^2}\int_0^\Lambda dp\, p^2\ (n_{+f,\gamma\gamma} - n_{-f,\gamma\gamma}) \tag{A.67}$$

$$\begin{aligned}\phi_{,\beta\beta\beta} = & -\sum_{f=u,d,s} \frac{N_c}{\pi^2} \int_0^\Lambda dp\, p^2 E_f \left(n_{+f,\beta\beta} + n_{-f,\beta\beta}\right) + \\ & + \sum_{f=u,d,s} (a_f + b_f\, M_f\, M_{f,\beta})\, M_f\, M_{f,\beta}\end{aligned} \tag{A.68}$$

Finally, by defining

$$H_f = F_{1f} + b_f\, M_f^2\,, \tag{A.69}$$

the chiral susceptibilities are

$$\begin{aligned}\chi_u = & \chi_d = \frac{\partial M_u}{\partial m_u} = \\ = & \frac{1 - 4\,G\,H_s}{1 - 4\,G(H_u + H_s) + 4\,H_u\,H_s(4\,G^2 - 2\,K\,G\,s - K^2\,u^2) + 2\,K\,s\,H_u}\end{aligned} \tag{A.70}$$

and

$$\begin{aligned}\chi_s = & \frac{\partial M_s}{\partial m_s} = \\ = & \frac{1 - (4\,G - 2\,K\,s)\,H_u}{1 - 4\,G(H_u + H_s) + 4\,H_u\,H_s(4\,G^2 - 2\,K\,G\,s - 2\,K^2\,u^2) + 2\,K\,s\,H_u}\,.\end{aligned} \tag{A.71}$$

A.3 Power series expansion of the scalar curvature in 2D

In this section we investigate the thermodynamic scalar curvature of a two dimensional manifold, which coordinates are the inverse temperature $\beta = 1/T$ and $\gamma = -\mu/T$, with μ chemical potential, by considering expansion at low μ. This expansion will be useful for the study of the phase diagram of strongly interacting matter by LATTICE QCD since it gives the pressure only for low values of γ^2.

Therefore in the calculation of the potential $\phi = P/T$, we consider a power series expansion in $\gamma^2 < 1$. By the expression of the pressure P as a power series around the point $\mu_B = 0$,

$$P(\beta,\gamma) = P_0 + P_2\,\gamma^2 + P_4\,\gamma^4 + P_6\,\gamma^6 + \cdots\ , \tag{A.72}$$

the thermodynamical potential $\phi = P/T$ can be express as

$$\phi(\beta,\gamma) = A(\beta) + B(\beta)\gamma^2 + C(\beta)\gamma^4 + D(\beta)\gamma^6 + \cdots\ , \tag{A.73}$$

The coefficients of the thermodynamical potential are given by

$$\begin{aligned} A(\beta) =& P_0(\beta)\ \beta\ , \\ B(\beta) =& P_2(\beta)\,\beta = \frac{\chi_2(\beta)}{2!\ \beta^3}\ , \\ C(\beta) =& P_4(\beta)\,\beta = \frac{\chi_4(\beta)}{4!\ \beta^3}\ , \\ D(\beta) =& P_6(\beta)\,\beta = \frac{\chi_6(\beta)}{6!\ \beta^3}\ , \end{aligned} \tag{A.74}$$

where $\chi_{2n} = \frac{\partial^{2n}}{\partial\gamma^{2n}}(P\ \beta^4)|_{\gamma=0} = (2n)!\ P_{2n}\,\beta^4$.

The metric element $g_{11} = \phi_{11}$ and the metric determinant g can be written by analogous power series, i.e.

$$g_{11}(\beta,\gamma) = A'' + B''\,\gamma^2 + +C''\,\gamma^4 + +D''\,\gamma^6 + \cdots\ , \tag{A.75}$$

$$g(\beta,\gamma) = g_{\mathcal{O}(0)} + g_{\mathcal{O}(2)}\,\gamma^2 + g_{\mathcal{O}(4)}\,\gamma^4 + g_{\mathcal{O}(6)}\,\gamma^6 + \cdots\ , \tag{A.76}$$

where

$$g_{\mathcal{O}(0)}(\beta) = 2B\ A'' \ , \tag{A.77}$$

$$g_{\mathcal{O}(2)} = 2\left(6\ C\ A'' + B\ B'' - 2\ B'^2\right) \ , \tag{A.78}$$

$$g_{\mathcal{O}(4)} = 2\Big(15\,D\,A'' + 6\,C\,B'' - 8\,B'\,C' + B\,C''\Big) \ , \tag{A.79}$$

$$g_{\mathcal{O}(6)} = 2\Big(28\,E\,A'' + 15\,D\,B'' - 12\,B'\,D' + B\,D'' + 6\,C\,C'' - 8\,C'^2\Big) \tag{A.80}$$

and the symbol "$'$" indicates the derivative with respect to β. Finally, the scalar curvature also can be express as:

$$R(\beta,\gamma) = \sum_{n=0} R_{\mathcal{O}(2\,n)}(\beta)\ \gamma^{2\,n} \ . \tag{A.81}$$

The coefficients $R_{\mathcal{O}(2n)}$ are functions of A, B, ... in Eqs. (A.73, A.74) and of their derivatives with respect to β. Particularly, one can see that the $2n$-coefficient $R_{\mathcal{O}(2n)}$ is a function of the first $2(n+1)$ coefficients of the expansion for the potential ϕ in EQ. (A.73).

In conclusion, if for example one knows the pressure up to γ^6, g and R can be calculated up to γ^4. For example, the zero-order term, $R_{\mathcal{O}(0)}$, depends on the first and second coefficients of the ϕ series expansion, and it is given by

$$R_{\mathcal{O}(0)} = \frac{1}{2}\,\frac{B'}{A''\,B}\left(\frac{A'''}{A''} - \frac{B'}{B}\right) = \frac{1}{2\,\ddot{P}_0}\ \left[3 + T\ \frac{\dot{\chi}_2}{\chi_2}\right]\left[\frac{\dddot{P}_0}{\ddot{P}_0} - \frac{\dot{\chi}_2}{\chi_2}\right] \ , \tag{A.82}$$

where " $'$ " and " $\dot{}$ " denote, respectively, the derivative with respect to β and T; $P_0(\beta)$ is the pressure and $\chi_2(\beta) = \partial^2(P/T^4)/\partial\gamma^2$, both at $\mu_B = 0$.

The other terms are:

$$\begin{aligned} R_{\mathcal{O}(2)}(\beta) = &- \frac{B'}{2\,BA''}\left(\frac{A'''}{A''} - \frac{B'}{B}\right)\left(\frac{6C}{B} + \frac{B''}{A''} - \frac{2\,B'^2}{BA''}\right) - \\ &- \frac{B''^2 - 3A'''C'}{B\,A''^2} + \frac{6\,C\,A''\,B''}{B^2\,A''^2} + \\ &+ \frac{B'}{2BA''}\left(\frac{B'''}{A''} - \frac{6\,C\,A'''}{B\,A''} - \frac{12\,C'}{B}\right) + \frac{B'^2B''}{2B^2A''^2} \ , \end{aligned} \tag{A.83}$$

$$
\begin{aligned}
R_{\mathcal{O}(4)}(\beta) =& \frac{B'}{2\,B\,A''}\left(\frac{A'''}{A''}-\frac{B'}{B}\right)\left[3\left(\frac{6C}{B}+\frac{B''}{A''}-\frac{2\,B'^2}{B\,A''}\right)^2-\frac{30\,D}{B}-\right.\\
&\left.-\frac{12\,C\,B''}{B\,A''}+\frac{16\,B'\,C'}{B\,A''}-\frac{2\,C''}{A''}\right]+\frac{C'(6CA'''+3BB'''+2B'B'')}{B^2A''^2}-\\
&-\frac{1}{B\,A''}\left(\frac{6\,C}{B}+\frac{B''}{A''}-\frac{2\,B'^2}{B\,A''}\right)\left[-\frac{2\,(B''^2-3A'''C')}{A''}+\right.\\
&\left.+\frac{12\,C\,B''}{B}+\frac{B'^2B''}{B\,A''}-B'\left(\frac{6CA'''}{B\,A''}+\frac{12\,C'}{B}-\frac{B'''}{A''}\right)\right]+\\
&+\frac{1}{2\,B\,A''}\left[\frac{15\,A'''D'}{A''}+\frac{60\,D\,B''}{B}+\frac{24\,C\,C''}{B}-\frac{36\,C'^2}{B}-\right.\\
&\qquad-\frac{45DA'''B'}{BA''}-\frac{30\,D'B'}{B}-\frac{6\,B'C\,B'''}{BA''}+\\
&\left.\qquad+\frac{B'C''''}{A''}-\frac{8\,B''C''}{A''}+\frac{3\,B'^2C''}{BA''}\right]
\end{aligned}
\tag{A.84}
$$

Bibliography

[1] I. Arsene et al. Quark gluon plasma and color glass condensate at RHIC? The Perspective from the BRAHMS experiment. *Nucl. Phys. A*, 757:1–27, 2005.

[2] B.B. Back et al. The PHOBOS perspective on discoveries at RHIC. *Nucl. Phys. A*, 757:28–101, 2005.

[3] John Adams et al. Experimental and theoretical challenges in the search for the quark gluon plasma: The STAR Collaboration's critical assessment of the evidence from RHIC collisions. *Nucl. Phys. A*, 757:102–183, 2005.

[4] K. Adcox et al. Formation of dense partonic matter in relativistic nucleus-nucleus collisions at RHIC: Experimental evaluation by the PHENIX collaboration. *Nucl. Phys. A*, 757:184–283, 2005.

[5] Bernd-Jochen Schaefer and Mathias Wagner. On the QCD phase structure from effective models. *Prog. Part. Nucl. Phys.*, 62:381, 2009.

[6] Murray Gell-Mann. A Schematic Model of Baryons and Mesons. *Phys. Lett.*, 8:214–215, 1964.

[7] G. Zweig. *An SU(3) model for strong interaction symmetry and its breaking. Version 2*, pages 22–101. 2 1964.

[8] David J. Gross, Robert D. Pisarski, and Laurence G. Yaffe. QCD and Instantons at Finite Temperature. *Rev. Mod. Phys.*, 53:43, 1981.

[9] D.J. Gross and Frank Wilczek. Asymptotically Free Gauge Theories - I. *Phys. Rev. D*, 8:3633–3652, 1973.

[10] D.J. Gross and Frank Wilczek. ASYMPTOTICALLY FREE GAUGE THEORIES. 2. *Phys. Rev. D*, 9:980–993, 1974.

[11] H.David Politzer. Reliable Perturbative Results for Strong Interactions? *Phys. Rev. Lett.*, 30:1346–1349, 1973.

[12] Sidney R. Coleman and David J. Gross. Price of asymptotic freedom. *Phys. Rev. Lett.*, 31:851–854, 1973.

[13] Richard P. Feynman. Very high-energy collisions of hadrons. *Phys. Rev. Lett.*, 23:1415–1417, 1969.

[14] Murray Gell-Mann and F.E. Low. Quantum electrodynamics at small distances. *Phys. Rev.*, 95:1300–1312, 1954.

[15] Kenneth G. Wilson. The Renormalization Group and Strong Interactions. *Phys. Rev. D*, 3:1818, 1971.

[16] Jr. Callan, Curtis G. Broken scale invariance in scalar field theory. *Phys. Rev. D*, 2:1541–1547, 1970.

[17] K. Symanzik. Small distance behavior in field theory and power counting. *Commun. Math. Phys.*, 18:227–246, 1970.

[18] Steven Weinberg. Nonabelian Gauge Theories of the Strong Interactions. *Phys. Rev. Lett.*, 31:494–497, 1973.

[19] David J. Gross and Frank Wilczek. Ultraviolet Behavior of Nonabelian Gauge Theories. *Phys. Rev. Lett.*, 30:1343–1346, 1973.

[20] D.A. Ross and J.C. Taylor. Renormalization of a unified theory of weak and electromagnetic interactions. *Nucl. Phys. B*, 51:125–144, 1973. [Erratum: Nucl.Phys.B 58, 643–643 (1973)].

[21] H.David Politzer. Asymptotic Freedom: An Approach to Strong Interactions. *Phys. Rept.*, 14:129–180, 1974.

[22] Frank Wilczek. Quantum Chromodynamics (QCD): The Modern Theory of the Strong Interaction. *Ann. Rev. Nucl. Part. Sci.*, 32:177–209, 1982.

[23] Michael Buballa. NJL model analysis of quark matter at large density. *Phys. Rept.*, 407:205–376, 2005.

[24] Helmut Satz. Extreme states of matter in strong interaction physics. An introduction. *Lect. Notes Phys.*, 841:1–239, 2012.

[25] Andre Roberge and Nathan Weiss. Gauge Theories With Imaginary Chemical Potential and the Phases of QCD. *Nucl. Phys. B*, 275:734–745, 1986.

[26] Hiroaki Kouno, Yuji Sakai, Takahiro Makiyama, Kouhei Tokunaga, Takahiro Sasaki, and Masanobu Yahiro. Quark-gluon thermodynamics with the Z(N(c)) symmetry. *J. Phys. G*, 39:085010, 2012.

[27] R. Hagedorn. Statistical thermodynamics of strong interactions at high-energies. *Nuovo Cim. Suppl.*, 3:147–186, 1965.

[28] R. Hagedorn and J. Ranft. Statistical thermodynamics of strong interactions at high-energies. 2. Momentum spectra of particles produced in pp-collisions. *Nuovo Cim. Suppl.*, 6:169–354, 1968.

[29] N. Cabibbo and G. Parisi. Exponential Hadronic Spectrum and Quark Liberation. *Phys. Lett. B*, 59:67–69, 1975.

[30] N.P. Landsman and C.G. van Weert. Real and Imaginary Time Field Theory at Finite Temperature and Density. *Phys. Rept.*, 145:141, 1987.

[31] J.I. Kapusta and Charles Gale. *Finite-temperature field theory: Principles and applications*. Cambridge Monographs on Mathematical Physics. Cambridge University Press, 2011.

[32] Michel Le Bellac. *Thermal Field Theory*. Cambridge Monographs on Mathematical Physics. Cambridge University Press, 3 2011.

[33] Krishna Rajagopal and Frank Wilczek. *The Condensed matter physics of QCD*, pages 2061–2151. World Scientific, 11 2000.

[34] Mark G. Alford, Andreas Schmitt, Krishna Rajagopal, and Thomas Schäfer. Color superconductivity in dense quark matter. *Rev. Mod. Phys.*, 80:1455–1515, 2008.

[35] Kenji Fukushima and Tetsuo Hatsuda. The phase diagram of dense QCD. *Rept. Prog. Phys.*, 74:014001, 2011.

[36] Roman Pasechnik and Michal ˇ Sumbera. Phenomenological Review on Quark–Gluon Plasma: Concepts vs. Observations. *Universe*, 3(1):7, 2017.

[37] Larry McLerran and Robert D. Pisarski. Phases of cold, dense quarks at large N(c). *Nucl. Phys. A*, 796:83–100, 2007.

[38] Michael J. Fromerth and Johann Rafelski. Hadronization of the quark Universe, arxiv:0211346.

[39] Marek Gazdzicki, Mark Gorenstein, and Peter Seyboth. Brief history of the search for critical structures in heavy-ion collisions. *Acta Phys. Polon. B*, 51:1033, 2020.

[40] Anton Andronic, Peter Braun-Munzinger, Krzysztof Redlich, and Johanna Stachel. Decoding the phase structure of QCD via particle production at high energy. *Nature*, 561(7723):321–330, 2018.

[41] Peter Braun-Munzinger, Volker Koch, Thomas Schäfer, and Johanna Stachel. Properties of hot and dense matter from relativistic heavy ion collisions. *Phys. Rept.*, 621:76–126, 2016.

[42] P. Castorina, R. V. Gavai, and H. Satz. The QCD Phase Structure at High Baryon Density. *Eur. Phys. J.*, C69:169–178, 2010.

[43] Ulrich W. Heinz and Maurice Jacob. Evidence for a new state of matter: An Assessment of the results from the CERN lead beam program. 1 2000.

[44] Márcio Rafael Baptista Ferreira. *QCD phase diagram under an external magnetic field*. PhD thesis, Coimbra U., 2015.

[45] H. Satz, *Statistical Mechanics of Quarks and Hadrons. Proceedings, International Symposium, Bielefeld, F.R. Germany, August 24-31, 1980*, 1981.

[46] R. Bock and R. Stock, editors. *Proceedings: Workshop on Future Relativistic Heavy Ion Experiments, Darmstadt, Germany, Oct 7-10, 1980*, 1981.

[47] T. E. O. Ericson, M. Jacob, H. Satz and W. Willis, *Quark Matter Formation and Heavy Ion Collisions: a Workshop Held at Bielefeld: Summary Report Prepared by the Organizing Committee, Bielefeld, Germany*, 1982.

[48] Helmut Satz and Reinhard Stock. Quark Matter: The Beginning. *Nuclear Physics A*, 956:898–901, 2016.

[49] S.V. Afanasiev et al. Energy dependence of pion and kaon production in central Pb + Pb collisions. *Phys. Rev. C*, 66:054902, 2002.

[50] Miklos Gyulassy and Larry McLerran. New forms of QCD matter discovered at RHIC. *Nucl. Phys. A*, 750:30–63, 2005.

[51] J. Barrette et al. Observation of anisotropic event shapes and transverse flow in Au + Au collisions at AGS energy. *Phys. Rev. Lett.*, 73:2532–2535, 1994.

[52] Berndt Muller, Jurgen Schukraft, and Boleslaw Wyslouch. First Results from Pb+Pb collisions at the LHC. *Ann. Rev. Nucl. Part. Sci.*, 62:361–386, 2012.

[53] J. Schukraft. Heavy ion physics at the Large Hadron Collider: what is new? What is next? *Phys. Scripta T*, 158:014003, 2013.

[54] A.N. Sissakian and A.S. Sorin. The nuclotron-based ion collider facility (NICA) at JINR: New prospects for heavy ion collisions and spin physics. *J. Phys. G*, 36:064069, 2009.

[55] V.D. Kekelidze, A.D. Kovalenko, I.N. Meshkov, A.S. Sorin, and G.V. Trubnikov. NICA at JINR: New prospects for exploration of quark-gluon matter. *Phys. Atom. Nucl.*, 75:542–545, 2012.

[56] Wit Busza, Krishna Rajagopal, and Wilke van der Schee. Heavy Ion Collisions: The Big Picture, and the Big Questions. *Ann. Rev. Nucl. Part. Sci.*, 68:339–376, 2018.

[57] Paolo Castorina, Salvatore Plumari, and Helmut Satz. Strangeness Production and Color Deconfinement. *Int. J. Mod. Phys.*, E26(12):1750081, 2017.

[58] S. Sarkar, H. Satz, and B. Sinha. The physics of the quark-gluon plasma. *Lect. Notes Phys., 785*, 2010.

[59] R. Hagedorn. Hadronic matter near the boiling point. *Nuovo Cim. A*, 56:1027–1057, 1968.

[60] J. Cleymans and H. Satz. Thermal hadron production in high-energy heavy ion collisions. *Z. Phys. C*, 57:135–148, 1993.

[61] P. Braun-Munzinger, J. Stachel, J.P. Wessels, and N. Xu. Thermal equilibration and expansion in nucleus-nucleus collisions at the AGS. *Phys. Lett. B*, 344:43–48, 1995.

[62] Francesco Becattini. A Thermodynamical approach to hadron production in e+ e- collisions. *Z. Phys. C*, 69(3):485–492, 1996.

[63] F. Becattini. Universality of thermal hadron production in p p, p anti-p and e+ e- collisions. In *Universality features in multihadron production and the leading effect. Proceedings, 33rd Workshop of the INFN Eloisatron Project, Erice, Italy, October 19-25, 1996*, pages 74–104, 1996.

[64] F. Becattini and Ulrich W. Heinz. Thermal hadron production in p p and p anti-p collisions. *Z. Phys. C*, 76:269–286, 1997. [Erratum: Z.Phys.C 76, 578 (1997)].

[65] V. Magas and H. Satz. Conditions for confinement and freezeout. *Eur. Phys. J.*, C32:115–119, 2003.

[66] E. Beth and G. Uhlenbeck. The quantum theory of the non-ideal gas. II. Behaviour at low temperatures. *Physica*, 4:915–924, 1937.

[67] Larry D. McLerran and T. Toimela. Photon and Dilepton Emission from the Quark - Gluon Plasma: Some General Considerations. *Phys. Rev. D*, 31:545, 1985.

[68] Rupa Chatterjee, Lusaka Bhattacharya, and Dinesh K. Srivastava. Electromagnetic probes. *Lect. Notes Phys.*, 785:219–264, 2010.

[69] F. Becattini. An Introduction to the Statistical Hadronization Model. In *International School on Quark-Gluon Plasma and Heavy Ion Collisions: past, present, future*, 1 2009.

[70] Ulrich Heinz and Raimond Snellings. Collective flow and viscosity in relativistic heavy-ion collisions. *Ann. Rev. Nucl. Part. Sci.*, 63:123–151, 2013.

[71] Paul Romatschke and Ulrike Romatschke. *Relativistic Fluid Dynamics In and Out of Equilibrium.* Cambridge Monographs on Mathematical Physics. Cambridge University Press, 5 2019.

[72] Xiaofeng Luo, Shusu Shi, Nu Xu, and Yifei Zhang. A Study of the Properties of the QCD Phase Diagram in High-Energy Nuclear Collisions. *Particles*, 3(2):278–307, 2020.

[73] James L. Nagle and William A. Zajc. Small System Collectivity in Relativistic Hadronic and Nuclear Collisions. *Ann. Rev. Nucl. Part. Sci.*, 68:211–235, 2018.

[74] T. Matsui and H. Satz. J/ψ Suppression by Quark-Gluon Plasma Formation. *Phys. Lett. B*, 178:416–422, 1986.

[75] Saumen Datta, Frithjof Karsch, Peter Petreczky, and Ines Wetzorke. Behavior of charmonium systems after deconfinement. *Phys. Rev. D*, 69:094507, 2004.

[76] Panagiota Foka and Małgorzata Anna Janik. An overview of experimental results from ultra-relativistic heavy-ion collisions at the CERN LHC: Hard probes. *Rev. Phys.*, 1:172–194, 2016.

[77] Robert L. Thews, Martin Schroedter, and Johann Rafelski. Enhanced J/ψ production in deconfined quark matter. *Phys. Rev. C*, 63:054905, 2001.

[78] P. Braun-Munzinger and J. Stachel. (Non)thermal aspects of charmonium production and a new look at J / psi suppression. *Phys. Lett. B*, 490:196–202, 2000.

[79] A. Andronic, P. Braun-Munzinger, K. Redlich, and J. Stachel. The thermal model on the verge of the ultimate test: particle production in Pb-Pb collisions at the LHC. *J. Phys. G*, 38:124081, 2011.

[80] J.D. Bjorken. Energy Loss of Energetic Partons in Quark - Gluon Plasma: Possible Extinction of High p(t) Jets in Hadron - Hadron Collisions. ., 8 1982.

[81] Miklos Gyulassy and Michael Plumer. Jet Quenching in Dense Matter. *Phys. Lett. B*, 243:432–438, 1990.

[82] Xin-Nian Wang and Miklos Gyulassy. Gluon shadowing and jet quenching in A + A collisions at s**(1/2) = 200-GeV. *Phys. Rev. Lett.*, 68:1480–1483, 1992.

[83] Georges Aad et al. Measurements of the Nuclear Modification Factor for Jets in Pb+Pb Collisions at $\sqrt{s_{\mathrm{NN}}} = 2.76$ TeV with the ATLAS Detector. *Phys. Rev. Lett.*, 114(7):072302, 2015.

[84] Johann Rafelski and Berndt Muller. Strangeness Production in the Quark - Gluon Plasma. *Phys. Rev. Lett.*, 48:1066, 1982. [Erratum: Phys.Rev.Lett. 56, 2334 (1986)].

[85] P. Koch, Berndt Muller, and Johann Rafelski. Strangeness in Relativistic Heavy Ion Collisions. *Phys. Rept.*, 142:167–262, 1986.

[86] Johann Rafelski. Melting Hadrons, Boiling Quarks. *Eur. Phys. J. A*, 51(9):114, 2015.

[87] Johann Rafelski. Formation and Observables of the Quark-Gluon Plasma. *Phys. Rept.*, 88:331, 1982.

[88] Johann Rafelski. Strangeness in Quark-Gluon Plasma. *South Afr. J. Phys.*, 6:37–43, 1983.

[89] Johann Rafelski. Strangeness Production in the Quark Gluon Plasma. *Nucl. Phys. A*, 418:215C–235C, 1984.

[90] J. Bartke et al. Neutral strange particle production in sulphur sulphur and proton sulphur collisions at 200-GeV/nucleon. *Z. Phys. C*, 48:191–200, 1990.

[91] C. Pinkenburg et al. Production and collective behavior of strange particles in Au + Au collisions at 2-AGeV - 8-AGeV. *Nucl. Phys. A*, 698:495–498, 2002.

[92] T. Abbott et al. Kaon and pion production in central Si + Au collisions at 14.6-A/GeV/c. *Phys. Rev. Lett.*, 64:847–850, 1990.

[93] F. Antinori et al. Enhancement of hyperon production at central rapidity in 158-A-GeV/c Pb-Pb collisions. *J. Phys. G*, 32:427–442, 2006.

[94] E. Andersen et al. Strangeness enhancement at mid-rapidity in Pb Pb collisions at 158-A-GeV/c. *Phys. Lett. B*, 449:401–406, 1999.

[95] Jaroslav Adam et al. Enhanced production of multi-strange hadrons in high-multiplicity proton-proton collisions. *Nature Phys.*, 13:535–539, 2017.

[96] F. Becattini, P. Castorina, J. Manninen and H. Satz. The Thermal Production of Strange and Non-Strange Hadrons in e^+e^- Collisions. *Eur. Phys. J. C* 56:493-510, 2008

[97] Jean Letessier, Johann Rafelski, and Ahmed Tounsi. Gluon production, cooling and entropy in nuclear collisions. *Phys. Rev. C*, 50:406–409, 1994.

[98] F. Becattini, P. Castorina, J. Manninen and H. Satz. The Thermal Production of Strange and Non-Strange Hadrons in e^+e^- Collisions. *Eur. Phys. J. C*, 56:493-510, 2008.

[99] Constantin Loizides. Experimental overview on small collision systems at the LHC. *Nucl. Phys.*, A956:200–207, 2016.

[100] Vardan Khachatryan et al. Observation of Long-Range Near-Side Angular Correlations in Proton-Proton Collisions at the LHC. *JHEP*, 09:091, 2010.

[101] Serguei Chatrchyan et al. Observation of Long-Range Near-Side Angular Correlations in Proton-Lead Collisions at the LHC. *Phys. Lett. B*, 718:795–814, 2013.

[102] Betty Abelev et al. Long-range angular correlations on the near and away side in p-Pb collisions at $\sqrt{s_{NN}} = 5.02$ TeV. *Phys. Lett. B*, 719:29–41, 2013.

[103] Georges Aad et al. Observation of Associated Near-Side and Away-Side Long-Range Correlations in $\sqrt{s_{NN}}$=5.02 TeV Proton-Lead Collisions with the ATLAS Detector. *Phys. Rev. Lett.*, 110(18):182302, 2013.

[104] A. Adare et al. Quadrupole Anisotropy in Dihadron Azimuthal Correlations in Central d+Au Collisions at $\sqrt{s_{NN}}$=200 GeV. *Phys. Rev. Lett.*, 111(21):212301, 2013.

[105] Georges Aad et al. Measurement with the ATLAS detector of multi-particle azimuthal correlations in p+Pb collisions at $\sqrt{s_{NN}}$ =5.02 TeV. *Phys. Lett. B*, 725:60–78, 2013.

[106] Serguei Chatrchyan et al. Multiplicity and Transverse Momentum Dependence of Two- and Four-Particle Correlations in pPb and PbPb Collisions. *Phys. Lett.*, B724:213–240, 2013.

[107] Serguei Chatrchyan et al. Study of the Production of Charged Pions, Kaons, and Protons in pPb Collisions at $\sqrt{s_{NN}} = 5.02$ TeV. *Eur. Phys. J. C*, 74(6):2847, 2014.

[108] Betty Bezverkhny Abelev et al. Multiplicity Dependence of Pion, Kaon, Proton and Lambda Production in p-Pb Collisions at $\sqrt{s_{NN}} =$ 5.02 TeV. *Phys. Lett.*, B728:25–38, 2014.

[109] Betty Bezverkhny Abelev et al. Long-range angular correlations of π, K and p in p-Pb collisions at $\sqrt{s_{\rm NN}} = 5.02$ TeV. *Phys. Lett. B*, 726:164–177, 2013.

[110] Betty Bezverkhny Abelev et al. Multiparticle azimuthal correlations in p -Pb and Pb-Pb collisions at the CERN Large Hadron Collider. *Phys. Rev. C*, 90(5):054901, 2014.

[111] Georges Aad et al. Measurement of long-range pseudorapidity correlations and azimuthal harmonics in $\sqrt{s_{NN}} = 5.02$ TeV proton-lead collisions with the ATLAS detector. *Phys. Rev. C*, 90(4):044906, 2014.

[112] Vardan Khachatryan et al. Long-range two-particle correlations of strange hadrons with charged particles in pPb and PbPb collisions at LHC energies. *Phys. Lett. B*, 742:200–224, 2015.

[113] B.I. Abelev et al. Long range rapidity correlations and jet production in high energy nuclear collisions. *Phys. Rev. C*, 80:064912, 2009.

[114] B. Alver et al. High transverse momentum triggered correlations over a large pseudorapidity acceptance in Au+Au collisions at s(NN)**1/2 = 200 GeV. *Phys. Rev. Lett.*, 104:062301, 2010.

[115] K. Aamodt et al. Harmonic decomposition of two-particle angular correlations in Pb-Pb collisions at $\sqrt{s_{NN}} = 2.76$ TeV. *Phys. Lett. B*, 708:249–264, 2012.

[116] G. Agakishiev et al. System size and energy dependence of near-side di-hadron correlations. *Phys. Rev. C*, 85:014903, 2012.

[117] Multiplicity dependence of multiparticle correlations in pPb and PbPb collisions. 5 2014.

[118] R. Granier de Cassagnac. CMS heavy-ion overview. *Nucl. Phys. A*, 931:13–21, 2014.

[119] Piotr Bozek and Wojciech Broniowski. Collective dynamics in high-energy proton-nucleus collisions. *Phys. Rev. C*, 88(1):014903, 2013.

[120] Morad Aaboud et al. Measurements of long-range azimuthal anisotropies and associated Fourier coefficients for *pp* collisions at $\sqrt{s} = 5.02$ and 13 TeV and p+Pb collisions at $\sqrt{s_{\mathrm{NN}}} = 5.02$ TeV with the ATLAS detector. *Phys. Rev.*, C96(2):024908, 2017.

[121] Vardan Khachatryan et al. Measurement of long-range near-side two-particle angular correlations in pp collisions at $\sqrt{s}$ =13 TeV. *Phys. Rev. Lett.*, 116(17):172302, 2016.

[122] Georges Aad et al. Observation of Long-Range Elliptic Azimuthal Anisotropies in $\sqrt{s}$ =13 and 2.76 TeV *pp* Collisions with the ATLAS Detector. *Phys. Rev. Lett.*, 116(17):172301, 2016.

[123] Vardan Khachatryan et al. Evidence for collectivity in pp collisions at the LHC. *Phys. Lett.*, B765:193–220, 2017.

[124] Ulrich Heinz et al. Exploring the properties of the phases of QCD matter - research opportunities and priorities for the next decade. 1 2015.

[125] Anthony Badea, Austin Baty, Paoti Chang, Gian Michele Innocenti, Marcello Maggi, Christopher Mcginn, Michael Peters, Tzu-An Sheng, Jesse Thaler, and Yen-Jie Lee. Measurements of two-particle correlations in e^+e^- collisions at 91 GeV with ALEPH archived data. *Phys. Rev. Lett.*, 123(21):212002, 2019.

[126] A. Abdesselam et al. Measurement of two-particle correlations in hadronic e^+e^- collisions at Belle. 8 2020.

[127] Vardan Khachatryan et al. Measurement of inclusive jet production and nuclear modifications in pPb collisions at $\sqrt{s_{\rm NN}} = 5.02$ TeV. *Eur. Phys. J. C*, 76(7):372, 2016.

[128] Wit Busza. Structure and fine structure in multiparticle production data at high energies. *Acta Phys. Polon. B*, 35:2873–2894, 2004.

[129] Jaroslav Adam et al. Multiplicity dependence of charged pion, kaon, and (anti)proton production at large transverse momentum in p-Pb collisions at $\sqrt{s_{\rm NN}} = 5.02$ TeV. *Phys. Lett.*, B760:720–735, 2016.

[130] J.E. Elias, W. Busza, C. Halliwell, David Luckey, P. Swartz, L. Votta, and C. Young. An Experimental Study of Multiparticle Production in Hadron - Nucleus Interactions at High-Energy. *Phys. Rev. D*, 22:13, 1980.

[131] B. Alver et al. Phobos results on charged particle multiplicity and pseudorapidity distributions in Au+Au, Cu+Cu, d+Au, and p+p collisions at ultra-relativistic energies. *Phys. Rev.*, C83:024913, 2011.

[132] Jaroslav Adam et al. Centrality dependence of the pseudorapidity density distribution for charged particles in Pb-Pb collisions at $\sqrt{s_{\rm NN}} = 5.02$ TeV. *Phys. Lett. B*, 772:567–577, 2017.

[133] B.B. Back et al. Centrality and energy dependence of charged-particle multiplicities in heavy ion collisions in the context of elementary reactions. *Phys. Rev. C*, 74:021902, 2006.

[134] Jan Fiete Grosse-Oetringhaus and Klaus Reygers. Charged-Particle Multiplicity in Proton-Proton Collisions. *J. Phys. G*, 37:083001, 2010.

[135] M. Basile, G. Cara Romeo, L. Cifarelli, A. Contin, G. D'Ali, C. Del Papa, P. Giusti, T. Massam, R. Nania and F. Palmonari, *et al.* The Leading Effect Explains the Charged Particle Multiplicity Distribution Observed at the {CERN} $p\bar{p}$ Collider. *Lett. Nuovo Cim.* 41:298, 1984.

[136] Georges Aad et al. Observation of Long-Range Elliptic Azimuthal Anisotropies in $\sqrt{s}$ =13 and 2.76 TeV pp Collisions with the ATLAS Detector. *Phys. Rev. Lett.*, 116(17):172301, 2016.

[137] Vardan Khachatryan et al. Observation of Long-Range Near-Side Angular Correlations in Proton-Proton Collisions at the LHC. *JHEP*, 09:091, 2010.

[138] Vardan Khachatryan et al. Measurement of long-range near-side two-particle angular correlations in pp collisions at $\sqrt{s}$ =13 TeV. *Phys. Rev. Lett.*, 116(17):172302, 2016.

[139] C. Aidala et al. Creation of quark–gluon plasma droplets with three distinct geometries. *Nature Phys.*, 15(3):214–220, 2019.

[140] Edward K. G. Sarkisyan, Aditya Nath Mishra, Raghunath Sahoo, and Alexander S. Sakharov. Centrality dependence of midrapidity density from GeV to TeV heavy-ion collisions in the effective-energy

universality picture of hadroproduction. *Phys. Rev.*, D94(1):011501, 2016.

[141] Constantin Loizides. Experimental overview on small collision systems at the LHC. *Nucl. Phys.*, A956:200–207, 2016.

[142] P. Castorina, D. Lanteri, and H. Satz. Strangeness enhancement and flow-like effects in e^+e^- annihilation at high parton density. *Under review*, arXiv:2011.06966.

[143] Paolo Castorina, Alfredo Iorio, Lanteri Daniele, Helmut Satz, and Martin Spousta. Universality in High Energy Collisions of small and large systems. Proceedings: 40th International Conference on High Energy Physics (ICHEP) 2020

[144] Paolo Castorina, Alfredo Iorio, Daniele Lanteri, Martin Spousta, and Helmut Satz. Universality in Hadronic and Nuclear Collisions at High Energy. *Phys. Rev. C*, 101(5):054902, 2020.

[145] S. Manly et al. System size, energy and pseudorapidity dependence of directed and elliptic flow at RHIC. *Nucl. Phys.*, A774:523–526, 2006.

[146] Rajeev S. Bhalerao and Jean-Yves Ollitrault. Eccentricity fluctuations and elliptic flow at RHIC. *Phys. Lett.*, B641:260–264, 2006.

[147] B. Alver et al. Importance of correlations and fluctuations on the initial source eccentricity in high-energy nucleus-nucleus collisions. *Phys. Rev.*, C77:014906, 2008.

[148] Tetsufumi Hirano and Yasushi Nara. Eccentricity fluctuation effects on elliptic flow in relativistic heavy ion collisions. *Phys. Rev.*, C79:064904, 2009.

[149] J. D. Bjorken, Hadron Final States in Deep Inelastic Processes. *Lect. Notes Phys.* 56:93, 1976.

[150] Constantin Loizides, Jason Kamin, and David d'Enterria. Improved Monte Carlo Glauber predictions at present and future nuclear colliders. *Phys. Rev.*, C97(5):054910, 2018. [erratum: Phys. Rev.C99,no.1,019901(2019)].

[151] Larry McLerran, Michal Praszalowicz, and Björn Schenke. Transverse Momentum of Protons, Pions and Kaons in High Multiplicity pp and pA Collisions: Evidence for the Color Glass Condensate? *Nucl. Phys.*, A916:210–218, 2013.

[152] Adam Bzdak, Bjoern Schenke, Prithwish Tribedy, and Raju Venugopalan. Initial state geometry and the role of hydrodynamics in proton-proton, proton-nucleus and deuteron-nucleus collisions. *Phys. Rev.*, C87(6):064906, 2013.

[153] Larry McLerran and Prithwish Tribedy. Intrinsic Fluctuations of the Proton Saturation Momentum Scale in High Multiplicity p+p Collisions. *Nucl. Phys.*, A945:216–225, 2016.

[154] M. Luscher, G. Munster, and P. Weisz. How Thick Are Chromoelectric Flux Tubes? *Nucl. Phys. B*, 180:1–12, 1981.

[155] P. Castorina, D. Kharzeev, and H. Satz. Thermal Hadronization and Hawking-Unruh Radiation in QCD. *Eur. Phys. J. C*, 52:187–201, 2007.

[156] Serguei Chatrchyan et al. Measurement of the elliptic anisotropy of charged particles produced in PbPb collisions at $\sqrt{s}_{NN}$=2.76 TeV. *Phys. Rev.*, C87(1):014902, 2013.

[157] Emil Avsar, Christoffer Flensburg, Yoshitaka Hatta, Jean-Yves Ollitrault, and Takahiro Ueda. Eccentricity and elliptic flow in proton–proton collisions from parton evolution. *Phys. Lett.*, B702:394–397, 2011.

[158] Betty Bezverkhny Abelev et al. Multi-strange baryon production at mid-rapidity in Pb-Pb collisions at $\sqrt{s_{NN}}$ = 2.76 TeV. *Phys. Lett.*, B728:216–227, 2014. [Erratum: Phys. Lett.B734,409(2014)].

[159] Paolo Castorina and Helmut Satz. Strangeness Production in AA and pp Collisions. *Eur. Phys. J.*, A52(7):200, 2016.

[160] P. Castorina, S. Plumari, and H. Satz. Universal Strangeness Production in Hadronic and Nuclear Collisions. *Int. J. Mod. Phys.*, E25(08):1650058, 2016.

[161] P. Castorina, S. Plumari, and H. Satz. Addendum to Strangeness Production and Color Deconfinement. *Int. J. Mod. Phys.*, E27:1891001, 2018.

[162] A. Adare et al. Scaling properties of fractional momentum loss of high-p_T hadrons in nucleus-nucleus collisions at $\sqrt{s_{NN}}$ from 62.4 GeV to 2.76 TeV. *Phys. Rev.*, C93(2):024911, 2016.

[163] Paolo Castorina, Salvatore Plumari, and Helmut Satz. Strangeness Production and Color Deconfinement. *Int. J. Mod. Phys.*, E26(12):1750081, 2017.

[164] P. Castorina, S. Plumari, and H. Satz. Addendum to Strangeness Production and Color Deconfinement. *Int. J. Mod. Phys.*, E27:1891001, 2018.

[165] A. Andronic, P. Braun-Munzinger, K. Redlich and J. Stachel, Decoding the phase structure of QCD via particle production at high energy. *Nature* 561(7723):321-330, 2018.

[166] J. Takahashi and R. Derradi de Souza. Strangeness production in STAR. In *24th Winter Workshop on Nuclear Dynamics (WWND 2008) South Padre Island, Texas, April 5-12, 2008*, 2008.

[167] Francesco Becattini, Marcus Bleicher, Thorsten Kollegger, Tim Schuster, Jan Steinheimer, and Reinhard Stock. Hadron Formation in Relativistic Nuclear Collisions and the QCD Phase Diagram. *Phys. Rev. Lett.*, 111:082302, 2013.

[168] L. Adamczyk et al. Bulk Properties of the Medium Produced in Relativistic Heavy-Ion Collisions from the Beam Energy Scan Program. *Phys. Rev.*, C96(4):044904, 2017.

[169] P. Castorina, M. Floris, S. Plumari, and H. Satz. Universal strangeness production and size fluctuactions in small and large systems. *PoS*, EPS-HEP2017:158, 2017.

[170] Paolo Castorina and Helmut Satz. Strangeness Production in AA and pp Collisions. *Eur. Phys. J.*, A52(7):200, 2016.

[171] P. Castorina, S. Plumari, and H. Satz. Universal Strangeness Production in Hadronic and Nuclear Collisions. *Int. J. Mod. Phys.*, E25(08):1650058, 2016.

[172] Betty Abelev et al. Centrality dependence of π, K, p production in Pb-Pb collisions at $\sqrt{s_{NN}} = 2.76$ TeV. *Phys. Rev.*, C88:044910, 2013.

[173] Betty Bezverkhny Abelev et al. K^0_S and Λ production in Pb-Pb collisions at $\sqrt{s_{NN}} = 2.76$ TeV. *Phys. Rev. Lett.*, 111:222301, 2013.

[174] Peter Kalinak. Strangeness production in Pb-Pb collisions with ALICE at the LHC. *PoS*, EPS-HEP2017:168, 2017.

[175] Jaroslav Adam et al. Multi-strange baryon production in p-Pb collisions at $\sqrt{s_{\mathbf{NN}}} = 5.02$ TeV. *Phys. Lett.*, B758:389–401, 2016.

[176] Shreyasi Acharya et al. Production of charged pions, kaons and (anti)protons in Pb-Pb and inelastic pp collisions at $\sqrt{s_{\mathrm{NN}}} = 5.02$ TeV. 2019.

[177] Larry McLerran, Michal Praszalowicz, and Björn Schenke. Transverse Momentum of Protons, Pions and Kaons in High Multiplicity pp and pA Collisions: Evidence for the Color Glass Condensate? *Nucl. Phys. A*, 916:210–218, 2013.

[178] Adam Bzdak, Bjoern Schenke, Prithwish Tribedy, and Raju Venugopalan. Initial state geometry and the role of hydrodynamics in proton-proton, proton-nucleus and deuteron-nucleus collisions. *Phys. Rev.*, C87(6):064906, 2013.

[179] Larry McLerran and Prithwish Tribedy. Intrinsic Fluctuations of the Proton Saturation Momentum Scale in High Multiplicity p+p Collisions. *Nucl. Phys.*, A945:216–225, 2016.

[180] Christian Klein-Bösing and Larry McLerran. Geometrical Scaling of Direct-Photon Production in Hadron Collisions from RHIC to the LHC. *Phys. Lett.*, B734:282–285, 2014.

[181] Betty Abelev et al. Centrality Dependence of Charged Particle Production at Large Transverse Momentum in Pb–Pb Collisions at $\sqrt{s_{\rm NN}} = 2.76$ TeV. *Phys. Lett.*, B720:52–62, 2013.

[182] Betty Bezverkhny Abelev et al. Energy Dependence of the Transverse Momentum Distributions of Charged Particles in pp Collisions Measured by ALICE. *Eur. Phys. J.*, C73(12):2662, 2013.

[183] S. Acharya et al. Transverse momentum spectra and nuclear modification factors of charged particles in pp, p-Pb and Pb-Pb collisions at the LHC. *JHEP*, 11:013, 2018.

[184] Shreyasi Acharya et al. Transverse momentum spectra and nuclear modification factors of charged particles in Xe-Xe collisions at $\sqrt{s_{\rm NN}}$ = 5.44 TeV. *Phys. Lett.*, B788:166–179, 2019.

[185] B. Alver et al. System size, energy, pseudorapidity, and centrality dependence of elliptic flow. *Phys. Rev. Lett.*, 98:242302, 2007.

[186] B. Alver et al. Elliptic Flow and Initial Eccentricity in Cu+Cu and Au+Au Collisions at RHIC. *J. Phys.*, G34:S887–892, 2007.

[187] Michelangelo L. Mangano and Benjamin Nachman. Observables for possible QGP signatures in central pp collisions. *Eur. Phys. J. C*, 78(4):343, 2018.

[188] B. G. Zakharov. Parton energy loss in the mini quark-gluon plasma and jet quenching in proton-proton collisions. *J. Phys.*, G41:075008, 2014.

[189] Georges Aad et al. Transverse momentum and process dependent azimuthal anisotropies in $\sqrt{s_{\rm NN}} = 8.16$ TeV p+Pb collisions with the ATLAS detector. *Eur. Phys. J. C*, 80(1):73, 2020.

[190] Shreyasi Acharya et al. Investigations of Anisotropic Flow Using Multiparticle Azimuthal Correlations in pp, p-Pb, Xe-Xe, and Pb-Pb Collisions at the LHC. *Phys. Rev. Lett.*, 123(14):142301, 2019.

[191] Albert M Sirunyan et al. Pseudorapidity and transverse momentum dependence of flow harmonics in pPb and PbPb collisions. *Phys. Rev. C*, 98(4):044902, 2018.

[192] Georges Aad et al. Measurement of flow harmonics correlations with mean transverse momentum in lead-lead and proton-lead collisions at $\sqrt{s_{NN}} = 5.02$ TeV with the ATLAS detector. *Eur. Phys. J. C*, 79(12):985, 2019.

[193] Nima Arkani-Hamed, Tao Han, Michelangelo Mangano, and Lian-Tao Wang. Physics opportunities of a 100 TeV proton–proton collider. *Phys. Rept.*, 652:1–49, 2016.

[194] Kenneth G. Wilson. Confinement of Quarks. pages 45–59, 2 1974.

[195] M. Tanabashi et al. Review of Particle Physics. *Phys. Rev. D*, 98(3):030001, 2018.

[196] Claudia Ratti. Lattice QCD and heavy ion collisions: a review of recent progress. *Rept. Prog. Phys.*, 81(8):084301, 2018.

[197] C. Patrignani et al. Review of Particle Physics. *Chin. Phys. C*, 40(10):100001, 2016.

[198] Holger Bech Nielsen and M. Ninomiya. No Go Theorem for Regularizing Chiral Fermions. *Phys. Lett. B*, 105:219–223, 1981.

[199] M. Luscher and P. Weisz. On-Shell Improved Lattice Gauge Theories. *Commun. Math. Phys.*, 97:59, 1985. [Erratum: Commun.Math.Phys. 98, 433 (1985)].

[200] Leonard Susskind. Lattice Fermions. *Phys. Rev. D*, 16:3031–3039, 1977.

[201] A. Bazavov et al. Fluctuations and Correlations of net baryon number, electric charge, and strangeness: A comparison of lattice QCD results with the hadron resonance gas model. *Phys. Rev. D*, 86:034509, 2012.

[202] Alexei Bazavov. The QCD equation of state. *Nucl. Phys. A*, 931:867–871, 2014.

[203] A. Bazavov et al. Equation of state in (2+1)-flavor QCD. *Phys. Rev.*, D90:094503, 2014.

[204] A. Bazavov et al. The QCD Equation of State to $\mathcal{O}(\mu_B^6)$ from Lattice QCD. *Phys. Rev.*, D95(5):054504, 2017.

[205] Volodymyr Vovchenko and Horst Stöcker. Surprisingly large uncertainties in temperature extraction from thermal fits to hadron yield data at LHC. *J. Phys. G*, 44(5):055103, 2017.

[206] F. Karsch, K. Redlich, and A. Tawfik. Hadron resonance mass spectrum and lattice QCD thermodynamics. *Eur. Phys. J. C*, 29:549–556, 2003.

[207] F. Becattini, J. Cleymans, A. Keranen, E Suhonen, and K. Redlich. Features of particle multiplicities and strangeness production in central heavy ion collisions between 1.7A-GeV/c and 158A-GeV/c. *Phys. Rev. C*, 64:024901, 2001.

[208] P. Braun-Munzinger, D. Magestro, K. Redlich, and J. Stachel. Hadron production in Au - Au collisions at RHIC. *Phys. Lett. B*, 518:41–46, 2001.

[209] Johann Rafelski and Jean Letessier. Testing limits of statistical hadronization. *Nucl. Phys. A*, 715:98–107, 2003.

[210] A. Andronic, P. Braun-Munzinger, and J. Stachel. Hadron production in central nucleus-nucleus collisions at chemical freeze-out. *Nucl. Phys. A*, 772:167–199, 2006.

[211] F. Becattini, J. Manninen, and M. Gazdzicki. Energy and system size dependence of chemical freeze-out in relativistic nuclear collisions. *Phys. Rev.*, C73:044905, 2006.

[212] P. Braun-Munzinger, I. Heppe, and J. Stachel. Chemical equilibration in Pb + Pb collisions at the SPS. *Phys. Lett. B*, 465:15–20, 1999.

[213] Peter Braun-Munzinger, Krzysztof Redlich, and Johanna Stachel. Particle production in heavy ion collisions. pages 491–599, 4 2003.

[214] E. Suhonen and S. Sohlo. Three Phase Description of Strongly Interacting Matter. *J. Phys. G*, 13:1487–1495, 1987.

[215] Dirk H. Rischke, Mark I. Gorenstein, Horst Stoecker, and Walter Greiner. Excluded volume effect for the nuclear matter equation of state. *Z. Phys. C*, 51:485–490, 1991.

[216] L.M. Satarov, V. Vovchenko, P. Alba, M.I. Gorenstein, and H. Stoecker. New scenarios for hard-core interactions in a hadron resonance gas. *Phys. Rev. C*, 95(2):024902, 2017.

[217] N. F. Carnahan and K. E. Starling. Equation of State for Nonattracting Rigid Spheres. *J. Chem. Phys.*, 51:635, 1969.

[218] V. Vovchenko, D.V. Anchishkin, and M.I. Gorenstein. Particle number fluctuations for the van der Waals equation of state. *J. Phys. A*, 48(30):305001, 2015.

[219] Volodymyr Vovchenko. Equations of state for real gases on the nuclear scale. *Phys. Rev.*, C96(1):015206, 2017.

[220] Yoichiro Nambu and G. Jona-Lasinio. Dynamical Model of Elementary Particles Based on an Analogy with Superconductivity. 1. *Phys. Rev.*, 122:345–358, 1961.

[221] Yoichiro Nambu and G. Jona-Lasinio. DYNAMICAL MODEL OF ELEMENTARY PARTICLES BASED ON AN ANALOGY WITH SUPERCONDUCTIVITY. II. *Phys. Rev.*, 124:246–254, 1961.

[222] John Bardeen, L.N. Cooper, and J.R. Schrieffer. Microscopic theory of superconductivity. *Phys. Rev.*, 106:162, 1957.

[223] M.K. Volkov. Meson Lagrangians in a Superconductor Quark Model. *Annals Phys.*, 157:282–303, 1984.

[224] T. Hatsuda and T. Kunihiro. POSSIBLE CRITICAL PHENOMENA ASSOCIATED WITH THE CHIRAL SYMMETRY BREAKING. *Phys. Lett. B*, 145:7–10, 1984.

[225] G. Ecker. Chiral perturbation theory. *Prog. Part. Nucl. Phys.*, 35:1–80, 1995.

[226] V. Bernard, Norbert Kaiser, and Ulf-G. Meissner. Chiral dynamics in nucleons and nuclei. *Int. J. Mod. Phys. E*, 4:193–346, 1995.

[227] P. Gerber and H. Leutwyler. Hadrons Below the Chiral Phase Transition. *Nucl. Phys. B*, 321:387–429, 1989.

[228] Thomas D. Cohen, R.J. Furnstahl, and David K. Griegel. Quark and gluon condensates in nuclear matter. *Phys. Rev. C*, 45:1881–1893, 1992.

[229] Gerard 't Hooft. Computation of the Quantum Effects Due to a Four-Dimensional Pseudoparticle. *Phys. Rev. D*, 14:3432–3450, 1976. [Erratum: Phys.Rev.D 18, 2199 (1978)].

[230] Edward V. Shuryak. Hadrons Containing a Heavy Quark and QCD Sum Rules. *Nucl. Phys. B*, 198:83–101, 1982.

[231] Thomas Schäfer and Edward V. Shuryak. Instantons in QCD. *Rev. Mod. Phys.*, 70:323–426, 1998.

[232] R. Brockmann and R. Machleidt. Relativistic nuclear structure. 1: Nuclear matter. *Phys. Rev. C*, 42:1965–1980, 1990.

[233] A.R. Bodmer. Collapsed nuclei. *Phys. Rev. D*, 4:1601–1606, 1971.

[234] Edward Witten. Cosmic Separation of Phases. *Phys. Rev. D*, 30:272–285, 1984.

[235] Adam Miklos Halasz, A.D. Jackson, R.E. Shrock, Misha A. Stephanov, and J.J.M. Verbaarschot. On the phase diagram of QCD. *Phys. Rev. D*, 58:096007, 1998.

[236] J.B. Natowitz, R. Wada, K. Hagel, T. Keutgen, M. Murray, Y.G. Ma, A. Makeev, L. Qin, P. Smith, and C. Hamilton. Caloric curves and critical behavior in nuclei. *Phys. Rev. C*, 65:034618, 2002.

[237] P. Braun-Munzinger, J. Stachel, and Christof Wetterich. Chemical freezeout and the QCD phase transition temperature. *Phys. Lett. B*, 596:61–69, 2004.

[238] Edwin Laermann and Owe Philipsen. The Status of lattice QCD at finite temperature. *Ann. Rev. Nucl. Part. Sci.*, 53:163–198, 2003.

[239] P. Zhuang, J. Hufner, and S.P. Klevansky. Thermodynamics of a quark - meson plasma in the Nambu-Jona-Lasinio model. *Nucl. Phys. A*, 576:525–552, 1994.

[240] T.M. Schwarz, S.P. Klevansky, and G. Papp. The Phase diagram and bulk thermodynamical quantities in the NJL model at finite temperature and density. *Phys. Rev. C*, 60:055205, 1999.

[241] A. Barducci, R. Casalbuoni, G. Pettini, and L. Ravagli. A NJL-based study of the QCD critical line. *Phys. Rev. D*, 72:056002, 2005.

[242] Yue Zhao, Lei Chang, Wei Yuan, and Yu-xin Liu. Chiral susceptibility and chiral phase transition in Nambu-Jona-Lasinio model. *Eur. Phys. J. C*, 56:483–492, 2008.

[243] D. Ebert and H. Reinhardt. Effective Chiral Hadron Lagrangian with Anomalies and Skyrme Terms from Quark Flavor Dynamics. *Nucl. Phys. B*, 271:188–226, 1986.

[244] Tetsuo Hatsuda and Teiji Kunihiro. Effects of Explicit Su-f(3) Breaking on the Quark Condensates. *Phys. Lett. B*, 198:126–130, 1987.

[245] P. Rehberg, S.P. Klevansky, and J. Hufner. Hadronization in the SU(3) Nambu-Jona-Lasinio model. *Phys. Rev. C*, 53:410–429, 1996.

[246] T. Kunihiro. Effects of the U(a)(1) Anomaly on the Quark Condensates and Meson Properties at Finite Temperature. *Phys. Lett. B*, 219:363–368, 1989. [Erratum: Phys.Lett.B 245, 687 (1990)].

[247] A. Barducci, R. Casalbuoni, G. Pettini, and L. Ravagli. A NJL-based study of the QCD critical line. *Phys. Rev.*, D72:056002, 2005.

[248] R. Friedberg and T.D. Lee. Fermion Field Nontopological Solitons. 1. *Phys. Rev. D*, 15:1694, 1977.

[249] R. Friedberg and T.D. Lee. Fermion Field Nontopological Solitons. 2. Models for Hadrons. *Phys. Rev. D*, 16:1096, 1977.

[250] R. Friedberg and T.D. Lee. QCD and the Soliton Model of Hadrons. *Phys. Rev. D*, 18:2623, 1978.

[251] D.U. Jungnickel and C. Wetterich. Effective action for the chiral quark-meson model. *Phys. Rev. D*, 53:5142–5175, 1996.

[252] Bernd-Jochen Schaefer and Jochen Wambach. The Phase diagram of the quark meson model. *Nucl. Phys. A*, 757:479–492, 2005.

[253] Marco Ruggieri, Motoi Tachibana, and Vincenzo Greco. Renormalized vs Nonrenormalized Chiral Transition in a Magnetic Background. *JHEP*, 07:165, 2013.

[254] M. Ruggieri, L. Oliva, P. Castorina, R. Gatto, and V. Greco. Critical Endpoint and Inverse Magnetic Catalysis for Finite Temperature and Density Quark Matter in a Magnetic Background. *Phys. Lett. B*, 734:255–260, 2014.

[255] Marco Frasca and Marco Ruggieri. Magnetic Susceptibility of the Quark Condensate and Polarization from Chiral Models. *Phys. Rev. D*, 83:094024, 2011.

[256] V. Skokov, B. Stokic, B. Friman, and K. Redlich. Meson fluctuations and thermodynamics of the Polyakov loop extended quark-meson model. *Phys. Rev. C*, 82:015206, 2010.

[257] V. Skokov, B. Friman, E. Nakano, K. Redlich, and B.-J. Schaefer. Vacuum fluctuations and the thermodynamics of chiral models. *Phys. Rev. D*, 82:034029, 2010.

[258] Jonathan T. Lenaghan and Dirk H. Rischke. The O(N) model at finite temperature: Renormalization of the gap equations in Hartree and large N approximation. *J. Phys. G*, 26:431–450, 2000.

[259] Andreas Zacchi and Jürgen Schaffner-Bielich. Effects of Renormalizing the chiral SU(2) Quark-Meson-Model. *Phys. Rev.*, D97(7):074011, 2018.

[260] John M. Cornwall, R. Jackiw, and E. Tomboulis. Effective Action for Composite Operators. *Phys. Rev.*, D10:2428–2445, 1974.

[261] Yue Zhao, Lei Chang, Wei Yuan, and Yu-xin Liu. Chiral susceptibility and chiral phase transition in Nambu-Jona-Lasinio model. *Eur. Phys. J.*, C56:483–492, 2008.

[262] G. Amelino-Camelia and So-Young Pi. Selfconsistent improvement of the finite temperature effective potential. *Phys. Rev.*, D47:2356–2362, 1993.

[263] Dominik J. Schwarz. Evolution of gravitational waves through cosmological transitions. *Mod. Phys. Lett. A*, 13:2771–2778, 1998.

[264] Dominik J. Schwarz. The first second of the universe. *Annalen Phys.*, 12:220–270, 2003.

[265] Yuki Watanabe and Eiichiro Komatsu. Improved Calculation of the Primordial Gravitational Wave Spectrum in the Standard Model. *Phys. Rev. D*, 73:123515, 2006.

[266] Paolo Castorina, Vincenzo Greco, and Salvatore Plumari. QCD equation of state and cosmological parameters in the early universe. *Phys. Rev. D*, 92(6):063530, 2015.

[267] P. Castorina, D. Lanteri, and S. Mancani. Deconfinement transition effects on cosmological parameters and primordial gravitational waves spectrum. *Phys. Rev. D*, 98(2):023007, 2018.

[268] D. Boyanovsky, H. J. de Vega, and D. J. Schwarz. Phase transitions in the early and the present universe. *Ann. Rev. Nucl. Part. Sci.*, 56:441–500, 2006.

[269] Szabolcs Borsanyi, Gergely Endrodi, Zoltan Fodor, Antal Jakovac, Sandor D. Katz, Stefan Krieg, Claudia Ratti, and Kalman K. Szabo.

The QCD equation of state with dynamical quarks. *JHEP*, 11:077, 2010.

[270] Szabocls Borsanyi, Zoltan Fodor, Christian Hoelbling, Sandor D. Katz, Stefan Krieg, and Kalman K. Szabo. Full result for the QCD equation of state with 2+1 flavors. *Phys. Lett. B*, 730:99–104, 2014.

[271] Matt Visser. Jerk and the cosmological equation of state. *Class. Quant. Grav.*, 21:2603–2616, 2004.

[272] Maciej Dunajski and Gary Gibbons. Cosmic Jerk, Snap and Beyond. *Class. Quant. Grav.*, 25:235012, 2008.

[273] M.C. Guzzetti, N. Bartolo, M. Liguori, and S. Matarrese. Gravitational waves from inflation. *Riv. Nuovo Cim.*, 39(9):399–495, 2016.

[274] Simon Schettler, Tillmann Boeckel, and Jurgen Schaffner-Bielich. Imprints of the QCD Phase Transition on the Spectrum of Gravitational Waves. *Phys. Rev. D*, 83:064030, 2011.

[275] Yoichi Aso, Yuta Michimura, Kentaro Somiya, Masaki Ando, Osamu Miyakawa, Takanori Sekiguchi, Daisuke Tatsumi, and Hiroaki Yamamoto. Interferometer design of the KAGRA gravitational wave detector. *Phys. Rev. D*, 88(4):043007, 2013.

[276] M. Punturo et al. The Einstein Telescope: A third-generation gravitational wave observatory. *Class. Quant. Grav.*, 27:194002, 2010.

[277] C.S. Unnikrishnan. IndIGO and LIGO-India: Scope and plans for gravitational wave research and precision metrology in India. *Int. J. Mod. Phys. D*, 22:1341010, 2013.

[278] G.L. Guardo, V. Greco, and M. Ruggieri. Energy density fluctuations in Early Universe. *AIP Conf. Proc.*, 1595(1):224–227, 2014.

[279] R. C. Rao. Information and accuracy attainable in the estimation of statistical parameters. *Bulletin of the Calcutta Mathematical Society*, 37:81–91, 1945.

[280] Shun ichi Amari. *Differential-Geometrical Methods in Statistics*.

[281] F. Weinhold. Metric geometry of equilibrium thermodynamics. *The Journal of Chemical Physics*, 63(6):2479–2483, 1975.

[282] F. Weinhold. Metric geometry of equilibrium thermodynamics. v. aspects of heterogeneous equilibrium. *The Journal of Chemical Physics*, 65(2):559–564, 1976.

[283] George Ruppeiner. Thermodynamics: A riemannian geometric model. *Phys. Rev. A*, 20:1608–1613, Oct 1979.

[284] Peter Salamon and R.Stephen Berry. Thermodynamic Length and Dissipated Availability. *Phys. Rev. Lett.*, 51:1127–1130, 1983.

[285] P. Salamon, J. Nulton, and E. Ihrig. On the relation between entropy and energy versions of thermodynamic length. *The Journal of Chemical Physics*, 80(1):436–437, 1984.

[286] Gavin E. Crooks. Measuring thermodynamic length. *Physical Review Letters*, 99(10), Sep 2007.

[287] George Ruppeiner. Riemannian geometric theory of critical phenomena. *Phys. Rev. A*, 44:3583–3595, Sep 1991.

[288] George Ruppeiner. Riemannian geometry in thermodynamic fluctuation theory. *Rev. Mod. Phys.*, 67:605–659, 1995. [Erratum: Rev. Mod. Phys.68,313(1996)].

[289] George Ruppeiner. Riemannian geometric approach to critical points: General theory. *Phys. Rev. E*, 57:5135–5145, May 1998.

[290] P. Salamon L. Diósi. *From Statistical Distances to Minimally Dissipative Processes. In: Sieniutycz S., De Vos A. (eds) Thermodynamics of Energy Conversion and Transport.* Springer, New York, NY, 2020.

[291] Anurag Sahay. Restricted thermodynamic fluctuations and the Ruppeiner geometry of black holes. *Phys. Rev.*, D95(6):064002, 2017.

[292] Carlo Cafaro and Paul M. Alsing. Decrease of fisher information and the information geometry of evolution equations for quantum mechanical probability amplitudes. *Physical Review E*, 97(4), Apr 2018.

[293] F. Schlögl. Thermodynamic metric and stochastic measures. *Zeitschrift für Physik B Condensed Matter*, 59:449, 1985.

[294] Dorje Brody and Nicolas Rivier. Geometrical aspects of statistical mechanics. *Phys. Rev. E*, 51:1006–1011, 1995.

[295] Karl Heinz Hoffmann, Bjarne Andresen, and Peter Salamon. Measures of dissipation. *Phys. Rev. A*, 39:3618–3621, Apr 1989.

[296] Jacob Burbea and C.Radhakrishna Rao. Entropy differential metric, distance and divergence measures in probability spaces: A unified approach. *Journal of Multivariate Analysis*, 12(4):575 – 596, 1982.

[297] Richard F. Greene and Herbert B. Callen. On the formalism of thermodynamic fluctuation theory. *Phys. Rev.*, 83:1231–1235, Sep 1951.

[298] Behrouz Mirza and Hosein Mohammadzadeh. Ruppeiner Geometry of Anyon Gas. *Phys. Rev.*, E78:021127, 2008.

[299] George Ruppeiner, Anurag Sahay, Tapobrata Sarkar, and Gautam Sengupta. Thermodynamic Geometry, Phase Transitions, and the Widom Line. *Phys. Rev.*, E86:052103, 2012.

[300] George Ruppeiner. Thermodynamic curvature from the critical point to the triple point. *Phys. Rev. E*, 86:021130, Aug 2012.

[301] Helge-Otmar May and Peter Mausbach. Riemannian geometry study of vapor-liquid phase equilibria and supercritical behavior of the lennard-jones fluid. *Phys. Rev. E*, 85:031201, Mar 2012.

[302] Helge-Otmar May, Peter Mausbach, and George Ruppeiner. Thermodynamic curvature for attractive and repulsive intermolecular forces. *Phys. Rev. E*, 88:032123, Sep 2013.

[303] G. Ruppeiner, P. Mausbach, and H.-0. May. Thermodynamic r-diagrams reveal solid-like fluid states. *Physics Letters A*, 379(7):646–649, 2015.

[304] H. Janyszek. Riemannian geometry and stability of thermodynamical equilibrium systems. *Journal of Physics A: Mathematical and General*, 23(4):477–490, feb 1990.

[305] Hiroshi Oshima, Tsunehiro Obata, and Hiroaki Hara. Riemann scalar curvature of ideal quantum gases obeying gentile's statistics. *Journal of Physics A: Mathematical and General*, 32(36):6373–6383, aug 1999.

[306] M. R. Ubriaco. The role of curvature in quantum statistical mechanics. *J. Phys.: Conf. Ser.*, 766:012007, 2016.

[307] M. R. Ubriaco. Stability and anyonic behavior of systems with m-statistics. *Physica A: Statistical Mechanics and its Applications*, 392(20):4868–4873, 2013.

[308] Hosein Mohammadzadeh Hossein Mehri-Dehnavi. Thermodynamic geometry of kaniadakis statistics. *Journal of Physics A: Mathematical and Theoretical*, 53(37):375009, 2020.

[309] B. Widom. The critical point and scaling theory. *Physica*, 73(1):107 – 118, 1974.

[310] H. Janyszek and R. Mrugala. Riemannian geometry and the thermodynamics of model magnetic systems. *Phys. Rev. A*, 39:6515–6523, Jun 1989.

[311] H. Janyszek and R. Mrugala. Riemannian and finslerian geometry and fluctuations of thermodynamic systems. *Advances in Thermodynamics, Vol. 3, Nonequilibrium Theory and Extremum Principles*, pages 159–174, 1990.

[312] R. Ruppeiner, N. Dyjack, A. McAloon, and J. Stoops. Solid-like features in dense vapors near the fluid critical point. *The Journal of Chemical Physics*, 146:224501, 2017.

[313] Helge-Otmar May, Peter Mausbach, and George Ruppeiner. Thermodynamic geometry of supercooled water. *Phys. Rev. E*, 91:032141, Mar 2015.

[314] G. Ruppeiner. Thermodynamic curvature measures interactions. *Am. J. Phys.*, 78:1170, 2010.

[315] Anshuman Dey, Pratim Roy, and Tapobrata Sarkar. Information geometry, phase transitions, and the Widom line: Magnetic and liquid systems. *Physica*, A392:6341–6352, 2013.

[316] Pankaj Chaturvedi, Anirban Das, and Gautam Sengupta. Thermodynamic Geometry and Phase Transitions of Dyonic Charged AdS Black Holes. *Eur. Phys. J.*, C77(2):110, 2017.

[317] Anurag Sahay, Tapobrata Sarkar, and Gautam Sengupta. On the Thermodynamic Geometry and Critical Phenomena of AdS Black Holes. *JHEP*, 07:082, 2010.

[318] G. G. Simeoni, T. Bryk, F. A. Gorelli, M. Krisch, G. Ruocco, M. Santoro, and T. Scopigno. The widom line as the crossover between liquid-like and gas-like behaviour in supercritical fluids. *Nature Physics*, 6:503, 2010.

[319] H. B. Callen. Thermodynamics and an introduction to thermostatistics, 1985, wiley ed.

[320] Giovanni Arcioni and Ernesto Lozano-Tellechea. Stability and critical phenomena of black holes and black rings. *Phys. Rev. D*, 72:104021, 2005.

[321] George Ruppeiner. Stability and fluctuations in black hole thermodynamics. *Phys. Rev.*, D75:024037, 2007.

[322] H. Poincaré. Sur l'équilibre d'une masse fluide animée d'un mouvement de rotation. *Acta Mathematica*, 7:259, 1885.

[323] Joseph Katz, I. Okamoto, and O. Kaburaki. Thermodynamic stability of pure black holes. *Class. Quant. Grav.*, 10:1323–1339, 1993.

[324] Isao Okamoto, Joseph Katz, and Renaud Parentani. A Comment on fluctuations and stability limits with application to 'superheated' black holes. *Class. Quant. Grav.*, 12:443–448, 1995.

[325] O. Kaburaki, I. Okamoto, and J. Katz. Thermodynamic Stability of Kerr Black holes. *Phys. Rev. D*, 47:2234–2241, 1993.

[326] Renaud Parentani. The Inequivalence of thermodynamic ensembles. 10 1994.

[327] A. Bazavov et al. Freeze-out Conditions in Heavy Ion Collisions from QCD Thermodynamics. *Phys. Rev. Lett.*, 109:192302, 2012.

[328] Patrick Steinbrecher. The QCD crossover at zero and non-zero baryon densities from Lattice QCD. *Nucl. Phys.*, A982:847–850, 2019.

[329] J.-P. Blaizot. Theory of the quark gluon plasma. *Lect. Notes Phys.*, 583:117–160, 2002.

[330] Michele Floris. Hadron yields and the phase diagram of strongly interacting matter. *Nucl. Phys.*, A931:103–112, 2014.

[331] Sabita Das. Identified particle production and freeze-out properties in heavy-ion collisions at RHIC Beam Energy Scan program. *EPJ Web Conf.*, 90:08007, 2015.

[332] Volodymyr Vovchenko, Mark I. Gorenstein, and Horst Stoecker. van der Waals Interactions in Hadron Resonance Gas: From Nuclear Matter to Lattice QCD. *Phys. Rev. Lett.*, 118(18):182301, 2017.

[333] Saumen Datta, Frithjof Karsch, Peter Petreczky, and Ines Wetzorke. Meson correlators above deconfinement. *J. Phys. G*, 31:S351–S356, 2005.

[334] Paolo Cea, Leonardo Cosmai, Francesca Cuteri, and Alessandro Papa. QCD flux tubes across the deconfinement phase transition. *EPJ Web Conf.*, 175:12006, 2018.

[335] P. Castorina and M. Mannarelli. Effective degrees of freedom of the quark-gluon plasma. *Phys. Lett. B*, 644:336–339, 2007.

[336] Paolo Castorina and Massimo Mannarelli. Effective degrees of freedom and gluon condensation in the high temperature deconfined phase. *Phys. Rev. C*, 75:054901, 2007.

[337] P. Castorina, G. Nardulli, and D. Zappala. Nambu Jona-Lasinio model of anti-q q Bose Einstein condensation and pseudogap phase. *Phys. Rev. D*, 72:076006, 2005.

[338] Bing He, Hu Li, C.M. Shakin, and Qing Sun. Calculation of temperature dependent hadronic correlation functions of pseudoscalar and vector currents. *Phys. Rev. D*, 67:114012, 2003.

[339] A. Wergieluk, D. Blaschke, Yu.L. Kalinovsky, and A. Friesen. Pion dissociation and Levinson‘s theorem in hot PNJL quark matter. *Phys. Part. Nucl. Lett.*, 10:660–668, 2013.

[340] Edward Shuryak. Are there flux tubes in quark-gluon plasma? 6 2018.

[341] P. Castorina, D. Lanteri, and S. Mancani. Thermodynamic geometry of Nambu-Jona Lasinio model. *Eur. Phys. J. Plus*, 135(1):43, 2020.

[342] Bonan Zhang, Shen-Song Wan, and Marco Ruggieri. Thermodynamic Geometry of the Quark-Meson Model. *Phys. Rev.*, D101(1):016014, 2020.

[343] Aharon Casher. Chiral Symmetry Breaking in Quark Confining Theories. *Phys. Lett.*, 83B:395–398, 1979.

[344] Tom Banks and A. Casher. Chiral Symmetry Breaking in Confining Theories. *Nucl. Phys.*, B169:103–125, 1980.

[345] P. Castorina and P. Cea. he role of chirality in demarcating confinement from liberation. *Phys. Lett.*, 112B:151–153, 1982.

[346] S. Digal, E. Laermann, and H. Satz. Deconfinement through chiral symmetry restoration in two flavor QCD. *Eur. Phys. J.*, C18:583–586, 2001.

[347] H. T. Ding, P. Hegde, F. Karsch, A. Lahiri, S. T. Li, S. Mukherjee, and P. Petreczky. Chiral phase transition of (2+1)-flavor QCD. *Nucl. Phys.*, A982:211–214, 2019.

[348] P. Castorina, M. Floris, S. Plumari, and H. Satz. Universal strangeness production and size fluctuactions in small and large systems. *PoS*, EPS-HEP2017:158, 2017.